Theoretical modeling combined with experimental spectroscopic measurements for the diagnosis of high-Z erosion and transport applications in plasmas

by

Curtis Alan Johnson

A dissertation submitted to the Graduate Faculty of
Auburn University
in partial fulfillment of the
requirements for the Degree of
Doctor of Philosophy

Auburn, Alabama
December 12, 2020

Keywords: Collisional Radiative Modeling, Tungsten, Erosion, Sheath Model

Approved by

David A. Ennis, Chair, Associate Professor of Physics
Stuart D. Loch, Co-Chair, Professor of Physics
Edward Thomas, Professor of Physics
Dennis Bodewits, Associate Professor of Physics
Evangelos Miliordos, Assistant Professor of Chemistry and Biochemistry

Abstract

Understanding plasma-material interaction (PMI) continues to be a challenge for future fusion reactors. High-Z materials (e.g. tungsten, molybdenum) have emerged as leading solutions for plasma facing materials. Erosion and transport of these high-Z elements remains an open area of research which warrants study.

The properties of emission from ions in a plasma provides both potential for plasma diagnostics and key information required for plasma modeling. Generalized collisional radiative theory is a powerful tool for modeling of low and moderately dense plasmas. A new Python program (ColRadPy) has been developed that solves the collisional-radiative and ionization balance equations within the Generalized Collisional-Radiative framework. It has applications to fusion, basic laboratory and astrophysical plasmas. It produces generalized coefficients that can be easily imported into existing plasma modeling codes and spectral diagnostics.

A spectral survey of tungsten emission in the ultraviolet region has been completed in the DIII-D tokamak and the Compact Toroidal Hybrid (CTH) torsatron to assess the potential benefit of UV emission for the diagnosis of gross W erosion. A total of 53 W I spectral lines are observed from the two experiments using both survey and high-resolution spectrometers between $\sim 200 - 400$ nm. The level identifications presented in this work are based upon a previous atomic structure calculation and new high quality atomic data for neutral W. Of the 53 W I observed lines, 32 have not previously been reported at fusion relevant divertor plasmas conditions ($T_\mathrm{e} \sim 10-20$ eV, $n_\mathrm{e} \sim 1\times10^{13}$ cm^{-3}), including an intense line at 265.65 nm which could be important for benchmarking the frequently employed line at 400.88 nm. The impact of metastable level populations on the W I emission spectrum and any erosion measurement utilizing a spectroscopic technique is potentially significant and is quantified

in this work. Nevertheless, the high density of W I emission in the UV region allows for determination of the relative metastable fractions and plasma parameters local to the erosion region. There are also over 15 singly ionized tungsten emission lines as well as more than 10 doubly ionization emission lines that are also observed in the UV. W IV spectral lines could be observed in the UV, which is consistent with CR modeling. While the W I emission lines can be used to measure the gross tungsten erosion, the simultaneous observation of W I emission combined with W II lines identified in this work could be used to estimate the net erosion of tungsten from plasma facing components. Similarly, the fraction of tungsten that is promptly re-deposited could also be inferred. Identified lines can be used for collisional radiative based diagnostics such as line ratio diagnostics.

Key to this study are the new spin-changing collisional rate coefficients between potential metastable levels allowing the dynamics of metastable levels to be explored in detail for the first time. Long-lived metastable states in neutral tungsten can potentially impact measurements of tungsten erosion from plasma facing components. Time-dependent collisional radiative modeling of neutral tungsten is used to analyze the role of these states in tungsten emission and ionization. The large number of non-quasistatic atomic states in neutral tungsten can take on the order of milliseconds to reach equilibrium, depending on plasma conditions, causing erosion measurements to be affected by the time-dependence of the metastable populations. Previous measurements using the 400.88 nm neutral tungsten emission line could be affected by these non-quasistatic metastable effects. Therefore, a scheme for measuring the relative metastable fractions is proposed through simultaneous observation of multiple ultraviolet spectral lines of neutral tungsten. The accuracy of erosion measurements could potentially be increased by including these previously unconsidered metastable effects.

The Chodura sheath provides a region of low electron density on the order of centimeters (orders of magnitude larger than the Debye sheath) making time-dependent effects important due to the large number of metastable levels in neutral tungsten. A simple model is developed

to account for the effects of the Chodura sheath on the time-dependent neutral tungsten system. Eroded tungsten is assumed to sputter into the plasma as ground state atoms with ballistic velocity through the sheath until ionized.

The collisional radiative coefficients used in erosion measurements can be modified by up to a factor of 10 by addition of the sheath model at high electron densities. The ratio of the 254.14 to the 265.65 nm neutral tungsten lines is shown to be a promising temperature diagnostic from collisional radiative modeling. Comparisons between Langmuir probe measured electron temperatures and temperatures inferred from collisional radiative modeling of the line ratio yields good agreement for CTH plasmas. Thus, the work of this dissertation, and the new atomic data for neutral tungsten that has been generated for this project, provide the basis for accurate tungsten erosion and redeposition measurements on fusion relevant devices and yield a general roadmap for how to model the spectral emission from complex species such as tungsten.

Acknowledgments

First and foremost, I would like to thank my advisors David Ennis and Stuart Loch for continued patience with me over the years as well as being pleasant people to work with. Through my work presented here, I have learned a great deal about atomic physics, spectroscopy and plasma physics. I also would like to thank Greg Hartwell for his expertise in experimental methods and the nuts and bolts knowledge of CTH and John Dawson for help with many of the electronics required in this work. I would like to thank Dave Maurer for supporting the experiments that I did at CTH. We decided to construct a Langmuir probe relatively late into this work. I would like to thank Ed Thomas for his help which allowed me to design, construct and operate the probe exponentially faster than I would have been able to do on my own. The research done in this thesis would not be possible without the atomic data that was made by our collaborators at Queen's Univeristy Belfast for which I am greatly indebted to Connor Ballance. I would also like to thank Noah Kim for his help with line identification.

Recognition should also go to the other graduate students involved with CTH for the countless hours spent operating CTH. While studying at Auburn University, the entire faculty was more than helpful when I had questions. I would like to thank the DIII-D collaboration which encompasses the efforts of many different individuals and our collaborators at LLNL Steve Allen, Cameron Samuell, Brian Victor and Ron Ellis. They were instrumental in the successful install of the spectrometers for the DIII-D tungsten rings campaign and spent many hours providing support during this time. I would also like to thank Zeke Unterberg and Tyler Abrams for their work on making the DIII-D tungsten rings campaign a reality. I would like to specifically thank Cameron Samuell for being an early adapter of ColRadPy and being a great champion of the code.

I would like to thank my parents, Lynn and Jeff Johnson, for their love and continuous support throughout my studies. I would specifically like to thank my mom for reading every page of this thesis. Words cannot express how much they helped me continue on throughout my graduate school "career." I would like to thank my girlfriend Ali Fisher for her support through much of my studies.

My friends have been instrumental in keeping me sane while studying such a difficult subject. I have made many friends during my time in Auburn, in particular the "Party Cru": Omar Eulogio Lopez Ortiz, Spencer "Tiny" Shackleford, Steve Williams, Ahmad Nimer and Ali Fisher.

Table of Contents

Abstract ii

Acknowledgments v

List of Figures xi

List of Tables xxix

1 Introduction to plasma wall material choices and thesis overview 1

1.1 Plasma facing component requirements in fusion environments 1

1.2 Low-Z materials as a plasma facing material 3

1.3 High-Z materials as a plasma facing material 4

1.4 Erosion, re-deposition and migration 5

1.5 Thesis overview 6

2 The DIII-D tokamak and the Compact Toroidal Hybrid 9

2.1 Tungsten rings in the DIII-D tokamak divertor 9

2.2 The Compact Toroidal Hybrid (CTH) 12

2.2.1 High-Z sourcing in CTH 14

2.3 Stellarnet survey spectrometers 15

2.4 The Auburn high-resolution UV spectrometer system 15

2.4.1 Aspheric corrected spectrometer 16

2.4.2 Ultraviolet optimized detector 17

2.4.3 Auburn high-resolution UV spectrometer control software 18

2.4.4 Spectrometer instrumental function 19

2.5 The High-Z Langmuir probe 19

2.5.1 Uncertainty analysis of Langmuir probe data 33

2.5.2 The Debye sheath 34

2.5.3 The Chodura sheath 35

3 Collisional Radiative Theory 39

3.1 Basic atomic processes 39

3.1.1 Electron impact excitation/de-excitation 40

3.1.2 Electron impact ionization 41

3.1.3 Spontaneous emission 43

3.1.4 Recombination 44

3.1.5 Three-body recombination 45

3.1.6 Thermal charge exchange 45

3.2 Time scales of collisional radiative processes 46

3.3 The collisional radiative set of equations 47

3.3.1 The coronal approximation 49

3.3.2 The limit of local thermodynamic equilibrium (LTE) 50

3.3.3 The quasi-static approximation 50

3.3.4 Photon Emissivity Coefficient (PEC) and line ratio diagnostics 53

3.3.5 Ionizations per photon (S/XB) to diagnose impurity influx 57

3.3.6 The generalized collisional radiative coefficients 58

3.3.7 Time-dependent solution of the collisional radiative matrix 60

3.3.8 Level splitting term-resolved PECs for low-Z elements 61

3.4 The ionization balance 63

3.4.1 Time independent ionization balance 65

3.4.2 The time-dependent solution 67

3.4.3 Time-dependent ionization balance with a source term 67

3.5 Low-Z test case (Carbon) 68

3.5.1 Carbon I PECs 68

3.5.2 C I Intermediate population mechanisms 68

3.5.3 C I time-dependent collisional radiative modeling 69

3.5.4 C I Generalized collisional radiative coefficients 70
3.6 High-Z test case (Molybdenum) 71
3.6.1 Mo I PECs 71
3.6.2 Mo I Intermediate population mechanisms 71
3.6.3 Mo I time-dependent collisional radiative modeling 73
4 Experimental measurements of low charge states of tungsten and molybdenum . 76
4.1 Line identification of intrinsic CTH impurities 77
4.1.1 Low-Z spectral line identification with ColRadPy 78
4.2 Tungsten spectral line identification in CTH and DIII-D 80
4.2.1 Tungsten probe scan in CTH 84
4.2.2 DIII-D strike point location on tungsten rings 87
4.2.3 Uncertainties in spectral line identification 95
4.3 Molybdenum as a PFC and line identification in CTH 97
4.3.1 Neutral molybdenum atomic data and theoretical methods 99
4.3.2 Singly ionized molybdenum atomic data and theoretical methods . . 100
5 Collisional radiative modeling and comparison to experimental W I observations 114
5.1 Tungsten atomic data and theoretical methods 115
5.1.1 Discussion of neutral tungsten atomic data 115
5.1.2 Collisional radiative modeling of W I 116
5.2 Results from neutral tungsten collisional radiative modeling 118
5.2.1 PEC and SCD metastable dependence 119
5.2.2 Intermediate populating mechanism 120
5.2.3 Loss rate analysis 124
5.2.4 Diagnosing metastable populations 127
5.2.5 Non-quasistatic solutions for neutral tungsten 128
5.2.6 Neutral tungsten equilibrium time scales 131
5.3 Modeling effective S/XB coefficients in the plasma sheath 134

5.3.1 Modeling effective S/XB coefficients in the sheath with ColRadPy . . 134
5.3.2 Comparison of selected W I S/XB and effective S/XB coefficients . . 138
5.4 Comparison of collisional radiative modeling with experimental spectra from CTH 154
5.4.1 Quantification of uncertainties in coronal line ratios 157
5.4.2 Qualification of uncertainty in derived CR coefficients 158
5.4.3 Validating the R-matrix neutral tungsten calculation using comparisons to CTH experimental data 158
6 Conclusion and future work 167
6.1 Experimental accomplishments 167
6.2 Theoretical accomplishments 168
6.3 Results from neutral tungsten measurements and modeling 168
6.4 Future work 170
Appendices 183
A ColRadPy Documentation 184
B Impurity spectral line identification in CTH 201
C Hardware drawing and descriptions 220
C.1 Spectrometer control software and calibration 220
C.1.1 Isoplane 320 spectrometer control software 220
C.1.2 Andor Newton 920 control software 221
C.1.3 Spectrometer dispersion calibration 221

List of Figures

1.1 Diagram of tokamak with various parts of the plasma and tokamak geometry labeled. The confined plasma is enclosed by the last closed flux surface. 3

2.1 UV survey spectrometer lines of sight viewing the DIII-D tokamak divertor highlighted in green and overlaid on a reconstruction of magnetic flux surfaces. Two toroidally displaced UV lenses provide independent views that can be aligned to tungsten coated inserts on either the divertor floor or shelf. The location of a Langmuir probe on the divertor shelf is shown in red. 10

2.2 Mechanical drawing of collection optics and photo of collection optics installed on DIII-D. at a toroidal angle of 75° and poloidally near the top of the machine (75R+2). 12

2.3 Rendering of DIII-D UV spectroscopy lines of sight into the vacuum vessel. The lines of sight are shown in red. The last closed flux surface from an equilibrium for shot 167210 at 2035 ms is depicted by the yellow surface. Courtesy of Bill Meyer. 13

2.4 UV survey spectrometer line of sight viewing the tungsten-tipped probe highlighted in green and overlaid on a reconstruction of magnetic flux surfaces. The W probe is located directly above the spectrometer collection optics, and the High-Z tip is well within the last closed flux surface when fully inserted. 16

2.5 Grating angle versus central wavelength location for the three gratings used with the Auburn high-resolution UV spectrometer. The black dashed line indicates the grating angle for optimized astigmatism correction (a). The instrument dispersion versus central wavelength (b). 17

2.6 Andor Newton 920 DU920P-BU2 quantum efficiency 18

2.7 Comparison of the IsoPlane spectrometer with the different gratings, the Stellarnet EPP2000 and Bluewave spectrometers for Hg I 296.728 nm $5d^{10}6s6d\ (^3D_1) \rightarrow 5d^{10}6s6p\ (^3P_0)$. A significant reduction in instrument transfer function corresponding to an increase in wavelength resolution is observed from the Stellarnet survey spectrometers to the IsoPlane spectrometer. 20

2.8 Debye lengths for a range of possible temperature densities in the edge of CTH plasmas. 22

2.9 Tungsten slug seen as the large piece of metal. The BN insulating sleeve is the white ceramic and the Langmuir probe is the smaller piece of metal sticking out of the BN insulator. The scale of the ruler is millimeters. 22

2.10 IV trace for an idealized single tipped Langmuir probe at $T_e = 30$ eV and $n_e = 1 \times 10^{18}$ m^{-3}. The black dashed line represents ion saturation current. The orange line is the electron saturation current for an idealized probe. The floating potential of the probe is solid black vertical line. 24

2.11 Waveform of voltage applied to the Langmuir probe. 25

2.12 Thermal rise of a single tipped Langmuir probe for possible CTH plasma conditions. Probe diameter of 1.5 mm and length of 0.5 mm. 26

2.13 Voltage and current measurements from Langmuir probe in CTH discharge 24 cm away from the mid-plane. Significant noise is associated with the start of the ohmic phase of the discharge at 1.62 s. 27

2.14 Langmuir probe voltage (a) during a CTH discharge. The current draw though Langmuir probe in blue (b). A single sweep is highlighted in red, the average using a median filter is over-plotted in black. 29

2.15 Current versus voltage of the Langmuir probe during a single voltage sweep is plotted in blue. The red line is a least-squares fit to the data using Equation 2.5 with the following parameters. $T_\mathrm{e} = 27.4$ eV, $n_\mathrm{e} = 2.5 \times 10^{12}$ cm^{-3} and $V_\mathrm{p} = 40.5$ V. 30

2.16 Plasma current during multiple CTH discharges(a). Mid-plane interferometer density measurement (b). Electron temperature measured by the Langmuir probe at various depths (c). Electron density measured by the Langmuir probe at various depths (d). Plasma potential measured by the Langmuir probe at various depths (e). 31

2.17 Log of the Langmuir probe current draw, offset by the ion saturation current versus probe voltage for one sweep plotted in blue. The linear fit to the data is shown in red with the coefficients $m = 0.0401$ and $b = 0.981$ giving $T_\mathrm{e} = 24.9$ eV and $n_\mathrm{e} = 2.0 \times 10^{12}$ cm^{-3}. 32

2.18 Cartoon diagram of the Chodura sheath. The three regions that make up the sheath region are seen separated by the dashed lines. Note that this figure is not to scale; the Chodura sheath is much larger than the Debye sheath. 36

2.19 Normalized electron density in the Chodura (solid line) and Deybe sheaths (dashed line where it exists). As a function of distance from the wall for various magnetic field incident angle. The plasma parameters for the sheath are $T_\mathrm{e} = 10$ eV, $T_\mathrm{i} = 1$ eV, $m_\mathrm{i} = 1$, $B_\mathrm{mod} = 0.6$ T, $n_\mathrm{e} = 1 \times 10^{13}$ cm^{-3}. 38

3.1 Burgess-Tully effective collision strength extrapolation. (a) Effective collisional strengths for Mo I $4d^5 5s(^7S_3) \leftrightarrow 4d^5 5s(^5F_1)$ transition is in blue. Extrapolated Burgess-Tully fit in red. Last R-matrix calculated point and infinite energy point are the blue dots. (b) Calculated effective collisional strength of the R-matrix is shown in blue. The extrapolation to higher temperatures is the red line. 42

3.2 ECIP ionization contour plot versus level number and electron temperature for C I, calculated with ColRadPy. 43

3.3 Electron temperature and density contours for the 102.1 and 132.9 nm C I line ratio. The line ratio is a good temperature diagnostic as there is a strong temperature dependence and a weak density dependence. 55

3.4 Comparison of spectral data from CTH (blue) with the unsplit (green) and split (red) collisional radiative modeling of C V at 40 eV and 1×10^{13} cm^{-3} 61

3.5 Ionization balance for C at $n_{\mathrm{e}} = 1 \times 10^{13}$ cm^{-3}. 65

3.6 Metastable resolved photon emissivity coefficient for C I 156.06 nm (a) and 113.98 nm (b). A calculation with only the ground state is illustrated by the dashed black line for each transition. Solid color lines blue and green are the ground state and first metastable level at their steady state equilibrium fraction. 68

3.7 Intermediate populating levels responsible for populating the two C I excited states. The vertical red lines in each plot correspond to the ground state contribution. (a) The main populating mechanisms are excitation from the ground and metastable state. (b) The majority of the population is excitation from the ground state. 69

3.8 Comparison of the full time-dependent and conventional solution for C I at $T_\mathrm{e} = 8\ eV$, $n_\mathrm{e} = 5 \times 10^{11}$ cm^{-3}. (a) Non-quasi-static solution is illustrated by the black dashed line; conventional solutions with different numbers of metastable states are solid color lines. (b) Eigenvalues from the non-quasi-static solution. The ground and metastable states have markedly different values than the excited states and are represented by the two highest points in the figure. 70

3.9 GCR coefficients for C I versus temperature at $n_\mathrm{e} = 1 \times 10^{13}$ cm^{-3}. These coefficients will also be dependent on density, for simplicity only one density has been plotted here. 72

3.10 Metastable resolved photon emissivity coefficient for Mo I at 379.8 nm (a) and 550.6 nm (b). The ground state only calculation is illustrated by the dashed black line for each transition. Solid color lines blue and green are the ground state and first metastable level at their steady state equilibrium fraction. 73

3.11 Intermediate populating levels responsible for populating the neutral Mo 4d^{5}5p(^{7}P$_4$) and 4d^{5}5p(^{5}P$_3$) energy levels. These levels produce strong emission lines at 379.8 and 550.6 nm. The red vertical lines in each plot correspond to the ground state contribution, see discussion in Section 3.6.2. (a) Populating levels for 4d^{5}5p(^{7}P$_4$), most of the population is being excited directly from the ground. (b) Populating levels for 4d^{5}5p(^{5}P$_3$), a majority of the population is coming from other excited states and metastables. 74

3.12 Comparison of time dependent and conventional solutions for Mo I at $T_\mathrm{e} = 8\ eV$, $n_\mathrm{e} = 5 \times 10^{11}$ cm^{-3}. (a) Full solution is illustrated by the black dashed line. Conventional solutions with different numbers of metastable states are the solid color lines. (b) Eigenvalues from the non-quasistatic solution show a ‘continuum’ of decreasing values with no clear distinction between metastable and excited states. 74

4.1 Photon emissivity coefficients (PECs) for W I (blue), W II (red), W III (green) and W IV (cyan) calculated with ColRadPy. All charge states were modeled at $T_\mathrm{e} = 20$ eV and $n_\mathrm{e} = 1 \times 10^{13}$ cm^{-3}. The fractional abundances of the charge states are set to 1. 77

4.2 Measured CTH and DIII-D spectra with the wavelengths for neutral tungsten lines identified. (a) Average CTH spectrum of three shots (16120944, 16120947, 16120952) from 30 ms exposures beginning 60 ms into each discharge with the W probe fully inserted into the plasma. (b) DIII-D spectrum viewing the divertor shelf W coated inserts resulting from a single 200 ms exposure starting at 1935 ms into shot 167350. 82

4.3 Measured CTH and DIII-D spectra with the wavelengths for neutral tungsten lines identified. (a) Average CTH spectrum of three shots (16120863, 16120864, 16120865) from 100 ms exposures integrating over each entire discharge with the W probe fully inserted into the plasma. (b) DIII-D spectrum viewing the divertor shelf W coated inserts resulting from a single 50 ms exposure starting at 5000 ms into shot 167215. 83

4.4 Intensities of tungsten and carbon impurity lines with varying W-tipped probe depth and Radial Field Coil (RFC) magnitude. The combinations of probe tip distance from the CTH midplane and RFC magnitude are listed in the legend from least plasma-probe interaction (25.9 cm, RFC high) to most interaction (19.9 cm, RFC off). (a) Carbon impurity line intensities increase modestly with probe insertion but are present for all configurations. (b) and (c) Tungsten lines demonstrate a significant dependence on probe depth and RFC magnitude. All tungsten lines are not present when the W-tipped probe is fully retracted with maximum applied radial field (25.9 cm, RFC high). 86

4.5 CTH spectrum from 216-227 nm, the tungsten probe was located at 21 cm from the midplane of CTH. W II lines are identified by the NIST observed wavelengths in green text and the W III lines are in orange text. The spectrum with the tungsten tipped probe is in blue, and the spectrum with the molybdenum tipped probe is in transparent red. 87

4.6 CTH spectrum from 233-242 nm, the tungsten probe was located at 21 cm from the midplane of CTH. W II lines are identified by the NIST observed wavelengths in green text. The spectrum with the tungsten tipped probe is in blue, and the spectrum with the molybdenum tipped probe is in transparent red. 90

4.7 CTH spectrum from 242-254 nm, the tungsten probe was located at 21 cm. W I lines are identified by the NIST observed wavelengths in black text and W II lines are identified by the NIST observed wavelengths in green text. The spectrum with the tungsten tipped probe is in blue, and the spectrum with the molybdenum tipped probe is in transparent red. 91

4.8 CTH spectrum from 254-267 nm, the tungsten probe was located at 21 cm. W I lines are identified by the NIST observed wavelengths in black text, W II lines are identified by the NIST observed wavelengths in green text and the W III lines lines are identified by the NIST observed wavelengths in coral text. The spectrum with the tungsten tipped probe is in blue, and the spectrum with the molybdenum tipped probe is in transparent red. 92

4.9 CTH spectrum from 254-267 nm with y axis scaling to allow for relative small W spectral lines to be seen. The tungsten probe was located at 21 cm. W I lines are identified by the NIST observed wavelengths in black text, W II lines are identified by the NIST observed wavelengths in green text and the W III lines lines are identified by the NIST observed wavelengths in coral text. The spectrum with the tungsten tipped probe is in blue, and the spectrum with the molybdenum tipped probe is in transparent red. 94

4.10 CTH spectrum from 268-278 nm, the tungsten probe was located at 21 cm. W I lines are identified by the NIST observed wavelengths in black text and W II lines are identified by the NIST observed wavelengths in green text. The spectrum with the tungsten tipped probe is in blue, and the spectrum with the molybdenum tipped probe is in transparent red. 95

4.11 CTH spectrum from 280-288 nm, the tungsten probe was located at 21 cm. W I lines are identified by the NIST observed wavelengths in black text and W II lines are identified by the NIST observed wavelengths in green text. The spectrum with the tungsten tipped probe is in blue, and the spectrum with the molybdenum tipped probe is in transparent red. 96

4.12 CTH spectrum from 293-296 nm, the tungsten probe located at 21 cm. W I lines are identified by the NIST observed wavelengths in black text and W II lines are identified by the NIST observed wavelengths in green text. The spectrum with the tungsten tipped probe is in blue, and the spectrum with the molybdenum tipped probe is in transparent red. 97

4.13 CTH spectrum from 301-304 nm, the tungsten probe located at 21 cm. W I lines are identified by the NIST observed wavelengths in black text and W II lines are identified by the NIST observed wavelengths in green text. The spectrum with the tungsten tipped probe is in blue, and the spectrum with the molybdenum tipped probe is in transparent red. 98

4.14 CTH spectrum from 304-314 nm, the tungsten probe located at 21 cm. W I lines are identified by the NIST observed wavelengths in black text and W II lines are identified by the NIST observed wavelengths in green text. The spectrum with the tungsten tipped probe is in blue, and the spectrum with the molybdenum tipped probe is in transparent red. 99

4.15 CTH spectrum from 314-323 nm, the tungsten probe located at 21 cm. W I lines are identified by the NIST observed wavelengths in black text and W II lines are identified by the NIST observed wavelengths in green text. The spectrum with the tungsten tipped probe is in blue, and the spectrum with the molybdenum tipped probe is in transparent red. 100

4.16 CTH spectrum from 326-334 nm, the tungsten probe located at 21 cm. W I lines are identified by the NIST observed wavelengths in black text and W II lines are identified by the NIST observed wavelengths in green text. The spectrum with the tungsten tipped probe is in blue, and the spectrum with the molybdenum tipped probe is in transparent red. 102

4.17 CTH spectrum from 361-365 nm, the tungsten probe located at 21 cm. W I lines are identified by the NIST observed wavelengths in black text and W II lines are identified by the NIST observed wavelengths in green text. The spectrum with the tungsten tipped probe is in blue, and the spectrum with the molybdenum tipped probe is in transparent red. 103

4.18 CTH spectrum from 377-387 nm, the tungsten probe located at 21 cm. W I lines are identified by the NIST observed wavelengths in black text and W II lines are identified by the NIST observed wavelengths in green text. The spectrum with the tungsten tipped probe is in blue, and the spectrum with the molybdenum tipped probe is in transparent red. 104

4.19 CTH spectrum from 400-411 nm, the tungsten probe located at 21 cm. W I lines are identified by the NIST observed wavelengths in black text and W II lines are identified by the NIST observed wavelengths in green text. The spectrum with the tungsten tipped probe is in blue, and the spectrum with the molybdenum tipped probe is in transparent red. 105

4.20 Time evolution of DIII-D shot 167350: (a) Radial position of the outer strike point (R_{OSP}) with the locations of the floor and shelf W inserts shown in green and red respectively, (b) and (c) raw (green) and ELM-free smoothed (blue) electron temperature and density on the W surface measured by a Langmuir probe, (d) W I, C II, and O V line intensities normalized to their maximum intensity during the discharge, (e) ratio of W I to C II line intensities. 106

4.21 CTH spectrum from 263-268 nm, the molybdenum probe was located at 21 cm from the CTH midplane from the midplane of CTH. Mo I lines are identified by the NIST observed wavelengths in olive text and Mo II are in blue text. Spectrum with the molybdenum tipped probe is in transparent red and spectrum from tungsten tipped probe is in light blue. 107

4.22 CTH spectrum from 277-288 nm, the molybdenum probe was located at 21 cm from the CTH midplane from the midplane of CTH. Mo II lines are identified by the NIST observed wavelengths in blue text. Spectrum with the molybdenum tipped probe is in transparent red and spectrum from tungsten tipped probe is in light blue. 108

4.23 CTH spectrum from 292-294 nm, the molybdenum probe was located at 21 cm from the CTH midplane from the midplane of CTH. Mo II lines are identified by the NIST observed wavelengths in blue text. Spectrum with the molybdenum tipped probe is in transparent red and spectrum from tungsten tipped probe is in light blue. 109

4.24 CTH spectrum from 307-310 nm, the molybdenum probe was located at 21 cm from the CTH midplane from the midplane of CTH. Mo II lines are identified by the NIST observed wavelengths in blue text. Spectrum with the molybdenum tipped probe is in transparent red and spectrum from tungsten tipped probe is in light blue. 110

4.25 CTH spectrum from 314-323 nm, the molybdenum probe was located at 21 cm from the CTH midplane from the midplane of CTH. Mo I lines are identified by the NIST observed wavelengths in olive text and Mo II are in blue text. Spectrum with the molybdenum tipped probe is in transparent red and spectrum from tungsten tipped probe is in light blue. 111

4.26 CTH spectrum from 329-335 nm, the molybdenum probe was located at 21 cm from the CTH midplane from the midplane of CTH. Mo I lines are identified by the NIST observed wavelengths in olive text and Mo II are in blue text. Spectrum with the molybdenum tipped probe is in transparent red and spectrum from tungsten tipped probe is in light blue. 112

4.27 CTH spectrum from 361-365 nm, the molybdenum probe was located at 21 cm from the CTH midplane from the midplane of CTH. Mo I lines are identified by the NIST observed wavelengths in olive text and Mo II are in blue text. Spectrum with the molybdenum tipped probe is in transparent red and spectrum from tungsten tipped probe is in light blue. 113

5.1 PEC theoretical spectrum of W I generated by collisional radiative modeling with $T_{\mathrm{e}} = 30$ eV, $n_{\mathrm{e}} = 5 \times 10^{13}$ cm^{-3}. 118

5.2 PEC values for four intense W I emission lines, for $n_{\mathrm{e}} = 1 \times 10^{13}$cm^{-3}. The total equilibrium temperature dependence for each PEC is illustrated by the dashed black line. The PECs weighted by their steady-state metastable populations are indicated by the solid colored lines. Results are shown for the (a) 255.14, (b) 253.36, (c) 265.65 and (d) 261.31 nm lines. 121

5.3 PEC values for four intense W I emission lines, for $n_{\mathrm{e}} = 1 \times 10^{13}$cm^{-3}. The total equilibrium temperature dependence for each PEC is illustrated by the dashed black line. The PECs weighted by their steady-state metastable populations are indicated by the solid colored lines. Results are shown for the (a) 261.31, (b) 254.72, (c) 400.88 and (d) 498.26 nm lines. 122

5.4 SCD values for W I as a function T_{e}, determined by collisional radiative modeling at $n_{\mathrm{e}} = 5 \times 10^{13}$ cm^{-3}. The metastable components are plotted with solid colored lines. The dashed line is the summation of the metastable components weighted by their steady-state metastable fractions. 123

5.5 Intermediate levels responsible for populating a selection of neutral W energy levels. The red vertical lines in each plot correspond to the ground state contribution. Populating levels for 5p^{6}5d6p(^{5}P$_1$) show most of the population is being excited directly from the ground (a). Populating levels for 5p^{6}5d6s(^{3}D$_1$) display a majority of the population is coming from other excited states and metastable states (b). Populating levels for 5p^{6}5d6s(^{7}S$_3$) indicate a majority of the population is coming from excited states (c). 125

5.6 Population loss rates from neutral tungsten levels for $T_{\mathrm{e}} = 30$ eV, $n_{\mathrm{e}} = 5 \times 10^{13}$ cm^{-3}. Levels are arranged in ascending energy. Horizontal red lines correspond to ground level loss rates with the horizontal green line representing a typical value for a strong electron dipole transition. The total loss rate out of an energy level (a). The loss rate only from spontaneous emission (b). The loss rate due to ionization (c). The loss rate due to excitation/de-excitation (d). 126

5.7 A comparison of the non-quasistatic (dashed line) and quasistatic approximations (colored solid lines) with varying numbers of metastable states included (a) for the widely used W I emission line at 400.88 nm. The eigenvalues from the non-quasistatic approximation with less negative numbers corresponding to longer lived states (b). There are a significant number of long-lived states that correspond to the large number of metastable states in neutral tungsten. 129

5.8 The time required for neutral tungsten to come to equilibrium as a function of electron density. The time to reach equilibrium decreases almost linearly with electron density. 133

5.9 The density profile in the Debye and Chodura sheaths (a), time changing population of W^{0^+} and W^{1+} (b). The normalized population of levels that produce intense spectral lines (c). 136

5.10 Comparison of sheath model from Guterel *et al.*[1] to the sheath model used in this thesis. 139

5.11 Time dependent SCD coefficient (a) and time-dependent PEC coefficients (b) for W I 255.14 in green and W I 400.88 in red. Parameters of the Chodura sheath model are: $T_{\mathrm{e}} = 20$ eV, $n_{\mathrm{e}} = 5 \times 10^{12}$ cm^{-3}, $B_{\mathrm{mod}} = 5.3$ T, $\alpha = 3.2°$. 140

5.12 W^{0+} SCD coefficient at $T_{\mathrm{e}} = 20$ eV versus electron density. The SCD coefficient using bulk T_{e} and n_{e} values is shown in blue. The steady-state Chodura sheath is depicted in red. The time-dependent solution in the Chodura sheath is the green line. 141

5.13 Comparison of bulk PEC (blue), steady-state sheath effective PEC (red) and time-dependent sheath effective PEC (green) versus electron density, $T_{\mathrm{e}} = 20$ eV. Results are shown for the (a) 255.14, (b) 253.36, (c) 265.65 and (d) 261.31 nm lines. 142

5.14 Comparison of bulk PEC (blue), steady-state sheath effective PEC (red) and time-dependent sheath effective PEC (green) versus electron density, $T_{\mathrm{e}} = 20$ eV. Results are shown for the (a) 261.31, (b) 243.60, (c) 400.88 and (d) 498.25 nm lines. 143

5.15 Comparison of bulk S/XB (blue), steady-state sheath effective S/XB (red) and time-dependent sheath effective S/XB (green) versus electron density, $T_{\mathrm{e}} = 20$ eV. Results are shown for the (a) 255.14, (b) 253.36, (c) 265.65 and (d) 261.31 nm lines. 144

5.16 Comparison of bulk S/XB (blue), steady-state sheath effective S/XB (red) and time-dependent sheath effective S/XB (green) versus electron density, $T_{\mathrm{e}} = 20$ eV. Results are shown for the (a) 261.31, (b) 243.60, (c) 400.88 and (d) 498.25 nm lines. 145

5.17 Comparison of W I 255.14 nm S/XB versus n_{e}, at $T_{\mathrm{e}} = 20$ eV for various sputtering velocities (plotted as the dashed lines). The steady-state S/XB is shown in blue, the steady-state Chodura sheath model S/XB is shown in red and the time-dependent Chodura sheath model is shown in green. Variations of the sputtering velocity are indicated as dash-dot and the dashed line. 147

5.18 Comparison of W I 400.88 nm S/XB versus n_e, at $T_\mathrm{e} = 20$ (eV) for various sputtering velocities (plotted as the dashed lines). The steady-state S/XB is shown in blue, the steady-state Chodura sheath model S/XB is shown in red and the time-dependent Chodura sheath model is shown in green. Variations of the sputtering velocity are indicated as the dash-dot and the dashed lines. 149

5.19 Steady-state population fraction of the $^7\mathrm{S}_3$ level versus electron density at multiple T_e values. 151

5.20 Comparison of the W I 400.88 nm S/XB (blue), steady-state effective S/XB (red) and time-dependent S/XB (green) at $T_\mathrm{e} = 20$ (eV) versus n_e while varying the $^7\mathrm{S}_3$ metastable fraction. The solid time-dependent line assumes 100% of the neutral tungsten atoms start in the ground state, the dashed line assumes 0.5% starts in the $^7\mathrm{S}_3$, the dashed-dot line assumes 2% starts in the $^7\mathrm{S}_3$ and the dotted line assumes 10% starts in the $^7\mathrm{S}_3$. 152

5.21 Comparison of the W I 255.14 nm S/XB (blue), steady-state effective S/XB (red) and time-dependent S/XB (green) at $T_\mathrm{e} = 20$ (eV) versus n_e while varying the $^7\mathrm{S}_3$ metastable fraction. The solid time-dependent line assumes 100% of the neutral tungsten atoms start in the ground state, the dashed line assumes 0.5% starts in the $^7\mathrm{S}_3$, the dashed-dot line assumes 2% starts in the $^7\mathrm{S}_3$ and the dotted line assumes 10% starts in the $^7\mathrm{S}_3$. 153

5.22 Spectroscopy data with the tungsten tipped Langmuir probe inserted to 24 cm into CTH is in blue. The skewed Lorentzian fit to the experimental data is shown in orange. 155

5.23 PEC ratio of W I 255.14 nm and 265.65 nm emission lines plotted as a function of electron temperature for various electron densities. 156

5.24 Calculated line ratio of emissivities for W I 255.14 nm and 265.65 nm. The line in orange is a bulk model and the line in blue uses a sheath model. 160

5.25 Comparison of measured electron temperature from the embedded tungsten Langmuir probe and from line ratio measurements of the W I 255.14 and 265.65 nm lines for four different probe depths. 161

5.26 Comparison of measured electron temperature from the embedded tungsten Langmuir probe and from line ratio measurements of the W I 255.14 and 265.65 nm lines with error bars from four different probe depths. 162

5.27 PEC ratio of W I 265.65 nm and 269.57 nm plotted as a function of electron temperature for various densities. 163

5.28 Comparison of measured electron temperature from the embedded tungsten Langmuir probe and temperature inferred from line ratio measurements of the W I 265.65 and 269.57 nm lines for four different probe depths. 164

B.1 CTH comparison to CR C II modeling 202

B.2 CTH comparison to CR C II modeling 203

B.3 CTH comparison to CR C II modeling 203

B.4 CTH comparison to CR C III modeling 204

B.5 CTH comparison to CR C III modeling 205

B.6 CTH comparison to CR N II modeling 206

B.7 CTH comparison to CR N II modeling 206

B.8 CTH comparison to CR N III modeling 208

B.9 CTH comparison to CR N III modeling 208

B.10 CTH comparison to CR N III modeling 209

B.11 CTH comparison to CR N III modeling 209

B.12 CTH comparison to CR N III modeling 210

B.13 CTH comparison to CR N IV modeling 210

B.14 CTH comparison to CR O II modeling 211

B.15 CTH comparison to CR O II modeling 212

B.16 CTH comparison to CR O II modeling 212

B.17 CTH comparison to CR O II modeling 213

B.18 CTH comparison to CR O II modeling 213

B.19 CTH comparison to CR O III modeling 214

B.20 CTH comparison to CR O III modeling 215

B.21 CTH comparison to CR O IV modeling 215

B.22 CTH comparison to CR O IV modeling 217

B.23 CTH comparison to CR O IV modeling 217

B.24 CTH comparison to CR O V modeling 219

C.1 Hg spectral feature at 265 nm moved across the CCD by moving the central wavelength of the spectrometer. 223

C.2 Difference between the fitted centroid of the line versus the NIST observed wavelength value in nm for each central wavelength setting is shown as the blue scatter points. The quadratic fit to the scatter points is the red line. The correction to the calculated dispersion is then a function of CCD pixel number 224

List of Tables

2.1 CTH parameters R is major radius, $\mathrm{a}_{\mathrm{vessel}}$ is the minor radius, $\mathrm{a}_{\mathrm{plasma}}$ is the plasma radius, B_0 is the magnetic field strength,I_{p} is the plasma current, $\mathrm{P}_{\mathrm{ECRH}}$ is the ECRH power, n_{e} is the electron density, T_{e} is the electron temperature,β is the ratio of the plasma pressure to magnetic pressure. 13

3.1 C V spectral lines identified in CTH 62

4.1 Table of W I emission lines from 200-300 nm observed during CTH experiments along with level identifications where possible. Previously observed lines are indicated by superscripts on the NIST defined wavelengths: [a],[2] [b],[3] [c],[4] [d],[5] [e],[6] and [f].[7] The lines identified in this table are shown with a comparison to a Mo spectrum in increasing wavelength in Figures 4.5 - 4.12. 88

4.2 Table of W I emission lines from 300-400 nm observed during CTH experiments along with level identifications where possible. Previously observed lines are indicated by superscripts on the NIST defined wavelengths: [a],[2] [b],[3] [c],[4] [d],[5] [e],[6] and [f].[7] The lines identified in this table are shown with a comparison to a Mo spectrum in increasing wavelength in Figure's 4.12 - 4.19 89

4.3 Table of W II emission lines observed between the DIII-D and CTH experiments along with level identifications where possible. 89

4.4 Table of W I emission lines observed between the DIII-D and CTH experiments along with level identifications where possible and confidence. Previously observed lines are indicated by superscripts on the NIST defined wavelengths: [a],[8] [b],[3] [c],[4] [d],[5] [e],[6] and [f].[7] 93

4.5 Table of Mo I emission lines from 200-400 nm observed during CTH experiments along with level identifications where possible. The lines identified in this table are shown with a comparison to a Mo spectrum in increasing wavelength in Figures 4.21 - 4.27 101

4.6 Table of Mo II emission lines from 200-400 nm observed during CTH experiments along with level identifications where possible. The lines identified in this table are shown with a comparison to a Mo spectrum in increasing wavelength in Figures 4.21 - 4.27 101

B.1 C II spectral lines identified in CTH 202

B.2 C III spectral lines identified in CTH 204

B.3 N II spectral lines identified in CTH 205

B.4 N III spectral lines identified in CTH 207

B.5 N IV spectral lines identified in CTH 207

B.6 O II spectral lines identified in CTH 211

B.7 O III spectral lines identified in CTH 214

B.8 O IV spectral lines identified in CTH 216

B.9 O V spectral lines identified in CTH 216

B.10 Table of W I emission lines observed in CTH along with level identifications where possible. Spectral lines that were either not in the *R*-matrix calculation or spectral lines that came from levels that could not be confidently shifted to NIST energies have "No ID" for the level identification. The comment column states why the spectral line is included in the appendix instead of Chapter 4. . . 218

B.11 Table of W II emission lines observed in CTH experiments along with level identifications where possible. Note that the final WD1 calculation has not yet been completed, this might more confidence in these W II emission lines. 218

B.12 Table of W III emission lines observed in CTH experiments along with level identifications where possible and confidence. 219

Chapter 1

Introduction to plasma wall material choices and thesis overview

1.1 Plasma facing component requirements in fusion environments

When it comes to designing a fusion reactor, there are several design requirements that remain unresolved. Many of these design requirements (such as machine size and cost) are often competing against one another. However, the most concerning is how the relatively hot dense plasma will interact with a material surface because all input power and nuclear power for a future fusion reactor must eventually diffuse from the plasma to the surrounding plasma facing surfaces. For a future fusion reactor, the amount of the power delivered to these surfaces will be significant, and so, the material selection and design of these plasma facing surfaces emerges as a critical design constraint that must be correctly addressed.

A few primary engineering requirements for Plasma Facing Components (PFCs) must be considered. First, PFCs must be able to handle high thermal heat flux. Unfortunately, heat fluxes to PFCs scales inversely proportional to the size of the machine and proportionally to the power produced. ITER (currently under construction) will be one of the first fusion devices to maintain a long stable plasma to produce net energy.[9] The heat flux of the ITER fusion plasma experiment is expected to be 10 MW m^{-2} (similar to heat fluxes experienced by spacecraft during reentry to the atmosphere).[10] Preliminary heat flux estimates from Kuang *et al.*[11] predicts that the SPARC tokamak divertor will experience heat fluxes of 250-350 MW m^{-2} partly because it is much smaller in size than ITER. Ideally a fusion reactor would be as small as possible (from a cost and engineering stand point) while still producing significant power; since the heat flux to PFCs can cause significant damage through melting, cracking or chipping, managing the heat flux becomes one of the prime concerns for a viable commercial fusion reactor. Additionally, Plasma-Material Interactions (PMI) can damage

PFCs through sputtering, implantation or by forming mixed material surfaces on top of PFCs. As a result, the relatively high heat fluxes that will exist in a fusion reactor become a strong driver for the material choice.

Another design requirement is that PFCs must be resilient to neutron damage because the deuterium tritium reaction produces a significant amount of high-energy neutrons which can both damage and activate PFCs. Additionally, PFCs must also have low retention rates for tritium. PFCs will absorb some of the tritium fuel, as a result these components will become radioactive. To minimize the amount of tritium that is absorbed, materials must be chosen wisely.

In most current fusion experiments as well as future proposed machines, a divertor will be utilized to transition from a high-temperature fusion plasma core to a cooler less dense plasma that will not damage PFCs. The divertor magnetic field configuration allows for density control of the plasma through divertor pumping, generally done with large internal cryopumps. Additionally, helium ash can be exhausted through the divertor geometry in a fusion reactor. Figure 1.1 is a diagram of the divertor geometry with many parts of plasma labeled that will be discussed in this paragraph. The divertor magnetic field is created with additional coils added to the plasma confinement coils which create the nested flux surfaces. The divertor configuration allows the edge of the plasma (the last closed flux surface) to interact with a target material usually referred to as the divertor. With additional magnetic coils, a null-point is created in the poloidal field called the "X-point" allowing for the inner strike-point (ISP) and outer strike-points (OPS) (the points where the last closed flux surface hits the divertor) to be created and forms a separation layer between the confined plasma and a region of open magnetic field lines called the scrape of layer (SOL). Both the heat and particles are deposited into a small area (∼1 mm in width). The divertor is of great interest for plasma material interactions (PMI) as it experiences the highest heat and particle flux load of the plasma device. Most of the work in this thesis is focused on the divertor region of a plasma where material erosion will be most significant. However, the measurement techniques presented could be applied to other PFCs in a reactor such as the main chamber.

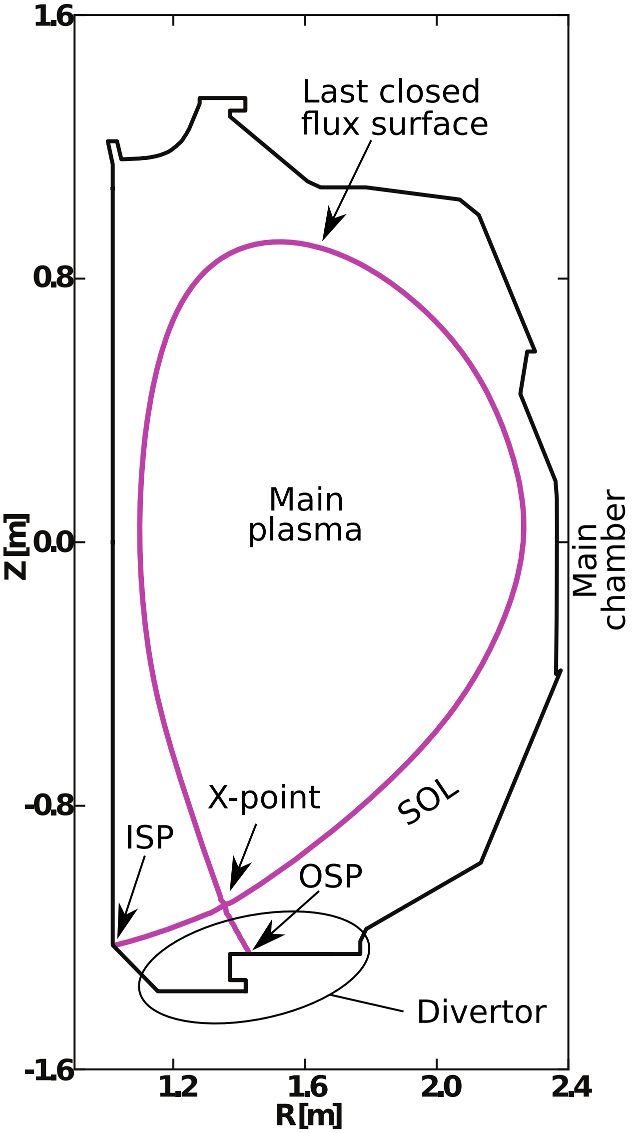

Figure 1.1: Diagram of tokamak with various parts of the plasma and tokamak geometry labeled. The confined plasma is enclosed by the last closed flux surface.

1.2 Low-Z materials as a plasma facing material

Many initial designs for fusion reactors as well as fusion relevant reactors use low-Z ($Z<10$) elements for PFCs (mainly C and Be). Low-Z elements are advantageous for fusion relevant machines as they become fully ionized at core plasma electron temperatures. When an atom is stripped of all electrons, power is no longer radiated away due to spectral emission. Loss rates from spectral emission can be significant if impurities atoms are not fully stripped in the plasma core.

Low-Z materials such as C can retain significant amounts of tritium and produce dust. Skinner *et al.*[12] investigated tritium retention in proposed ITER plasma facing materials including carbon and found that carbon absorbed and retained significant amounts of tritium compared to other materials such as tungsten. This dust is produced by material erosion. If there is a significant amount of tritium absorbed in the dust, the dust would be radioactive as some fraction could be tritium. While not a significant engineering or physical problem, tritium retention would be a significant political problem as well as a possible safety concern because of the radioactivity. Both chemical sputtering and physical sputtering can also be significant for low-Z PFCs especially at high temperatures.[13] Chemical sputter is caused because of a chemical reaction with the Plasma Facing Material (PFM), and the fuel, in the case of carbon, would be H and C. Physical sputter is caused by impact impurities exhausted by the SOL on a PFM. Erosion of PFCs in a fusion reactor could be a source of a significant amount of down time as these materials would need to be changed out regularly. Beryllium, while not having the same problems with retention or chemical sputtering, has a relatively low melting point making it unsuitable for the divertor region with high heat fluxes.[14]

1.3 High-Z materials as a plasma facing material

High-Z materials (e.g. tungsten, molybdenum) are leading candidates for plasma facing materials (specifically in the divertor) as they satisfy requirements for power exhaust, thermal conductivity, melting point and tritium retention. Both domestic and international fusion relevant devices have upgraded or have plans to upgrade to high-Z PFCs. DIII-D has previously installed W PFCs[15] and presently has plans for a tungsten coated Small Angle Slot (SAS) divertor in its five year plan. NSTX-U has plans to upgrade to high-Z PFCs as presented at its 37th program advisory committee meeting. JET has upgraded to the

W ITER-like wall,[10] and both ASDEX-U and WEST have a majority of PFCs made from tungsten. ITER will use tungsten for the divertor region with beryllium used as the main chamber PFM.[10]

Thus far, there has been more interest in tungsten than molybdenum as a PFM because tungsten was chosen as the divertor material for ITER. As a result, this thesis will focus more on tungsten, though some molybdenum line identification is detailed in Chapter 4. While sputtering of high-Z elements is significantly reduced compared with low-Z materials, wall erosion could still be on the order of thousands of kilograms per year in a fusion reactor.[16] Therefore, there is a need to understand models of plasma interaction with high-Z materials, as a concentration of tungsten as low as 10^{-5} is predicted to degrade fusion performance in the core plasma.[17]

1.4 Erosion, re-deposition and migration

The flux of ions onto PFMs will cause the sputtering and migration of the PFC material. The two main sources of sputtering are physical and chemical. Physical sputter is a result of particle collisions while chemical sputtering is a result of chemical reactions occurring usually between the hydrogen isotopes and the wall material. This thesis is focused on tungsten, and therefore only physical sputter will be considered as chemical sputtering of tungsten in the plasma is virtually non-existent. There is not any significant chemical reaction between tungsten and the hydrogen fuel, however, Brezinsek *et al*. was able to measure emission from the WD molecule[18] which was much smaller than physical sputtering.

Physical sputter arises due to the energy transfer between incoming energetic ions from the plasma and atoms that make up the PFM (for current scale devices impurity ions dominate the physical sputtering shown by Guterl *et al*.[19]). Physical sputtering happens to all materials, however the yield (i.e. the amount of sputtered material) depends on many factors such as the ion mass, velocity and incidence angle. Melting can also lead to sputtering of materials. Yet, in normal operating conditions, the divertor plasma region in ITER will not reach temperatures close to the melting point of tungsten. Off-normal operating scenarios where melting occurs are not considered here but are important for operation of any fusion relevant device.

After sputtering from a PFC, atoms are later re-deposited onto other PFCs (this is known as a mixed material) unless the sputtered atoms are pumped out of the vacuum vessel. For the case of tungsten, the majority of sputtered atoms are promptly re-deposited (within one gyro-radius) back onto the surface near the original sputtered location.[20] The total tungsten that is eroded from the surface is referred to as the "gross erosion". The eroded tungsten that is not promptly re-deposited back onto the surface is referred to as the "net erosion". The work in this thesis focuses on the gross erosion which only requires modeling and spectral interpretation of the neutral tungsten system. Net erosion requires modeling at least singly ionized tungsten and perhaps higher charge states. While this will be mentioned in this dissertation as outlined in the future work, it is not the main focus.

1.5 Thesis overview

This thesis seeks to improve spectral measurement techniques for gross erosion of tungsten by both experimental and theoretical means. Erosion can be diagnosed in real time through the combination of an observed spectral line intensity and a calculated atomic physics coefficient as described in Section 3.3.5. Chapter 2 briefly introduces the DIII-D tokamak and the Compact Toroidal Hybrid (CTH) torsitron. The measurements presented in this thesis come from these two experiments. Diagnostics key to this work for both DIII-D and CTH are then discussed including the newly designed Langmuir probe in CTH and a high-resolution spectrometer commissioned at CTH for installation on DIII-D. A brief theoretical discussion of the sheath formation is then given as it will be shown that sheaths can be important for gross erosion diagnosis.

Chapter 3 gives a description of basic atomic processes in plasmas that are important for the collisional radiative (CR) calculations completed in this work. The theory of the collisional radiative set of equations is provided as implemented in the collisional radiative solver ColRadPy. In addition to the new models for the diagnosis of tungsten erosion, ColRadPy is one of main achievements of this work. ColRadPy is a general collisional radiative code that is currently being applied in many different plasma applications in addition to the work presented here. ColRadPy is being applied to low temperature basic plasmas as well as impurity fraction measurements and machine learning. Examples of the application of ColRadPy to a low-Z species (C) and a high-Z species (Mo) are then presented.

Chapter 4 details spectral line identification for tungsten and molybdenum. Prior to this thesis, limited spectral line identification of low charge state high-Z elements for fusion plasmas had been completed. While there has been significant work to identify spectral lines in NIST atomic database, fusion relevant plasma conditions are often at high temperatures and with electron densities orders of magnitude higher which can significantly impact the intensities of specific spectral lines. The work presented here is the first detailed line identification effort for fusion relevant plasma conditions. The spectral lines identified in Chapter 4 are good candidate lines for collisional radiative based diagnostics such as erosion, T_e and n_e as these are the spectral lines that can be experimentally measured.

Chapter 5 includes three main results. First (Section 5.1.1), collisional radiative modeling of neutral tungsten is described. A discussion of both previously used atomic calculations for neutral tungsten in addition to the new atomic calculations employed in this work is given. The results of collisional radiative modeling for various lines and other coefficients are provided demonstrating that neutral tungsten behaves very differently from previous low-Z materials. Second (Section 5.3), the impact of a plasma sheath model on neutral tungsten CR modeling is investigated for plasma conditions ranging from CTH densities($n_\mathrm{e} \sim 1\times10^{12}$ cm^{-3}) up to projections for ITER plasma conditions ($n_\mathrm{e} \sim 1\times10^{15}$ cm^{-3}). The addition of a sheath is shown to impact derived coefficients (e.g. S/XB or Generalized Collisional Radiative (GCR) coefficients) at high bulk electron densities (the conditions that would be present in ITER). Lastly (Section 5.4), a comparison between electron temperatures inferred from neutral tungsten spectral line ratios and measurements from the CTH Langmuir probe will be detailed. Line ratios were chosen that are predicted be temperature sensitive, based upon the atomic data, and the temperatures diagnosed from these line ratios were found to be in good agreement with electron temperature measurements from the Langmuir probe. This suggests that for the spectral lines investigated, the neutral tungsten atomic data is of high quality.

Chapter 2

The DIII-D tokamak and the Compact Toroidal Hybrid

This chapter details the two plasma confinement devices that were used to the collect tungsten spectroscopy data. In addition, the major diagnostics used to collect data are described for each machine. The DIII-D tokamak is described in Section 2.1. CTH is described in Section 2.2. The survey spectrometer use on both CTH and DIII-D are discussed in Section 2.3 The high-resolution ultraviolet spectrometer install on CTH is discussed in Section 2.4 The Langmuir probe designed and installed installed in CTH is described in Section 2.5 The spectra taken from these experiments are shown in detail in Chapter 4 and compared with modeling results using the new atomic data that were generated for this project in Chapter 5.

2.1 Tungsten rings in the DIII-D tokamak divertor

In normal operation, the DIII-D tokamak uses carbon as the main Plasma Facing Component (PFC) for the divertor. During a mini-campaign (summer 2015), tungsten was introduced into the lower divertor region by installing two continuous rings of tungsten coated inserts on the divertor shelf and floor.[15] The main chamber Plasma Facing Material (PFM) was still carbon. Experiments were conducted in the DIII-D tokamak with the tungsten coated titanium-zirconium-molybdenum inserts in the divertor to investigate tungsten sourcing and transport.[21,22] Tungsten emission was observed with passive UV spectroscopy using survey spectrometers (detailed in Section 2.3) with collection optics located at a toroidal angle of 75° and poloidally near the top of the machine (75R+2).

Two UV transmitting 78 mm fused silica lenses provide simultaneous measurements of the tungsten coated inserts in the lower divertor using two of the three survey spectrometers

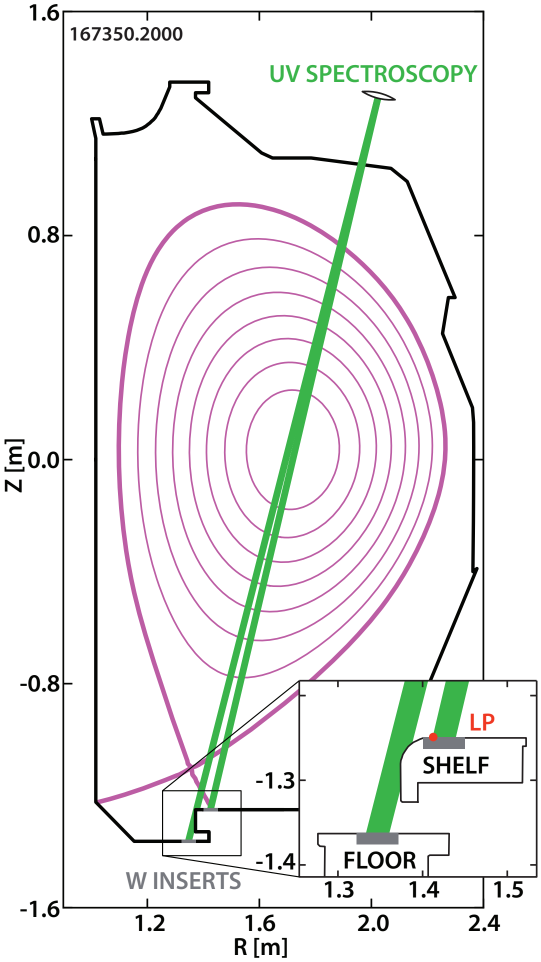

Figure 2.1: UV survey spectrometer lines of sight viewing the DIII-D tokamak divertor highlighted in green and overlaid on a reconstruction of magnetic flux surfaces. Two toroidally displaced UV lenses provide independent views that can be aligned to tungsten coated inserts on either the divertor floor or shelf. The location of a Langmuir probe on the divertor shelf is shown in red.

that can be independently aligned to tungsten rings on either the divertor shelf or divertor floor. The optical lines of sight for the spectrometers are shown in Figure 2.1 overlaid on an equilibrium reconstruction of magnetic flux surfaces for DIII-D shot 167350 at 1935 ms. The optical path was $\sim$ 292 cm giving a small solid angle for neutral tungsten light collection. A single Langmuir probe was used to assess the electron temperature and density at the tungsten surface; this is shown in the inset. The line-of-sight terminating at the floor ring was partially obstructed by the divertor nose due to the location of the collection optics. As seen in the insert of Figure 2.1 and also in the 3D rendering of Figure 2.3, the collection spot size on the divertor tiles was 3.3 cm in diameter for both the divertor floor and shelf. These distances were significantly larger than the W I ionization scale length ($\sim$1 mm) and totally encompassed within the 5 cm wide W coated tile insert. The relatively small ionization length scale of $\sim$1 mm meant that neutral tungsten emission was localized around the tungsten inserts. UV transmitting lenses and 1000 μm diameter 5 m long fused-silica fibers were selected to maximize transmitted light as UV wavelengths are severely attenuated along optical fibers. The attenuation of UV emission in optical fibers highlights the experimental difficulties of working at these wavelengths. The small solid angle of observation coupled with significant loss of light in optical fibers meant that tungsten UV signal levels were relatively small requiring exposure times of at least 30 ms, sometimes up to 2000 ms, depending on plasma conditions. Note that these exposure times are significantly longer than the time scale of an Edge Localized Mode (ELM), $\sim$ 2 ms, discussed in more detail in Chapter 5. Absolute calibration of the spectrometer sensitivity is necessary to measure W erosion via the S/XB method or to compare the relative intensities of emission lines at different wavelengths as the system's photon efficiency can vary substantially with wavelength across the UV range. However, an in-situ absolute intensity calibration of the UV survey spectrometers and collection optics on DIII-D was restricted by the limited throughput of the survey spectrometers to calibration sources between 350-400 nm. A calibration between 200-350

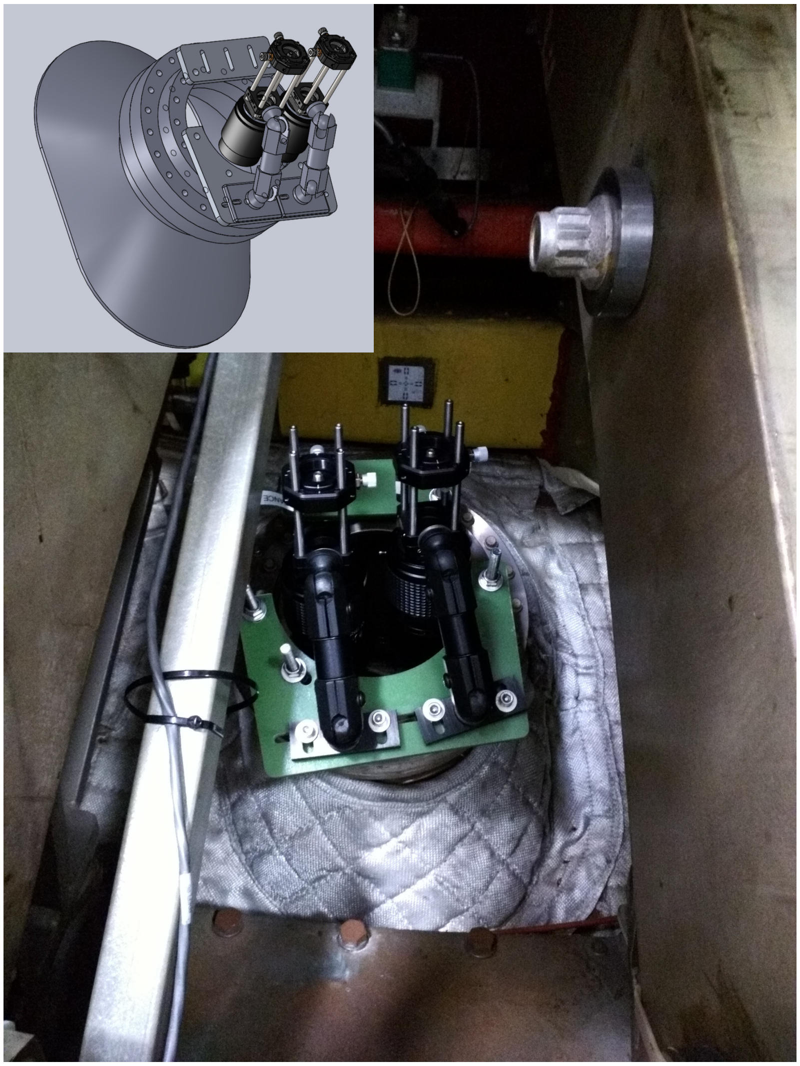

Figure 2.2: Mechanical drawing of collection optics and photo of collection optics installed on DIII-D. at a toroidal angle of 75° and poloidally near the top of the machine (75R+2).

nm was not possible though most tungsten spectral emission happens in this wavelength region.

2.2 The Compact Toroidal Hybrid (CTH)

The Compact Toroidal Hybrid (CTH)[23] is a combination of a tokamak and a five-field period torsitron limited at five locations by C, Mo and stainless steel. CTH was originally designed to investigate stability limits associated with three-dimensional magnetic field shaping. CTH is able to operate in a pure stellarator mode or in a tokamak-stellarator hybrid

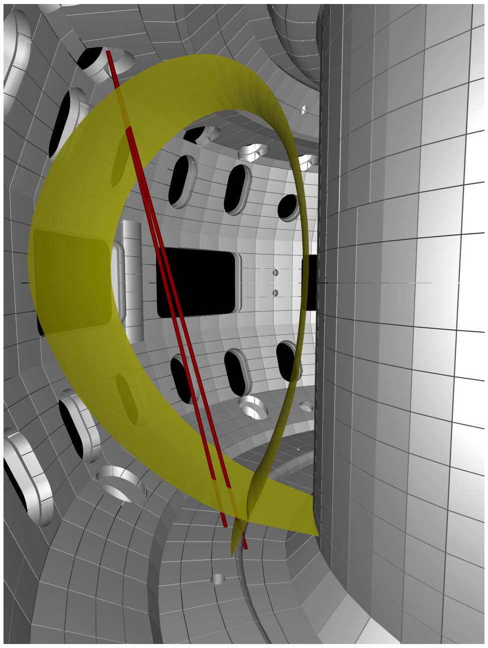

Figure 2.3: Rendering of DIII-D UV spectroscopy lines of sight into the vacuum vessel. The lines of sight are shown in red. The last closed flux surface from an equilibrium for shot 167210 at 2035 ms is depicted by the yellow surface. Courtesy of Bill Meyer.

mode. Experiments for this work utilized CTH at the lowest possible vacuum transform available to CTH. A low vacuum transform (0.02) was chosen to decrease the shot cycle time, as well as to create more consistent plasma discharges.

Basic parameters and estimates for CTH are listed in Table 2.1. CTH has a suite of magnetic diagnostics as well as x-ray based diagnostics not touched on in this thesis (see Hartwell *et al.*[23] for more information). A three-channel millimeter wave interferometer has been installed on CTH to measure the line-integrated electron density of the plasma. One of

Table 2.1: CTH parameters R is major radius, $\mathrm{a_{vessel}}$ is the minor radius, $\mathrm{a_{plasma}}$ is the plasma radius, B_0 is the magnetic field strength,I_p is the plasma current, $\mathrm{P_{ECRH}}$ is the ECRH power, n_e is the electron density, T_e is the electron temperature,β is the ratio of the plasma pressure to magnetic pressure.

Parameter	Value	Parameter	Value
R	0.75 m	$\mathrm{P_{ECRH}}$	≤ 3 kW
$\mathrm{a_{vessel}}$	0.289 m	n_e	$\leq 4 \times 10^{13}$ cm^{-3}
$\mathrm{a_{plasma}}$	≤ 0.2 m	T_e	≤ 100 eV
B_0	≤ 0.6 T	β	≤ 0.5 %
I_p	$\leq$70 kA		

the three chords passes through the horizontal mid-plane, while the other two are located at 7 cm and −11 cm from the mid-plane. A complete description of the interferometer system is given by ArchMiller *et al.*[24] The density measured with this system was used to correlate with density measurements made at the edge of the plasma with the high-Z Langmuir probe described in Section 2.5. An intensity calibration on CTH was not possible because CTH does not have access to an intensity calibration source.

2.2.1 High-Z sourcing in CTH

High-Z elements are introduced into the CTH experiment locally using a vertically translating high-Z-tipped probe which was later updated to include an embedded Langmuir probe (see Section 2.5). The initial probe is also described in detail by Johnson *et al.*[25] The probe is constructed with a 0.75" (1.91 cm) diameter 1.0" (2.54 cm) long cylindrical tungsten tip backed by a 9.5" (24.13 cm) long boron nitride sleeve. The tungsten probe can be retracted from the plasma to 25.9 cm or inserted to 19.9 cm (limiters are located at 26 cm). When the probe is inserted to 22.9 cm, the W probe tip is well within the last closed flux surface of the plasma, corresponding to a normalized toroidal flux of approximately 0.6 (Figure 2.4). Additionally, the vertical position of the plasma can be adjusted to move the plasma away from the probe tip by use of a radial field coil. To assess the increase of background emission during probe insertion, molybdenum and stainless steel tipped probes can also be inserted into CTH plasmas. The use of multiple probe tip materials allows for confidence when identifying impurity lines, highlighted in Chapter 4. The UV collection optics used for both the survey spectrometers (Section 2.3) and the high resolution spectrometer (Section 2.4) are located directly opposite from the high-Z probe as shown in Figure 2.4. A UV lens of focal length 50 mm (Universe Kogaku, UV5035B) is used in combination with a 1.6 m fused silica fiber to produce a collection spot size equal to that of the probe tip cross section (0.75" (1.91 cm) diameter). The shorter distance between the collection optics and the W source and consequently larger solid angle (as compared to the DIII-D optical setup) results in more intense and less polluted measurements of W spectral lines.

2.3 Stellarnet survey spectrometers

Two StellarNet EPP2000 spectrometers[26] sensitive between 189-302 nm and 296-408 nm were used on both DIII-D and CTH for the work presented here. Additionally, a StellarNet Bluewave spectrometer sensitive between 192-410 with lower resolution was also used. Each spectrometer has a crossed Czerny-Turner design f/4 with a 2400 grooves/mm ruled plane grating, an entrance slit of 7 μm and a resolution of $\sim$ 0.1 nm. Both spectrometers utilize a Sony ILX511 CCD detector with 2048 pixels. During DIII-D experiments, the UV survey spectrometers were housed in a neutron and x-ray shield box. Spectrometer exposure times ranged from 30 to 2000 ms, but typical W signal levels in DIII-D required integration times greater than 100 ms. A wavelength calibration over the entire range of the spectrometers was accomplished using Hg-Ne, Hg-Ar and Zn pen lamps. The resolving power of the UV survey spectrometers made it possible to identify W I spectral lines that have potential diagnostic utility.

2.4 The Auburn high-resolution UV spectrometer system

The Auburn high-resolution UV spectrometer system was optimized and designed for single channel low charge state high-Z spectroscopy. Near neutral high-Z systems produce spectral lines that are close in wavelength (see Section 5.1.1, Figure 5.1) which requires a relatively high-resolution instrument (0.7 nm/mm dispersion). The high groove/mm gratings were chosen (detailed more in Section 2.4.1) to resolve the high density of spectral lines. Near neutral high-Z systems emit mainly in the ultraviolet region as shown in Figure 5.1. A detector was chosen to maximize sensitivity to UV emission as described in Section 2.4.2.

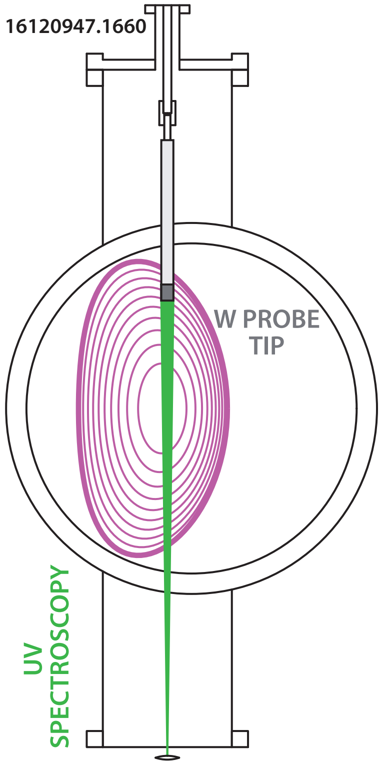

Figure 2.4: UV survey spectrometer line of sight viewing the tungsten-tipped probe highlighted in green and overlaid on a reconstruction of magnetic flux surfaces. The W probe is located directly above the spectrometer collection optics, and the High-Z tip is well within the last closed flux surface when fully inserted.

2.4.1 Aspheric corrected spectrometer

After testing options from both Andor and Princetron Instruments, the spectrometer chosen was the Princeton Instruments IsoPlane SCT 320 Schmidt-Czerny-Turner spectrometer.[27] This spectrometer design adds an aspheric correction optics over a conventional Schmidt-Turner spectrometer. The spectrometer allows for astigmatic aberrations to be canceled out for a grating angle of 16.4°. The correction of astigmatic aberrations allows for a smaller instrument function effectively improving spectral resolution over non-corrected spectrometers. Astigmatic correction is of great importance when utilizing the entire image plane of the spectrometer. The grating angle for a given central wavelength for the three gratings installed in the spectrometer is shown in Figure 2.5 (a). The further from the optimized angle the more asymmetric a spectral line will look, meaning that the instrumental function will change as a function of the grating angle. While line shape is not of great importance for the work here, the instrumental function as a function of grating angle can be calculated as describe by Verhaegh.[28] The dispersion for the various gratings as a function of central wavelength is plotted in Figure 2.5 (b). The dispersion decreases with increased central wavelength giving more spectral resolution at shorter wavelengths. This gives a slight increase in resolution for UV wavelengths where low charge state tungsten emits the most.

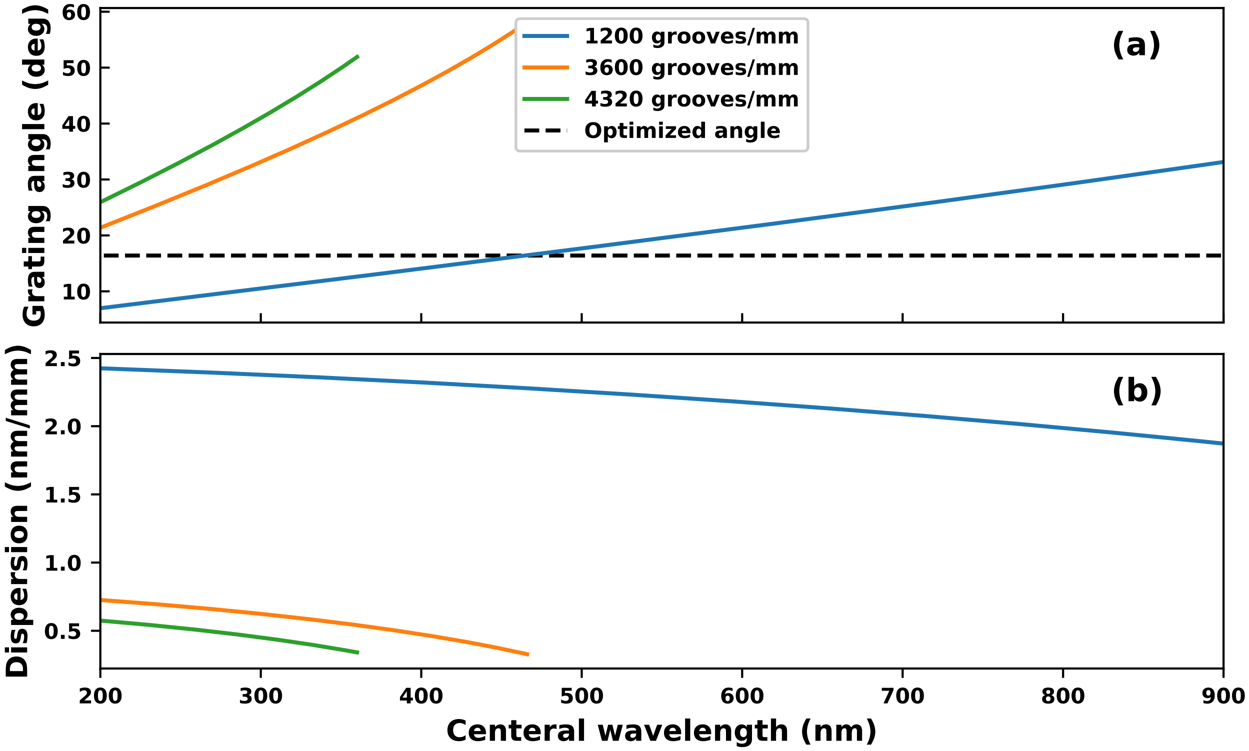

Figure 2.5: Grating angle versus central wavelength location for the three gratings used with the Auburn high-resolution UV spectrometer. The black dashed line indicates the grating angle for optimized astigmatism correction (a). The instrument dispersion versus central wavelength (b).

2.4.2 Ultraviolet optimized detector

The detector used with the Auburn High-resolution UV spectrometer is an Andor Newton DU920P-BU2 CCD. The detector has a pixel size of 26×26 μm arranged in a 1024×256 array. The frame rate is variable from 144 Hz using full vertical bin to over 1000 Hz vertically binning only 20 rows on the bottom of the CCD detector. The CCD detector can be cooled to -80 °C to minimize dark current. The system was designed as a single point measurement for optimal signal to noise ratio, as opposed to many fusion spectroscopy systems which are generally multi-point. The Newton 920 was chosen because of its relatively high quantum efficiency in the UV region ($>$ 50% in the near and middle UV) where low charge state high-Z elements radiate the most. The efficiency of the CCD detector can be seen in Figure 2.6. This efficiency is much higher in the UV wavelength region than the more widely used EMCCD detectors for fusion spectroscopy. Intensified cameras generally are limited to less than 30% quantum efficiency. If a multi-point system was desired, a EMCCD or CMOS detector would be necessary for the improvement of full frame readout rates.

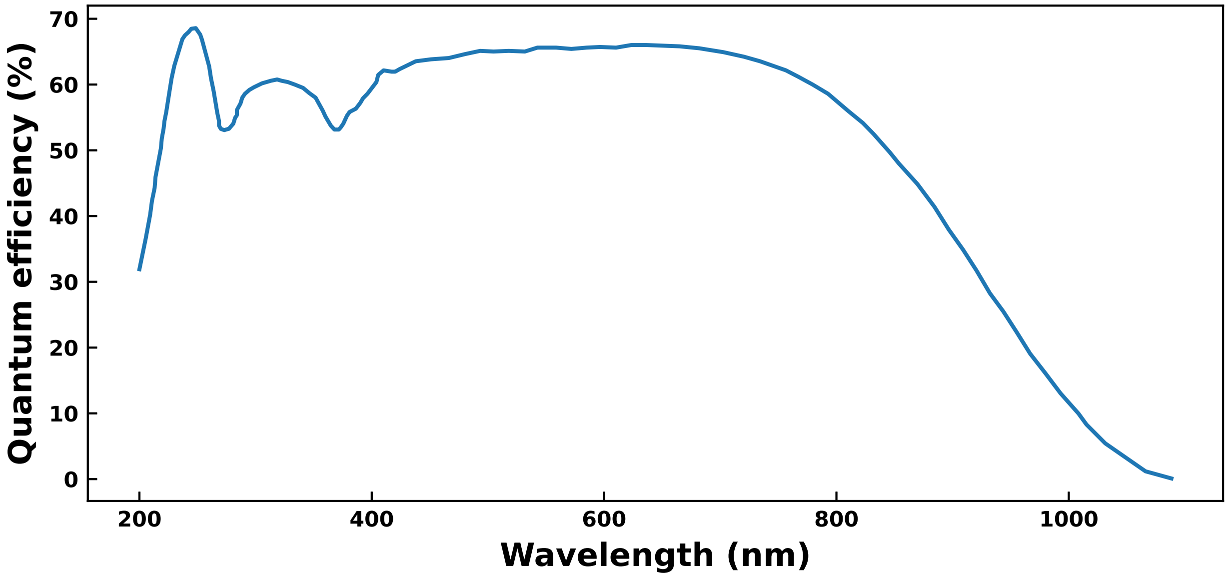

Figure 2.6: Andor Newton 920 DU920P-BU2 quantum efficiency

2.4.3 Auburn high-resolution UV spectrometer control software

Custom software was written in Python to control both the camera and the spectrometer. The Princeton Instruments spectrometer is controlled via serial communications over USB 2.0 with Python. The details of the control software as well as commands are explained in Appendix C. The Andor camera is controlled with the Andor SDK that allows a C++

interface to the camera. Cython is used to interface Python with the C++ SDK and allows for the camera to be controlled via Python.

2.4.4 Spectrometer instrumental function

The instrument function depends most strongly on the grating parameters as seen in Figure 2.5 (b), then on the grating angle and finally on spectral line position from the center of the detector. The instrument function line shape can be measured using various calibration lines from calibration light sources. These light sources have low temperatures so almost all spectral broadening is due to instrument function. Calibration lamps Hg-Ar, Hg-Ne, Cd and Zn provide good spectral coverage in both UV and visible wavelength regions.

The IsoPlane was designed to produce Lorentzian rather than Gaussian instrument functions. These Lorentzian functions are asymmetric due to coma aberrations.[29] An example from a Hg-Ne pen lamp in Figure 2.7 shows the asymmetric instrument function for different gratings of the Hg I line at 296.73 nm. This function is described by Equation 2.1, a skewed Lorentzian, where A is the amplitude of the spectral line, X_0 is the centroid of a spectral line, a is the width of the spectral line and both b and c are skew parameters for each side of x_0. A Python program described in Appendix C will fit a function comprised of an arbitrary number of asymmetric Lorentzians to a spectrum.

$$L(x) = \begin{cases} \left(\frac{A}{1+4(\frac{x-x02pt}{a})^2} \right)^b, & x \geq x_0 \\ \left(\frac{A}{1+4(\frac{x-x02pt}{a})^2} \right)^c, & x \leq x_0 \end{cases} \tag{2.1}$$

2.5 The High-Z Langmuir probe

As will be discussed in detail in Chapter 3, spectral line intensities are dependent on the local T_e and n_e. A combined high-Z probe with a Langmuir probe tip was thus constructed

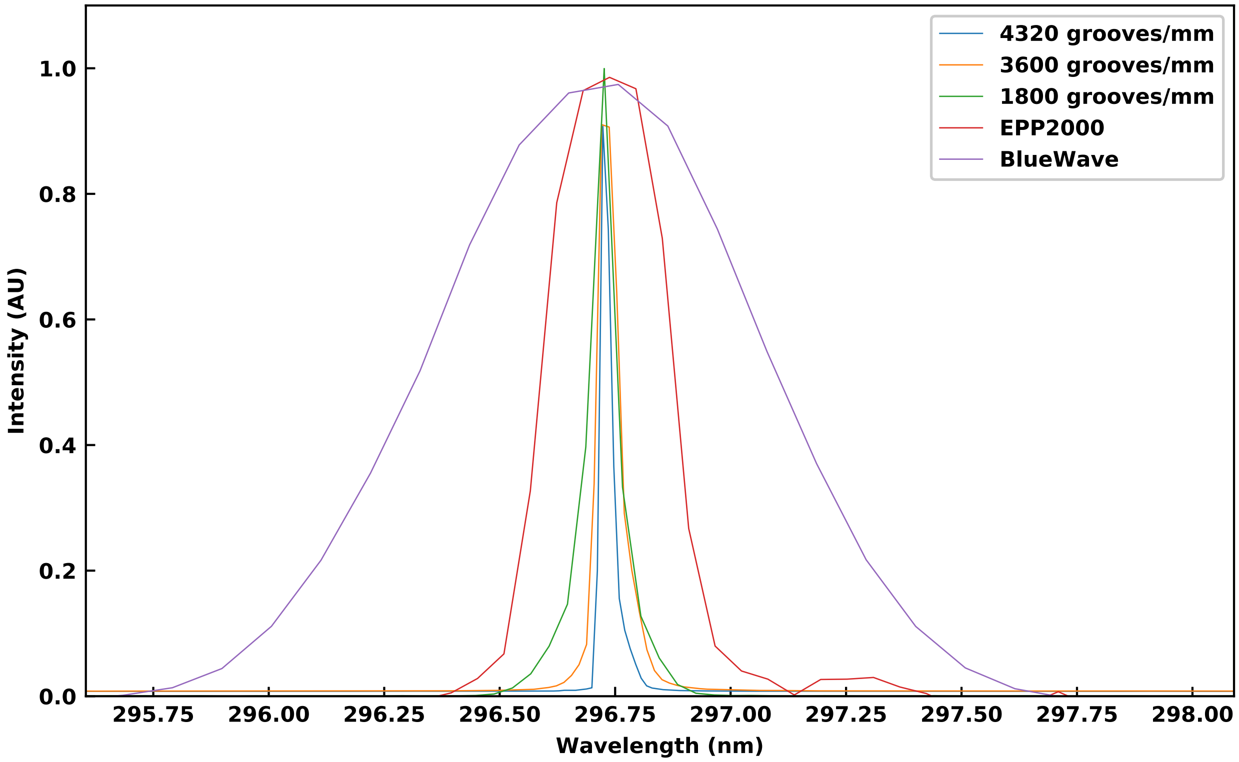

Figure 2.7: Comparison of the IsoPlane spectrometer with the different gratings, the Stellarnet EPP2000 and Bluewave spectrometers for Hg I 296.728 nm $5d^{10}6s6d$ ($^3D_1$) $\rightarrow$ $5d^{10}6s6p$ ($^3P_0$). A significant reduction in instrument transfer function corresponding to an increase in wavelength resolution is observed from the Stellarnet survey spectrometers to the IsoPlane spectrometer.

to simultaneously observe high-Z spectra while also constraining free parameters (T_e & n_e) in the collisional radiative modeling using the Langmuir probe measurements.

Langmuir probes come in multiple configurations, which are defined by the number of probe tips that are utilized. The most common are single, double and triple tip probes. The theory of single tipped probes will be discussed here along with design choices for implementation on CTH. The single tipped probe was chosen for simplicity of design and the simplicity of the theory. The single tipped Langmuir probe also allows for increased spatial measurement density in future CTH edge probe diagnostics compared to the other probe types. This is because probe tips must be many Deybe lengths away from each other so the sheath that is formed around one probe tip does impact other probe tips.

It is worth considering the Debye length in more detail. The bulk plasma is made up of free electrons and ions. In the presence of a conducting surface such as a probe, charged particles will redistribute in a way that eliminates an induced electric field. This phenomenon is known as Debye shielding; electrons dominate the process as they are more mobile than the heavier ions. A sheath is formed with a length that is governed by local plasma parameters. The thickness of this sheath region is governed by Equation 2.2 where λ_{D} is the Debye length in meters, ϵ_0 is the permittivity of free space, T_{e} is electron temperature in eV, n is the electron density in the bulk plasma and e is the charge of the electron.

$$\lambda_{\mathrm{D}} = \sqrt{\frac{\epsilon_0 T_{\mathrm{e}}}{n e^2}} \tag{2.2}$$

The plasma outside of the Debye length does not feel the effects of electric fields existing further than a Debye length away. The Debye length for plasma parameters relevant across a wide range of possible CTH plasma edge parameters is depicted in Figure 2.8. The Langmuir probe will be electrically insulated but surrounded by a larger tungsten slug; it is therefore very important that the probe be outside the Debye sheath of the larger tungsten slug. If the probe is within the sheath of the larger tungsten slug, the Langmuir probe will not sample the bulk density outside the Debye length of the probe but rather some other density within the sheath of the larger tungsten block. The design has a boron nitride (BN) insulator separating the Langmuir probe tip ∼1 mm away from the tungsten slug for even moderate CTH plasma conditions. The probe tip thus is located ∼100 times farther from the tungsten block than the Debye length, and therefore, the Langmuir probe tip should sample the bulk plasma.

A probe that is electronically isolated will eventually build up a charge until it floats up to the plasma floating potential. This is due to differences in the thermal speeds of electrons and ions. The electrons move faster and therefore have a greater flux to the probe. The current density to a probe is given by $J = e(n_{\mathrm{i}} v_{\mathrm{th_i}} - n_{\mathrm{e}} v_{\mathrm{th_e}})$. The probe then quickly charges up negatively until electrons are repelled and the total current to the probe is zero.

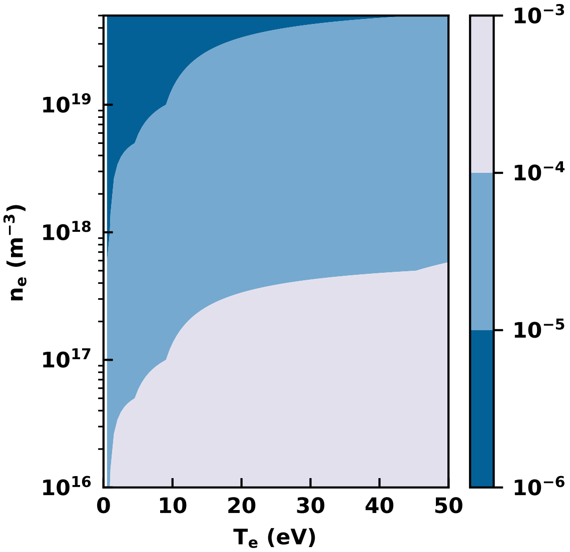

Figure 2.8: Debye lengths for a range of possible temperature densities in the edge of CTH plasmas.

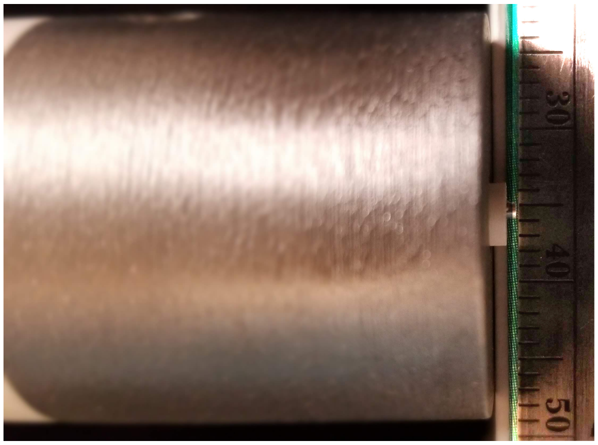

Figure 2.9: Tungsten slug seen as the large piece of metal. The BN insulating sleeve is the white ceramic and the Langmuir probe is the smaller piece of metal sticking out of the BN insulator. The scale of the ruler is millimeters.

The probe tip can be biased externally to repel electrons so that the current collected by the probe is entirely due to ions; this is called ion saturation $I_{\mathrm{sat_i}}$. Ion saturation current is then given from the Bohm criterion given in Equation[30] 2.3, where $I_{\mathrm{sat_i}}$ is the ion saturation current, e is the charge of an electron, n_e is the electron density, T_e is the electron temperature, m_i is the mass of the ion and A_s is the surface area of the probe. This equation assumes that $T_\mathrm{i} << T_\mathrm{e}$.

$$I_{\mathrm{sat_i}} = 1/2en_\mathrm{e}\sqrt{T_\mathrm{e}/m_\mathrm{i}}A_\mathrm{s} \tag{2.3}$$

In a simplified model, it is assumed that ions are collected when the probe is biased lower than the plasma potential and otherwise repelled. This will, however, depend on the thermal speed of incoming ions. In the ideal case of electron saturation, the current saturates for increasing voltage.

$$I_{\mathrm{sat_e}} = 1/2en_\mathrm{e}\sqrt{T_\mathrm{e}/m_\mathrm{e}}A_\mathrm{s} \tag{2.4}$$

The current as a function of voltage in the transition region is given by Equation 2.5 where e is the charge of an electron, the potential drop across the plasma sheath is $\phi_\mathrm{sh} = \phi_{textp} - \phi_\mathrm{probe}$ (the difference in probe and plasma potential), A_s is then the total cross-sectional area of the probe.

$$I_\mathrm{t} = I_{\mathrm{sat_i}} - e^{-1/2}en_\mathrm{e}\sqrt{T_\mathrm{e}/m_\mathrm{e}e^{e\phi_\mathrm{sh}/T_\mathrm{e}}A_\mathrm{s}} \tag{2.5}$$

Using the above equations, the "IV" (current vs. voltage) trace of the probe for plasma conditions relevant for CTH are shown in Figure 2.8.

The temperature rise of a Langmuir probe in hot plasmas is potentially of great concern as there is a potential for melting. The probe tip diameter and length were chosen to minimize current draw while maintaining enough thermal mass to maintain temperatures below the melting point of tungsten during the discharge. The temperature rise of the probe

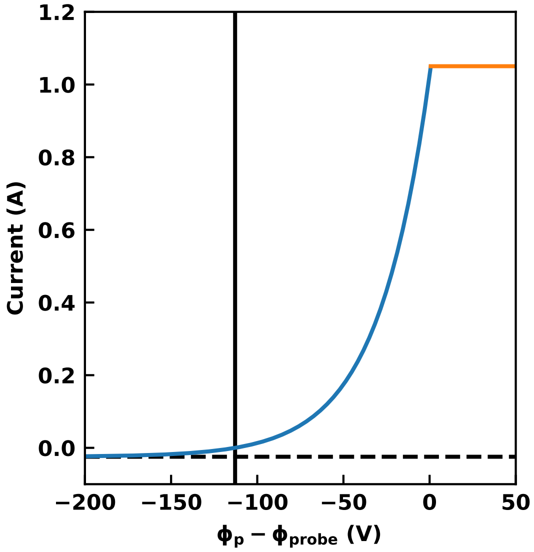

Figure 2.10: IV trace for an idealized single tipped Langmuir probe at $T_e = 30$ eV and $n_e = 1 \times 10^{18}$ m^{-3}. The black dashed line represents ion saturation current. The orange line is the electron saturation current for an idealized probe. The floating potential of the probe is solid black vertical line.

can be estimated with Equation 2.6 from Shunko.[31] P_e is the power deposited to the probe, A_s is the surface area of the probe, $n\langle v\rangle$ is the average electron density, k is Boltzmann's constant and T_e is the electron temperature.

$$P_e = A_s n\langle v\rangle kT_e \tag{2.6}$$

A single tipped probe was chosen being swept from ion saturation into the the transition portion of the IV curve seen in Figure 2.10. A triangle waveform was chosen to minimize the amount of time a significant number of electrons would be collected to minimize thermal issues as well as to increase data collection for points in the transition region. The IV trace is shown in Figure 2.11

The number of electrons drawn to the probe can be calculated, assuming that the electrons impact the probe with some thermal energy $k_B T_e$. The power deposited to the probe can be calculated with Equation 2.6.

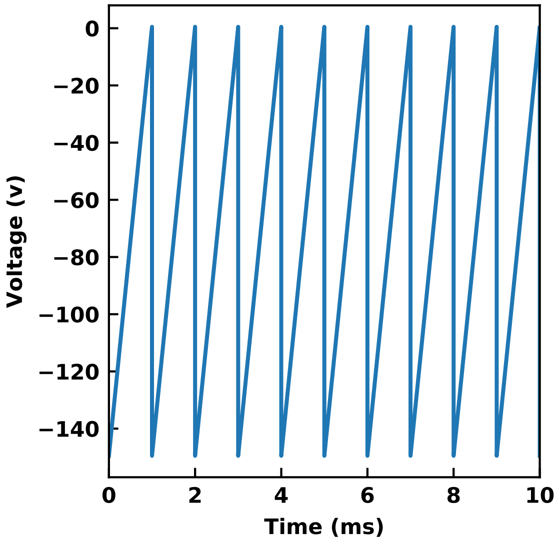

Figure 2.11: Waveform of voltage applied to the Langmuir probe.

The thermal rise of the probe is then calculated with Equation 2.7 where m_{w} is the mass of tungsten (6.93×10^{-5} kg) in the probe tip, $c_{\mathrm{w}} = 135$ Jkg^{-1}k^{-1} is the thermal capacity of tungsten and dt is the time step.

$$\Delta T = \frac{P_{\mathrm{e}} dt}{m_{\mathrm{w}} c_{\mathrm{w}}} \tag{2.7}$$

Using the voltage trace as shown in Figure 2.11, the flux of electrons $n_e \langle v_e \rangle$ is calculated with Equation 2.5 neglecting the charge of the electron e. The temperature rise for two different possible CTH plasma conditions is depicted in Figure 2.12. This would assume constant plasma conditions over entire CTH discharge and thus is a worse case scenario. Clearly, the thermal rise of the probe over the course of a shot is much less than the melting point of tungsten (3400 °C) and therefore should not be an issue.

Sample Langmuir probe analysis

An overview of the analysis procedure for the movable CTH Langmuir probe will be discussed. Data is digitized from a LM741 op-amp for voltage measurement and an AD629 comparative op-amp for the current measurement. Data is digitized by a DTAQ system

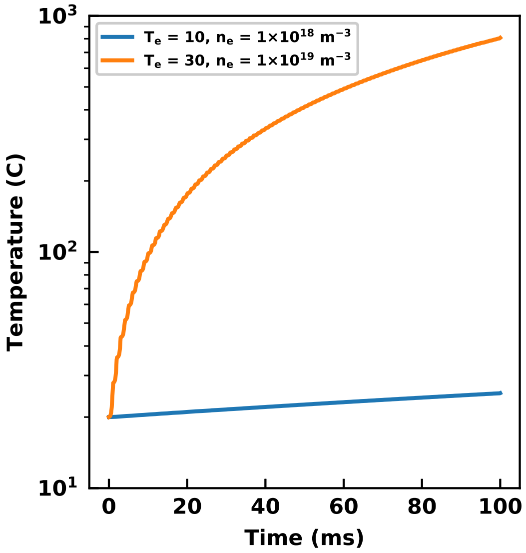

Figure 2.12: Thermal rise of a single tipped Langmuir probe for possible CTH plasma conditions. Probe diameter of 1.5 mm and length of 0.5 mm.

at 50 kHz and stored in a MDSplus tree (voltage under “ACQ1963:INPUT_42” and current under “ACQ1963:INPUT_41”). Digitizer channels have voltage ranges ±10 V. Voltage was measured using voltage divider with a factor of 20. The current measurement utilized various multiplication ratios depending on expected current draw of a particular discharge. The multiplication factors ranged from $100X$ in ECRH discharges to $1X$ in ohmic heated discharges when the probe was past the last closed flux surface.

An example of raw voltage and current traces as functions of time can be seen in Figure 2.13. The data shown is from an ohmic heated discharge when the probe was located at 24 cm (2 cm past the last closed flux surface). A triangle waveform was chosen to minimize time spent at the two extremes of the sweep. The triangle waveform gives a linear variation to the voltage trace. The sweep rate of the power supply was limited to 443 Hz.

Temperature and density measurements were obtained for individual voltage sweeps. An individual sweep is identified in Figure 2.10 as the red region. The power supply for the Langmuir probe is not triggered relative to the CTH discharge time, therefore, the relative timing of the voltage sweep is not known. In order to find the timing of sweeps relative to other CTH diagnostics timings, a triangle waveform is fit to the voltage signal. With this

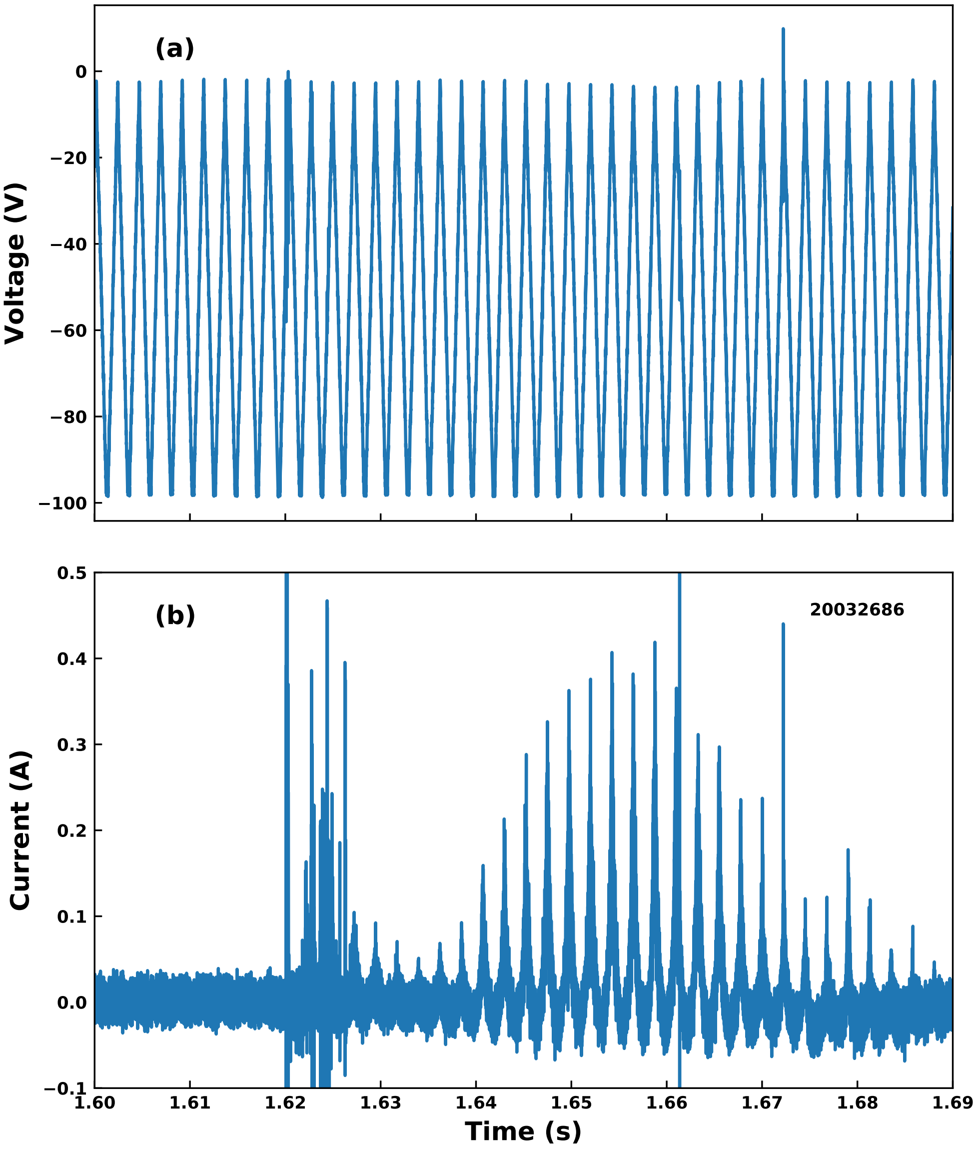

Figure 2.13: Voltage and current measurements from Langmuir probe in CTH discharge 24 cm away from the mid-plane. Significant noise is associated with the start of the ohmic phase of the discharge at 1.62 s.

information, the relative timing information can be calculated. A median filter is applied to the current trace shown as the relatively smooth black line. The median filter uses Numpy's "medfilt" function with a kernel of 61. Various sized median filters have been tested; the size of the median filter does not impact the final inferred temperature, density or plasma potential greatly.

Once an individual sweep has been identified, the current draw from the Langmuir probe tip can be plotted against the voltage sweep as depicted in Figure 2.14. The blue dots are current and voltage pairs after the median filter has been applied. The voltage and current data can then be fit directly to the single tipped Langmuir probe governing equations. The ion-saturation region can be fit using Equation 2.3 and the transition region with Equation 2.5. The probe is operated such that the Langmuir probe never reaches electron saturation in ohmic discharges, in order to minimize heat flux and resulting melting and erosion of the probe tip. The above equations are fit directly with SciPy's leastsq function taking T_e, n_e and V_p as free parameters. The fitted function to the measured IV trace in Figure 2.10 is the red line with the following parameters $T_\mathrm{e} = 27.4$ eV, $n_\mathrm{e} = 2.5 \times 10^{12}$ cm^{-3} and $V_\mathrm{p} = 40.5$ V.

The measured electron parameters from fitting the raw Langmuir probe data are reasonable for CTH discharges. While there is no temperature measurement to compare with, Langmuir probe density measurements can be compared to density profiles measured with interferometry. Qualitative trends can be investigated by varying the probe location as well as looking at the time dependence of measurements during the discharge. Clear trends are observed in Figure 2.16. Density measurements from the Langmuir probe clearly increase with position to the mid-plane. Both the inferred temperature and density have expected trends over the course of the discharge, increasing with plasma current then decreasing as the plasma current decreases.

As a check of how well the fitting equation describes the measured data, the variation in the fitted parameters (2σ from taking the diagonal of the covarient matrix resulting from least squares fit to the data) is indicated by vertical bars on each data point in Figure 2.16.

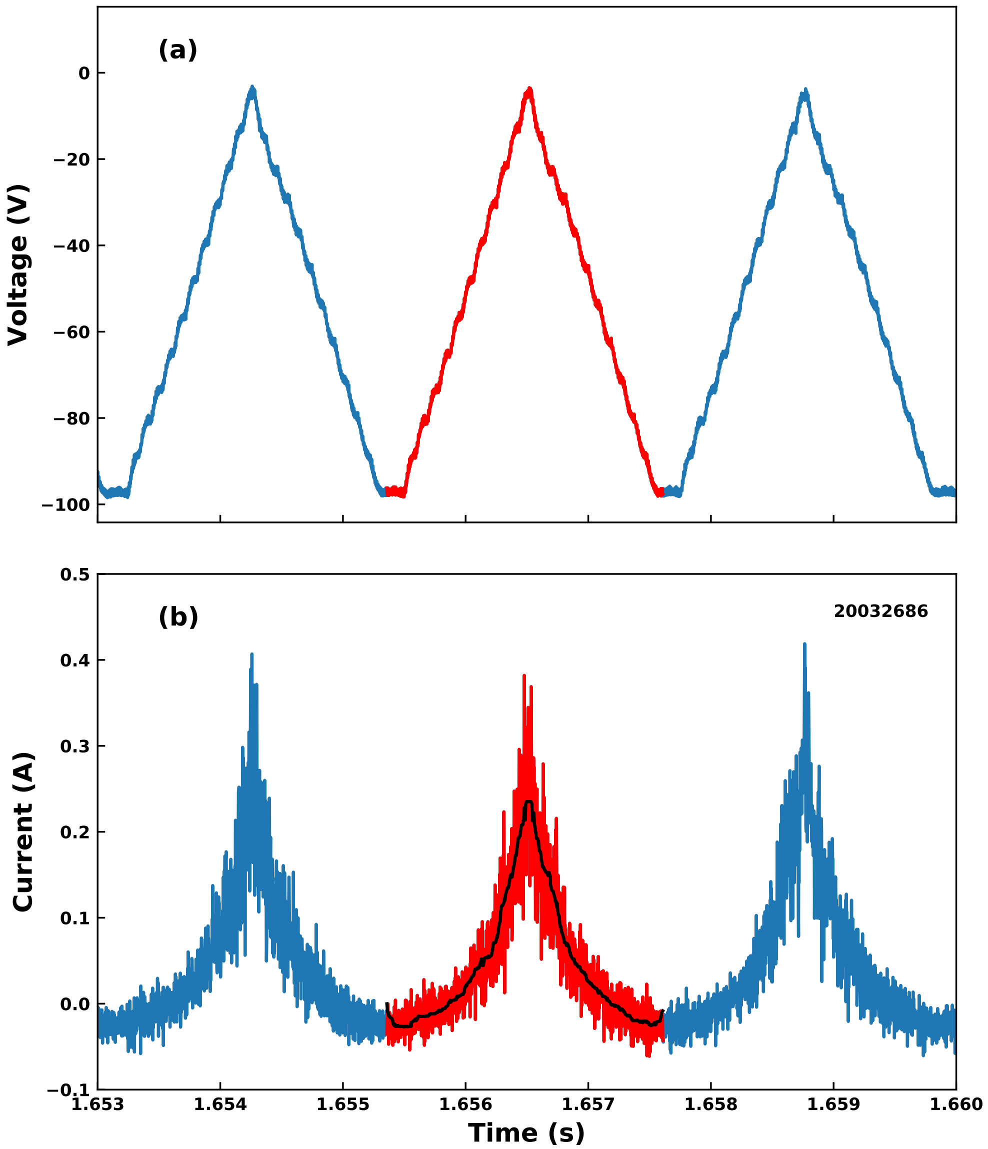

Figure 2.14: Langmuir probe voltage (a) during a CTH discharge. The current draw though Langmuir probe in blue (b). A single sweep is highlighted in red, the average using a median filter is over-plotted in black.

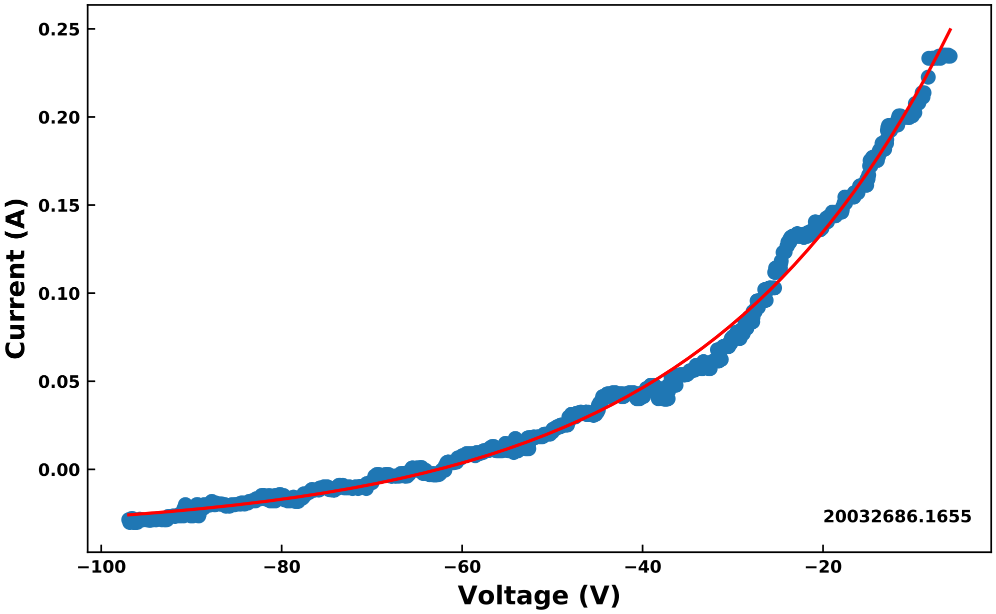

Figure 2.15: Current versus voltage of the Langmuir probe during a single voltage sweep is plotted in blue. The red line is a least-squares fit to the data using Equation 2.5 with the following parameters. $T_\mathrm{e} = 27.4$ eV, $n_\mathrm{e} = 2.5 \times 10^{12}$ cm^{-3} and $V_\mathrm{p} = 40.5$ V.

These variations are a small percentage of the values of the fitted parameters and suggest a good fit to the data.

The temperature and density from a voltage sweep can also be calculated using a different method by first subtracting off the ion saturation current and then plotting the log of current versus density. The process is described by Equation 2.8 where I_s is the ion saturation current, q is a unit of charge, T_e is the electron temperature, $V_\mathrm{bias} - V_\mathrm{f}$ would be the voltage of the probe tip and V_f is the floating potential.

$$\ln|I_\mathrm{p} - I_\mathrm{s}| = \frac{q}{k_\mathrm{B} T_\mathrm{e}}(V_\mathrm{bias} - V_\mathrm{f}) + \mathrm{const} \tag{2.8}$$

Note that electron temperature in (eV) can be related to the Boltzmann constant with Equation 2.9.

$$\frac{k_\mathrm{B} T_\mathrm{e}}{q} = T_\mathrm{e}\ (\mathrm{eV}) \tag{2.9}$$

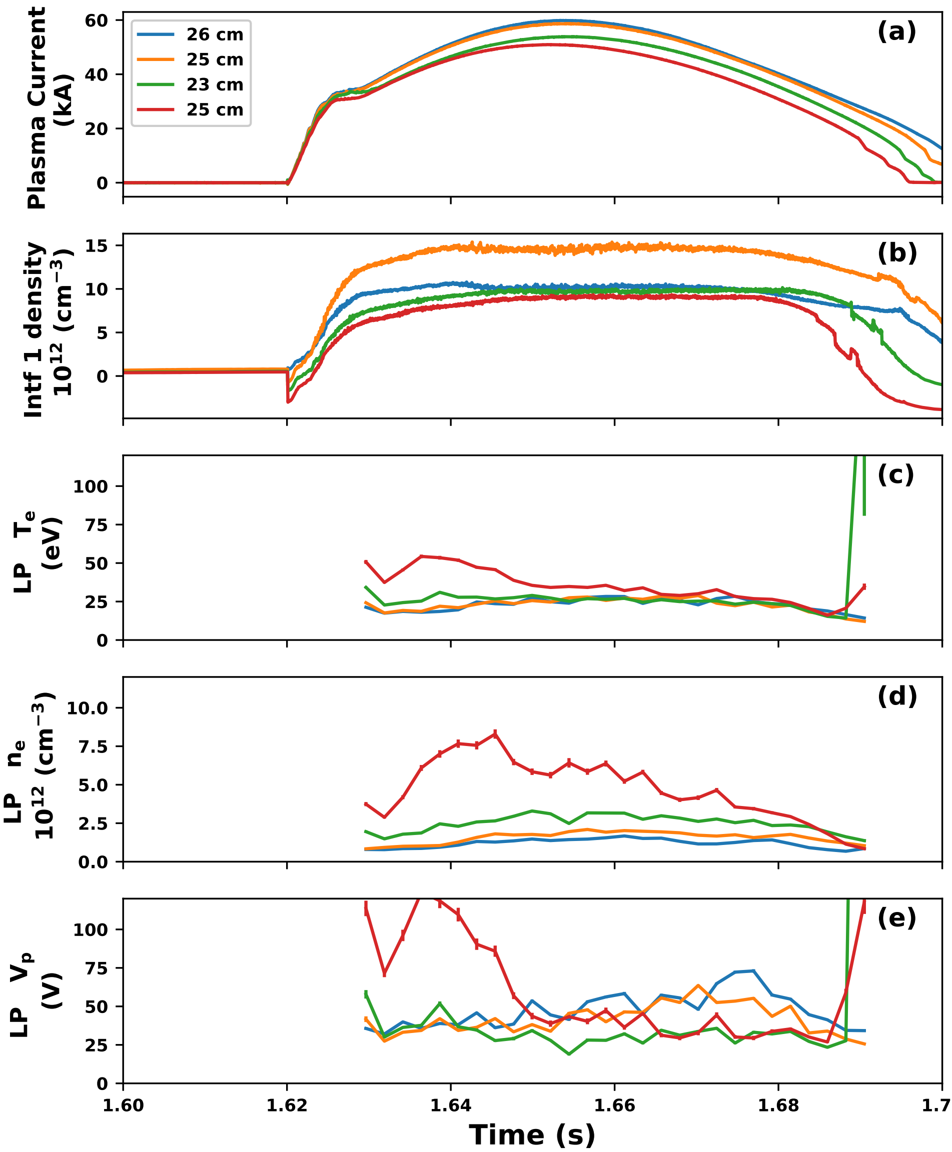

Figure 2.16: Plasma current during multiple CTH discharges(a). Mid-plane interferometer density measurement (b). Electron temperature measured by the Langmuir probe at various depths (c). Electron density measured by the Langmuir probe at various depths (d). Plasma potential measured by the Langmuir probe at various depths (e).

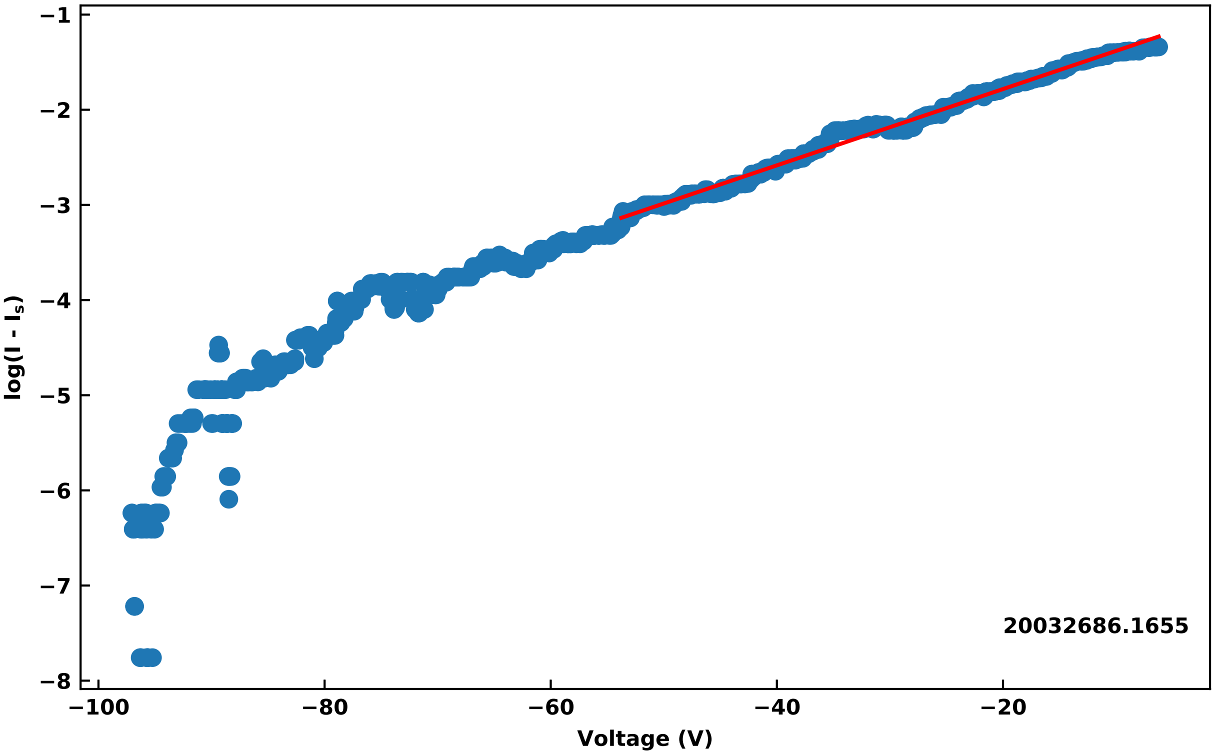

Figure 2.17: Log of the Langmuir probe current draw, offset by the ion saturation current versus probe voltage for one sweep plotted in blue. The linear fit to the data is shown in red with the coefficients $m = 0.0401$ and $b = 0.981$ giving $T_\mathrm{e} = 24.9$ eV and $n_\mathrm{e} = 2.0 \times 10^{12}$ cm^{-3}.

Figure 2.17 shows the transition region fitted with the linear equation in red of the form of Equation 2.10.

$$y = mx + b \tag{2.10}$$

Once the linear equation has been fit to the data, the electron temperature T_e in eV is then obtained with Equation 2.11.

$$T_\mathrm{e} = 1/m \tag{2.11}$$

The electron density is backed out with Equation 2.12 where I_s is the measured ion saturation current obtained from b in the linear fit of Equation 2.10, q is the fundamental charge, A_s is the surface area of the probe tip, m is the mass of the ion species (in these cases hydrogen), k_B is Boltzmann's constant and T_e is the electron temperature that was obtained from fitting the linear line.

$$n_\mathrm{e} = \frac{I_\mathrm{s}}{qA_\mathrm{s}\exp(-1/2)}\sqrt{\frac{m}{k_\mathrm{B}T_\mathrm{e}}} \tag{2.12}$$

The process of fitting a linear line to the probe data is applied to same data of Figure 2.10 in Figure 2.17. The linear fitting method gives $T_\mathrm{e} = 24.9$ eV and $n_\mathrm{e} = 2.0 \times 10^{12}$ cm^{-3}, which are very close to the parameters fit in the direct fitting method of $T_\mathrm{e} = 27.4$ eV and $n_\mathrm{e} = 2.5 \times 10^{12}$ cm^{-3}.

2.5.1 Uncertainty analysis of Langmuir probe data

There are multiple approaches for determining the uncertainty of measurements derived from Langmuir probes. The most basic method assumes that the underlying equations of Langmuir probe theory[32] are valid and uses statistical uncertainty to estimate error bars. There are known problems with the basic set of probe equations (Equations 2.3 and 2.4) that can lead to uncertainties due to the model such as non-maxwellian temperatures at the edge of the plasma.[33] CTH ohmic plasmas are reasonably ionized ($\sim$ 0.1 - 1% neutral fraction) leading to the almost idealized current versus voltage traces in Figure 2.10. The almost idealized curves should lead to any error introduced by the model being relatively small as the data is well described by the model so error propagation due to the Langmuir probe model will not be included and a purely statistical approach will be taken.

The relatively slow sweep rate of the probe power supply (443 Hz) leads to a limited number of data points to be fit during the CTH ohmic discharge. Often there are 15-20 usable sweeps (those that can be fit well by a least-squares approach) during the ohmic phase of the CTH discharge. The small number of sweeps does not allow for averaging many sweeps at constant plasma parameters. The plasma parameters evolve over time with ohmic discharge, meaning that a statistical method cannot be used to estimate the uncertainty.

As there is not another diagnostic for T_e measurements, a cross-reference cannot be done to estimate the errors.

The limitations of the Langmuir probe implementation on CTH require uncertainty to be estimated using the standard error for a parameter from an Ordinary Least-squares method.[34] Note that this method of error bar estimation is most likely much smaller than a proper treatment of the uncertainty would obtain. However, this does provide a lower bound on the uncertainty from the Langmuir probe. The standard error can be calculated with Equation 2.13 where s is the standard error of the regression, f_c is the cost function of the least squares fit, n is number of data points, p is the number of free parameters and C_{jj} is the covariance matrix from least-squares process.

$$s = \sqrt{\frac{f_c}{n-p}}\sqrt{C_{jj}} \tag{2.13}$$

Error bars using this method have been included in data analysis shown in Chapter 5.

2.5.2 The Debye sheath

The layer of positive space charge arising from the difference in the sound speed between electrons and ions is called the Debye sheath (DS). The generation of space charge necessitates that $n_\mathrm{e} < n_\mathrm{i}$ with the characteristic length given by the familiar Equation 2.14 for the Debye length. The DS is also characterized by the Bohm criterion which requires that the ion velocity be equal to or greater than the plasma sound speed[35] where λ_D is the Debye length, ϵ_0 is the permittivity of free space, k_B is Boltzmann's constant, T_e is the electron temperature, e is the charge of an electron and n_e is the electron density.

$$\lambda_\mathrm{D} = \sqrt{\epsilon_0 k_\mathrm{B} T_\mathrm{e}/e^2 n_\mathrm{e}} \tag{2.14}$$

2.5.3 The Chodura sheath

The constraints of heat flux to plasma facing components (particularly the divertor) in a fusion reactor requires oblique angles of incidence for particles on surfaces. The small angles effectively reduce heat flux to PFCs allowing for reactors to operate at higher power densities. The Chodura sheath occurs due to the gyro-motion effects of ions and electrons at oblique angles first described by Chodura.[36] Unlike the Debye sheath, the Chodura sheath (CS), also known as the Magnetic Presheath (MPS), is quasi-neutral; however, there is a significant electron field oriented perpendicular to the surface. The model developed by Chodura is constrained by the boundary conditions at the entrance to the MPS (the Chodura criterion state that the ion velocity must be at or greater to the sound speed at the angle of the magnetic field) and at the entrance to the DS (Bohm criterion). The total drop across the Chodura and Debye sheaths is also limited to $\sim 3kT_\mathrm{e}$. Figure 2.18 is a cartoon diagram of the sheath region showing the Chodura and Debye sheaths.

The fluid model by Stangeby[37] expanded on the work of Chodura and found that the Dybe sheath disappears for magnetic field angles below an incidence angle threshold. Stangby's paper presents a comprehensive derivation of the fluid Chodura sheath and therefore this derivation will not be repeated here, however, the critical angle (α^*) for this disappearance of the Debye sheath is given by

$$\alpha^* \equiv \sin^{-1}\left\{\left[\left(\frac{2\pi m_\mathrm{e}}{m_\mathrm{i}}\right)\left(1+\frac{T_\mathrm{i}}{T_\mathrm{e}}\right)\right]^{1/2}\right\} \tag{2.15}$$

T_e is the electron temperature, T_i the ion temperature , m_i is the mass of the main ion species, B_mod is the magnetic field strength and α is the angle the magnetic field makes with the surface.

The sheath model in this work is that of Stangeby's[37] taking the form of a Python code with the following parameters: T_e is the electron temperature, T_i is the ion temperature, n_inf is the bulk density, m_i is the mass of the main ion species, B_mod is the magnetic field

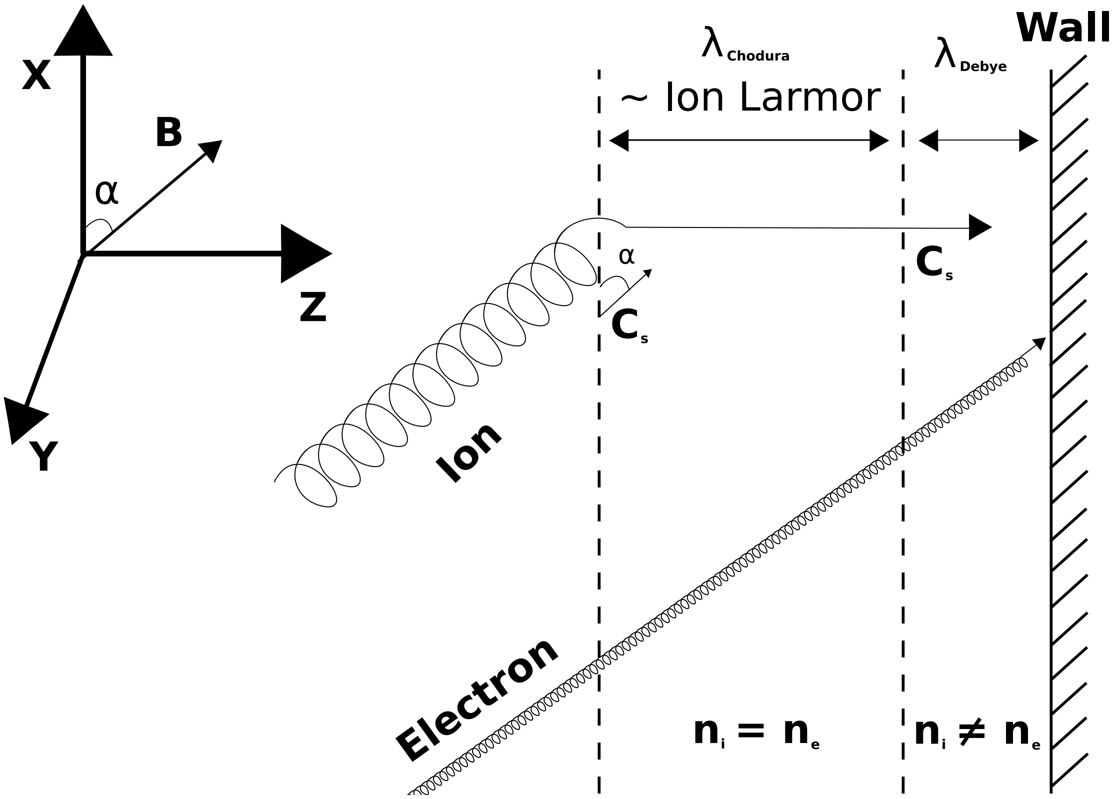

Figure 2.18: Cartoon diagram of the Chodura sheath. The three regions that make up the sheath region are seen separated by the dashed lines. Note that this figure is not to scale; the Chodura sheath is much larger than the Debye sheath.

strength and α is the angle that the magnetic field makes with a surface. The Python code then computes an electron density profile through the sheath for CR modeling. The electron temperature is assumed to be constant in the sheath region in this model; however, particle simulations suggest there is temperature variation within the sheath.[38] The complexity of temperature variation has been included in this model. Variations within the sheath could create similar effects to the addition of a density gradient. However, a new study would have to be completed to assess these effects.

The density profile for various magnetic field incidence angles for both the Deybe sheath (when present) and Chodura sheath are shown in Figure 2.19. The two smallest angles of incidence are below the critical angle for the formation of the Debye sheath, therefore no Debye sheath is present. The entire potential drop from the bulk region occurs within the Chodura sheath. The two larger incidence angles have an associated Debye sheath (dashed line) because both are above the critical angle. For the parameters chosen in Figure 2.19, the critical angle is $\sim 3.5^\circ$.

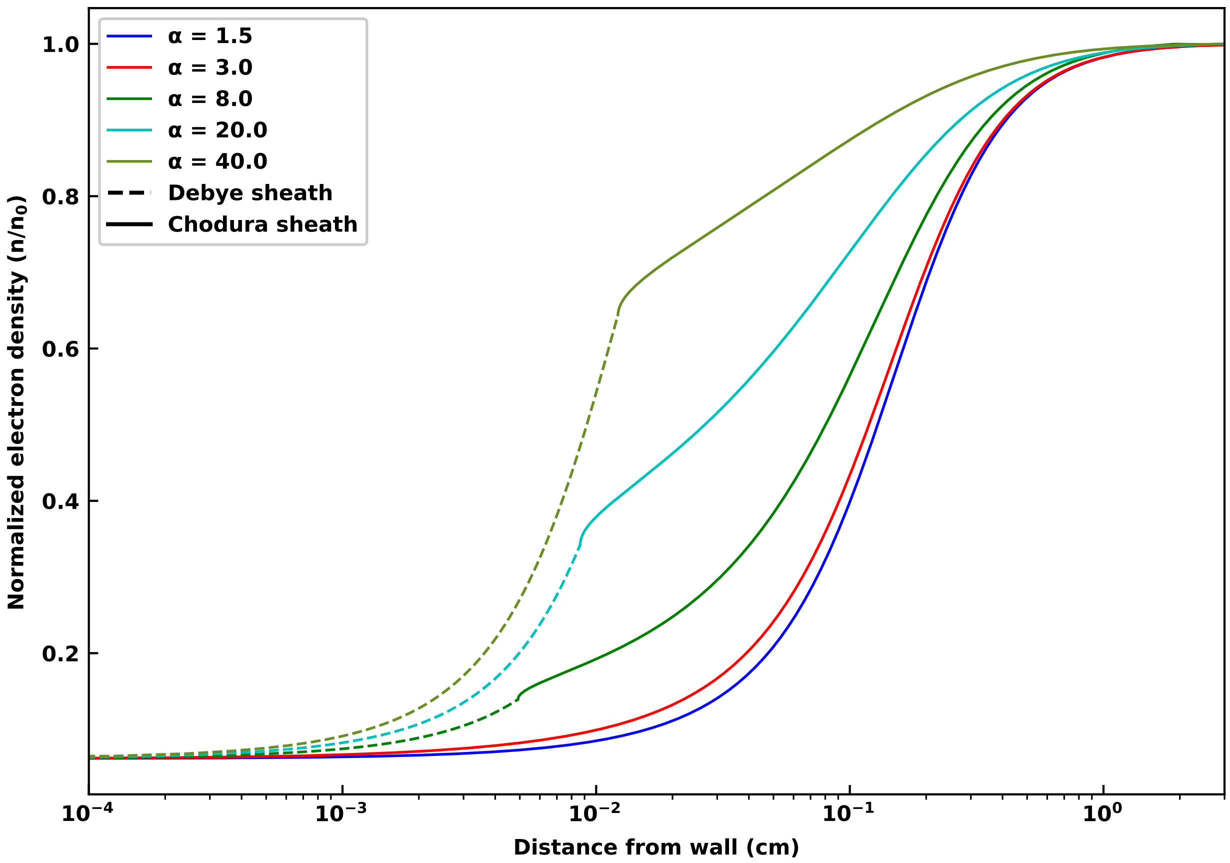

Figure 2.19: Normalized electron density in the Chodura (solid line) and Deybe sheaths (dashed line where it exists). As a function of distance from the wall for various magnetic field incident angle. The plasma parameters for the sheath are $T_{\mathrm{e}} = 10$ eV, $T_{\mathrm{i}} = 1$ eV, $m_{\mathrm{i}} = 1$, $B_{\mathrm{mod}} = 0.6$ T, $n_{\mathrm{e}} = 1 \times 10^{13}$ cm^{-3}.

Chapter 3

Collisional Radiative Theory

Collisional radiative theory originally developed by Bates, Kingston and McWhirter[39] connects atomic physics and plasma physics. The work was later expanded to include the role of metastables states by Summers *et al.*[40] Generalized collisional radiative theory has been successful in accurately modeling both astrophysical (Bryans *et al.*[41]) and laboratory plasmas (Behringer *et al.*[42]). A number of collisional radiative codes exist, including those in the ADAS suite of codes,[43] the CHIANTI suite of codes,[44] atomdb[45] and ColRadPy.[46]

The cross sections for atomic process in the plasma (e.g., excitation, ionization, recombination) impact the behavior of plasmas through transport of impurity ions and radiative power loss. The fundamental cross sections for these processes are converted into transition rate coefficients and combined with collisional-radiative equations to produce coefficients used for plasma modeling and diagnostics. Plasma phenomenon, like transport, depend heavily on collisional radiative theory to determine the charge state balance of a plasma as well as radiated power. The major equations from collisional radiative theory will be derived in this chapter including the collisional radiative set of equations in Section 3.3 and the ionization balance equations in Section 3.4. The collisional radiative code ColRadPy[46] will also be described.

3.1 Basic atomic processes

Fundamental atomic processes drive different plasma phenomena such as detachment and transport. The basic atomic processes also allow for spectroscopic measurements of erosion (Equation 3.32), electron temperature (Section 3.3.4) and electron density (Section 3.3.4). These processes are determined by cross sections which are related to the probability that a process will occur between two different bodies. Cross sections are generally calculated with codes that solve the quantum mechanical dynamics for these processes.[47] The cross sections are then convolved with the appropriate distribution of energies for a given species. Many plasmas have a Maxwellian distribution of free electrons, which is often used, though other distributions could be applicable in some regimes (such as a Kappa distribution). The plasma conditions and physics of interest in this thesis are dominated by electron collisions. However, other processes such as proton collisions may be important in other plasmas applications.

3.1.1 Electron impact excitation/de-excitation

The main driving mechanism for populating excited levels that produce intense spectral lines at fusion relevant plasma parameters is electron impact excitation. During electron impact excitation, a free electron interacts with an atom or ion that is not fully ionized; the free electron can either impart or absorb from the electrons that are bound to the ion. Energy is conserved in the process as shown below; therefore $\Delta E_{ij} = \epsilon_i - \epsilon_j$ where ϵ_i and ϵ_j are the energies of the incoming and outgoing free electron (the energy difference is equation to the energy difference in the bound states involved in the excitation), X denotes the ion, Z the charge state and e denotes the electron with the various energies of the charge state denoted by i and j.

$$X^Z(i) + e(\epsilon_i) \leftrightarrow X^Z(j) + e(\epsilon_j) \tag{3.1}$$

Electron impact excitation cross sections can be calculated by various quantum mechanical methods that can be divided into those using perturbation theory (e.g., plane-wave Born and distorted-wave[48] approaches), or those that do not use perturbation theory (e.g., the R-Matrix[49] or Time-Dependent Close-Coupling[50] methods) which are more accurate for near neutral charge states. Cross sections can also be measured through various atomic experiments.

Electron impact excitation/de-excitation extrapolation to higher temperatures

Extrapolation of electron impact excitation/de-excitation rates to temperatures higher than originally calculated from atomic codes can be accomplished with ColRadPy and requires the atomic data file to include calculated infinite energy limit points and is achieved via the Burgess-Tully extrapolation.[51] The practical use of the Burgess-Tully extrapolation will be discussed more in Section 3.6.

Near neutral high-Z elements require more computational resources to calculate the underlying atomic data than previous low-Z elements due to the larger continuum basis set size and the number of levels and number of electrons associated with each electronic configuration that is required, see Smyth *et al.*[52] The finite basis sets used for the calculation of high-Z elements in an R-matrix calculation means that there is a limit to how high in energy the cross sections can be calculated, with a corresponding limit to the temperatures at which the rates can be calculated. The data therefore requires extrapolation to apply the calculation to possible fusion relevant divertor conditions where near neutral systems exist. While extrapolation can be applied to any system where an infinite energy point is calculated, it is generally complex near neutral systems that require this extrapolation. For example, the Mo neutral calculation from Smyth *et al.*[52] was only calculated up to 17 eV, and this is typical for high-Z near neutral systems. Divertor plasmas can also produce higher temperatures. Figure 3.1 shows the extrapolation to higher temperatures for a transition between two neutral Mo levels $4d^5 5s(^7S_3)$ and $4d^5 5s(^5F_1)$ While the extrapolation can be carried out to infinite temperature, the error in the extrapolation is reduced for temperatures closer to the last calculated value.

3.1.2 Electron impact ionization

Electron-impact ionization occurs when a free electron causes a parent atom to lose a bound electron. The previously bound electron then becomes free within the plasma. Energy

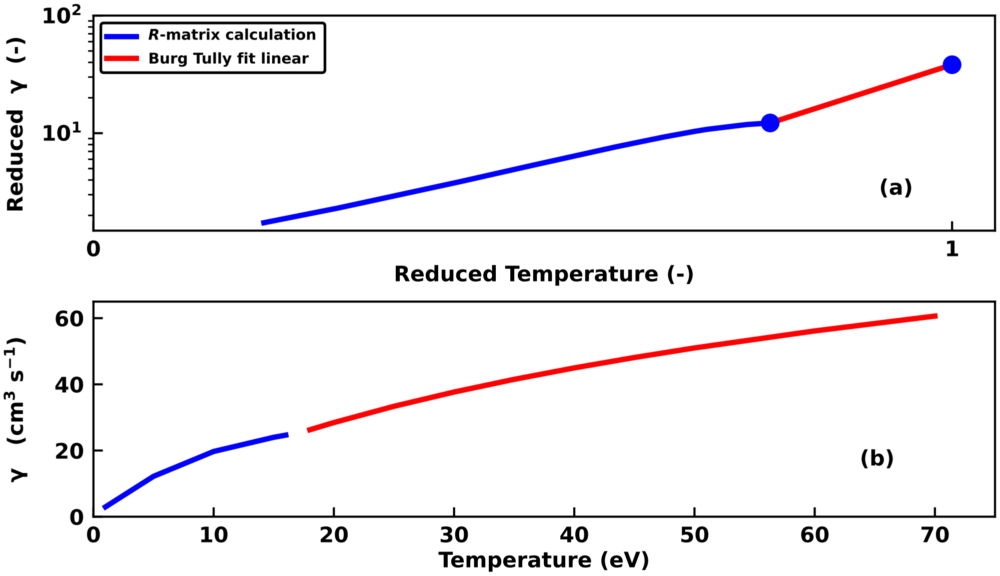

Figure 3.1: Burgess-Tully effective collision strength extrapolation. (a) Effective collisional strengths for Mo I 4d^{5}5s(^{7}S$_3$) ↔ 4d^{5}5s(^{5}F$_1$) transition is in blue. Extrapolated Burgess-Tully fit in red. Last *R*-matrix calculated point and infinite energy point are the blue dots. (b) Calculated effective collisional strength of the *R*-matrix is shown in blue. The extrapolation to higher temperatures is the red line.

is conserved as shown in Equation 3.2. As before, X and e represent the ion and electrons with the subscripts denoting energies.

$$X^Z(i) + e(\epsilon_i) \rightarrow X^{Z+1}(j) + e(\epsilon_j) + e(\epsilon_k) \tag{3.2}$$

Electron Classical Exchange Impact Parameter (ECIP)

ColRadPy is capable of generating some basic atomic data such as Exchange Classical Impact Parameter (ECIP) ionization.[53] ECIP ionization rates can be made within ColRadPy by providing energy difference between levels of interest and the ionization potential as well as electron temperature (which is contained in the fundamental adf04 data file that is used for the modeling). ECIP is generally used when ionization data made with a more sophisticated method is not available for a given level. The rate of ECIP ionization is proportional to the square of the difference in energy between a given level and the ionization potential. The rate will also be dependent upon electron temperature and density.

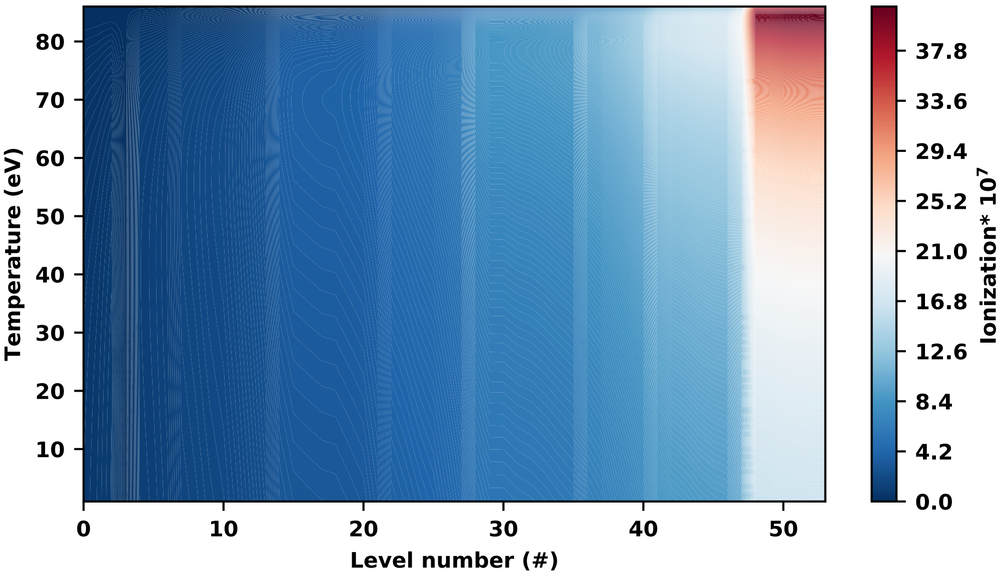

Figure 3.2: ECIP ionization contour plot versus level number and electron temperature for C I, calculated with ColRadPy.

3.1.3 Spontaneous emission

Spontaneous emission in a plasma occurs when an electron in an excited state spontaneously decays down to a lower level and emits a photon in the process. Again, both energy and charge are conserved in this process. The process of spontaneous emission is shown in Equation 3.3 and is the mechanism by which spectroscopy is possible. The photon that is emitted in this process can be measured by a spectrometer or other optical diagnostic. The photon $h\widetilde{\nu}$ that is emitted has exactly the difference in energy between the two levels of the atom.

$$X^Z(j) \rightarrow X^Z(i) + h\widetilde{\nu} \tag{3.3}$$

The rate of spontaneous emission from the upper level is given by the Einstein A-coefficient. These rates are generally obtained from the atomic structure calculation that was used to calculate the electron impact excitation rates.

3.1.4 Recombination

Recombination is the opposite process to ionization (see Section 3.1.2) in which a free electron becomes bound to an atom. Again, energy is conserved in this process; the general recombination process is described by Equation 3.4.

$$X^{Z}(i) + e(\epsilon_i) \rightarrow X^{Z-1}(j) \tag{3.4}$$

Dielectronic Recombination

Dielectronic recombination is the dominate recombination process for many plasmas. Dielectronic recombination is a two-step process. It involves first a resonance capture of a free electron, in which the core electron configuration gets excited.

$$X^{Z+1}(i) + e(\epsilon_i) \rightarrow X^{+Z}(j, nl) \tag{3.5}$$

The recombined ion, now in an excited state, can undergo two different types of radiative stabilization (spontaneous emission).

$$\begin{aligned} X^{+Z}(j, nl) &\rightarrow X^{+Z}(i, nl) + h\widetilde{\nu} \quad \text{(Type I)} \\ &\rightarrow X^{+Z}(j, n'l') + h\widetilde{\nu} \quad \text{(Type II)} \end{aligned} \tag{3.6}$$

Where the Type I radiative process produces a photon by a change to the core electronic configuration that is very close in energy to an ordinary emission line, see Section 3.1.3. A Type II configuration is a result of a change to outer electronic configuration (valence electron).

Radiative Recombination

During radiative recombination, an electron is captured and a photon is emitted at the same time. Radiative recombination is generally not a significant process in most laboratory plasmas as radiative recombination rate coefficients decrease dramatically as the electron temperature increases, so it is strongest in very low temperature plasmas. Radiative recombination produces a continuum of photons as the free electron e_ϵ can have any energy.

$$X^{z+1} + e_\epsilon \rightarrow X^z(i) + h\widetilde{\nu} \tag{3.7}$$

3.1.5 Three-body recombination

Three-body recombination can be calculated directly through a detailed balance relation with electron-impact ionization rate coefficients.[54] ColRadPy will automatically calculate three-body recombination for any system that has ionization data using the detailed balance relation. An example three body recombination reaction is given by Equation 3.8.

$$X^{z+1} + e + e \rightarrow X^z + e \tag{3.8}$$

3.1.6 Thermal charge exchange

Thermal charge exchange refers to charge exchange with a population of neutral atoms that have a Maxwellian distribution. Note that this is different from beam charge exchange where the neutral atoms have a very peaked energy distribution. Significant thermal charge exchange in fusion relevant plasmas only comes from hydrogen (and isotopes) because other elements have much smaller concentrations.

In the thermal charge exchange reaction represented by Equation 3.9, an incoming neutral atom H transfers an electron to an impurity atom in some charge state X^Z leaving the neutral atom singly ionized H^+ and the impurity atom in a lower ionization state X^{Z-1}.

$$X^Z(j) + H(k) \rightarrow X^{Z-1}(i) + H^+(l) \tag{3.9}$$

Thermal charge exchange can have impacts on both the collisional radiative set of equations in addition to the ionization balance equations. Charge exchange has not been investigated as a populating source for low charge states of tungsten in tokamak divertors. Thermal charge exchange is expected to be small when compared to electron-impact processes and thus will not be considered in this dissertation.

3.2 Time scales of collisional radiative processes

There are various time scales of importance in generalized collisional radiative (GCR) theory that can vary greatly. The main atomic lifetimes of concern in fusion plasmas are that of ground, metastable and excited states. These lifetimes impact populations of various levels which determine the most appropriate modeling approach. There are two distinct groups, intrinsic (those that do not depend on plasma parameters) and extrinsic (those that depend on plasma parameters). The first consists of rates that are intrinsic to the atomic physics. These time scales will be the same for all plasmas: the metastable radiative decay rate (or the rate at which metastables radiate to the ground state), the radiative decay of excited states to either ground or metastable states and the auto-ionizing decay. The time scales of this group are generally ordered as

$$\tau_{\mathrm{a}} < \tau_{\mathrm{o}} < \tau_{\mathrm{m}} < \tau_{\mathrm{g}} \tag{3.10}$$

where τ_{a} is the auto ionization lifetime, τ_{o} is the lifetime for an excited states, τ_{m} is the lifetime of a metastable state and τ_{g} is the lifetime of a ground state.

The second extrinsic group consists the lifetimes of electron-electron $\tau_{\mathrm{e-e}}$, ion-ion $\tau_{\mathrm{i-i}}$, and ion-electron $\tau_{\mathrm{i-e}}$, ionization τ_{ion} and recombination τ_{rec}. The time ordering is

$$\tau_{\mathrm{ion,rec}} >> \tau_{\mathrm{i-e}} >> \tau_{\mathrm{i-i}} >> \tau_{\mathrm{e-e}} \tag{3.11}$$

These time scales can then be compared with each other and the plasma time scales τ_{plasma} such as ELM time scales. When τ_{plasma} is shorter than τ_{m}, as will be shown for neutral tungsten in Chapter 5, time-dependent modeling must be done.

$$\tau_{\mathrm{plasma}} \sim \tau_{\mathrm{g}} \sim \tau_{\mathrm{m}} >> \tau_{\mathrm{o}} >> \tau_{\mathrm{e-e}} \tag{3.12}$$

$$\tau_{\mathrm{m}} \sim 10/Z^8\mathrm{s},\ \tau_{\mathrm{o}} \sim 10^{-8}/Z^4\mathrm{s},\ \tau_{\mathrm{a}} \sim 10^{-13}\mathrm{s} \tag{3.13}$$

3.3 The collisional radiative set of equations

There are three regimes normally considered in collisional-radiative modeling. At low electron densities the excited states are described by coronal conditions, and intermediate densities they are in the collisional-radiative regime, and at high electron densities they are in the Local Thermodynamic Equilibrium (LTE) regime. Each of these will be described below. The following is the set of collisional radiative rate equations. To illustrate metastable resolved coefficients, consider a system that has both ground and metastable states. Metastable states are long lived states that do not electric dipole decay to any lower level. Therefore, metastable states can have lifetimes (i.e. the time to reach steady-state conditions for a given plasma electron temperature and density) on the order of milliseconds compared to excited states which have lifetimes on the order of microseconds or quicker. Two adjacent charge states and the excited states of the lower charge states are considered. In the lower charge state, the ground is denoted by σ_1 and the metastable by σ_2. The excited levels of the lower charge state are described by i. The upper charge state ground is denoted by ν_1 and metastable by ν_2. The equations show the time evolution of both ground state, metastable states and excited states. Note that excited states do not have long lifetimes and contain only a small fraction of the total population. Not all processes are included in Equation 3.14 for simplicity (e.g. thermal charge exchange is not included). The inclusion of these additional processes in the equation would just introduce more terms. The collisional radiative equations then take the form of Equation 3.14 where N denotes the population of a given level, σ and ν denote a metastable level, n_{e} is electron density, q denotes electron impact excitation/de-excitation, S represents ionization, A is spontaneous emission and R is recombination.

$$\begin{aligned}
\frac{dN_{\sigma_1}}{dt} &= -n_\mathrm{e}\left(\sum_{j\neq 1} q_{\sigma_1\to j} + S_{\sigma_1}\right) N_{\sigma_1} + \sum_{j\neq\sigma_1}(A_{j\to\sigma_1} + n_\mathrm{e} q_{j\to\sigma_1})N_j + n_\mathrm{e}\sum_k R_{\nu_k\to\sigma_1}N_{\nu_k} \\
\frac{dN_{\sigma_2}}{dt} &= -\left(\sum_{j\neq 1} n_\mathrm{e} q_{\sigma_2\to j} + n_\mathrm{e} S_{\sigma_2} + A_{\sigma_2\to j}\right) N_{\sigma_2} + \sum_{j\neq\sigma_2}(A_{j\to\sigma_2} + n_\mathrm{e} q_{j\to\sigma_2})N_j + n_\mathrm{e}\sum_k R_{\nu_k\to\sigma_1}N_{\nu_k} \\
\frac{dN_i}{dt} &= -\left(\sum_{j\neq i} n_\mathrm{e} q_{i\to j} + n_\mathrm{e} S_i + A_{i\to j}\right) N_i + \sum_{j\neq i}(A_{j\to i} + n_\mathrm{e} q_{j\neq i})N_j + n_\mathrm{e}\sum_k R_{\nu_k\to i}N_{\nu_k} \\
\frac{dN_{\nu_1}}{dt} &= n_\mathrm{e}\left(\sum_j S_j N_j\right) - n_\mathrm{e} N_{\nu_1}\sum_j R_{\nu_1\to j} \\
\frac{dN_{\nu_2}}{dt} &= n_\mathrm{e}\left(\sum_j S_j N_j\right) - n_\mathrm{e} N_{\nu_2}\sum_j R_{\nu_1\to j}
\end{aligned} \tag{3.14}$$

Equation 3.14 can be put into a matrix form with entries C_{ij} (Equation 3.15) that represent the combination of all atomic rates between the different levels shown in Equation 3.16.

$$\mathrm{C}_{ij} = -\left(\sum_{j\neq i} n_\mathrm{e} q_{i\to j} + n_\mathrm{e} S_i + A_{i\to j}\right) N_i + \sum_{j\neq i}(A_{j\to i} + n_\mathrm{e} q_{j\neq i})N_j \tag{3.15}$$

The diagonal of the matrix encompasses all of the loss mechanisms for the ith level. The loss rates are excitation/de-excitation, spontaneous emission and ionization. The off diagonal terms are then the ways that level i gets populated from the j^{th} level. This can happen through excitation/de-excitation, spontaneous emission from a higher level or recombination from the next ion into the i^{th} level of the ion of interest. The collisional-radiative matrix includes the ground and metastables of the higher ion stage and individual rows, but does not include the excited states of the higher charge state. This ion stage receives population from the lower charge state through ionizations, and therefore, these are S_i where i is the level of in the lower ion that the atom came from. Additionally, the higher charge state ion can lose population to the lower charge state ion through recombination. This is denoted as R. The collisional radiative matrix is a balanced rate equation, and as a result, every column must sum to zero. The total number of atoms does not change so all of the columns will sum to zero and also be thought of as a gain into one level that comes from the loss in another level.

$$\begin{bmatrix} dN_{\sigma_1}/dt \\ dN_{\sigma_2}/dt \\ dN_3/dt \\ \ldots \\ \ldots \\ dN_n/dt \\ dN_{\nu_1}/dt \\ dN_{\nu_2}/dt \end{bmatrix} = \begin{bmatrix} C_{11} & C_{12} & C_{13} & \ldots & \ldots & C_{1n} & R_{\nu_1 1} n_\mathrm{e} & R_{\nu_2 1} n_\mathrm{e} \\ C_{21} & C_{22} & C_{23} & \ldots & \ldots & C_{2n} & R_{\nu_1 2} n_\mathrm{e} & R_{\nu_2 2} n_\mathrm{e} \\ C_{31} & C_{32} & C_{33} & \ldots & \ldots & C_{3n} & R_{\nu_1 3} n_\mathrm{e} & R_{\nu_2 3} n_\mathrm{e} \\ \ldots & \ldots & \ldots & \ldots & \ldots & \ldots & \ldots & \ldots \\ \ldots & \ldots & \ldots & \ldots & \ldots & \ldots & \ldots & \ldots \\ C_{n1} & C_{n2} & C_{n3} & \ldots & \ldots & C_{nn} & R_{\nu_1 n} n_\mathrm{e} & R_{\nu_2 n} n_\mathrm{e} \\ n_\mathrm{e} S_1 & n_\mathrm{e} S_2 & n_\mathrm{e} S_3 & \ldots & \ldots & n_\mathrm{e} S_n & -\sum_n R_{\nu_1 n} n_\mathrm{e} & 0 \\ n_\mathrm{e} S_1 & n_\mathrm{e} S_2 & n_\mathrm{e} S_3 & \ldots & \ldots & n_\mathrm{e} S_n & 0 & -\sum_n R_{\nu_2 n} n_\mathrm{e} \end{bmatrix} \begin{bmatrix} N_{\sigma_1} \\ N_{\sigma_2} \\ N_3 \\ \ldots \\ \ldots \\ N_n \\ N_{\nu_1} \\ N_{\nu_2} \end{bmatrix} \tag{3.16}$$

3.3.1 The coronal approximation

The coronal limit to the collisional radiative set of equations is a low electron density limit, which assumes that excited states are only populated from the ground state through electron impact excitation and decay only via spontaneous emission to all levels. The simple coronal approximation does not allow for cascade transitions to populated excited states from higher excited states. Population gain from cascades will be allowed in the full collisional radiative treatment outlined in Section 3.3.3. The simple coronal population for an excited state is then given by the relatively simple form below.

$$\frac{dN_i}{dt} = N_1 n_{\mathrm{e}} q_{1\to j} - N_i \sum_j A_{j\to i} \tag{3.17}$$

The excited states are assumed to have no time changing population $dN/dt = 0$ (expanded upon more in Section 3.3.3) leading to Equation 3.18.

$$N_i = \frac{N_1 n_{\mathrm{e}} q_{1\to j}}{\sum_j A_{j\to i}} \tag{3.18}$$

Equation 3.18 simplifies the set of equations in Equation 3.14 to two rates which also the population to be solved without a matrix inversion. The population of a level then becomes the excitation from the ground state divided by the summation of the spontaneous emission rates out of the level.

3.3.2 The limit of local thermodynamic equilibrium (LTE)

The Local Thermodynamic Equilibrium (LTE) is the high electron density limit, where collisional processes dominate over spontaneous emission timescales. The ratio below will hold for plasmas in LTE.

$$\frac{\sum_j A_{j\to i}}{n_{\mathrm{e}} \sum_j q_{j\to i}} < 1 \tag{3.19}$$

The populations of bound states in LTE then have a Boltzmann population distribution where ω is the statistical weight of a given level, E_i and E_j correspond to the energies of levels N_i and N_j respectively.

$$\frac{N_i}{N_j} = \frac{\omega_i}{\omega_j} e^{-\frac{E_i - E_j}{kT_{\mathrm{e}}}} \tag{3.20}$$

3.3.3 The quasi-static approximation

A distinction must now be made between two different types of levels. There are levels whose populations vary on timescales of the plasma known as ‘metastable’ and levels that vary on time scales faster than plasma variations. Time scales are in Section 3.2. These have no special denotation, referred to here just as 'levels'. In simple low-Z systems, metastables can generally be defined as any level that cannot decay radiatively to a lower level via an electric dipole spontaneous emission. In complex high-z systems, the definition of metastable becomes less concrete. The lowest lying levels are considered to be metastable, but there could be higher metastables as well. To identify these higher metastables when the rules of simple systems do not apply, the diagonal of collision radiative matrix can provide some insight. The diagonal consists of all the different loss mechanisms. These loss rates consist of emission, collisional excitation/de-excitation and ionization. If there are other levels that have a lower loss rate than a known metastable that has the highest loss rate, those other levels might also need to be considered metastables as well. The collisional radiative matrix can now be solved for the populations of the levels that change faster than plasma time scales as those levels are in steady-state. The same assumption cannot be made for the metastable states. These states vary slowly, and their population can change drastically with plasma conditions. The upper non-metastable levels can be solved as a function of the metastable levels and is where the term 'driving population' originates from. To solve for these non-metastable levels, the approximation $dN/dt = 0$ can be applied for the non-metastable states as they will vary very quickly, being in nearly instantaneous equilibrium with the time-evolving ground and metastable states.

The delineation of two different types of levels will allow the set of linear equations to be solved. Metastables levels are given Greek letters to differentiate them from regular levels. The first two metastable levels would then be written as dN_{σ_1}/dt and dN_{σ_2}/dt. Electron temperature and density can significantly impact the populations of levels. These parameters can drastically change the relative intensities of spectral lines within an ion and can alter the upper level population and also modify the relative metastable populations of the ion.

The quasistatic approximation has been applied to Equation 3.16 leading to Equation 3.21 where the time changing populations of excited states have been set to zero.

$$\begin{bmatrix} dN_{\sigma_1}/dt \\ dN_{\sigma_2}/dt \\ 0 \\ 0 \\ 0 \\ 0 \\ dN_{\nu_1}/dt \\ dN_{\nu_2}/dt \end{bmatrix} = \begin{bmatrix} C_{11} & C_{12} & C_{13} & ... & ... & C_{1n} & R_{\nu_1 1} n_{\mathrm{e}} & R_{\nu_2 1} n_{\mathrm{e}} \\ C_{21} & C_{22} & C_{23} & ... & ... & C_{2n} & R_{\nu_1 2} n_{\mathrm{e}} & R_{\nu_2 2} n_{\mathrm{e}} \\ C_{31} & C_{32} & C_{33} & ... & ... & C_{3n} & R_{\nu_1 3} n_{\mathrm{e}} & R_{\nu_2 3} n_{\mathrm{e}} \\ ... & ... & ... & ... & ... & ... & ... & ... \\ ... & ... & ... & ... & ... & ... & ... & ... \\ C_{n1} & C_{n2} & C_{n3} & ... & ... & C_{nn} & R_{\nu_1 n} n_{\mathrm{e}} & R_{\nu_2 n} n_{\mathrm{e}} \\ n_{\mathrm{e}} S_1 & n_{\mathrm{e}} S_2 & n_{\mathrm{e}} S_3 & ... & ... & n_{\mathrm{e}} S_n & -\sum_n R_{\nu_1 n} n_{\mathrm{e}} & 0 \\ n_{\mathrm{e}} S_1 & n_{\mathrm{e}} S_2 & n_{\mathrm{e}} S_3 & ... & ... & n_{\mathrm{e}} S_n & 0 & -\sum_n R_{\nu_2 n} n_{\mathrm{e}} \end{bmatrix} \begin{bmatrix} N_{\sigma_1} \\ N_{\sigma_2} \\ N_3 \\ ... \\ ... \\ N_n \\ N_{\nu_1} \\ N_{\nu_2} \end{bmatrix} \tag{3.21}$$

The rows corresponding to the metastables in both the child and parent ion can be eliminated from the equation leading to Equation 3.22. This matrix now only involves the short lived excited states in the child ion.

$$\begin{bmatrix} -C_{31} N_{\sigma_1} - C_{32} N_{\sigma_2} - R_3 N_{\nu_1} - R_3 N_{\nu_2} \\ -C_{41} N_{\sigma_1} - C_{42} N_{\sigma_2} - R_4 N_{\nu_1} R_4 N_{\nu_2} \\ -... - ... - ... \\ -... - ... - ... \\ -C_{n1} N_{\sigma_1} - C_{n2} N_{\sigma_2} - R_n N_{\nu_1} - R_4 N_{\nu_2} \end{bmatrix} = \begin{bmatrix} C_{33} & C_{34} & ... & ... & C_{3n} \\ C_{43} & C_{44} & ... & ... & C_{4n} \\ ... & ... & ... & ... & ... \\ ... & ... & ... & ... & ... \\ C_{n3} & C_{n4} & ... & ... & C_{nn} \end{bmatrix} \begin{bmatrix} N_3 \\ N_4 \\ ... \\ ... \\ N_n \end{bmatrix} \tag{3.22}$$

These states can be solved as functions of the ground and metastable driving populations with a matrix inversion of the reduced collisional-radiative matrix and solving for the excited populations (seen in Equation 3.23).

$$\begin{bmatrix} N_3 \\ N_4 \\ \dots \\ \dots \\ N_n \end{bmatrix} = \begin{bmatrix} C_{33} & C_{34} & \dots & \dots & C_{3n} \\ C_{43} & C_{44} & \dots & \dots & C_{4n} \\ \dots & \dots & \dots & \dots & \dots \\ \dots & \dots & \dots & \dots & \dots \\ C_{n3} & C_{n4} & \dots & \dots & C_{nn} \end{bmatrix}^{-1} \begin{bmatrix} -C_{31}N_{\sigma_1} - C_{32}N_{\sigma_2} - R_3N_{\nu_1} - R_3N_{\nu_2} \\ -C_{41}N_{\sigma_1} - C_{42}N_{\sigma_2} - R_4N_{\nu_1}R_4N_{\nu_2} \\ -\dots - \dots - \dots \\ -\dots - \dots - \dots \\ -C_{n1}N_{\sigma_1} - C_{n2}N_{\sigma_2} - R_nN_{\nu_1} - R_4N_{\nu_2} \end{bmatrix} \tag{3.23}$$

The excited state population terms can then be written out in terms of individual matrix elements.

$$N_i = \sum_{\sigma} -N_\sigma \sum_{j} C'^{-1}_{ij} C_{j\sigma} + \sum_{\nu} N_\nu \sum_{j} C'^{-1}_{ij} R_{j\nu} \tag{3.24}$$

The Numpy linear algebra package[55] is used to invert the CR matrix in ColRadPy (seen in Equation 3.23). When possible, matrix operations are used to increase the speed of the Python code. All data related to the calculation is stored in a Python dictionary and is easily accessible.

3.3.4 Photon Emissivity Coefficient (PEC) and line ratio diagnostics

A photon emissivity coefficient (PEC) is a derived coefficient that is associated with a single spectral line. A PEC can be thought of as a scaled spectral line intensity, the excitation portion of the PEC is given by Equation 3.25. The total PEC is the combination of the excitation, recombination and change exchange components (see Summers *et al.* for more detail).

$$\mathrm{PEC}^{\mathrm{excit}}_{j\to i} = N^{\mathrm{excit}}_{j} A_{j\to i}/n_{\mathrm{e}} \tag{3.25}$$

Equation 3.26 relates the spectral line intensity for transition from level $j \to i$. The spectral intensity I is the summation of the individual Photon Emissivity Coefficient (PEC) multiplied by the metastable population and electron density and then integrated over the line of sight.

$$I_{j\to i} = \int \Sigma_\sigma \mathrm{PEC}_{\sigma,j\to i} N_\sigma n_\mathrm{e} dx \tag{3.26}$$

It is convenient to consider the relative contribution to intensity from a particular metastable state (see Equation 3.27). Note that the emitted intensity can be thought of as having a component that is driven by each of the metastables for that ion. A study for neutral tungsten will be preformed in Section 5.2.1. Contributions to the line intensity both when the N_σ/N_tot is in steady-state and when it is not will be considered in later sections.

$$I^\mathrm{rel}_{\sigma,\, j\to i} = \int \mathrm{PEC}_{\sigma,j\to i}(N_\sigma/N_\mathrm{tot}) dx \tag{3.27}$$

Diagnosing electron temperature

Electron temperature can be diagnosed from experimental observation of two spectral lines. The electron temperature is diagnosed by choosing two lines whose intensities behave differently with electron temperature leaving the ratio dependent on electron temperature. Generally, these lines are chosen to have a similar electron density dependence so that the electron density dependence cancels out. The best combination of lines to choose for temperature line ratio diagnostics is one spectral line that requires a spin changing transition in its dominant populating mechanisms and one spectral line that does not require a spin changing transition. Spin changing transitions become weaker relatively quickly as the electron temperature increases where non-spin changing transitions do not vary as quickly.

Figure 3.3 shows a line ratio of C I emission lines that have a strong temperature dependence but has a weak density dependence 2s2p^{2}3s (^{5}P) → 2$s^2$2p^2 (^{3}P) and 2s2p^3 (^{3}P) → 2$s^2$2p^2 (^{3}P). A contour plot for a line ratio that has a temperature dependence but no density dependence would have contours lines along constant temperature. Figure 3.3

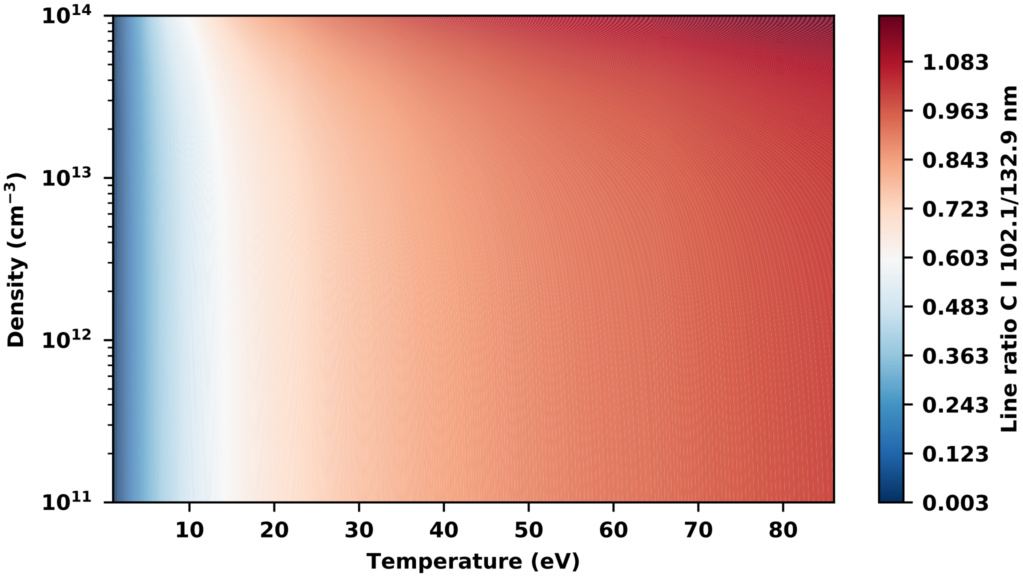

Figure 3.3: Electron temperature and density contours for the 102.1 and 132.9 nm C I line ratio. The line ratio is a good temperature diagnostic as there is a strong temperature dependence and a weak density dependence.

illustrating the chosen C I line ratio has relatively vertical lines for $n_\mathrm{e} > 10^{13}$. At higher electron density, the line ratio starts to have a density dependence.

Equation 3.28 uses two spectral lines to evaluate the electron temperature. I is the measured spectral intensity of two lines from the same charge state. The PECs represent the calculated photon emissivity coefficients from Equation 3.25. ColRadPy calculates PEC's as a function of electron temperature and density on either a grid or pairs of temperatures and densities.

$$I_{T_{e_{j\to i}}}/I_{T_{\mathrm{e}_{l\to k}}} \approx \left(\frac{PEC_{T_{\mathrm{e}_{j\to i}}}(T_e)}{PEC_{T_{\mathrm{e}_{l\to k}}}(T_\mathrm{e})}\right) \tag{3.28}$$

Diagnosing electron density

Electron density can be diagnosed with line ratios similar to electron temperature as detailed in Section 3.3.4. Spectral lines of a charge state can have a different density dependence, often choosing a spectral line that is dominated by the recombination portion of the PEC. Recombination PECs are often more sensitive to electron density than excitation

PECs. Recombination dependence on density is clearly seen in three-body recombination (Section 3.1.5) where the rates are dependent on n_{e}^2.

$$I_{n_{e_{j\to i}}}/I_{n_{e_{l\to k}}} \approx \left(\frac{PEC_{n_{e_{j\to i}}}(n_e)}{PEC_{n_{e_{l\to k}}}(n_{\mathrm{e}})}\right) \tag{3.29}$$

Diagnosing metastable populations

If one metastable state in a system dominantly drives a spectral line of interest, it is possible to measure the metastable population for the given species. The metastable population can be measured from line ratios like electron temperature or density. For example, the ratio of the ground 5d^{4}6s^2 (^{5}D$_0$) to metastable 5d^5(^{6}S)6s (^{7}S$_3$) of neutral tungsten could be determined through Equation 5.1

$$I_{i\to(^7S_3)}/I_{j\to(^5D_0)} \approx \left(\frac{PEC_{i\to(^7S_3)}}{PEC_{j\to(^5D_0)}}\right)\left(\frac{N_{(^7S_3)}}{N_{(^5D_0)}}\right) \tag{3.30}$$

where I represents the intensities of spectral lines decaying to the ^{7}S$_3$ metastable and ^{5}D$_0$ ground. N is the relative populations of the ^{7}S$_3$ metastable and ^{5}D$_0$ ground. By measuring the line ratio, the relative metastable population could be determined. The inferred relative metastable population is then a combination of measured spectral intensity ratio and calculated PECs. The line ratio method described is only possible when spectral lines are dominantly populated by a single metastable. The approximation of Equation 5.1 will become worse if spectral lines are not dominated by a single spectral line. It will be shown in Chapter 5 that many tungsten spectral lines of interest are dominated by a single metastable level and therefore can make use of Equation 5.1.

Line ratio under the coronal approximation

The coronal approximation to the collisional radiative set of equations was described in Section 3.3.1. It will be established in Chapter 5 that some transitions of interest in neutral tungsten obey the coronal approximation. The impact of the coronal approximation on line ratios will later become important to simplify uncertainty analysis. These transitions will also be shown to be dominated by (i.e. driven by) a single metastable state.

From Equation 3.18, a line intensity ratio in the coronal approximation is given by the ratio of two spectral intensities denoted by I, different atomic states are given by i, j, k and l. The metastable states which drive the excited states are given by σ_1 and σ_2. The spontaneous emission from excited states is given by A, and the excitation from metastable states to excited states is given by q.

$$I_{j\to i}/I_{l\to k} \approx \left(\frac{q_{\sigma_1\to j}}{\Sigma_{i'<j}A_{j\to i'}}\right)\left(\frac{\Sigma_{k'<l}A_{l\to k'}}{q_{\sigma_2\to l}}\right)\left(\frac{A_{j\to i}}{A_{l\to k}}\right) \tag{3.31}$$

3.3.5 Ionizations per photon (S/XB) to diagnose impurity influx

The metastable resolved S/XB coefficient is given in Equation 3.32 and represents the ratio of the metastable resolved effective ionization coefficient (SCD) to the metastable resolved PEC. This was originally defined by Behringer *et al.*[42]

$$\mathrm{S/XB}_{j\to i} = \frac{\Sigma_\sigma \mathrm{SCD}_\sigma (N_\sigma/N_{\mathrm{tot}})}{\Sigma_\sigma \mathrm{PEC}_{\sigma,\, j\to i}(N_\sigma/N_{\mathrm{tot}})} \tag{3.32}$$

As discussed in the upcoming sections, metastable state populations become important in modeling when steady state conditions for given plasma parameters have not yet been reached. The relative intensity of spectral lines can vary in time as N_σ can vary in time in Equation 3.27 can change drastically due to non-steady-state effects. When the metastable levels are in steady state, all the populations are determined solely by the local electron temperature and density. Note that while metastable levels may not be in steady-state, it is normal to assume that excited state populations are in equilibrium with the time changing ground and metastable levels (known as the quasi-static approximation[40]).

The erosion rate Γ is then related to the observed spectral intensity of an emission line I_{obs} and the S/XB along a line of sight dx through equation 3.33.

$$\Gamma = \int_0^\infty \text{S/XB}\, I_{\text{obs}}\, dx \tag{3.33}$$

Prompt redeposition and net erosion measurements with the S/XB method

An atom is considered promptly re-deposited if it redeposited back onto the surface near the original sputtered location within one gyro-radius. The total tungsten that is eroded from the surface is referred to as the "gross erosion". The eroded tungsten that is not promptly re-deposited back onto the surface is referred to as the "net erosion". Net erosion requires modeling at least singly ionized tungsten and perhaps higher charge states. The difference in inferred erosion rates between the neutral charge state Γ_{neut} and the singly ionized charge state Γ_{singly} would then be an approximate estimate of the net erosion rate Γ_{net}.

$$\Gamma_{\text{net}} \approx \Gamma_{\text{neut}} - \Gamma_{\text{singly}} \tag{3.34}$$

3.3.6 The generalized collisional radiative coefficients

The GCR coefficients as defined by Burgess and Summers[53] represent all the ways to redistribute population between ground and metastable levels in connecting ionization stages. An ionization balance can then be preformed to determine both the steady state and time-dependent fractional abundances of all the metastable states. Populations of excited states do not need to be considered here because their population and lifetimes are very small when compared to metastable states. The contributions of the excited states are present in the GCR coefficients as will be shown in the next Sections.

The GCR coefficients are the summation of all the pathways through all of the states. Note that one can get the individual contributions to the population of a state by looking at the components of the summation and will be used later to determine how some of the levels in neutral tungsten are populated. For instance, the intermediate level that populated a level of interest can be calculated with Equation 3.35 if the summation is not carried out.

The GCR coefficients are used in transport codes in addition to ionization balance (Section 3.4) problems. A variety of transport codes are used to track impurities from the edge to the core plasma using collisional radiative modeling such as STRALH,[56] ERO,[57] UDEGE and many others. Transport codes must also track ionization states of impurity ions. In some cases, ionization states are 'bundled'[58] together to reduce computational time.[59]

Metastable cross-coupling coefficient (QCD)

The metastable cross-coupling coefficient connects the metastable states in the same charge state together. The coefficient encompasses all of the different ways that an ion can transfer out of one metastable state and then end up in a different one including direct excitation, excitation to another level and radiative decay as well as excitation to an intermediate level and then de-excitation or excitation. Note that in the following notation, the convention is that repeated indices are summed over, as in standard Einstein notation.

$$QCD = Q_{\sigma\rightarrow\sigma'} = (C_{\sigma'\sigma} - C_{\sigma'j}C'^{-1}_{ji}C_{i\sigma})/n_{\mathrm{e}} \tag{3.35}$$

Effective ionization coefficient (SCD)

The effective ionization rate coefficient is similar to the metastable cross-coupling coefficient, except it encompasses all the ways to start out in a child ground or metastable level σ and then end up in a parent ion metastable ν.

$$SCD = S_{\sigma\rightarrow\nu} = S_{\nu\sigma} - S_{\nu j}C'^{-1}_{ji}C_{i\sigma} \tag{3.36}$$

Effective recombination rate coefficient (ACD)

Similar to the above two equations, the effective recombination rate coefficient encompasses all the ways to start out in a parent ion ν and end up in a child ion σ. So, the ACD is the opposite of the SCD.

$$ACD = \alpha_{\nu \to \sigma'} = R_{\sigma'\nu} - C'^{-1}_{\sigma' j} C_{ji} R_{i\nu} \tag{3.37}$$

Effective charge exchange recombination coefficient (CCD)

The charge exchange GCR coefficient CCD behaves very similar to the ACD coefficient, except instead of electrons causing the recombination, a population of thermal neutral hydrogen causes the recombination.

$$CCD = \alpha^{n_H}_{\nu \to \sigma'} = R^{n_H}_{\sigma'\nu} - C'^{-1}_{\sigma' j} C_{ji} R^{n_H}_{i\nu} \tag{3.38}$$

Parent cross-coupling coefficient (XCD)

Lastly, the parent cross-coupling coefficient is defined as all the ways that an ion starts in parent state ν, then makes a recombination transition to the child levels i,j, then ionizes back to the parent ion stage ν'.

$$\chi_{\nu' \to \nu} = n_e S_{\nu j} C'^{-1}_{ji} R_{i\nu'} \tag{3.39}$$

3.3.7 Time-dependent solution of the collisional radiative matrix

The collisional radiative equations (Equation 3.14) can be solved time-dependently through the method of R. LeVeque.[60] When the equations are solved with this method, the quasi-static approximation is not assumed. Effectively, every level is treated as metastable. The non-quasi-static solution can then be compared to the more widely used quasi-static approximation (Section 3.3.3) solving the excited states as functions of the ground and metastable states while using a non-equilibrium ionization balance (discussed in Section 3.4.2) to get the time-dependent population of the ground and metastable states. An example of this is shown for both a high-Z system (Section 3.6.3) and a low-Z system (Section 3.5).

3.3.8 Level splitting term-resolved PECs for low-Z elements

Atomic calculations for low-Z species are generally performed only up to term (i.e. LS) resolution because light species energy levels within an LS term are closer to degenerate than heavy species. As such, proton collisions can efficiently redistribute population among levels within a term which effectively statistically populates the levels in a given term.

Even with spectrometers with relatively low spectral dispersion, emission lines from individual j levels can be resolved. Therefore, to accurately model j-resolved spectral lines, the PECs calculated for terms must be split to level resolution. ColRadPy is capable of splitting term averaged PECs for electric dipole transitions into level resolution using the statistical splitting of Condon and Shortley.[61]

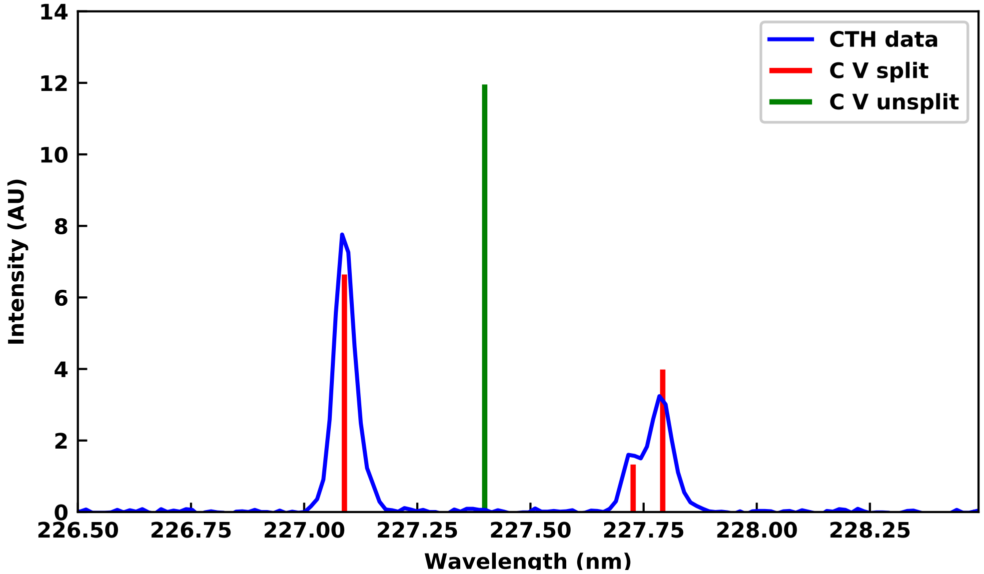

Figure 3.4: Comparison of spectral data from CTH (blue) with the unsplit (green) and split (red) collisional radiative modeling of C V at 40 eV and 1×10^{13} cm^{-3}

Table 3.1: C V spectral lines identified in CTH

NIST λ (nm)	Upper level	Lower level
227.089	1s2p (^{3}P$*_2$)	1s2s (^{3}S$_1$)
227.727	1s2p (^{3}P$*_0$)	1s2s (^{3}S$_1$)
227.792	1s2p (^{3}P$*_1$)	1s2s (^{3}S$_1$)

The following is the set of equations used to split term resolved electron dipole PECs into level resolved PECs. Here S, L and J are the standard quantum numbers representing spin, angular momentum and total angular momentum from Russels-Saunders coupling. The coefficient that allows transformation of LS results into LSJ resolution is given by

When $L' = L - 1$:

$$\begin{aligned} I(\gamma SLJ, \gamma' SL-1J+1) &= \frac{(J+S-L+1)(L+S-J)(J+S-L+2)(L+S-J-1)}{4(J+1)} I_{LS} \\ I(\gamma SLJ, \gamma' SL-1J) &= (2J+1)\frac{(J+L-S)(J+S-L+1)(S+L+1+j)(S+L-J)}{4J(J+1)} I_{LS} \\ I(\gamma SLJ, \gamma' SL-1J-1) &= \frac{(J+L-S-1)(J+L-S)(S+L+J+1(S+L+J)}{4J} I_{LS} \end{aligned} \tag{3.40}$$

When $L' = L$:

$$\begin{aligned} I(\gamma SLJ, \gamma' SLJ+1) &= \frac{(J-S+L+1)(J+S-L+1)(S+L+J+2)(S+L-J)}{4(J+1)} I_{LS} \\ I(\gamma SLJ, \gamma' SLJ) &= (2J+1)\frac{[J(J+1)-S(S+1)+L(L+1)]^2}{4J(J+1)} I_{LS} \\ I(\gamma SLJ, \gamma' SLJ-1) &= \frac{(J-S+L)(J+S-L)(S+L+J+1)(S+L+1-J)}{4J} I_{LS} \end{aligned} \tag{3.41}$$

When $L' = L + 1$:

$$
\begin{aligned}
I(\gamma SLJ, \gamma' SLJ+1) &= \frac{(J+S-L+1)(L+S-J)(J+S-L+2)(L+S-J-1)}{4(J+1)} I_{LS} \\
I(\gamma SLJ, \gamma' SLJ) &= (2J+1)\frac{(J+L-S)(J+S-L+1)(S+L+1+J)(S+L-J)}{4J(J+1)} I_{LS} \\
I(\gamma SLJ, \gamma' SLJ-1) &= \frac{(J+L-S-1)(J+L-S)(S+L+J+1)(S+L+J)}{4J} I_{LS}
\end{aligned}
\tag{3.42}
$$

In practice, ColRadPy splits each term in the calculation to every possible level. The energies of the levels are then shifted to values from the National Institutes of Standards and Technology (NIST) atomic database[62] (from here on called NIST) by matching the configuration, term and J of a given level between NIST and ColRadPy. After all levels are split, the rules from Equations 3.40, 3.41 and 3.42 are applied to get the relative contribution of the levels from a given term.

3.4 The ionization balance

The time-dependent and steady state populations of ground and metastable populations can be tracked through the GCR coefficients. A new ODE system can be then constructed with the GCR coefficients (Section 3.3.6) to include ground and metastable populations for every charge state of interest.

$$
\begin{aligned}
\frac{dN_{\sigma_1}}{dt} &= -n_{\mathrm{e}}(\Sigma_{\sigma_i}(QCD_{\sigma_1\to\sigma_i} + XCD_{\sigma_1\to\sigma_i}) + \Sigma_{\rho_i}SCD_{\sigma_1\to\rho_i})N_{\sigma_1} + n_{\mathrm{e}}(\Sigma_{\sigma_i}(QCD_{\sigma_i\to\sigma_1} + XCD_{\sigma_i\to\sigma_1})N_{\sigma_i} + ACD_{\rho_i\to\sigma_1}N_{\rho_i}) \\
\frac{dN_{\sigma_2}}{dt} &= -n_{\mathrm{e}}(\Sigma_{\sigma_i}(QCD_{\sigma_2\to\sigma_i} + XCD_{\sigma_2\to\sigma_i}) + \Sigma_{\rho_i}SCD_{\sigma_2\to\rho_i})N_{\sigma_2} + n_{\mathrm{e}}(\Sigma_{\sigma_i}(QCD_{\sigma_i\to\sigma_2} + XCD_{\sigma_i\to\sigma_2})N_{\sigma_i} + \Sigma_{\rho_i}ACD_{\rho_i\to\sigma_2}N_{\rho_i}) \\
&\cdots \\
&\cdots \\
\frac{dN_{\rho_1}}{dt} &= -n_{\mathrm{e}}(\Sigma_{\sigma_i}ACD_{\rho_1\to\sigma_i} + \Sigma_{\rho_i}QCD_{\rho_1\to\rho_i})N_{\rho_1} + n_{\mathrm{e}}(\Sigma_{\sigma_i}SCD_{\sigma_i\to\rho_1} + \Sigma_{\rho_i}QCD_{\rho_i\to\rho_1})N_{\sigma_i} \\
\frac{dN_{\rho_2}}{dt} &= -n_{\mathrm{e}}(\Sigma_{\sigma_i}ACD_{\rho_2\to\sigma_i} + \Sigma_{\rho_i}QCD_{\rho_1\to\rho_2})N_{\rho_2} + n_{\mathrm{e}}(\Sigma_{\sigma_i}SCD_{\sigma_i\to\rho_2} + \Sigma_{\rho_i}QCD_{\rho_i\to\rho_2})N_{\sigma_i}
\end{aligned}
\tag{3.43}
$$

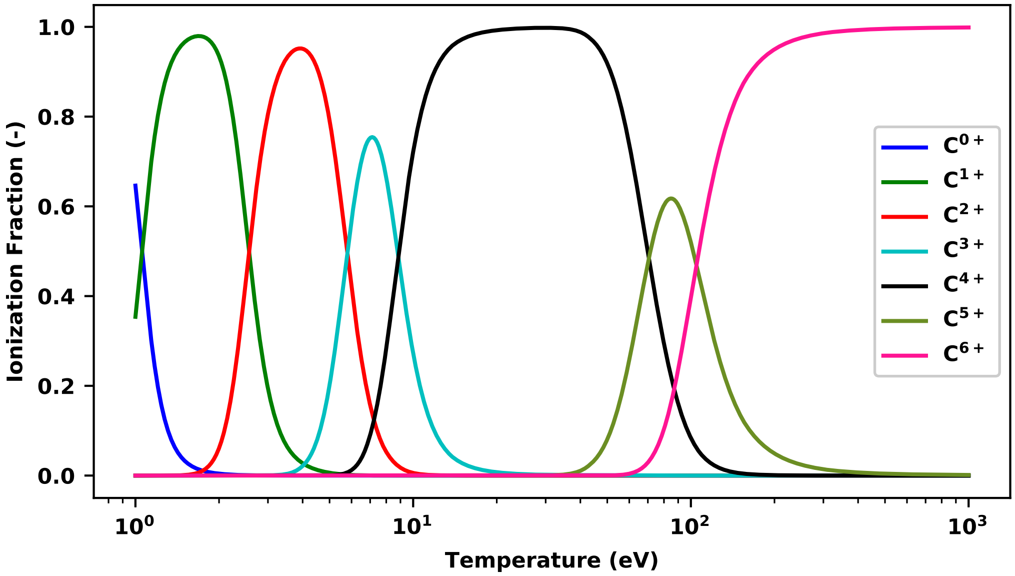

Figure 3.5: Ionization balance for C at $n_\mathrm{e} = 1 \times 10^{13}\ \mathrm{cm}^{-3}$.

In this Equation 3.43, N_{σ_i} and N_{ρ_i} represent the ground and metastable of the two charge states; n_e is the electron density. The GCR coefficients have been defined above in Section 3.3.6. The system of equations in Equation 3.43 can be represented in matrix form with Equation 3.44.

3.4.1 Time independent ionization balance

The simplest case that exhibits all of the different possibilities is a system with two charge states each with two metastables states. In this system, all of the GCR coefficients are present and serve as a simple example that can be extended to any number of charge states. The system described with Equation 3.43 has the same general form as that of Equation 3.14 and can be solved at equilibrium or time-dependently.

$$\begin{bmatrix} \frac{dN_{\sigma_1}}{dt} \\ \frac{N_{\sigma_2}}{dt} \\ \frac{N_{\rho_1}}{dt} \\ \frac{N_{\rho_1}}{dt} \end{bmatrix} \begin{bmatrix} -(Q_{\sigma_1\to\sigma_2} + \Sigma_{\rho_i} S_{\sigma_1\to\rho_i} + X_{\rho_1\to\rho_i}) & Q_{\sigma_2\to\sigma_1} + X_{\rho_2\to\rho_1} & A_{\rho_1\to\sigma_1} & A_{\rho_2\to\sigma_1} \\ Q_{\sigma_1\to\sigma_2} + X_{\rho_1\to\rho_2} & -(Q_{\sigma_2\to\sigma_1} + \Sigma_{\rho_i} S_{\sigma_2\to\rho_i} + X_{\rho_2\to\rho_i}) & A_{\rho_1\to\sigma_2} & A_{\rho_2\to\sigma_2} \\ S_{\sigma_1\to\rho_1} & S_{\sigma_2\to\rho_1} & -(\Sigma_{\sigma_i} A_{\rho_1\to\sigma_i} + Q_{\rho_1\to\rho_i}) & Q_{\rho_2\to\rho_1} \\ S_{\sigma_1\to\rho_2} & S_{\sigma_2\to\rho_2} & Q_{\rho_1\to\rho_2} & -(\Sigma_{\sigma_i} A_{\rho_2\to\sigma_i} + Q_{\rho_2\to\rho_i}) \end{bmatrix} \begin{bmatrix} N_{\sigma_1} \\ N_{\sigma_2} \\ N_{\rho_1} \\ N_{\rho_1} \end{bmatrix} \tag{3.44}$$

3.4.2 The time-dependent solution

The collisional radiative set of equations, (Equation 3.14) described in Section 3.3, can also be solved time-dependently. Time-dependence can be important for systems with a significant population in many excited states or where ultra-fast timescales need to be considered. For lighter species, this is generally when there are high electron densities driving significant population to excited states compared to ground and metastable states. Instead of the quasi-static approximation used in Equation 3.21 where excited states are assumed to have no population change, the matrix is solved as a system of ordinary differential equations $N'(t) = CN(t)$. The method used to solve the system of equations was adapted from R. LeVeque.[60] The solution to this is modified when a source term of particles is included.

These time-dependent effects of excited states will also be shown to be important for high-Z atoms, namely molybdenum in Section 3.6 and tungsten in Section 5.1 at magnetic fusion densities. These high-Z atoms behave differently from low-Z atoms at magnetic fusion densities. As an example of this, a comparison will be done for carbon in Section 3.5 and molybdenum in Section 3.6

3.4.3 Time-dependent ionization balance with a source term

The ionization balance problem can be expanded to include a source term of particles. A source term can arise in fusion plasmas near plasma facing components where there is erosion of neutral particles. Equation 3.43 can be modified to include a source term. In simplified notation, it takes the form of Equation 3.45 where N is the time changing population, A is matrix and B is vector.

$$N' = \underline{\underline{A}}N + \underline{B} \tag{3.45}$$

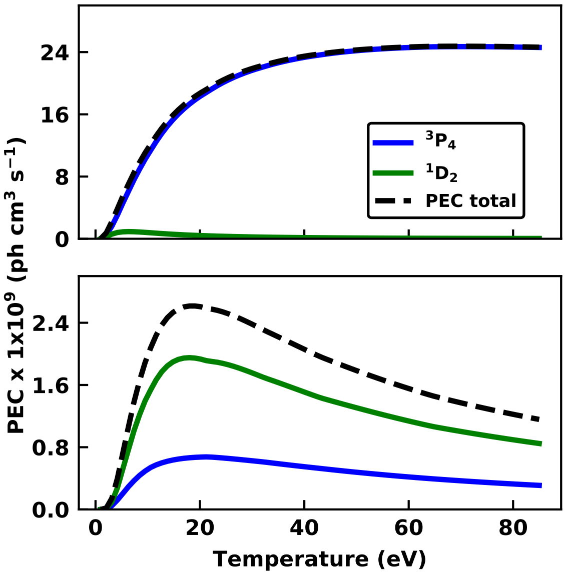

Figure 3.6: Metastable resolved photon emissivity coefficient for C I 156.06 nm (a) and 113.98 nm (b). A calculation with only the ground state is illustrated by the dashed black line for each transition. Solid color lines blue and green are the ground state and first metastable level at their steady state equilibrium fraction.

3.5 Low-Z test case (Carbon)

As an example of a low-Z species, C I will be analyzed with ColRadPy to show contrasts between low-Z and high-Z atomic systems. Low-Z systems have been studied extensively in the past.[40]

3.5.1 Carbon I PECs

C I has a ground and two long lived metastable states, as can be seen in Figure 3.8. The different PEC coefficients of C I have different dependencies on the long lived states. Figure 3.6 depicts the behavior of two different PECs. The PEC in Figure 3.6 (a) is mostly dependent on the ground state while the PEC in (b) is mainly dependent on the $^1D_2$ metastable.

3.5.2 C I Intermediate population mechanisms

ColRadPy also allows the user to determine which intermediate levels populate a level of interest with Equation 3.35, if the summation is not carried out allowing one to determine

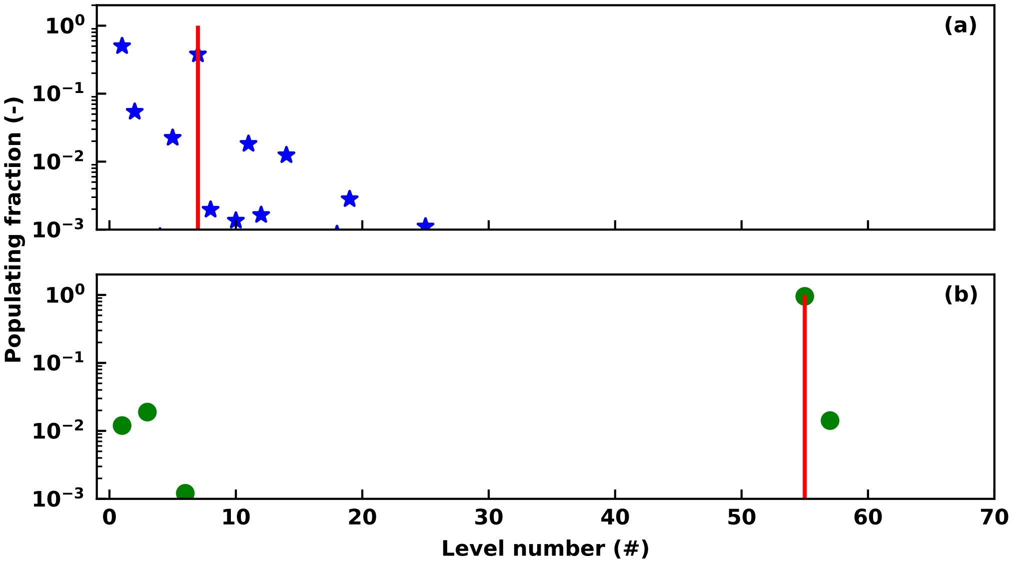

Figure 3.7: Intermediate populating levels responsible for populating the two C I excited states. The vertical red lines in each plot correspond to the ground state contribution. (a) The main populating mechanisms are excitation from the ground and metastable state. (b) The majority of the population is excitation from the ground state.

which levels in a calculation are important to modeling the spectral lines of interest. Figure 3.7 displays the populating fractions for two different excited states. A level that is populated from many different levels is shown in (a). The level in (b) is populated almost entirely from the ground state in one excitation. A description of how to interpret graphs such as Figure 3.7 can be seen in the examples of Section 3.6.2.

3.5.3 C I time-dependent collisional radiative modeling

As mentioned above, the collisional radiative equation can be solved time-dependently through the method of R. LeVeque.[60] When the equations are solved with this method, the quasi-static approximation is not assumed. Effectively every level is treated as metastable. The non-quasi-static solution can then be compared to the more widely used method solving the excited states as functions of the ground and metastable states while using a non-equilibrium ionization to get the time-dependent population of the ground and metastable states.

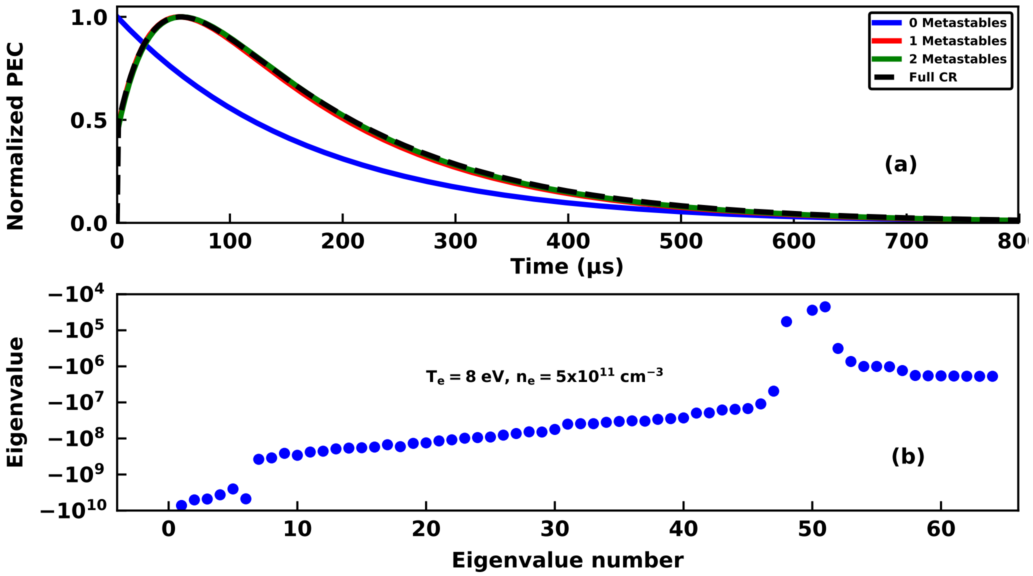

Figure 3.8: Comparison of the full time-dependent and conventional solution for C I at $T_\mathrm{e} = 8\ eV$, $n_\mathrm{e} = 5 \times 10^{11}$ cm^{-3}. (a) Non-quasi-static solution is illustrated by the black dashed line; conventional solutions with different numbers of metastable states are solid color lines. (b) Eigenvalues from the non-quasi-static solution. The ground and metastable states have markedly different values than the excited states and are represented by the two highest points in the figure.

A comparison can be made between the non-quasi-static solution and the quasi-static approximation. For systems with no metastable states or very few (such as light systems), one would expect that the conventional method should reproduce the full solution once all metastable states have been accounted for in the ionization balance.

3.5.4 C I Generalized collisional radiative coefficients

Figure 3.9 illustrates the GCR coefficients as functions of temperature at $n_\mathrm{e} = 10^{13}$ cm^{-3}. The QCD coefficient in (a) shows the discrepancy of population transfer from the ground level ^3P to the metastable ^1D leading to a build up of population starting from the ground and transferring to the metastable state. Electron population can transfer effectively from the ground to the metastable state but are not able to effectively transfer back from the metastable to the ground state. The SCD in (b) shows the total ionization from the ground and metastable level considered in C I to the ground and metastable levels of C II. There can be a significant difference in ionization rates between the various levels considered. The SCD coefficients in general increase with electron temperature and then eventually decrease with electron temperature. The ACD in (c) shows similar trends to the SCD with great variation of rates between the various levels. However, the ACD rate coefficient in general decreases as the electron temperature increases. The XCD in (d) is the smallest coefficient by far, and in most cases, does not impact the results significantly. For C I, it is 10 orders of magnitude smaller than any other coefficient.

3.6 High-Z test case (Molybdenum)

3.6.1 Mo I PECs

Metastables can also have a significant contribution to the PEC intensity. The black dashed lines in both (a) and (b) of Figure 3.10 represent the sum of the contributions to the PECs from the ground and metastable in equilibrium. The solid color lines are the individual contributions to the PEC from both the ground and metastable. It is clear that in Figure 3.10 (a), most of the contribution to the PEC comes from the ground state while in (b) there is a larger contribution to the PEC from the metastable level. For case (a) the results are dominated by a single driving population.

3.6.2 Mo I Intermediate population mechanisms

The Mo case study shows two interesting types of levels: those that are populated directly from the ground and those that are populated through intermediate steps as can be seen in figure 3.11. In the collisional radiative equations, population starts in the ground state and then is distributed among other levels. The populating mechanism directly to the level of interest from the ground is seen as a spike at the number level of the level being investigated. For example, Figure 3.11 (a) the ground is level 50 which shows a large peak at level 50 corresponding to a large fraction of the population coming directly from the ground state. From Equation 3.35, the term $C_{50,50}C^{-1}_{50,0}N_0$ will show up as a spike at level 50.

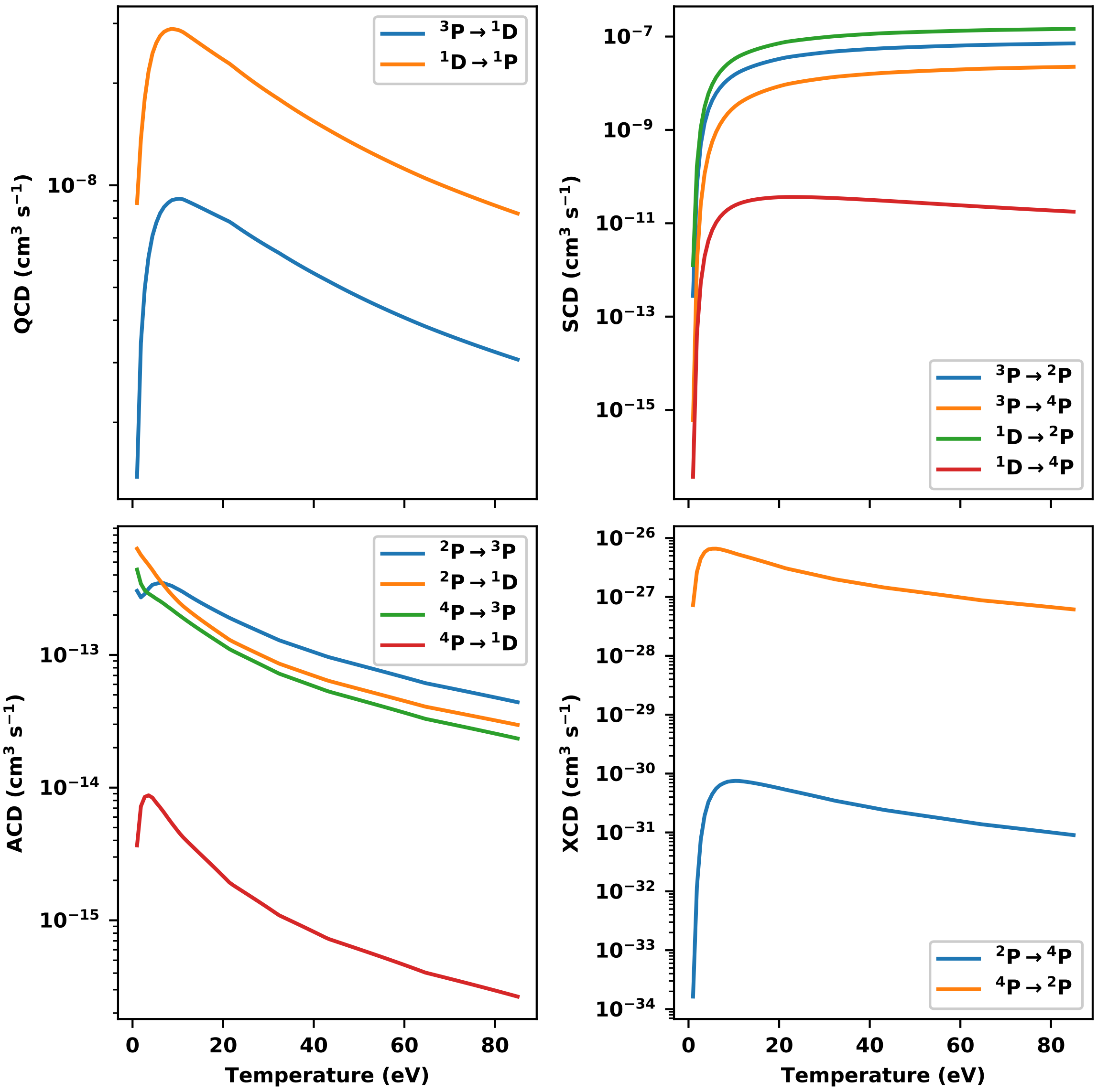

Figure 3.9: GCR coefficients for C I versus temperature at $n_e = 1 \times 10^{13}$ cm^{-3}. These coefficients will also be dependent on density, for simplicity only one density has been plotted here.

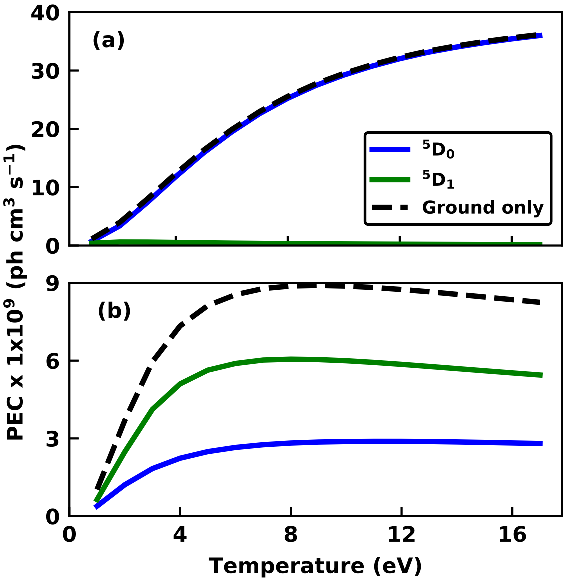

Figure 3.10: Metastable resolved photon emissivity coefficient for Mo I at 379.8 nm (a) and 550.6 nm (b). The ground state only calculation is illustrated by the dashed black line for each transition. Solid color lines blue and green are the ground state and first metastable level at their steady state equilibrium fraction.

Conversely, in Figure 3.11 (b), there is still a peak at level 71 corresponding to the ground directly populating level 71. There is also a significant fraction of population mechanisms coming from other excited states seen as the small peaks. When viewing this kind of plot, it becomes obvious that some levels such as $4d^55p$ ($^7P_4$) (level 50) producing the 379.8 nm line can be modeled using only excitation from the ground and then a spontaneous emission down to the ground state. Plots of population fraction identify which transitions are required to accurately model spectral lines and make it possible to simplify complex systems such as high-Z near neutral systems.

3.6.3 Mo I time-dependent collisional radiative modeling

In heavy species, spectral lines that are populated significantly from metastable states (for example Mo I at 379.8 nm) have two additional complications. First, the metastable and ground state can take a significant amount of time to reach equilibrium and therefore might need to be modeled time-dependently. Metastables can also have a significant contribution

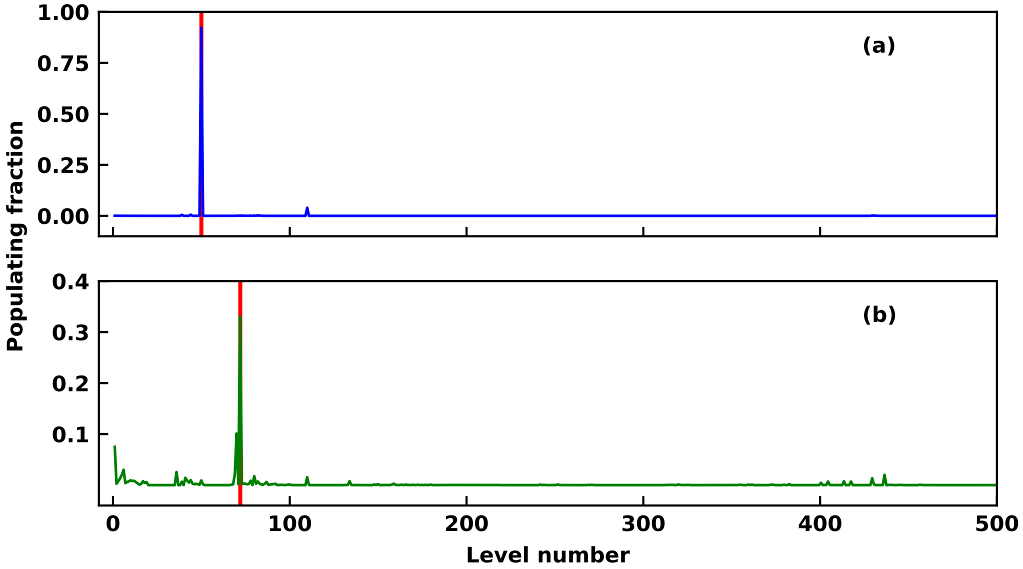

Figure 3.11: Intermediate populating levels responsible for populating the neutral Mo 4d^{5}5p(^{7}P$_4$) and 4d^{5}5p(^{5}P$_3$) energy levels. These levels produce strong emission lines at 379.8 and 550.6 nm. The red vertical lines in each plot correspond to the ground state contribution, see discussion in Section 3.6.2. (a) Populating levels for 4d^{5}5p(^{7}P$_4$), most of the population is being excited directly from the ground. (b) Populating levels for 4d^{5}5p(^{5}P$_3$), a majority of the population is coming from other excited states and metastables.

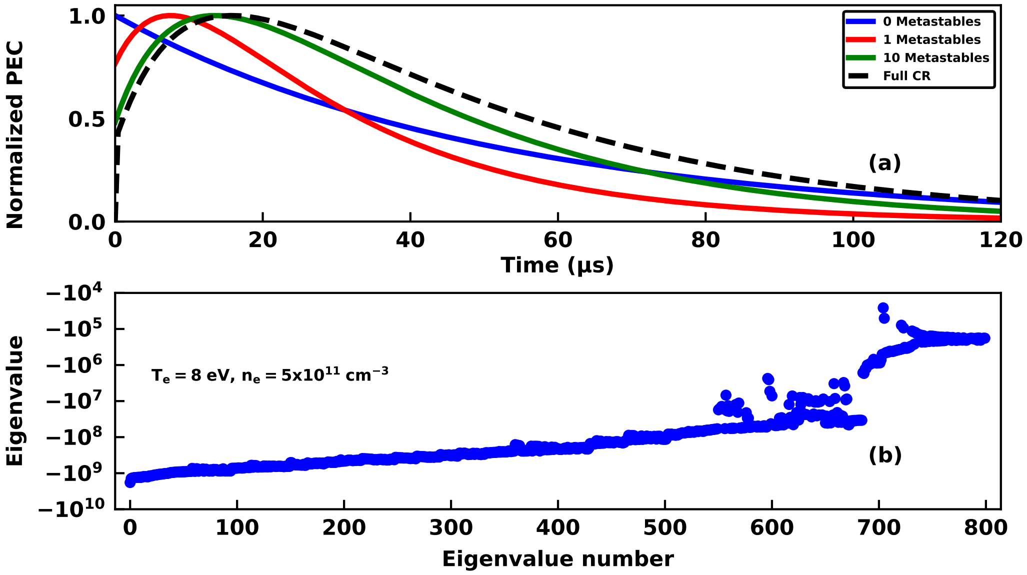

Figure 3.12: Comparison of time dependent and conventional solutions for Mo I at $T_\mathrm{e} = 8\ eV$, $n_\mathrm{e} = 5 \times 10^{11}$ cm^{-3}. (a) Full solution is illustrated by the black dashed line. Conventional solutions with different numbers of metastable states are the solid color lines. (b) Eigenvalues from the non-quasistatic solution show a 'continuum' of decreasing values with no clear distinction between metastable and excited states.

to the PEC intensity. The black dashed lines in both (a) and (b) of Figure 3.10 represent the sum of the contributions to the PECs from the ground and metastable in equilibrium. The solid color lines are the individual contributions to the PEC from both the ground and metastable. It is clear that in Figure 3.10 (a) most of the contribution to the PEC comes from the ground state while in (b) there is a larger contribution to the PEC from the metastable level. The second complication is that a large number of excited states are not well described by the quasi-static approximation requiring a significant number to be modeled time-dependently. In the case of Figure 3.12, even 10 metastables are not sufficient to reproduce the results from the non-quasi-static CR model, see the difference between the red and black dashed lines. The use of bundling methods[58] may allow for closer reproduction of the full solution while maintaining a small number of metastables and is investigated in later sections. It is assumed that all the population starts in the ground state as opposed to some fraction of the population beginning in a metastable state and requires that any atom eroded from a plasma facing material would come off the surface in its ground state. Experimental verification could be accomplished by observing spectral line emission near the plasma facing components. Experimental measurements from Marenkov *et al.*[63] suggest that most of the population starts in the ground state.

Chapter 4

Experimental measurements of low charge states of tungsten and molybdenum

There is a significant body of work describing the spectrum produced by low-Z elements in the NIST atomic database[62] including high precision of spectral wavelength (down to 0.00001 nm)in addition to atomic level identification generally given in Russel-Saunders notation. Low-Z atoms have also been extensively studied in fusion relevant plasmas.[42,64,65] In comparison, high-Z materials are relatively new to fusion relevant experiments. Additionally, high-Z atoms emit most strongly at UV wavelengths making experimental measurements difficult as these wavelengths are severely attenuated in fiber optics and CCD quantum efficiencies are reduced when compared to visible emission. Many fusion relevant experiments lack the ability to measure spectral lines in these ultraviolet wavelength ranges. Before the installation of the UV survey spectrometers on DIII-D described in Johnson *et al.*[25] , no spectral coverage from 200-360 nm was available in DIII-D. Figure 4.1 highlights the lack of emission in visible wavelength ranges and the high density emission range in the UV for near tungsten charge states.

This chapter lays the ground work to identify near neutral tungsten and molybdenum lines that can be used in various diagnostic applications as described in Chapter 5. This work includes the identification of many tungsten and molybdenum lines for the first time in a relatively hot and dense plasma (~ 20 eV, $\sim 5 \times 10^{12}$ cm^{-3}) that is relevant to fusion edge plasma parameters. In addition to wavelength identification, atomic level identification for many of the excited states is provided for the first time.

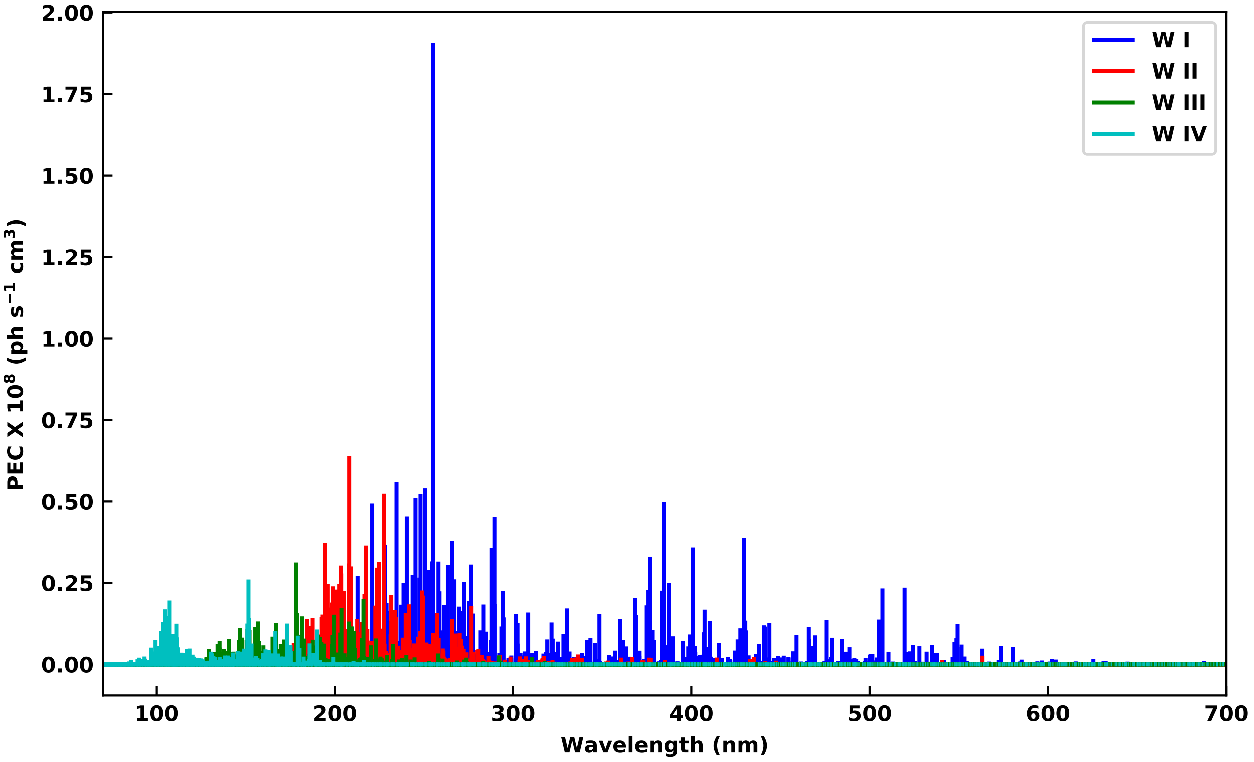

Figure 4.1: Photon emissivity coefficients (PECs) for W I (blue), W II (red), W III (green) and W IV (cyan) calculated with ColRadPy. All charge states were modeled at $T_e = 20$ eV and $n_e = 1 \times 10^{13}$ cm^{-3}. The fractional abundances of the charge states are set to 1.

4.1 Line identification of intrinsic CTH impurities

CTH, like all other plasma devices, has some fraction of impurities that are always present during plasma operation. These include elements that leak through vacuum components such as nitrogen and oxygen. Intrinsic impurities also come from plasma facing components. In CTH, there are carbon, stainless steel and molybdenum limiting surfaces. Carbon is the most prevalent impurity that comes from PFCs in CTH. Many fusion plasma devices have a mixture of materials that are used as PFCs, often making spectral emission from the plasma complex.

Blended impurity spectral lines can contaminate measurements and can lead to erroneous diagnostic results or mistaken line identification for a spectra of interest. Therefore, identifying intense intrinsic impurity lines is important when choosing spectral lines for diagnostics so that these impurity lines can be avoided. The S/XB (see Section 3.3.5) method for measuring erosion (discussed more in detail in Chapter 5) is dependent on the absolute number of measured photons, making it very susceptible to contamination lines. Thus, it is very important when choosing spectral lines to use for erosion measurements to select those free from blended impurities of other elements, or from different charge states or lines from the same element. This is one of the aims of the work of this dissertation: to produce a set of recommended spectral lines for measurements of tungsten erosion.

A scheme for spectral line identification using broad survey spectrometers is given by Johnson *et al.*;[25] the scheme for a survey spectrometer will also be discussed in Section 4.2 and can work well to maximize the use of relatively low-resolution spectrometers. The low-resolution spectrometers were used to identify CTH intrinsic impurity lines in combination with collisional radiative modeling as described in Section 4.1.1. A high-resolution spectrometer was then used to confirm tungsten spectral lines originally identified with the survey spectrometers as well as to identify many new low charge state tungsten lines. The high-resolution spectrometer discussed in Section 2.4 can resolve spectral lines better than the broad survey spectrometers at the sacrifice of wavelength coverage. A high-resolution spectrometer allows for more confidence in the wavelength location of spectral lines allowing easier line identification. Therefore, the majority of line identification in this chapter uses this improved high-resolution spectrometer.

4.1.1 Low-Z spectral line identification with ColRadPy

The most prevalent intrinsic impurity species in CTH are low-Z elements, namely carbon, nitrogen and oxygen. Atomic rates for low-Z species are generally calculated using a term averaged manner (see Section 3.3.8 for more detail). The atomic structure of low-Z species produces levels that are very close in energy within a given term when compared to high-Z species. The small difference in energy of the levels within a term allows ion collisions to effectively redistribute population within the J-resolved levels of a LS term. These terms then get statistically populated due to ion collisions making term resolved atomic modeling relatively accurate. Electron impact excitation is still the dominate mechanism to change electron populations between different LS terms. Ion collisions could be included into a level resolved calculation; however, there has not been much work or atomic data on this to date. Instead, electron impact excitation calculations are evaluated at term resolution, which later allows the populations to get split statistically amongst the levels of each term.

Even the survey spectrometers are able to resolve the wavelength difference due to spectral transitions from different levels within a term. Thus, to accurately model these low-Z spectral lines, the term averaged PECs must be split to level resolution (note that even higher resolution spectrometers could require additional splitting such as splitting due to the Zeeman effect). Condon and Shortley[61] provide equations to split term average PECs; this is described in Section 3.3.8. ColRadPy is capable of automatically splitting term resolved calculations using the method developed by Condon and Shortley, a feature that is unique to ColRadPy when compared to other CR codes (note that ADAS has a routine to allow the user to manually split the term resolved PECs using the method of Condon and Shortley). The newly split levels in the calculation are then shifted to NIST tabulated energies to produce spectroscopically accurate wavelengths. Note that ColRadPy is able to shift level resolved atomic structures to NIST automatically for the cases where NIST has the levels fully identified. The atomic structure codes that are used to calculate atomic collision rates (see Section 3.1 for more detail) generally do not produce level energies that are accurate enough to calculate spectral wavelengths to the precision required for direct comparison with spectral measurements. So, the energies in these underlying structure calculations must be shifted to NIST energies for spectral comparisons. This is particularly beneficial for complex species such as tungsten when there are many transitions close in wavelength.

Spectral lines in CTH were thus primarily identified with the high-resolution spectrometer and ColRadPy. Also note that the R-matrix calculation for neutral tungsten had many of its levels shifted to NIST values so the calculation already produced spectroscopically accurate wavelengths. In addition, ColRadPy uses collisional radiative modeling so that it yields accurate relative intensities of spectral lines at any electron temperature and density (when compared to coronal or LTE approximations). The NIST line tables also show relative intensities, but these are generally from experiments performed at low electron density. Therefore, NIST can report relative intensities that are very different from what would be observed in the high temperature and density environments of fusion relevant devices (and hence are generally used as a rough guide on what lines should be strong, but not for detailed intensity comparisons). Spectroscopically accurate wavelengths were calculated for synthetic spectra C V multiplet as shown in Section 3.3.8 as an example of this process. Similar plots are shown in Appendix B for charge states of major CTH impurities. The identification of low-Z intrinsic impurities was necessary to distinguish between low-Z impurity spectral lines and the high-Z spectral lines of interest for W and Mo.

4.2 Tungsten spectral line identification in CTH and DIII-D

Tungsten spectral line emission on CTH, when compared with the background spectra, is more intense than when measured on DIII-D. Measured tungsten spectral lines in CTH are stronger due to the greater solid angle of W emission as viewed by the CTH collection optics. The larger W signal to noise ratio in the CTH experiment significantly improves the confidence of W line identification in the DIII-D spectrum. The high density of W emission lines in the UV region allows for the possibility of simultaneous S/XB measurements and the evaluation of the effect of metastable levels on the relative intensities. Additionally, electron temperature and density measurements at the plasma boundary interface can also be determined by taking ratios of W I lines. These subjects are discussed in detail in Chapter 5.

The limited spectral resolution of the UV survey spectrometers (described in Section 2.3 ~ 0.1 nm) means that spectral lines from other impurities could be blended with the W lines of interest. Thus, methods in addition to wavelength agreement with the NIST Atomic Spectra Database[66] were needed to positively identify lines resulting from W in contrast to background impurity lines. One technique utilized in the CTH experiment to identify W spectral lines involved probe depth scans of the probe discussed in Section 2.2.1. As the W probe tip is inserted, plasma-probe interactions should increase as more W is eroded; thus, line intensities from W should intensify more than other intrinsic impurities in CTH plasmas. Some background impurity line intensities also increase with probe insertion depth but not at the same rate as W lines. Additionally, stainless steel and Mo-tipped probes also yield spectra for comparison allowing the increase in base impurity emission to be determined as a function of probe insertion. The probe experiments in CTH allow for the W source to be completely removed from the plasma by retracting the probe tip behind the limiters. Lines that increase in intensity when both the stainless steel and Mo probes are inserted are assumed to be CTH intrinsic impurities or lines coming from the boron nitride probe sleeve. For measurements in DIII-D, ratios of lines are examined to distinguish intrinsic impurities lines from W spectral lines. As the strike point sweeps from carbon tiles to W inserts in the divertor, the ratio of spectral intensities from W to C should increase (see Section 2.1 for details). The ratio of spectral lines from background impurities in DIII-D compared to C lines does not increase when the strike point sweeps over a W insert.

As an illustration of the types of comparisons that could be done, and of the spectra obtained, consider the wavelength range from 250 to 275 nm. Numerous W I lines are identified between the CTH and DIII-D experiments in the range from 250 to 275 nm with a selection highlighted in Figure 4.2 (CTH and DIII-D survey resolution) and 4.8 (CTH high-resolution). Only three of the lines in this range (255.13 nm, 266.28 nm, and 268.14 nm) have been previously observed experimentally. Additionally, the first observation and identification of a particularly intense W I line at 265.65 nm that does not appear to be blended with other background emission is presented. Emission from the CTH experiment in Figure 4.8 was acquired with the W-tipped probe inserted to 16.9 cm from the midplane while the DIII-D spectrum results were acquired from observation of a W coated insert on the divertor shelf (see Sections 2.1 and 2.2 for more description of the geometry and experimental setup). The same W I lines observed in both devices increases the confidence that the identified lines are primarily W and not blended with other impurities. The multiple strong W I lines existing in this region provide ample opportunity for erosion diagnosis. However, the corresponding tungsten erosion rate could not be determined from this spectra because an absolute intensity calibration of the spectrometer for this wavelength range was not possible.

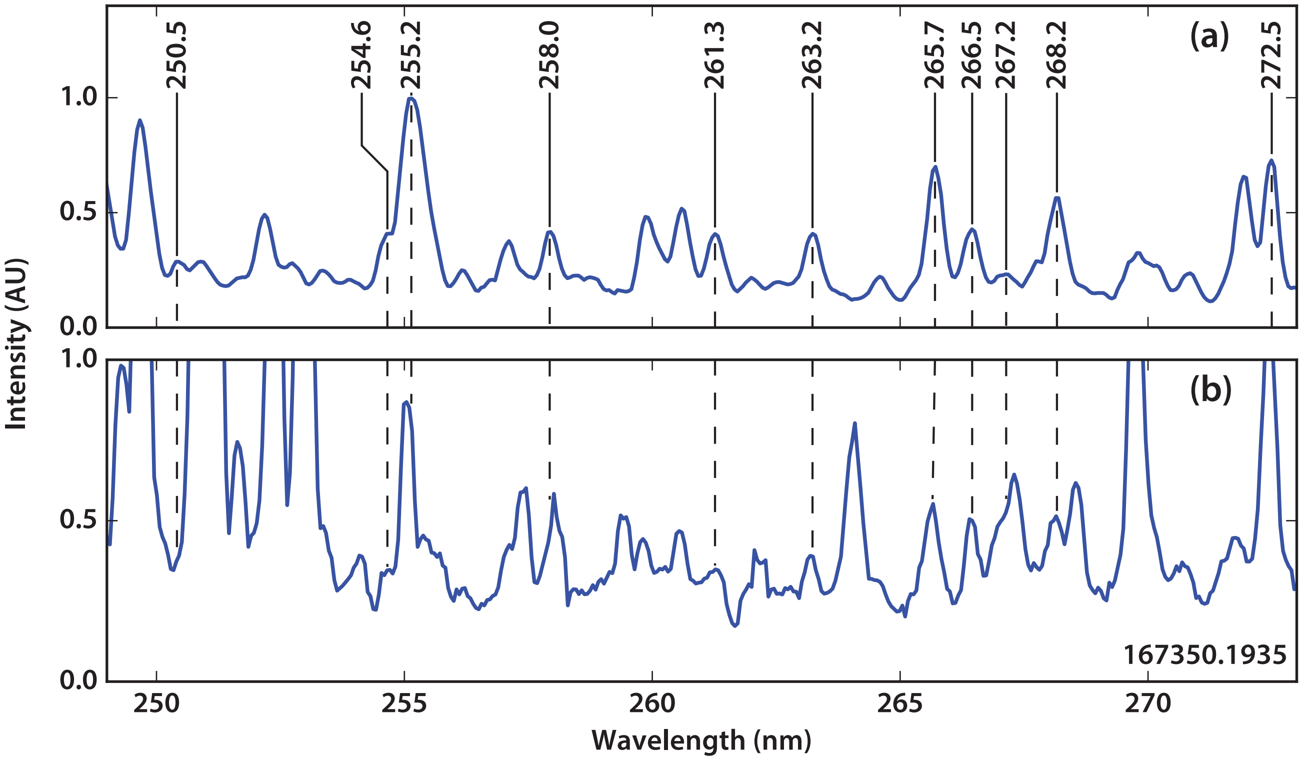

Figure 4.2: Measured CTH and DIII-D spectra with the wavelengths for neutral tungsten lines identified. (a) Average CTH spectrum of three shots (16120944, 16120947, 16120952) from 30 ms exposures beginning 60 ms into each discharge with the W probe fully inserted into the plasma. (b) DIII-D spectrum viewing the divertor shelf W coated inserts resulting from a single 200 ms exposure starting at 1935 ms into shot 167350.

It should also be noted that in addition to W I emission, a limited number of W II and W III lines have also been observed as listed in Tables 4.3 and B.12. However, the most intense W II spectral lines identified from the list of NIST measured W II lines are

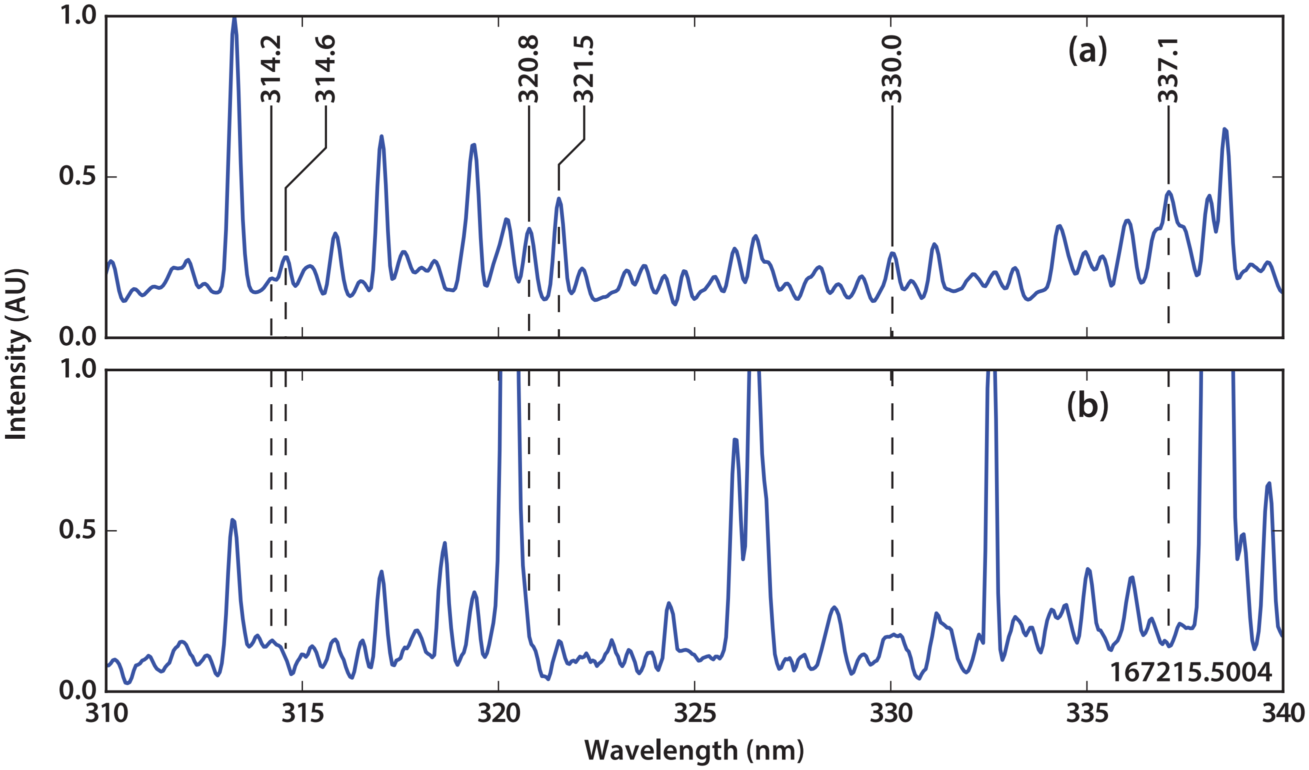

Figure 4.3: Measured CTH and DIII-D spectra with the wavelengths for neutral tungsten lines identified. (a) Average CTH spectrum of three shots (16120863, 16120864, 16120865) from 100 ms exposures integrating over each entire discharge with the W probe fully inserted into the plasma. (b) DIII-D spectrum viewing the divertor shelf W coated inserts resulting from a single 50 ms exposure starting at 5000 ms into shot 167215.

less intense than the W I lines reported in Table 4.1. Consequently, any contribution from W II and W III radiation blended with the measured W I intensities should be insignificant with the measured spectra. Spectral lines from W IV could not be identified in the ~190-400 nm wavelength region; this is consistent with the predicted emission from collisional radiative modeling of W IV as shown in Figure 4.1. The distribution of emission for higher charge states of tungsten continues the trend established in Figure 4.1 emitting farther into the vacuum ultra-violet wavelength ranges. As a result, no strong lines from charge states higher than W III are likely to be observed in the ~190-400 nm wavelength range.

A summary of all the W I spectral lines achieving an 'A', 'B', or 'C' rating between the two experiments, with the relatively low-resolution survey spectrometers, described in Section 2.3 is provided in Table 4.4 along with full level identifications where possible. Tables

4.1 and 4.2 include much of the same information but were produced with data only from CTH, but using the high spectral resolution spectrometer discussed in Section 2.4. The high-resolution spectrometer allowed for more confident line identification due to the smaller probability of blended impurity lines. In addition to the first observation of many of these neutral tungsten spectral lines, the first possible level identifications based on a structure calculation from Smyth *et al.*[52] are provided for many of the excited states. The previous level identification on NIST for many upper excited states of W I are limited to J values as shown by Kramida *et al.*[67] Level identifications have also been proposed by Smirnov *et al.*[3] In this work, upper level identifications are obtained by combining the NIST Atomic Spectra Database[66] with a prior structure calculation by Smyth *et al.*,[52] but in some cases, the upper level identification cannot be uniquely determined so a partial identification is provided. For these cases, empty square brackets are used with the J-value as a subscript ($[\,]_J$). The two observed emission lines at 294.69 nm are most likely multiplets which cannot be resolved by the UV survey spectrometers. Therefore, the individual components of each multiplet are identified separately, but the exact composition of the observed multiplet is not known. The table also indicates which lines have been previously observed in other fusion relevant experiments. It should be noted that the lowest six energy levels of neutral tungsten are long-lived states (either ground or metastable states) and could have quite large populations. These are the 5 J-values of the $5d^46s^2$ (^{5}D) term ($J = 0, 1, 2, 3, 4$) and $5d^56s$ ($^7S_3$) level. It is interesting that the majority of the observed lines in Table 4.1 have a lower level that is one of these six lower states suggesting the observed lines are being mostly populated from these levels and is later confirmed by the analysis in Chapter 5.

4.2.1 Tungsten probe scan in CTH

Tungsten and molybdenum experiments using CTH were conducted with two different probes, the high-Z probes are described in Sections 2.2.1 and 2.5. Probe experiments in CTH allow high-Z tipped probes to be inserted into the plasma at varying depths. These experiments included both tips with and without an embedded Langmuir probes for T_e and n_e measurements. CTH also employs a Radial Field Coil (RFC) which can be used to push the plasma down and away from the fully retracted probe, essentially moving the plasma boundary even further from the probe tip. Figure 4.4 highlights a selection of results from W-tipped probe experiments in CTH with varying amounts of plasma-probe interaction by adjusting the distance of the probe tip from the CTH midplane and the RFC magnitude. In general, as the probe is inserted into the plasma towards the midplane, the W lines become more intense and are most notable for the 255.13, 265.65, and 400.88 nm lines. The increase in W emission is consistent with more sputtering from the W-tipped probe closer to the plasma core. Other large impurity lines such as C IV and C III, also present in Figure 4.4, demonstrate a similar trend with probe insertion, but the impurity intensities do not change as rapidly as the W lines. Furthermore, when the probe is fully retracted (25.9 cm from the CTH midplane) and the RFC maximally energized (RFC high), the W line emission completely disappears while other impurity lines remain at a reduced intensity. The same effect is seen when the new probe with a longer linear travel distance was retracted to 38 cm from the midplane. The increase in intensity of lines other than W is attributed to greater plasma-probe interaction with higher density and temperature plasma parameters toward the core.

The tungsten probe scan experiment in CTH was utilized to confirm all W lines listed in Table 4.1. Identical probe scans were completed in CTH using both Mo, stainless steel and SiC probe tips. Quite notably, no lines were observed at 400.88 (Figure 4.19), 265.65 or 255.13 (Figure 4.8) nm during the Mo and stainless steel probe scans. These lines are either the currently used diagnostic lines (400.88 nm) or are part of our proposed diagnostic lines (265.65 and 255.13 nm). Yet, when the W probe is fully inserted, these are some of the strongest spectral lines. The background emission dependence on probe depth was investigated using Mo and stainless steel probe tips as there is no source of W in the CTH

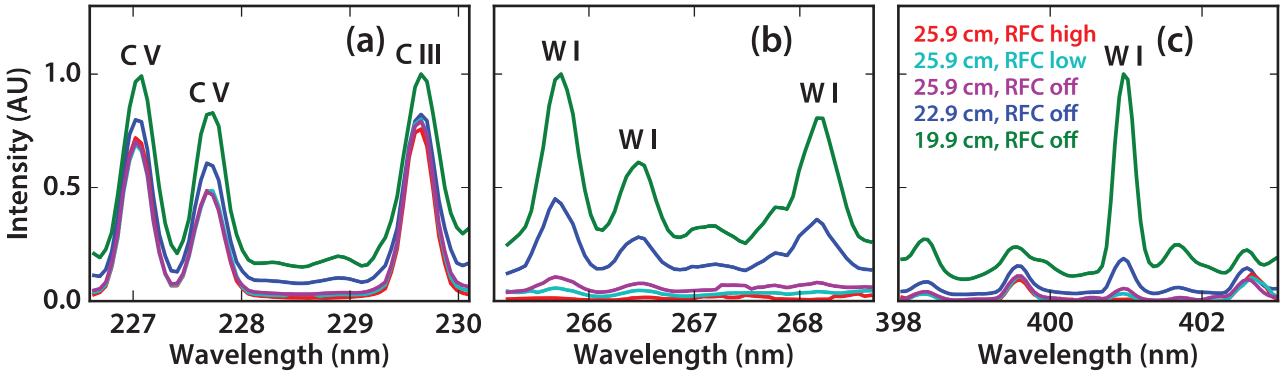

Figure 4.4: Intensities of tungsten and carbon impurity lines with varying W-tipped probe depth and Radial Field Coil (RFC) magnitude. The combinations of probe tip distance from the CTH midplane and RFC magnitude are listed in the legend from least plasma-probe interaction (25.9 cm, RFC high) to most interaction (19.9 cm, RFC off). (a) Carbon impurity line intensities increase modestly with probe insertion but are present for all configurations. (b) and (c) Tungsten lines demonstrate a significant dependence on probe depth and RFC magnitude. All tungsten lines are not present when the W-tipped probe is fully retracted with maximum applied radial field (25.9 cm, RFC high).

device. Comparison of the emission from the three probe tips allowed for persistent impurity lines to be distinguished from the W emission lines.

Electron temperatures and densities at the probe tip in CTH plasmas were measured with the newer Langmuir probe setup described in Chapter 2. These measurements were not available for all spectral wavelength ranges. Simultaneous measurements of spectroscopy and Langmuir probe parameters were not necessary for the line identification presented in this chapter, but were needed for the analysis in Chapter 5. Electron temperatures in CTH varied from 15-30 eV with electron densities between $1 - 7 \times 10^{12}$ cm^{-3} depending on the probe position in the plasma.

The magnetic field at the probe tip varied from 0.54 T for a probe depth of 25.9 cm to 0.60 T for a probe depth of 19.9 cm with incidence angle of the magnetic field onto the probe of $\sim 12°$. Another cluster of W I lines that has not been previously reported in fusion relevant plasmas exists in the region between 310 and 340 nm. The spectra in Figures 4.15 and 4.16 were acquired during plasma conditions similar to Figure 4.8. The six lines identified in Figure 4.3 have not been previously observed in any fusion relevant plasma experiments.

Only one of the lines could be clearly distinguished in DIII-D (321.6 nm) with the UV survey spectrometer. Nevertheless, the wavelength range in Figure 4.3 could be very promising for future high-resolution measurements. Moreover, the longer UV wavelengths have the benefit of increased transmission in optical fibers as well as higher quantum efficiency for widely available CCD detectors.

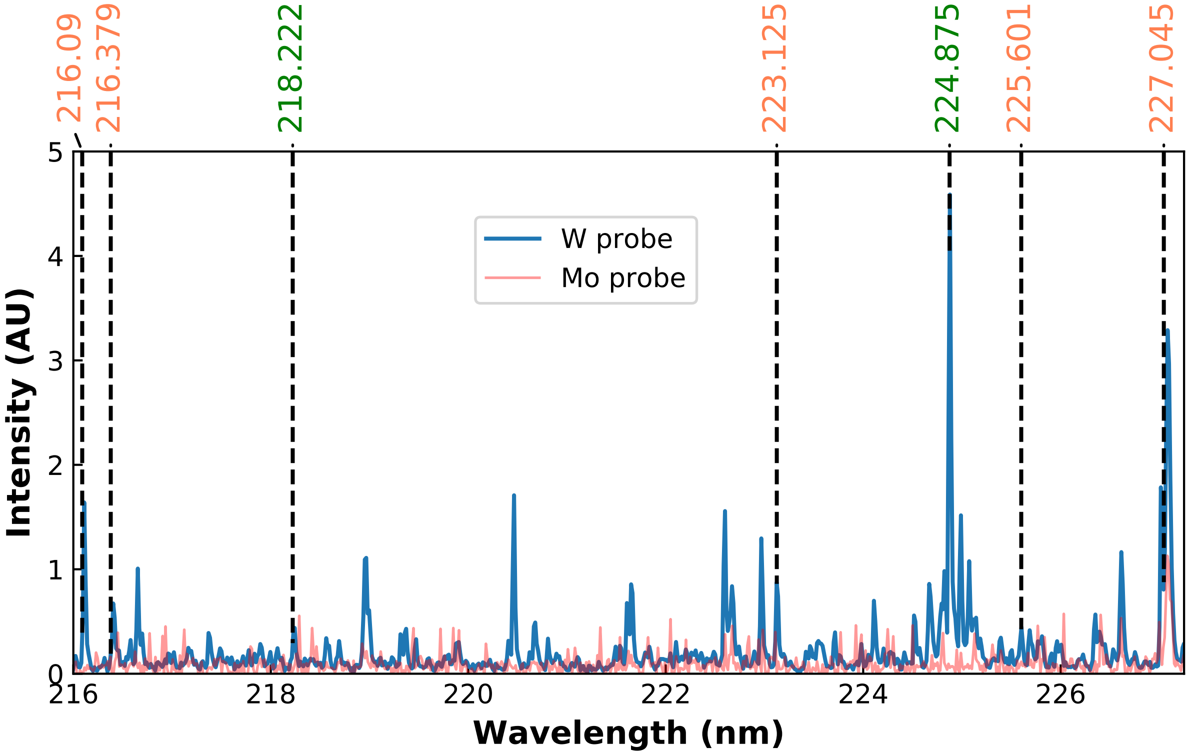

Figure 4.5: CTH spectrum from 216-227 nm, the tungsten probe was located at 21 cm from the midplane of CTH. W II lines are identified by the NIST observed wavelengths in green text and the W III lines are in orange text. The spectrum with the tungsten tipped probe is in blue, and the spectrum with the molybdenum tipped probe is in transparent red.

4.2.2 DIII-D strike point location on tungsten rings

Tungsten emission lines are among the least intense impurity UV lines present in measured DIII-D spectra, consistent with the low sputtering yield of tungsten[68]; yet, W I spectral line identification could still be accomplished. Other intrinsic impurities such as carbon and boron dominate the DIII-D UV spectrum. Electron temperatures in the DIII-D

Table 4.1: Table of W I emission lines from 200-300 nm observed during CTH experiments along with level identifications where possible. Previously observed lines are indicated by superscripts on the NIST defined wavelengths: ^{a},[2] ^{b},[3] ^{c},[4] ^{d},[5] ^{e},[6] and ^{f}.[7] The lines identified in this table are shown with a comparison to a Mo spectrum in increasing wavelength in Figures 4.5 - 4.12.

NIST wavelength (nm)	Upper level	Lower level
243.596	$5d^46s6p$ ($^5F_4$)	$5p^65d^46s^2$ ($^5D_3$)
244.406	$5d^46s6p$ ($^5F_1$)	$5p^65d^46s^2$ ($^5D_1$)
245.200	$5d^36s^26p$ ($^3D_1$)	$5p^65d^46s^2$ ($^5D_0$)
246.431	$5d^46s6p$ ($^5F_1$)	$5p^65d^46s^2$ ($^5D_2$)
248.013	$5d^46s6p$ ($^5F_2$)	$5p^65d^46s^2$ ($^5D_1$)
250.470	$5d^46s6p$ ($^5D_2$)	$5p^65d^46s^2$ ($^5D_1$)
254.534	$5p^65d^56p$ ($^5P_3$)	$5p^65d^46s^2$ ($^5D_2$)
254.714	$5d^46s6p$ ($^5F_1$)	$5p^65d^46s^2$ ($^5D_2$)
255.135^{a,b,d}	$5p^65d^56p$ ($^5P_1$)	$5p^65d^46s^2$ ($^5D_0$)
255.675	$5d^36s^26p$ ($^3D_1$)	$5p^65d^46s^2$ ($^5D_1$)
256.197	$5d^46s6p$ ($^5D_3$)	$5p^65d^46s^2$ ($^5D_3$)
258.049	$5p^65d^56p$ ($^5P_1$)	$5p^65d^46s^2$ ($^5D_1$)
260.354	$5d^46s6p$ ($^5G_2$)	$5p^65d^46s^2$ ($^5D_3$)
261.308	$5d^46s6p$ ($^5D_2$)	$5p^65d^46s^2$ ($^5D_2$)
263.313	$5d^46s6p$ ($^3P_1$)	$5p^65d^46s^2$ ($^5D_1$)
265.654	$5p^65d^56p$ ($^7P_4$)	$5p^65d^56s$ ($^7S_3$)
266.284	$5p^65d^56p$ ($^5P_2$)	$5p^65d^46s^2$ ($^5D_2$)
266.978	$5d^36s^26p$ ($^3D_1$)	$5p^65d^46s^2$ ($^5D_2$)
268.142^{a,d}	$5p^65d^56p$ ($^7P_4$)	$5p^65d^56s$ ($^7S_3$)
269.567	$5p^65d^56p$ ($^5P_1$)	$5p^65d^46s^2$ ($^5D_2$)
272.436	$5p^65d^56p$ ($^7P_3$)	$5p^65d^56s$ ($^7S_3$)
276.234^{b}	$5d^36s^26p$ ($^5F_1$)	$5p^65d^46s^2$ ($^5D_0$)
277.400	$5p^65d^56p$ ($^5P_2$)	$5p^65d^46s^2$ ($^5D_3$)
279.993^{b}	$5d^46s6p$ ($^5P_2$)	$5p^65d^46s^2$ ($^5D_2$)
283.138^{b,c}	$5d^36s^26p$ ($^3H_4$)	$5p^65d^56s$ ($^7S_3$)
283.363	$5p^65d^56p$ ($^5P_3$)	$5p^65d^46s^2$ ($^5D_4$)
284.157	$5d^46s6p$ ($^5G_2$)	$5p^65d^46s^2$ ($^5D_3$)
287.940^{b,c}	$5d^36s^26p$ ($^3D_1$)	$5p^65d^46s^2$ ($^5D_0$)
289.601^{b,c}	$5d^36s^26p$ ($^5F_1$)	$5p^65d^46s^2$ ($^5D_1$)
289.644^{b,c}	$5p^65d^56p$ ($^7P_2$)	$5p^65d^56s$ ($^7S_3$)
293.500^{b,c}	$5d^46s6p$ ($^3F_2$)	$5p^65d^46s^2$ ($^5D_1$)
294.440^{b,c}	$5p^65d^56p$ ($^7P_2$)	$5p^65d^56s$ ($^7S_3$)
294.699^{b,c}	$5p^65d^56p$ ($^7P_3$)	$5p^65d^56s$ ($^7S_3$)

Table 4.2: Table of W I emission lines from 300-400 nm observed during CTH experiments along with level identifications where possible. Previously observed lines are indicated by superscripts on the NIST defined wavelengths: [a],[2] [b],[3] [c],[4] [d],[5] [e],[6] and [f].[7] The lines identified in this table are shown with a comparison to a Mo spectrum in increasing wavelength in Figure's 4.12 - 4.19

.

NIST wavelength (nm)	Upper level	Lower level
301.744[b,c]	5d^{4}6s6p (^{5}D$_4$)	5p^{6}5d^{5}6s (^{7}S$_3$)
302.493[b,c]	5d^{3}6s^{2}6p (^{3}D$_1$)	5p^{6}5d^{4}6s^2 (^{5}D$_1$)
302.526	5d^{4}6s6p (^{5}F$_1$)	5p^{6}5d^{4}6s^2 (^{3}P$_0$)
304.186	5d^{3}6s^{2}6p (^{5}F$_1$)	5p^{6}5d^{4}6s^2 (^{5}D$_2$)
304.644[b]	5d^{3}6s^{2}6p (^{5}F$_2$)	5p^{6}5d^{4}6s^2 (^{5}D$_1$)
314.554	5d^{4}6s6p (^{3}H$_4$)	5p^{6}5d^{4}6s^2 (^{5}D$_4$)
319.157	5d^{4}6s6p (^{5}D$_1$)	5p^{6}5d^{4}6s^2 (^{5}D$_0$)
319.884	5d^{4}6s6p (^{5}D$_4$)	5p^{6}5d^{4}6s^2 (^{5}D$_3$)
320.828	5d^{3}6s^{2}6p (^{5}F$_2$)	5p^{6}5d^{4}6s^2 (^{5}D$_2$)
325.966	5d^{4}6s6p (^{5}H$_3$)	5p^{6}5d^{4}6s^2 (^{5}D$_3$)
330.082	5d^{4}6s6p (^{5}F$_4$)	5p^{6}5d^{4}6s^2 (^{5}D$_3$)
337.100	5d^{3}6s^{2}6p (^{5}F$_2$)	5p^{6}5d^{4}6s^2 (^{5}D$_3$)
361.752[b,e]	5d^{4}6s6p (^{5}D$_3$)	5p^{6}5d^{5}6s (^{7}S$_3$)
363.194[b,e]	5d^{4}6s6p (^{5}D$_2$)	5p^{6}5d^{4}6s^2 (^{5}D$_1$)
378.077[b]	5d^{4}6s6p (^{5}P$_2$)	5p^{6}5d^{5}6s (^{7}S$_3$)
383.506[b]	5d^{4}6s6p (^{5}P$_2$)	5p^{6}5d^{4}6s^2 (^{5}D$_2$)
386.799[b]	5d^{4}6s6p (^{7}D$_4$)	5p^{6}5d^{5}6s (^{7}S$_3$)
400.875[a,b,d,f]	5d^{4}6s6p (^{7}P$_4$)	5p^{6}5d^{5}6s (^{7}S$_3$)
400.901	5p^{6}5d^{5}6p (^{5}P$_1$)	5p^{6}5d^{5}6s (^{5}S$_2$)
401.923[b]	5d^{4}6s6p (^{7}D$_1$)	5p^{6}5d^{4}6s^2 (^{5}D$_2$)
410.294	5d^{4}6s6p (^{5}D$_2$)	5p^{6}5d^{4}6s^2 (^{5}D$_3$)

Table 4.3: Table of W II emission lines observed between the DIII-D and CTH experiments along with level identifications where possible.

NIST Wavelength (nm)	Upper Level	Lower Level
224.875	5d^{3}6s6p (^{6}F$_{1/2}$)	5d^4(^{5}D)6s (^{6}D$_{1/2}$)
239.293	5d^3(^{4}F)6s(^{5}F)6p (^{6}G$_{9/2}$)	5d^4(^{5}D)6s (^{6}D$_{7/2}$)
242.749		5d^4(^{5}D)6s (^{6}D$_{5/2}$)
247.780	5d^3(^{4}F)6S(^{5}F)6p (^{6}G$_{9/2}$)	5d^4(^{5}D)6s (^{6}D$_{9/2}$)
248.877	5d^4(^{5}D)6p (^{6}p$_{3/2}$)	5d^5 (^{6}S$_{5/2}$)
248.923	5d^4(^{5}D)6p (^{6}F$_{7/2}$)	5d^4(^{5}D)6s (^{6}D$_{7/2}$)
232.831	('5p65d36s6p(6F)', 6, 3, 0.5,	('5p65d46s(6D)', 6, 2, 1.5, 1518.829)
245.148	('5p65d46p(6D)', 6, 2, 1.5,	('5p65d46s(6D)', 6, 2, 1.5,

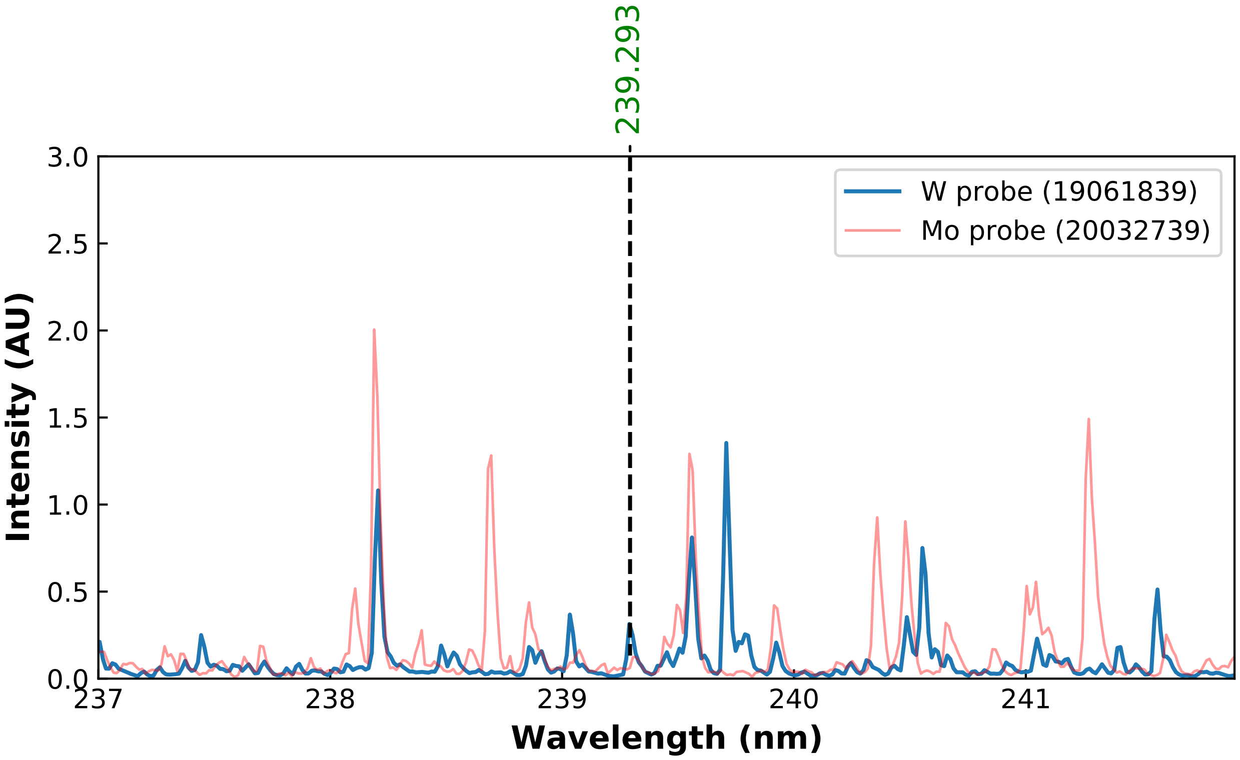

Figure 4.6: CTH spectrum from 233-242 nm, the tungsten probe was located at 21 cm from the midplane of CTH. W II lines are identified by the NIST observed wavelengths in green text. The spectrum with the tungsten tipped probe is in blue, and the spectrum with the molybdenum tipped probe is in transparent red.

divertor region between Edge Localized Modes (ELMs) mainly varied from 25-50 eV, with densities between $1 - 3 \times 10^{13}$ cm^{-3}. As mentioned, the limited resolution of the UV survey spectrometers may lead to overlap of other impurity emission lines with the W lines. The possibility of overlapping emission necessitated the use of the metrics explained in Section 4.2 to positively identify W spectral lines. The high-resolution UV spectrometer was not available for DIII-D data collection.

Identification of W line emission was achieved in the DIII-D experiment by observing transitions of the divertor strike point location from carbon to tungsten coated inserts. Figure 4.20 depicts the time evolution of DIII-D shot 167350 with the UV spectrometers viewing a W coated insert on the divertor shelf for exposure times of 200 ms. During this discharge, the outer strike point moves from the outboard portion of the lower divertor

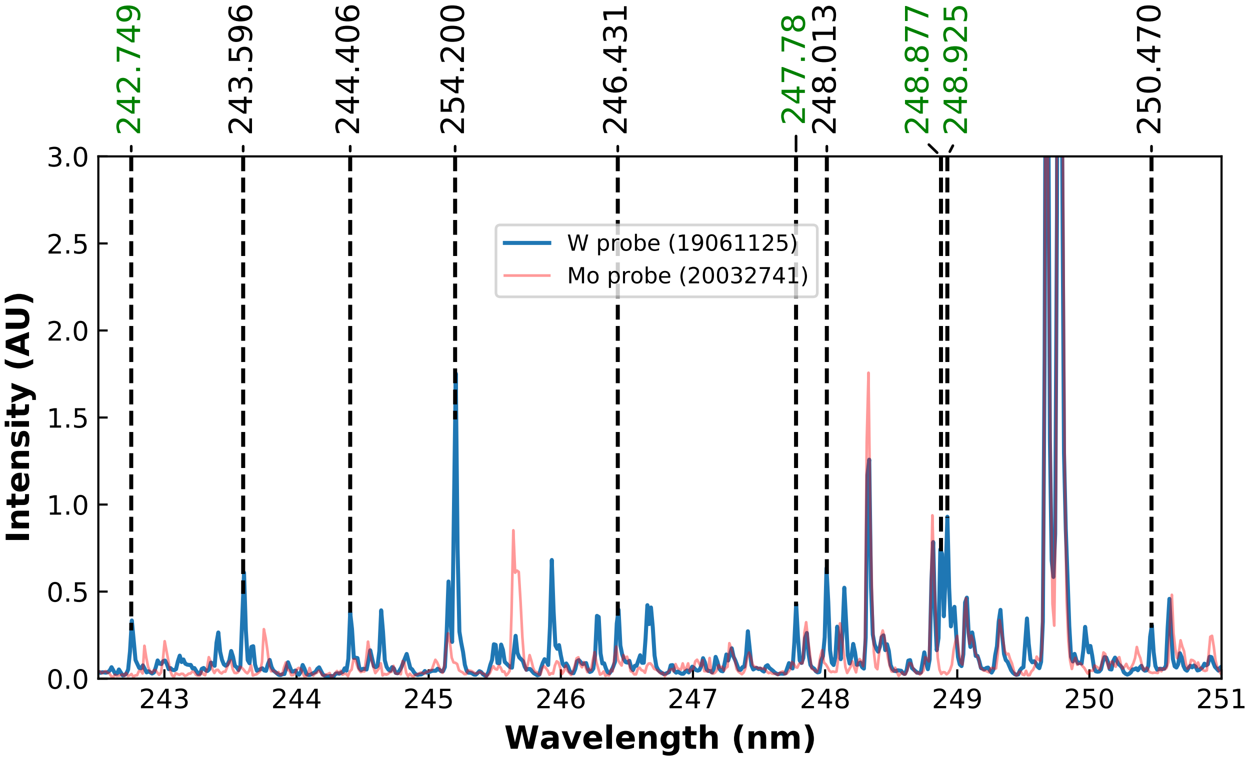

Figure 4.7: CTH spectrum from 242-254 nm, the tungsten probe was located at 21 cm. W I lines are identified by the NIST observed wavelengths in black text and W II lines are identified by the NIST observed wavelengths in green text. The spectrum with the tungsten tipped probe is in blue, and the spectrum with the molybdenum tipped probe is in transparent red.

to the W coated inserts on the shelf where it is held fixed for approximately 3 seconds. Electron temperature and density on the W surface are measured by a single Langmuir probe embedded in the divertor shelf tile at the same radial location as the UV spectrometer collection spot.[69] The raw Langmuir probe data is plotted along with a trace having the ELM periods removed and smoothed over 101 points. Intensities of the W I, C II and O V emission lines observed by the UV survey spectrometer throughout the discharge are binned using a 0.2 nm window encompassing the full width at half maximum of each spectral line and are shown normalized to their maximum intensity. The intensities of all lines increase when the strike point is swept over the W insert; yet, the W I line increases later in time than the C II and O V impurity lines. Additionally, the ratio of the W I to C II emission also doubles when the strike point is swept over the W insert, where a ratio of 0.1 corresponds to

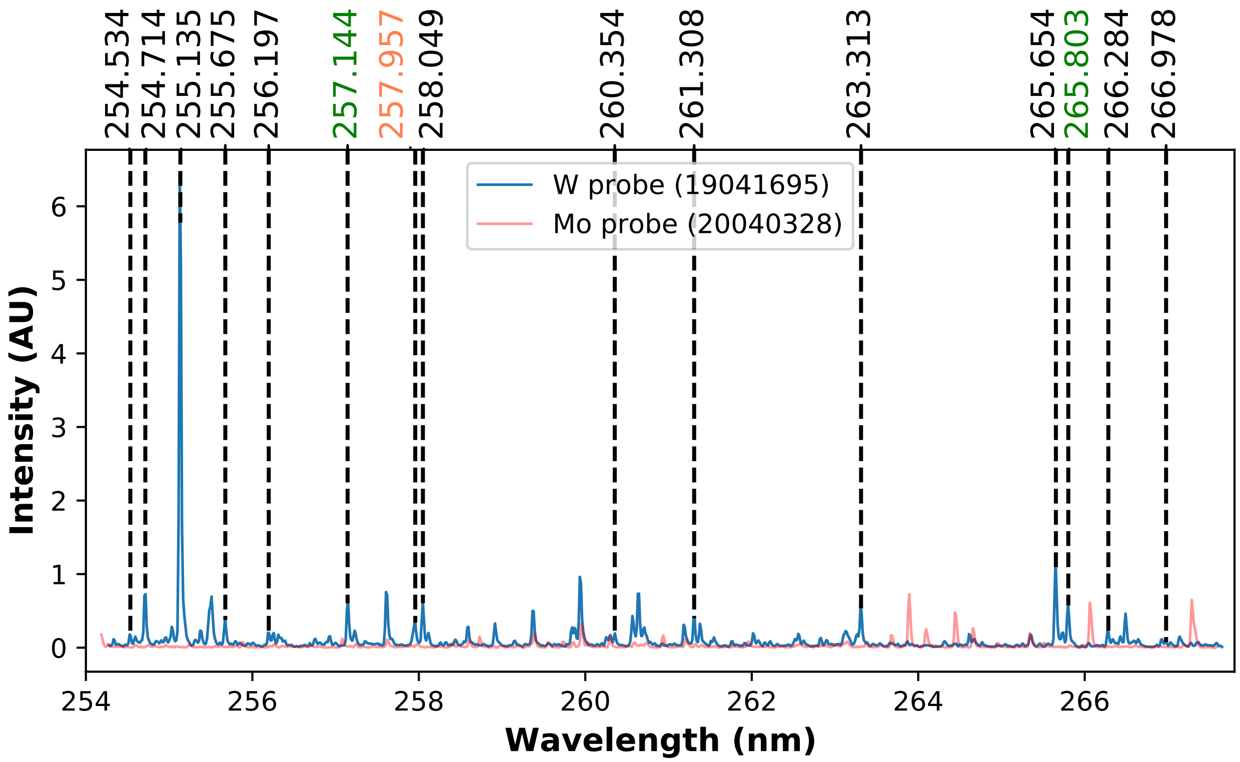

Figure 4.8: CTH spectrum from 254-267 nm, the tungsten probe was located at 21 cm. W I lines are identified by the NIST observed wavelengths in black text, W II lines are identified by the NIST observed wavelengths in green text and the W III lines lines are identified by the NIST observed wavelengths in coral text. The spectrum with the tungsten tipped probe is in blue, and the spectrum with the molybdenum tipped probe is in transparent red.

the noise floor of the W I line at 265.65 nm while a ratio of 0.2 corresponds to measurable W I signal. The increase in W I lines relative to C lines assisted in discriminating W I radiation from other impurity lines in the DIII-D divertor.

While the high-resolution spectrometer is a more sensitive and precise instrument than the survey spectrometers, tungsten spectral lines identified with the survey spectrometers in DIII-D still give confidence to the spectral line identification. Spectral lines identified in both CTH and DIII-D with the lower resolution survey spectrometers are listed in Table 4.4. Many of the spectral lines identified in Table 4.4 were later confirmed with the high-resolution spectrometer on CTH (see Tables 4.1 and 4.2), including lines that were previously blended because of the relatively resolving power of the survey spectrometer.

Table 4.4: Table of W I emission lines observed between the DIII-D and CTH experiments along with level identifications where possible and confidence. Previously observed lines are indicated by superscripts on the NIST defined wavelengths: [a],[8] [b],[3] [c],[4] [d],[5] [e],[6] and [f].[7]

Observed Wavelength [nm]	NIST Wavelength [nm]	Upper Level	Lower Level	Confidence
233.23	233.28	5d^{4}6s6p (^{3}I$_5$)	5d^{4}6s^2 (^{5}D$_4$)	B
	233.28	5d^{4}6s6p (^{5}P$_3$)	5d^{4}6s^2 (^{5}D$_4$)	B
243.48	243.60	5d^{4}6s6p (^{5}D$_4$)	5d^{4}6s^2 (^{5}D$_3$)	B
246.24	246.28	([]$_1$)	5d^{4}6s^2 (^{5}D$_1$)	C
247.25	247.41	5d^{4}6s6p (^{5}F$_4$)	5d^{4}6s^2 (^{5}D$_4$)	B
250.45	250.47	5d^{4}6s6p ([]$_2$)	5d^{4}6s^2 (^{5}D$_1$)	B
254.61	254.71	5d^{4}6s6p (^{5}F$_1$)	5d^{4}6s^2 (^{5}D$_2$)	B
255.15	255.13[a,b,d]	5d^{4}6s6p (^{3}P$_1$)	5d^{4}6s^2 (^{5}D$_0$)	A
256.18	256.20	([]$_3$)	5d^{4}6s^2 (^{5}D$_3$)	C
257.95	258.05	5d^{4}6s6p (^{5}P$_1$)	5d^{4}6s^2 (^{5}D$_1$)	A
261.28	261.31	5d^{4}6s6p (^{5}F$_2$)	5d^{4}6s^2 (^{5}D$_2$)	B
263.24	263.31	([]$_1$)	5d^{4}6s^2 (^{5}D$_1$)	C
265.69	265.65	5d^{5}6p (^{7}P$_4$)	5d^5(^{6}S)6s (^{7}S$_3$)	A
266.46	266.28[b]	([]$_2$)	5d^{4}6s^2 (^{5}D$_2$)	C
267.15	267.15	5d^{4}6s6p (^{3}F$_3$)	5d^{4}6s^2 (^{5}D$_3$)	B
268.18	268.14[a,d]	5d^{4}6s6p (^{5}G$_4$)	5d^5(^{6}S)6s (^{7}S$_3$)	A
272.51	272.44	5d^{5}6p (^{7}P$_3$)	5d^5(^{6}S)6s (^{7}S$_3$)	A
284.89	284.80	5d^{4}6s6p (^{3}D$_3$)	5d^5(^{6}S)6s (^{7}S$_3$)	B
294.69	294.44[b,c]	5d^{5}6p (^{7}P$_2$)	5d^5(^{6}S)6s (^{7}S$_3$)	B
	294.70[b,c]	5d^{4}6s6p (^{5}F$_3$)	5d^5(^{6}S)6s (^{7}S$_3$)	B
	294.74[b,c]	5d^{4}6s6p (^{5}I$_4$)	5d^{4}6s^2 (^{5}D$_3$)	B
301.74	301.74	5d^{4}6s6p (^{5}D$_4$)	5d^5(^{6}S)6s (^{7}S$_3$)	B
314.20	314.14	5d^{4}6s6p (^{5}F$_4$)	5d^{4}6s^2 (^{3}H$_4$)	B
314.57	314.52	5d^{4}6s6p (^{3}H$_5$)	5d^{4}6s^2 (^{3}H$_5$)	B
320.79	320.83	5d^{4}6s6p (^{5}F$_2$)	5d^{4}6s^2 (^{5}D$_2$)	B
321.53	321.56	5d^{4}6s6p (^{5}F$_5$)	5d^{4}6s^2 (^{5}D$_4$)	A
330.03	330.08	5d^{4}6s6p (^{5}F$_4$)	5d^{4}6s^2 (^{5}D$_3$)	B
337.09	337.10	5d^{4}6s6p (^{5}F$_2$)	5d^{4}6s^2 (^{5}D$_3$)	B
361.80	361.75[b,e]	5d^{4}6s(^{6}D)6p (^{5}P$_3$)	5d^5(^{6}S)6s (^{7}S$_3$)	A
378.08	378.08[b]	5d^{4}6s(^{6}D)6p (^{5}P$_2$)	5d^5(^{6}S)6s (^{7}S$_3$)	B
383.54	383.51[b]	5d^{4}6s(^{6}D)6p (^{5}P$_2$)	5d^{4}6s^2 (^{5}D$_2$)	B
386.81	386.80[b]	5d^{4}6s(^{6}D)6p (^{7}D$_4$)	5d^5(^{6}S)6s (^{7}S$_3$)	B
400.96	400.88[a,d,f]	5d^{4}6s6p (^{7}P$_4$)	5d^5(^{6}S)6s (^{7}S$_3$)	A

[1] Only the upper level configuration and J-value are identified for the 250.47 nm line, while only the upper level J-value is identified for the 246.28, 256.20, 263.31, and 266.28 nm lines.

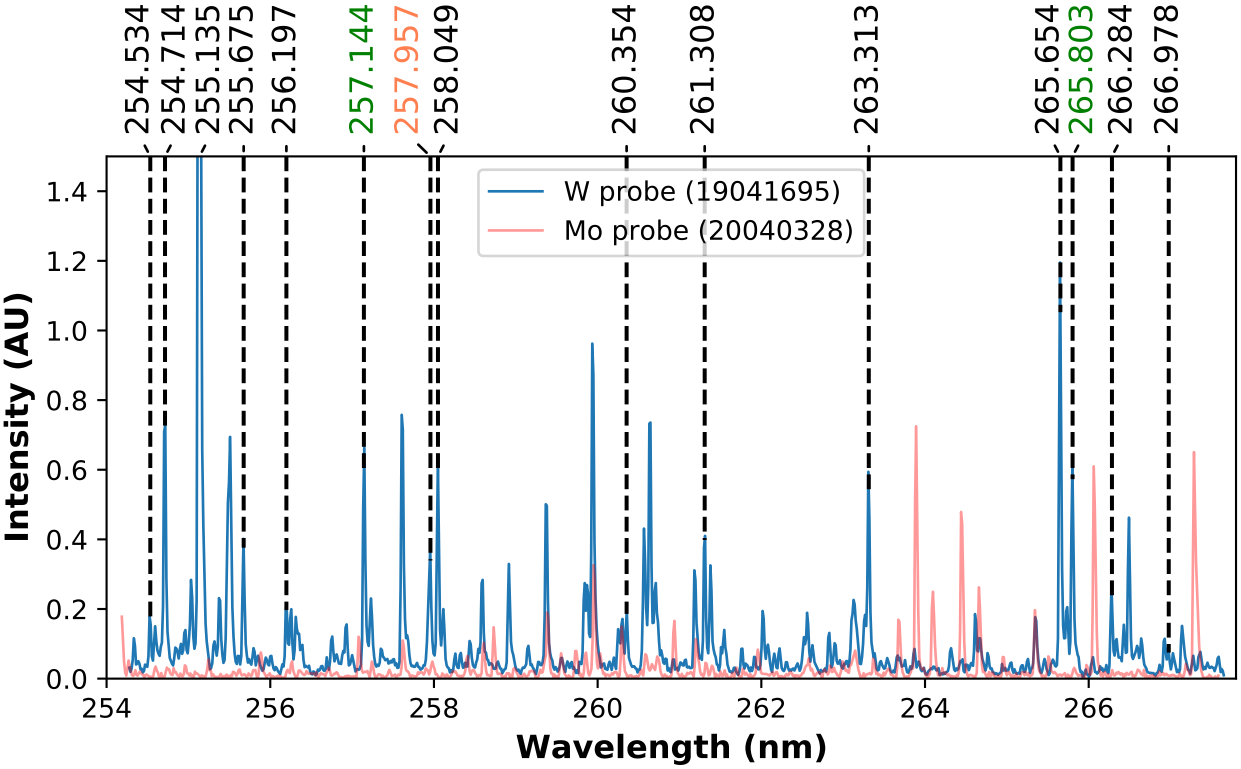

Figure 4.9: CTH spectrum from 254-267 nm with y axis scaling to allow for relative small W spectral lines to be seen. The tungsten probe was located at 21 cm. W I lines are identified by the NIST observed wavelengths in black text, W II lines are identified by the NIST observed wavelengths in green text and the W III lines lines are identified by the NIST observed wavelengths in coral text. The spectrum with the tungsten tipped probe is in blue, and the spectrum with the molybdenum tipped probe is in transparent red.

A correlation analysis of W line intensities for UV wavelengths in DIII-D with various plasma parameters including ELM intensity was attempted, as previously reported in JET and DIII-D using the 400.88 nm line.[6,68] However, the exposure time of the UV survey spectrometers (typically $\sim$ 100 ms) was such that multiple ELMs occurred during a single exposure. Therefore, signals from a D_α filterscope system[70] were used as a proxy for the ELM intensity. The correlation analysis found no conclusive trend between multiple W I line intensities (including the 400.88 nm line) as measured by the UV survey spectrometers and D_α emission. The correlation analysis was repeated using a high-resolution visible spectrometer[71] viewing only the 400.88 nm, and a correlation with the D_α intensity was confirmed that is similar to the correlation found by DenHarder *et al.*[72] The limited spectral

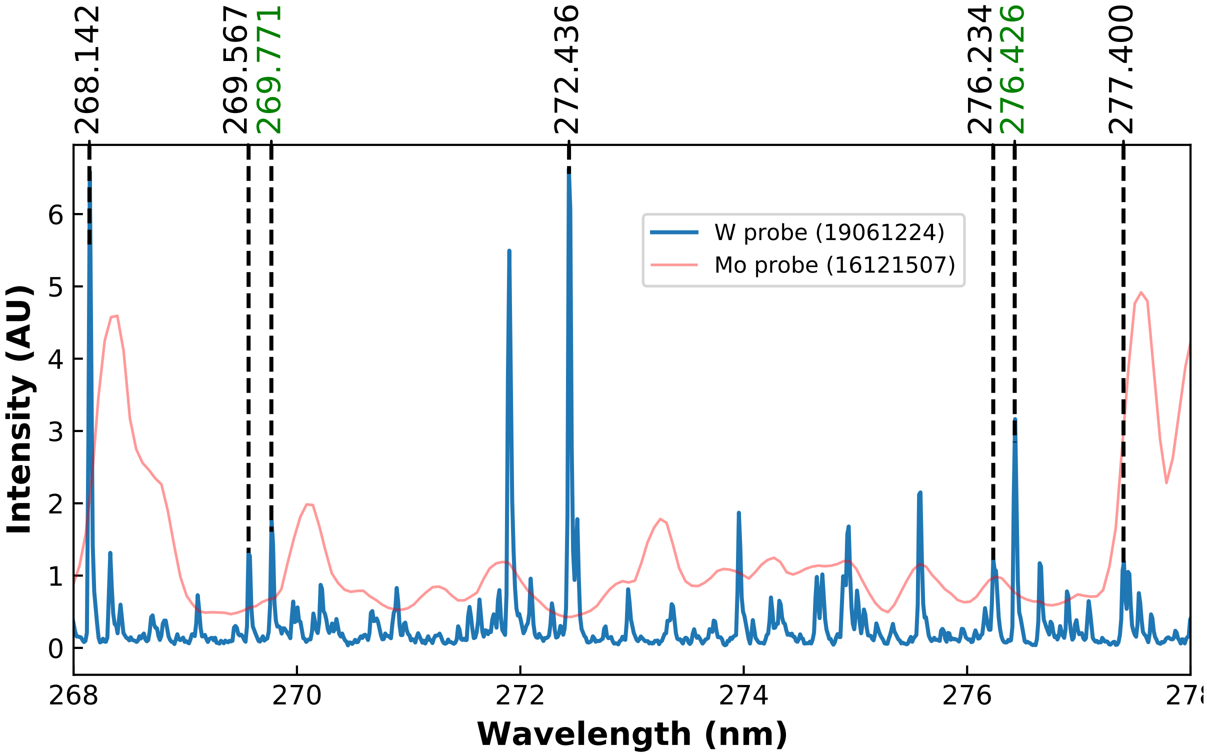

Figure 4.10: CTH spectrum from 268-278 nm, the tungsten probe was located at 21 cm. W I lines are identified by the NIST observed wavelengths in black text and W II lines are identified by the NIST observed wavelengths in green text. The spectrum with the tungsten tipped probe is in blue, and the spectrum with the molybdenum tipped probe is in transparent red.

resolution and throughput of the UV survey spectrometers likely resulted in lower signal to noise ratios that masked any correlated dynamics in the W I emission. It is anticipated that a higher-resolution spectrometer, sensitive to UV wavelengths, would similarly detect a correlation between the W I lines identified in Table 4.1 and ELM strength.

4.2.3 Uncertainties in spectral line identification

As with any experimental measurement, there is some uncertainty associated with the wavelengths observed by the spectrometer. The wavelength uncertainty will depend on several operation variables chosen for the spectrometer such as groove density of the diffraction grating, chosen central wavelength and entrance slit width. Uncertainties shown here were calculated for the 4320 g/mm grating with a central wavelength of 261 nm and a 25 μm slit

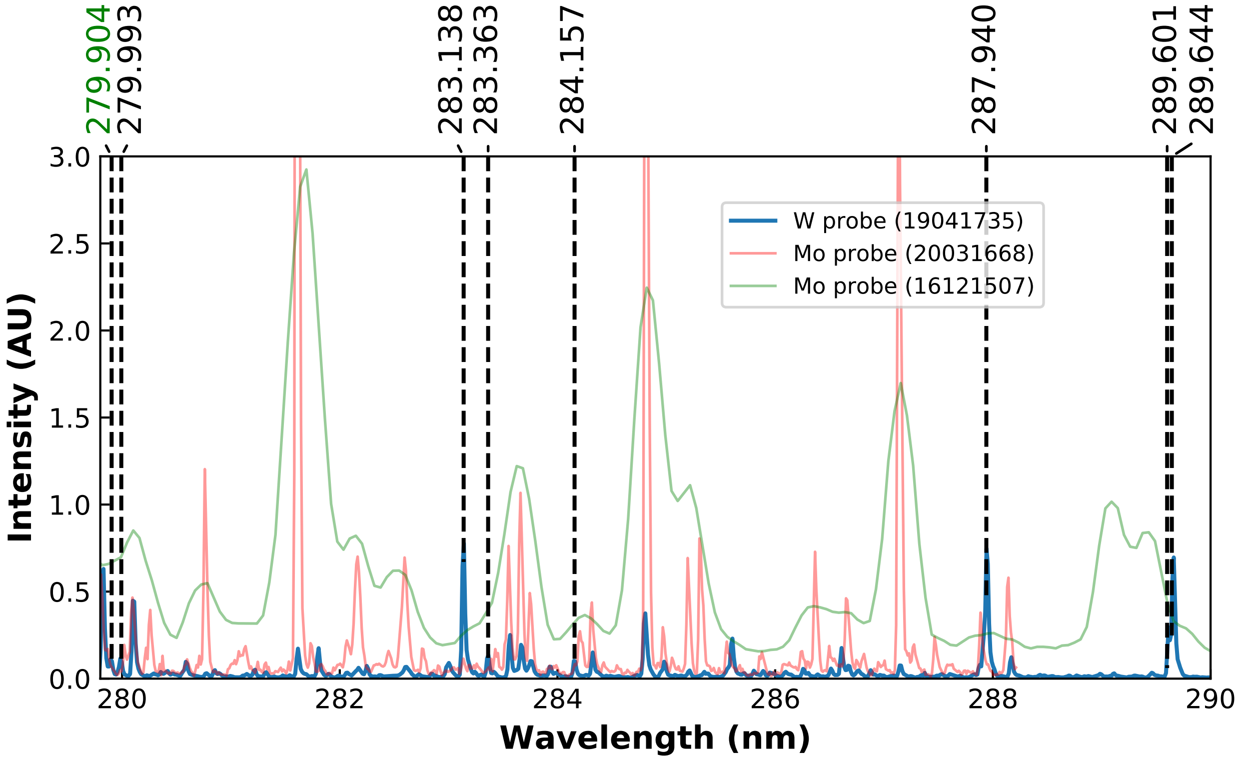

Figure 4.11: CTH spectrum from 280-288 nm, the tungsten probe was located at 21 cm. W I lines are identified by the NIST observed wavelengths in black text and W II lines are identified by the NIST observed wavelengths in green text. The spectrum with the tungsten tipped probe is in blue, and the spectrum with the molybdenum tipped probe is in transparent red.

width. These are the operational parameter of greatest interest in this thesis. The calculated dispersion of the spectrometer is shown in Figure 2.5. Due to various optical aberrations, the measured dispersion can vary up to 0.075 nm compared to calculations for the 4320 g/mm grating used for line identification in this section. Figure C.2 shows the correction required for the Hg I 265 nm feature measured from a calibration source. The largest contribution to the uncertainty in the wavelength from the spectrometer is a lack of spectral lines that can be used to measure the dispersion across the entire CCD detector simultaneously for a given grating position (this could be addressed by use of a tunable laser). The wavelength accuracy of the spectrometer at a central wavelength of 261 nm has been measured to be ∼0.027 nm (about 2 pixels) though the edges of the detector can show larger deviations. The wavelength accuracy can be clearly seen in Figures 4.8 and 4.9.

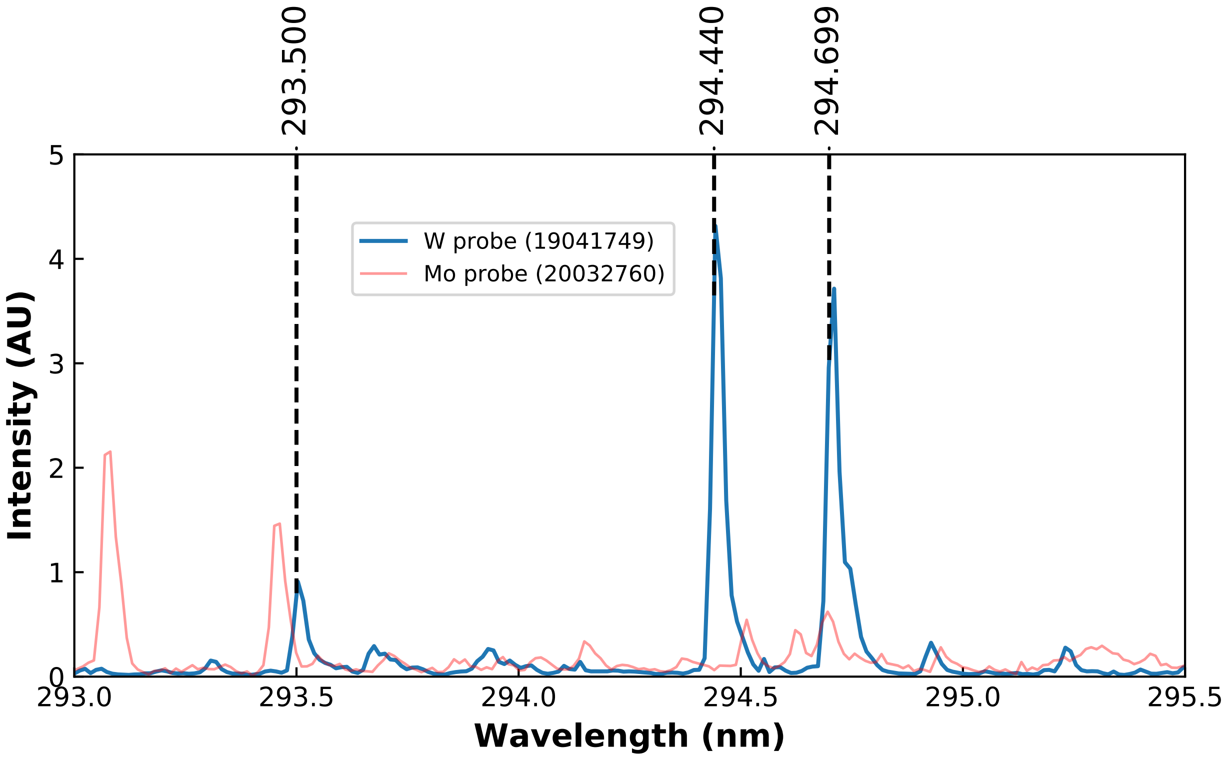

Figure 4.12: CTH spectrum from 293-296 nm, the tungsten probe located at 21 cm. W I lines are identified by the NIST observed wavelengths in black text and W II lines are identified by the NIST observed wavelengths in green text. The spectrum with the tungsten tipped probe is in blue, and the spectrum with the molybdenum tipped probe is in transparent red.

There is also uncertainty that arises due to repeatability of the stepper motor that rotates the diffraction grating. However, this uncertainty is relatively small on the order of a few picometers.

4.3 Molybdenum as a PFC and line identification in CTH

Molybdenum is another high-Z element that is being considered as a first wall material for fusion experiments. There have been multiple experiments conducted using Mo PFC in fusion relevant machines,[73] making near neutral Mo spectral lines of great interest for the same reasons as tungsten. Near neutral Mo systems have many of the same complexities required for accurate CR modeling that neutral tungsten does.

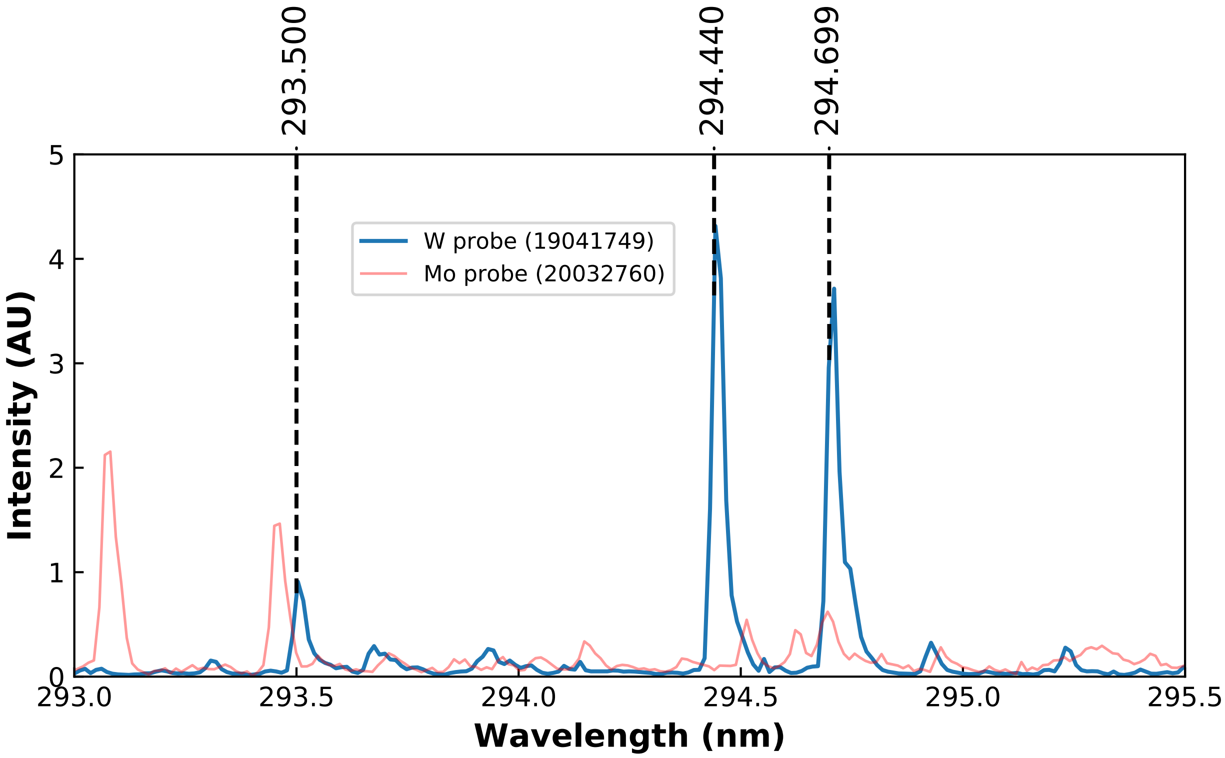

Figure 4.13: CTH spectrum from 301-304 nm, the tungsten probe located at 21 cm. W I lines are identified by the NIST observed wavelengths in black text and W II lines are identified by the NIST observed wavelengths in green text. The spectrum with the tungsten tipped probe is in blue, and the spectrum with the molybdenum tipped probe is in transparent red.

Molybdenum was used as a first wall material in Alcator C-Mod described by May *et al.*[74] NSTX-U is planning to transition from graphite PFC to a full high-Z PFC with Mo being the leading candidate as stated in the five year plan.[75] The DIII-D metal rings campaign utilized a titanium-zirconium-molybdenum (TMZ) substrate with a tungsten coating.[15]

No dedicated Mo experiments were run in DIII-D, so the only Mo data in this work is from CTH experiments. Similar to the tungsten probe scan, a molybdenum probe scan was preformed in CTH. The Mo scan allowed for multiple new Mo I and Mo II lines to be identified that could possibly be used for fusion relevant machines with Mo PFCs.

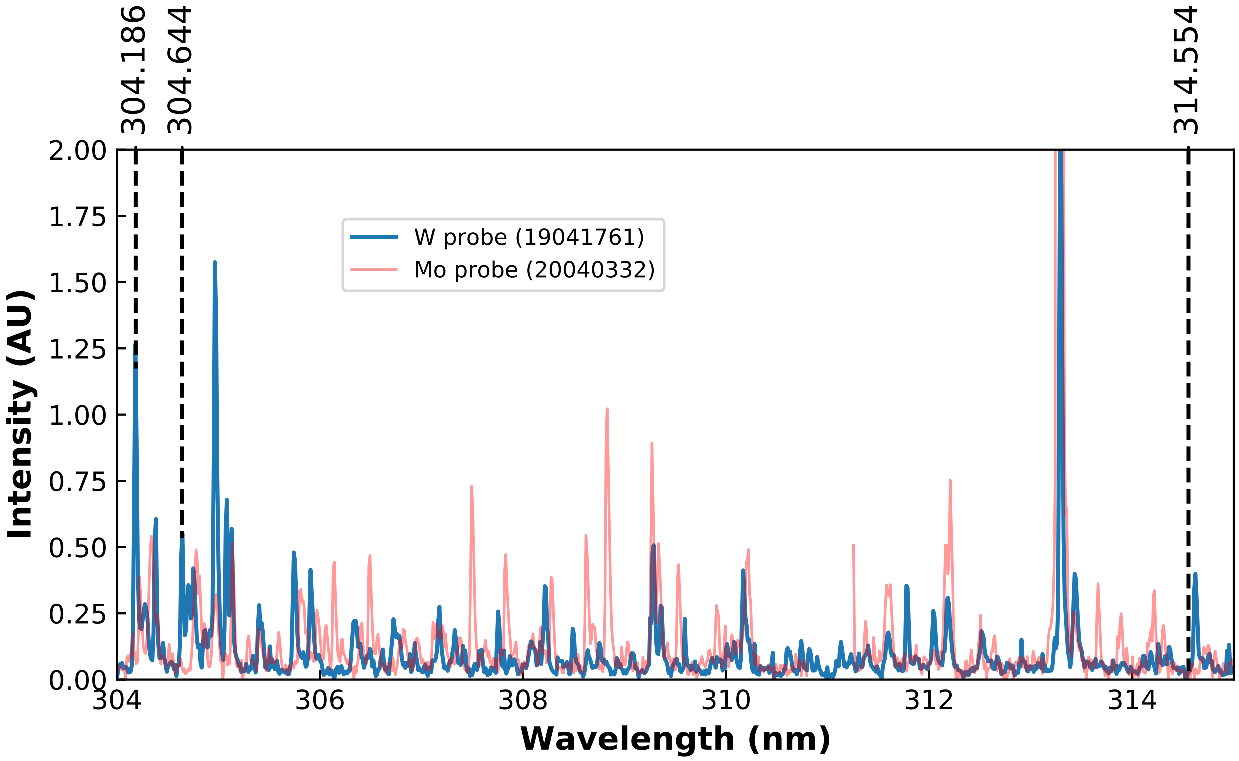

Figure 4.14: CTH spectrum from 304-314 nm, the tungsten probe located at 21 cm. W I lines are identified by the NIST observed wavelengths in black text and W II lines are identified by the NIST observed wavelengths in green text. The spectrum with the tungsten tipped probe is in blue, and the spectrum with the molybdenum tipped probe is in transparent red.

4.3.1 Neutral molybdenum atomic data and theoretical methods

Neutral molybdenum has had little atomic modeling to date with previous modeling done by Badnell *et al.*[76] in 1996 which used a relatively small calculation due to the relatively limited computing power when compared to modern supercomputers. In this work, excitation rates come from a new non-preturbative Dirac R-matrix electron impact calculation preformed by Smyth *et al.*[77] Electron-impact ionization rates used for the analysis were calculated using the ECIP method with ColRadPy using the energy levels from Smyth *et al.*. The accuracy of the diagnostic is directly related to the accuracy of the atomic data. Recombination of Mo II has not been included in the model as it is expected to be insignificant compared to electron-impact excitation/de-excitation and ionization at fusion relevant

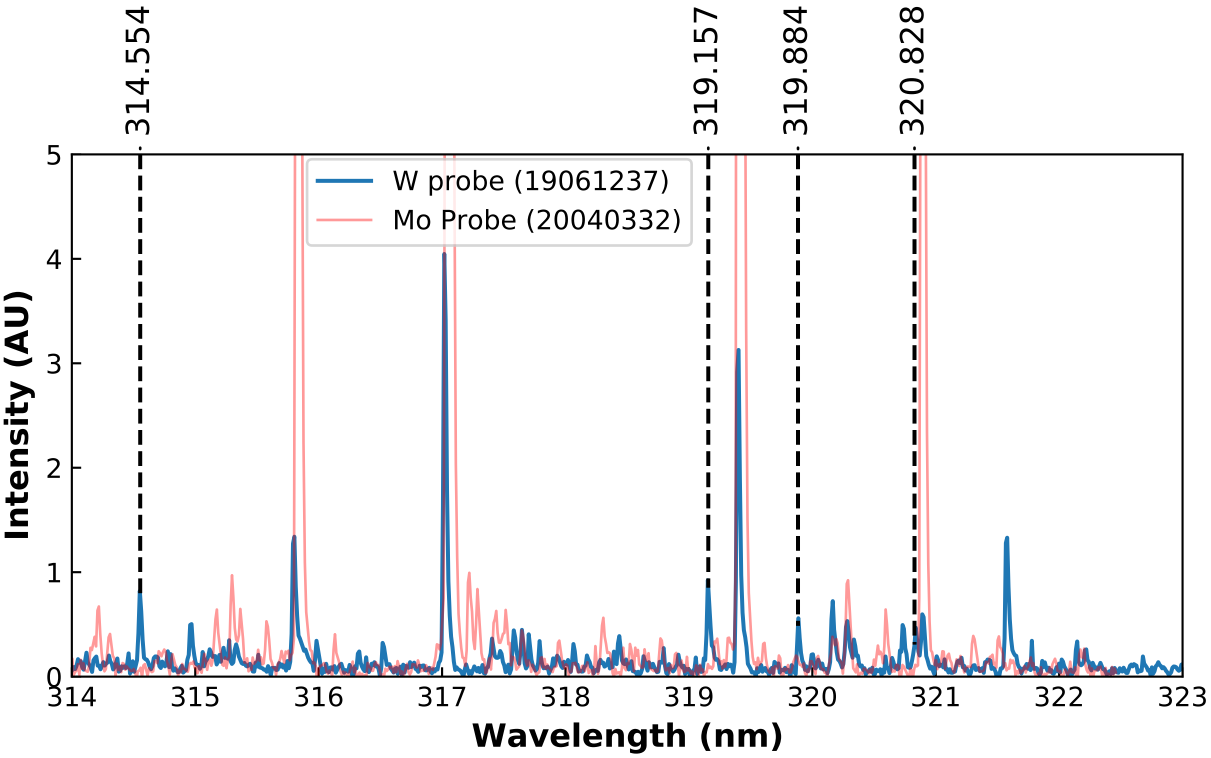

Figure 4.15: CTH spectrum from 314-323 nm, the tungsten probe located at 21 cm. W I lines are identified by the NIST observed wavelengths in black text and W II lines are identified by the NIST observed wavelengths in green text. The spectrum with the tungsten tipped probe is in blue, and the spectrum with the molybdenum tipped probe is in transparent red.

plasma conditions. Collisional radiative modeling using this dataset was carried out as an example in Section 3.6.2 to show the behavior of high-Z materials.

4.3.2 Singly ionized molybdenum atomic data and theoretical methods

Table 4.5: Table of Mo I emission lines from 200-400 nm observed during CTH experiments along with level identifications where possible. The lines identified in this table are shown with a comparison to a Mo spectrum in increasing wavelength in Figures 4.21 - 4.27

NIST wavelength (nm)	Upper level	Lower level
264.098	$4d^45s5p$ ($^5P_2$)	$4d^45s^2$ ($^5D_3$)
315.817	$4p^64d^45s5p$ ($^7D_3$)	$4p^64d^55s^1$ ($^7S_3$)
317.034	$4p^64d^45s5p$ ($^7P_3$)	$4p^64d^55s^1$ ($^7S_3$)
319.400	$4p^64d^45s5p$ ($^7P_2$)	$4p^64d^55s^1$ ($^7S_3$)
320.884	$4p^64d^45s5p$ ($^7D_2$)	$4p^64d^55s^1$ ($^7S_3$)
328.900	$4p^64d^45p^2$ ($^7D_4$)	$4p^64d^45s5p$ ($^7P_4$)
329.082	$4p^64d^45s5p$ ($^1D_2$)	$4p^64d^45s^2$ ($^3D_1$)
334.473	$4p^64d^55p^1$ ($^3S_1$)	$4p^64d^55s^1$ ($^5F_2$)

Table 4.6: Table of Mo II emission lines from 200-400 nm observed during CTH experiments along with level identifications where possible. The lines identified in this table are shown with a comparison to a Mo spectrum in increasing wavelength in Figures 4.21 - 4.27

NIST wavelength (nm)	Upper level	Lower level
263.667	$4d^45p$ ($^6D_0$)	$4d^45s$ ($^6D_1$)
263.876	$4d^45p$ ($^6D_3$)	$4d^45s$ ($^6D_2$)
264.435	$4d^45p$ ($^6D_4$)	$4d^45s$ ($^6D_3$)
266.058	$4d^45p$ ($^6D_2$)	$4d^45s$ ($^6D_1$)
267.284	$4d^45p$ ($^6D_3$)	$4d^45s$ ($^6D_3$)
267.327	$4d^45p$ ($^4F_4$)	$4d^5$ ($^4G_5$)
277.540	$4d^45p$ ($^6P_3$)	$4d^45s$ ($^6D_4$)
278.004	$4d^45p$ ($^6P_2$)	$4d^45s$ ($^6D_3$)
278.499	$4d^45p$ ($^4F_4$)	$4d^5$ ($^4D_3$)
280.776	$4d^45p$ ($^4P_1$)	$4d^45s$ ($^6D_2$)
281.615	$4d^45p$ ($^6F_5$)	$4d^45s$ ($^6D_4$)
284.823	$4d^45p$ ($^6F_4$)	$4d^45s$ ($^6D_3$)
285.323	$4d^45p$ ($^4I_7$)	$4d^45s$ ($^4H_6$)
286.669	$4d^45p$ ($^4F_3$)	$4d^5$ ($^4D_2$)
287.151	$4d^45p$ ($^6F_3$)	$4d^45s$ ($^6D_2$)
287.288	$4d^45p$ ($^4P_2$)	$4d^45s$ ($^4P_1$)
292.339	$4d^45p$ ($^6F_2$)	$4d^45s$ ($^6D_2$)
292.432	$4d^45p$ ($^4I_4$)	$4d^45s$ ($^4H_3$)
293.006	$4d^45p$ ($^4D_1$)	$4d^45s$ ($^4F_1$)
293.050	$4d^45p$ ($^6F_1$)	$4d^45s$ ($^6D_1$)
293.430	$4d^45p$ ($^6F_0$)	$4d^45s$ ($^6D_0$)
307.766	$4d^45p$ ($^2J_6$)	$4d^45s$ ($^2I_5$)
308.762	$4d^45p$ ($^4H_6$)	$4d^45s$ ($^4H_6$)
315.282	$4d^45p$ ($^4H_4$)	$4d^45s$ ($^4H_4$)
317.203	$4d^45p$ ($^2F_2$)	$4d^5$ ($^2D_2$)
317.274	$4d^45p$ ($^4P_0$)	$4d^5$ ($^4P_1$)
329.231	$4d^45p$ ($^4D_3$)	$4d^45s$ ($^4D_3$)
332.090	$4d^45p$ ($^4G_2$)	$4d^5$ ($^2S_0$)
332.937	$4d^45p$ ($^4D_1$)	$4d^45s$ ($^4D_1$)

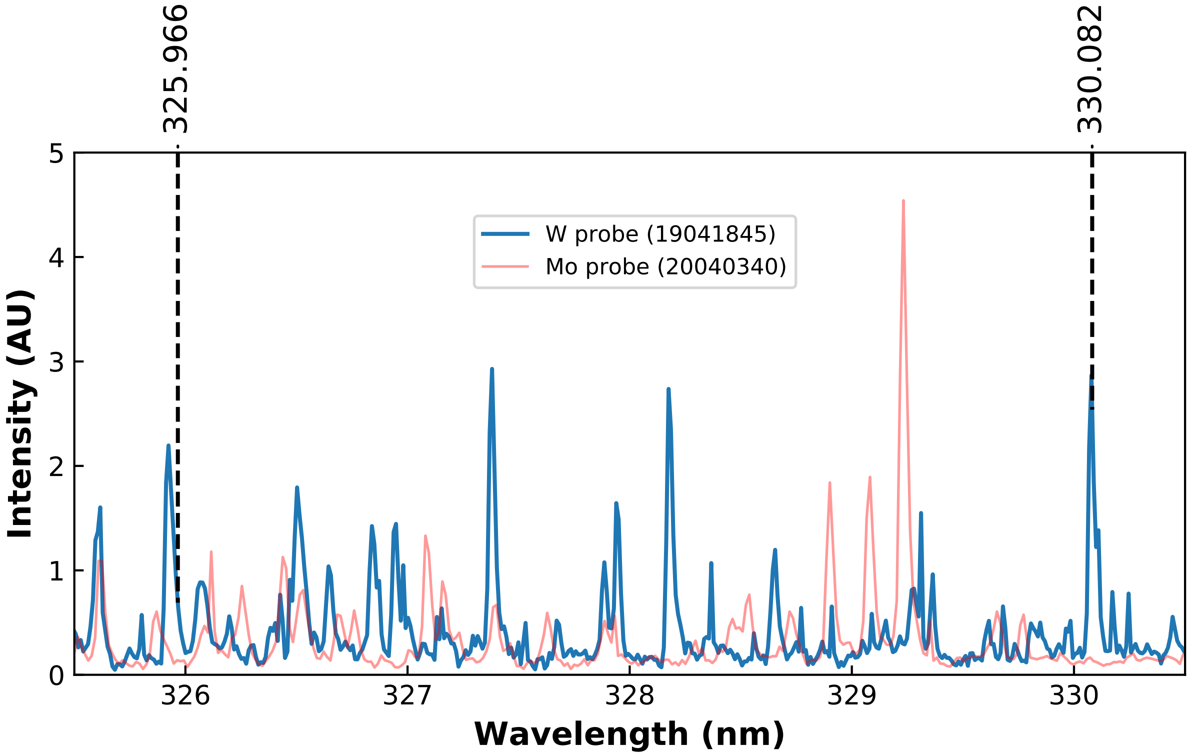

Figure 4.16: CTH spectrum from 326-334 nm, the tungsten probe located at 21 cm. W I lines are identified by the NIST observed wavelengths in black text and W II lines are identified by the NIST observed wavelengths in green text. The spectrum with the tungsten tipped probe is in blue, and the spectrum with the molybdenum tipped probe is in transparent red.

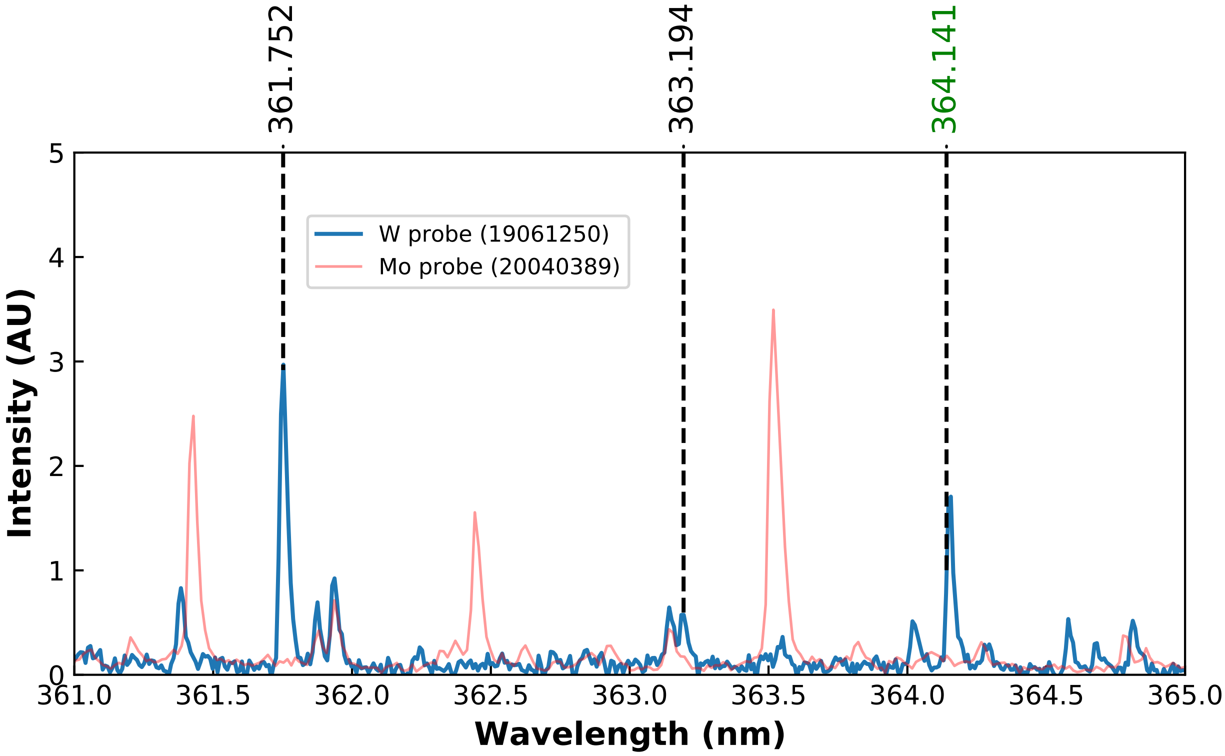

Figure 4.17: CTH spectrum from 361-365 nm, the tungsten probe located at 21 cm. W I lines are identified by the NIST observed wavelengths in black text and W II lines are identified by the NIST observed wavelengths in green text. The spectrum with the tungsten tipped probe is in blue, and the spectrum with the molybdenum tipped probe is in transparent red.

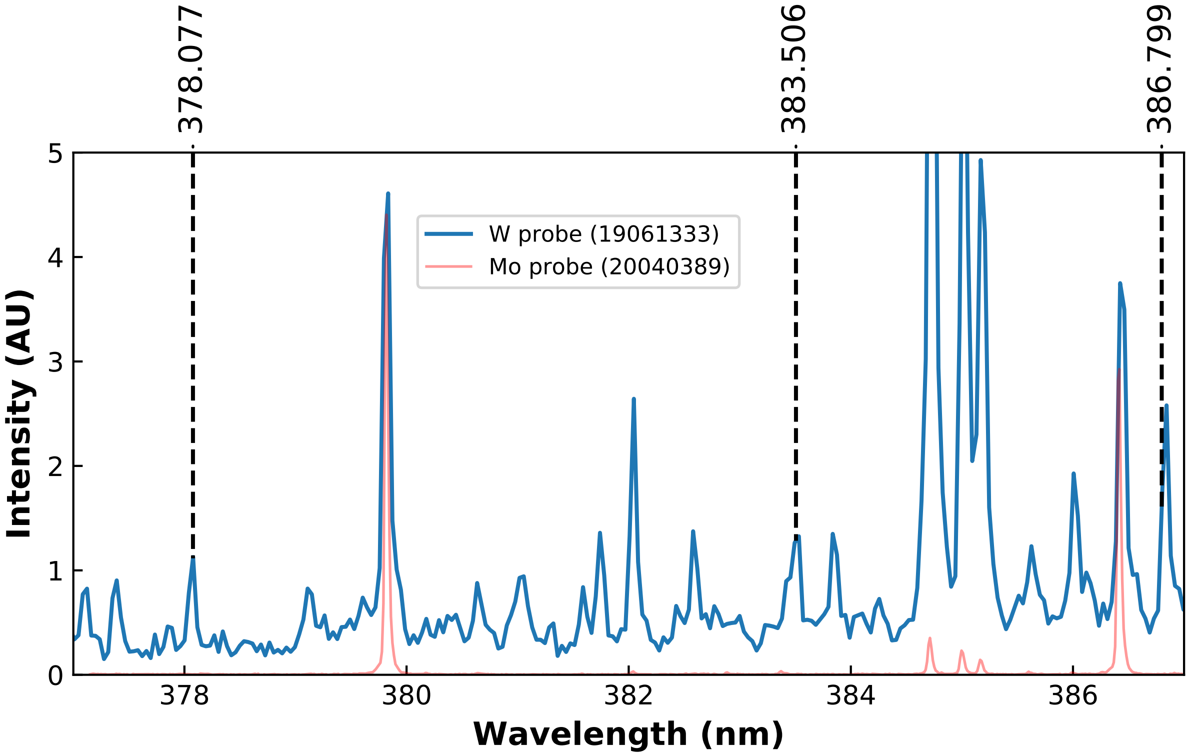

Figure 4.18: CTH spectrum from 377-387 nm, the tungsten probe located at 21 cm. W I lines are identified by the NIST observed wavelengths in black text and W II lines are identified by the NIST observed wavelengths in green text. The spectrum with the tungsten tipped probe is in blue, and the spectrum with the molybdenum tipped probe is in transparent red.

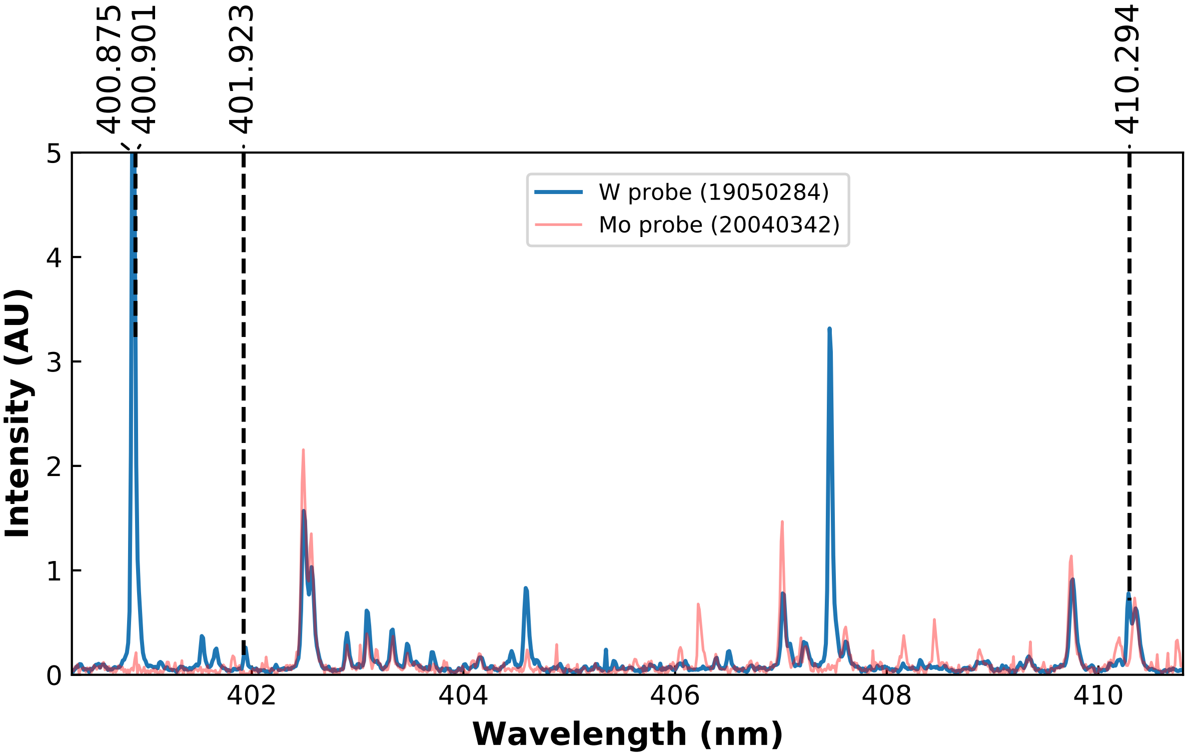

Figure 4.19: CTH spectrum from 400-411 nm, the tungsten probe located at 21 cm. W I lines are identified by the NIST observed wavelengths in black text and W II lines are identified by the NIST observed wavelengths in green text. The spectrum with the tungsten tipped probe is in blue, and the spectrum with the molybdenum tipped probe is in transparent red.

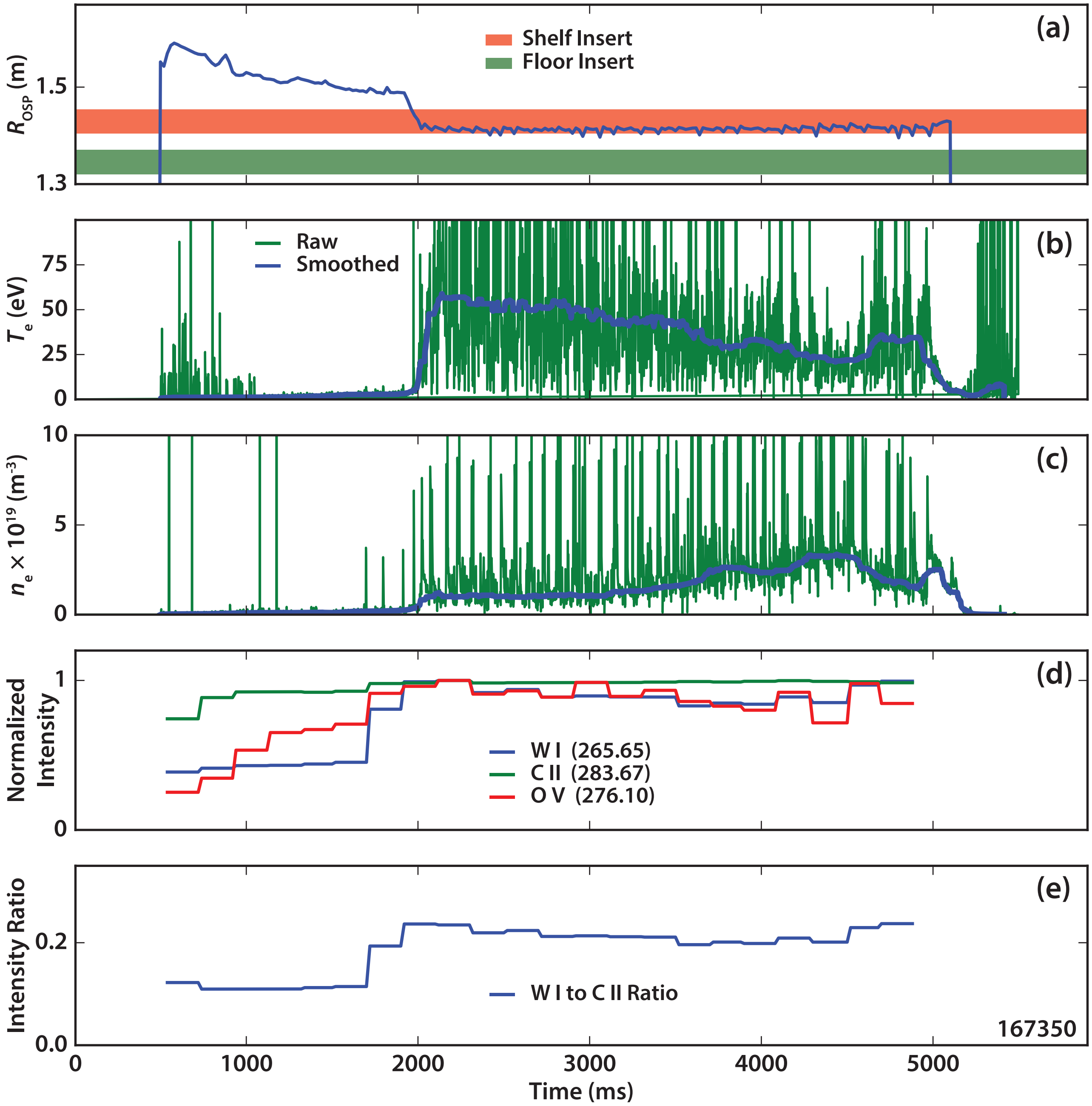

Figure 4.20: Time evolution of DIII-D shot 167350: (a) Radial position of the outer strike point (R_{OSP}) with the locations of the floor and shelf W inserts shown in green and red respectively, (b) and (c) raw (green) and ELM-free smoothed (blue) electron temperature and density on the W surface measured by a Langmuir probe, (d) W I, C II, and O V line intensities normalized to their maximum intensity during the discharge, (e) ratio of W I to C II line intensities.

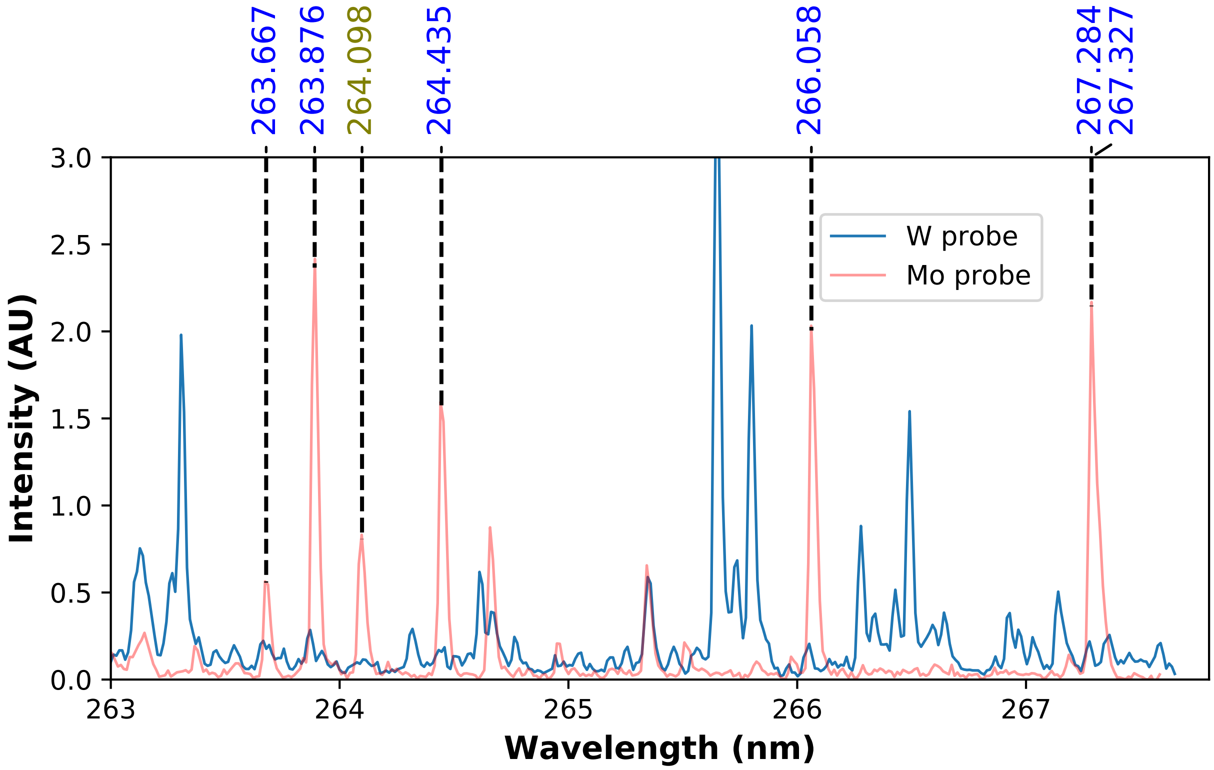

Figure 4.21: CTH spectrum from 263-268 nm, the molybdenum probe was located at 21 cm from the CTH midplane from the midplane of CTH. Mo I lines are identified by the NIST observed wavelengths in olive text and Mo II are in blue text. Spectrum with the molybdenum tipped probe is in transparent red and spectrum from tungsten tipped probe is in light blue.

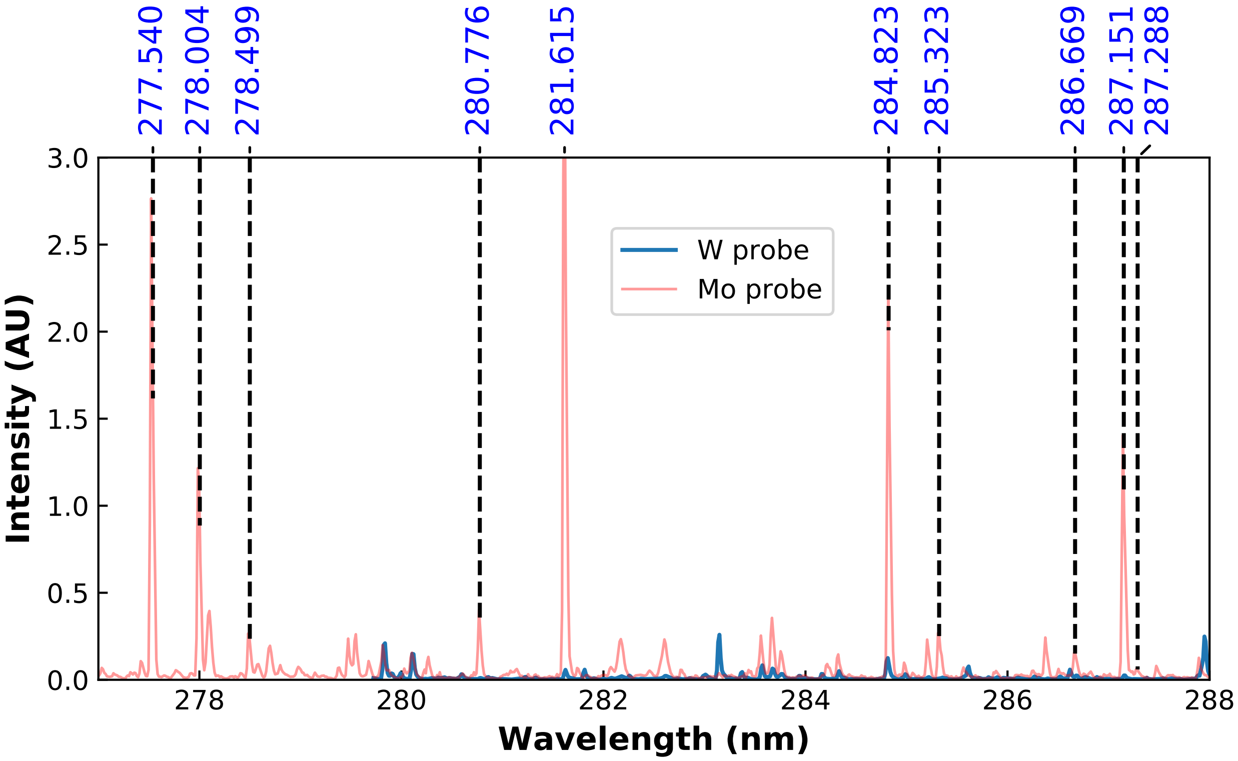

Figure 4.22: CTH spectrum from 277-288 nm, the molybdenum probe was located at 21 cm from the CTH midplane from the midplane of CTH. Mo II lines are identified by the NIST observed wavelengths in blue text. Spectrum with the molybdenum tipped probe is in transparent red and spectrum from tungsten tipped probe is in light blue.

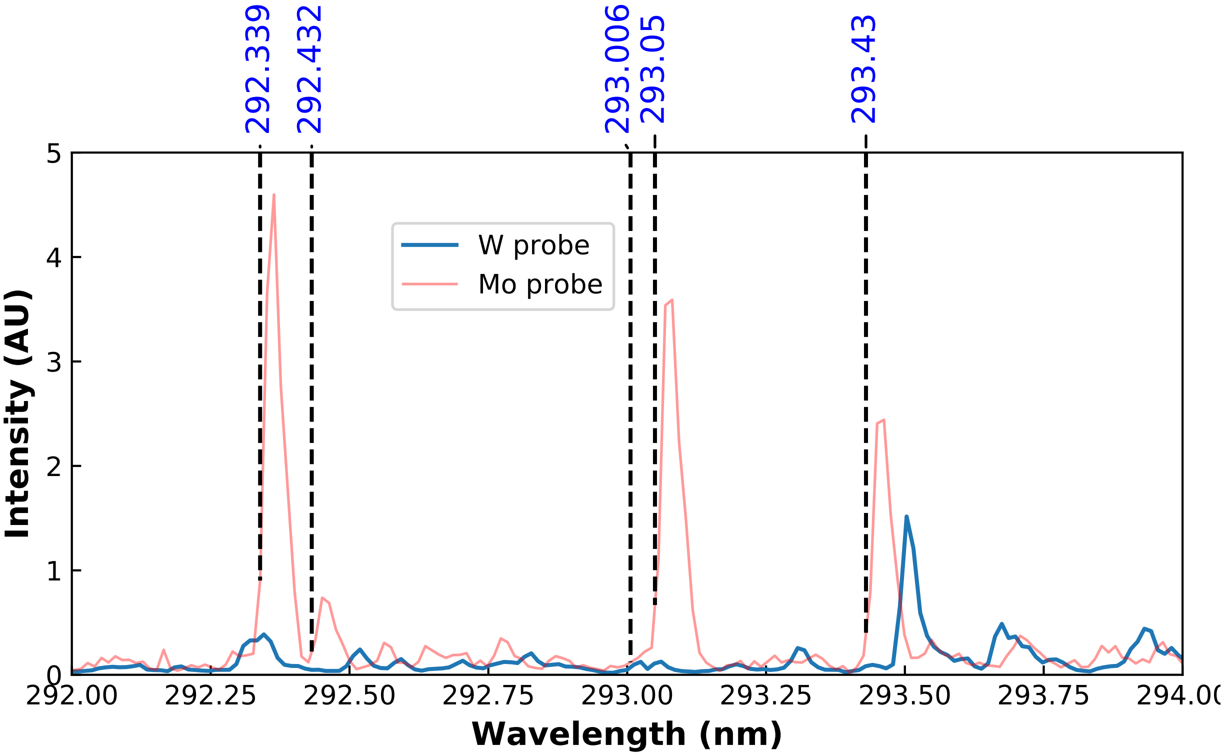

Figure 4.23: CTH spectrum from 292-294 nm, the molybdenum probe was located at 21 cm from the CTH midplane from the midplane of CTH. Mo II lines are identified by the NIST observed wavelengths in blue text. Spectrum with the molybdenum tipped probe is in transparent red and spectrum from tungsten tipped probe is in light blue.

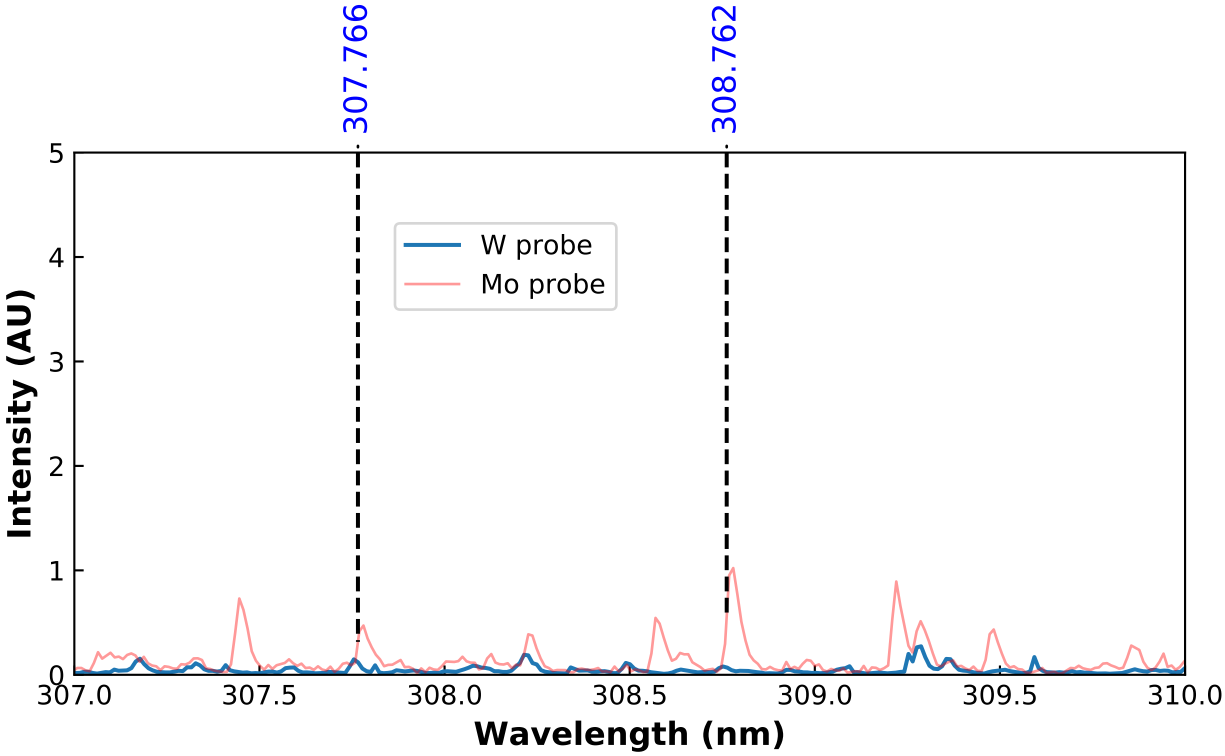

Figure 4.24: CTH spectrum from 307-310 nm, the molybdenum probe was located at 21 cm from the CTH midplane from the midplane of CTH. Mo II lines are identified by the NIST observed wavelengths in blue text. Spectrum with the molybdenum tipped probe is in transparent red and spectrum from tungsten tipped probe is in light blue.

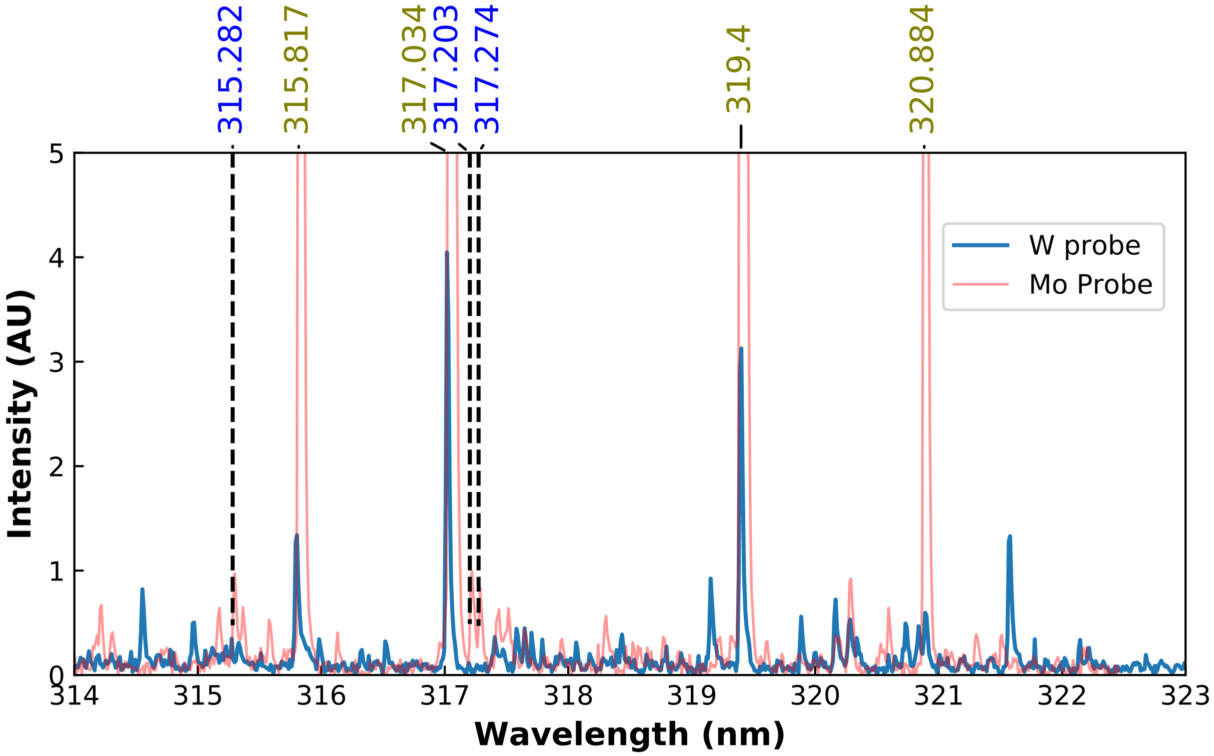

Figure 4.25: CTH spectrum from 314-323 nm, the molybdenum probe was located at 21 cm from the CTH midplane from the midplane of CTH. Mo I lines are identified by the NIST observed wavelengths in olive text and Mo II are in blue text. Spectrum with the molybdenum tipped probe is in transparent red and spectrum from tungsten tipped probe is in light blue.

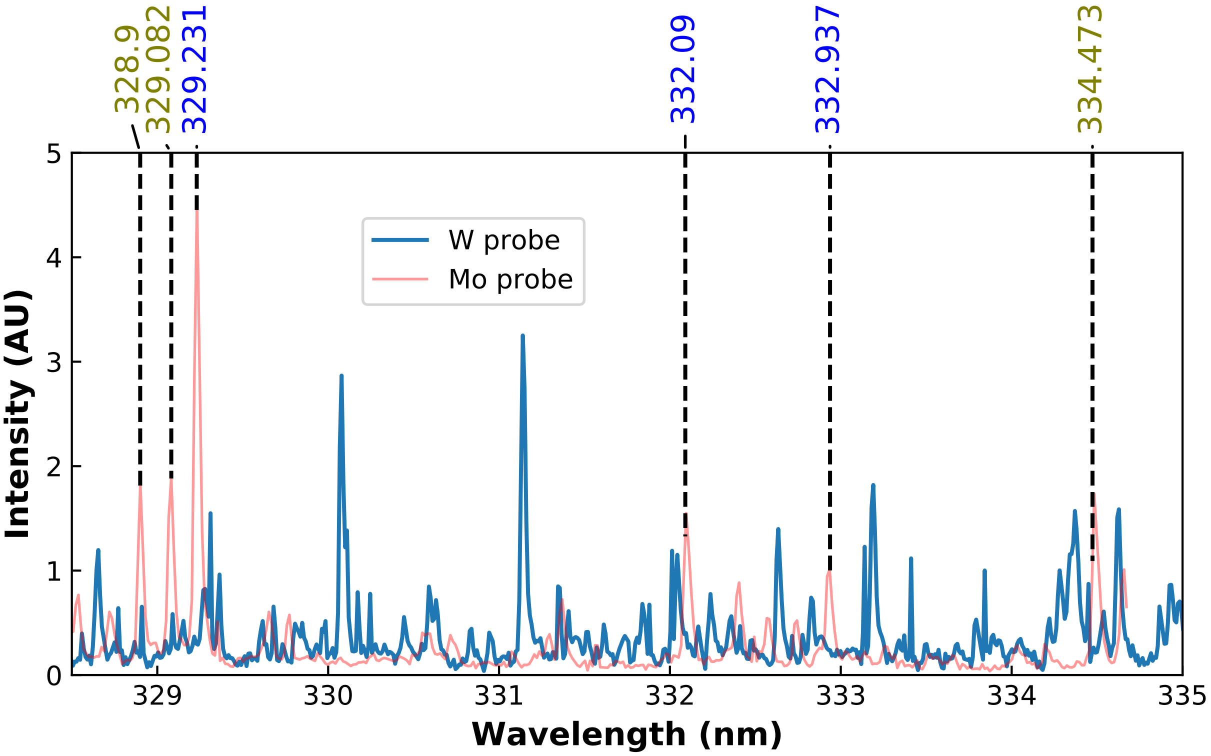

Figure 4.26: CTH spectrum from 329-335 nm, the molybdenum probe was located at 21 cm from the CTH midplane from the midplane of CTH. Mo I lines are identified by the NIST observed wavelengths in olive text and Mo II are in blue text. Spectrum with the molybdenum tipped probe is in transparent red and spectrum from tungsten tipped probe is in light blue.

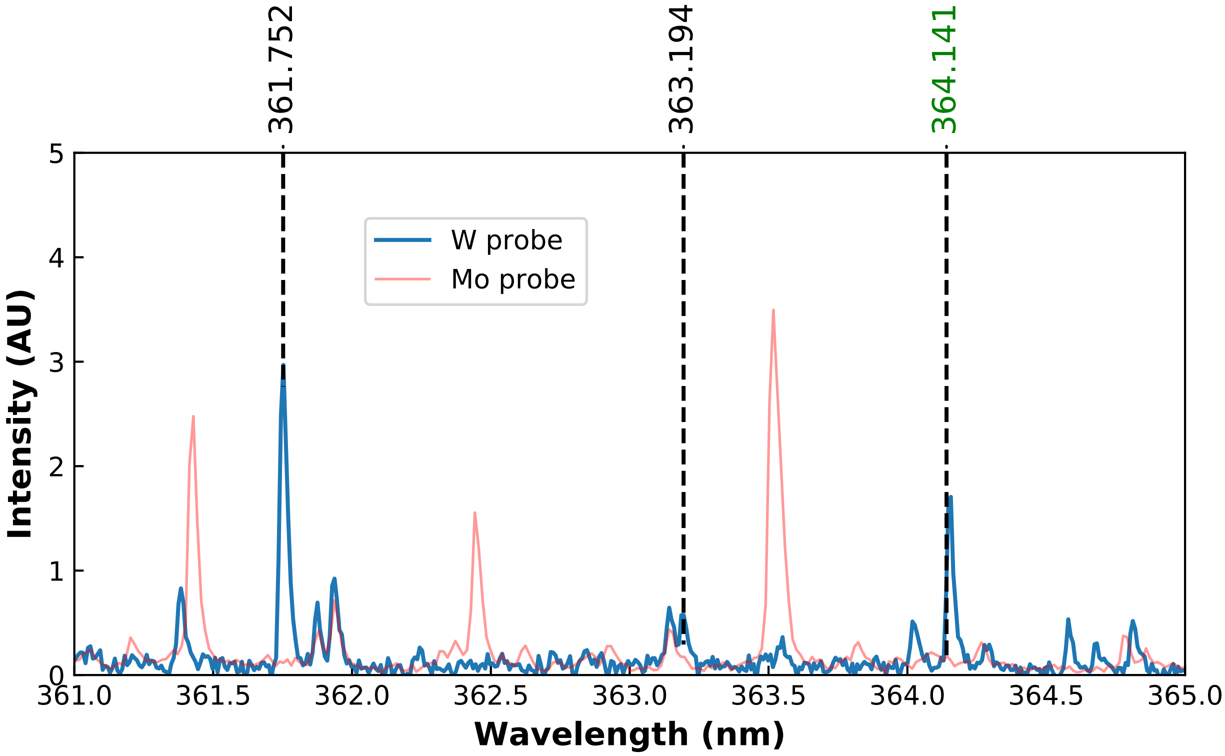

Figure 4.27: CTH spectrum from 361-365 nm, the molybdenum probe was located at 21 cm from the CTH midplane from the midplane of CTH. Mo I lines are identified by the NIST observed wavelengths in olive text and Mo II are in blue text. Spectrum with the molybdenum tipped probe is in transparent red and spectrum from tungsten tipped probe is in light blue.

Chapter 5

Collisional radiative modeling and comparison to experimental W I observations

Three main topics will be discussed in this chapter. First, an in-depth look at collisional radiative modeling for neutral tungsten will be presented. Next, the collisional radiative modeling will be extended to include a plasma sheath model. Finally, the collisional radiative sheath model will be compared to experimental data from CTH.

Accurate atomic data, combined with Collisional Radiative (CR) modeling, is necessary to produce S/XB values for use in erosion measurements. Low-Z materials were previously favored in fusion relevant experiments, and thus, there is a mature body of work describing erosion and impurity transport.[78,2,79] In atomic systems, metastable levels are important for spectral modeling and impurity transport. Metastable levels are long-lived states that can hold a significant population of electrons when compared to the total population of a charge state. In low-Z systems, metastable states must often be tracked time dependently to obtain accurate emission and transport results.[40,80,81] The atomic structure of high-Z materials leads to many more potential metastable states than are possible in low-Z atomic systems as more atomic energy levels are possible from the ground configuration in high-Z elements. As a result, there are a significant number of levels that cannot decay via an electric dipole radiative transition to the lower levels.[82,52,67] In addition, modeling of molybdenum has shown a significant dependence of the excited populations on metastable states.[46,63] There are indications that metastable levels also could play an important role in tungsten CR modeling.[25,5]

Experimental measurements of neutral tungsten S/XBs have been completed in both low temperature and density linear machines[83] and fusion relevant toroidal devices.[68,84] Comparisons of these measurements with theoretical S/XBs have assumed that the atomic levels of neutral tungsten metastable levels have reached their equilibrium (steady-state) values. However, this thesis will present evidence that neutral tungsten populations for these systems are likely not in steady-state and require a line-integrated S/XB that accounts for the metastable dependence, as opposed to the steady-state S/XB values that have been previously used for erosion measurements.

The first detailed modeling of metastable states in neutral tungsten will be presented in Section 5.2 in order to address two open questions: First, how many metastable levels in neutral tungsten are required to model W I spectral line intensities, S/XB coefficients and tungsten erosion? Second, what are the time scales for the metastable states to reach equilibrium conditions in their plasma environment and what are the implications to transport studies (Section 5.2.6)?

5.1 Tungsten atomic data and theoretical methods

The various sources of atomic data for the neutral tungsten collisional radiative modeling in this thesis are discussed in Section 5.1.1. A brief summary of the actual collisional radiative model is presented in Section 5.1.2.

5.1.1 Discussion of neutral tungsten atomic data

Erosion measurements performed with the S/XB method require atomic transition rates such as electron-impact excitation/de-excitation and ionization to be calculated. The accuracy of the diagnostic is directly related to the accuracy of the atomic data. Until recently there have been two main datasets widely used for CR modeling of neutral tungsten. Both data sets employed perturbative atomic calculations, which are not always appropriate for near neutral systems, but provided an initial attempt at S/XB coefficients, which in turn enabled erosion diagnostic studies to be performed. In the first data set, created by Beigman *et al.*,[5] excitation was calculated from the semi-empirical van Regemorter formulas and ionization was calculated using the Born-Ochkur ionization cross-section calculated with the

ATOM[85] code. The second data set used by Brezinsek *et al.*[86] was generated by Martin O'Mullane as part of the ADAS project from plane-wave Born electron-impact excitation data calculated with wave functions from the large atomic structure calculation of Quinet *et al.*[82] In this second data set, ionization was calculated using the Exchange Classical Impact Parameter (ECIP)[40] method using ADAS[43] from the level energies from Quinet *et al.*[82]

In this work, excitation rates come from a new, non-perturbative Dirac *R*-matrix electron-impact calculation performed by Smyth *et al.*,[52] representing the only non-perturbative excitation/de-excitation calculation for W I. Key to this study are the new spin-changing collisional rate coefficients between potential metastable levels, including the $5d^4 6s^2$ ($^5D_0$) ground term and $5d^5 6s$ ($^7S_3$) metastable level, which allow the dynamics of metastable levels to be explored. Ionization used for the analysis was calculated using the ECIP method with ColRadPy[46] from the level energies of Smyth *et al.*[52] Recombination of W II[87] has not been included in the model as it is insignificant when compared to electron-impact excitation/de-excitation and ionization for net erosion regimes in the divertor.

5.1.2 Collisional radiative modeling of W I

Collisional radiative modeling for this study was performed with the open source Python CR solver ColRadPy,[46] which has been benchmarked against the widely used ADAS codes[40] and found to be in close agreement. ColRadPy provides additional functionality[46] including the determination of the relative populating mechanisms (see Section 5.2.2) and a fully time-dependent solution of the CR equations (see Section 5.3). A complete description of the collisional radiative theory can be found in Summers *et al.*[40] The two quantities utilized most frequently in this work include the emission line intensities and S/XB ratios. Equation (3.26) relates the spectral line intensity for transition $j \rightarrow i$, to the summation of the individual Photon Emissivity Coefficient (PEC) multiplied by the metastable population and integrated over the line of sight. Note that the definition of the PEC is given in Summers *et al.*[40] and Johnson *et al.*[25]

The generalized CR approach allows for calculation of the fractional population of N_σ compared to the total neutral tungsten population. Thus, it is convenient to consider the relative contribution to intensity from a particular driving metastable state (see Equation 3.27). Two cases are considered, when contributions to the line intensity $N_\sigma/N_{\mathrm{tot}}$ is in steady-state and when it is not.

The metastable resolved S/XB coefficient is given in Equation 3.32 and represents the ratio of the metastable resolved effective ionization coefficient (SCD) to the metastable resolved PEC. While it is not very common to use non-equilibrium metastables in S/XB diagnostics, they have been considered before (for example, Behringer *et al.*[81] used them for oxygen).

As discussed in the upcoming sections, metastable state populations become important in modeling when steady-state atomic population conditions for given plasma parameters have not been reached. The relative intensity of spectral lines can vary in time as N_σ in Equation 3.27 can change drastically because of non-steady-state values. When the metastable levels are in steady-state, all populations are determined solely by the local electron temperature and density. While metastable levels may not be in steady-state, it is normal to assume that excited state populations are in equilibrium with the time changing ground and metastable levels; this is known as the quasistatic approximation.[40]

Figure 5.1 presents a W I spectrum of PEC values for typical divertor plasma conditions produced from the new W I dataset described in Section 5.1.1.[52] The W I spectrum is generated for steady-state metastable conditions and highlights wavelength regions of high spectral emission density. The high density of W I lines in the ultraviolet (UV), relative to other wavelength regions, makes the UV a region of interest for both erosion and metastable diagnostics. The insert in Figure 5.1 highlights a wavelength region encompassing a selection of intense W I spectral lines that will be considered in Section 5.2.1. Many lines in the UV region have been experimentally observed by Johnson *et al.*[25]

Erosion diagnostic lines are generally chosen from the most intense spectral lines to minimize experimental error. Erosion measurements to date have primarily used the 400.88 nm line, 5d^{4}6s6p (^{7}P$_4$) → 5d^5(^{6}S)6s (^{7}S$_3$). Visible spectral lines are generally preferred experimentally as UV transmission in fiber optic cables and quantum efficiencies of UV detectors are lower than those at visible wavelengths. As will be shown, the 400.88 nm spectral line is highly dependent on the 5d^5(^{6}S)6s (^{7}S$_3$) metastable state; however, the implications of this have not been previously explored. Erosion measurements based solely on the 400.88 nm line could thus be susceptible to error if the metastable states are not in equilibrium.

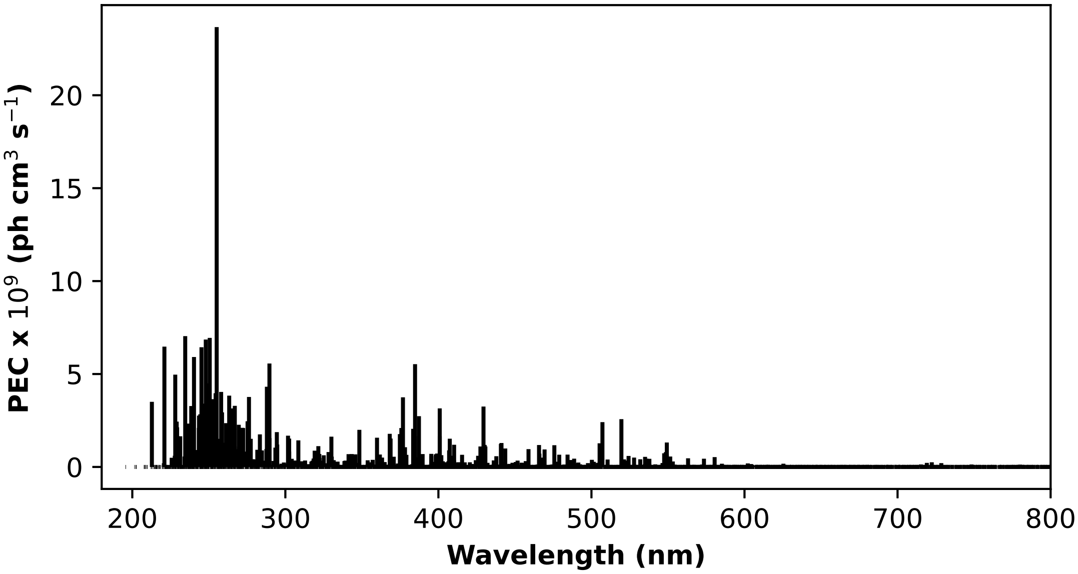

Figure 5.1: PEC theoretical spectrum of W I generated by collisional radiative modeling with $T_e = 30$ eV, $n_e = 5 \times 10^{13}$ cm^{-3}.

5.2 Results from neutral tungsten collisional radiative modeling

Section 5.2 will outline the impact of metastable levels on W I spectral modeling as well as presenting a broader discussion of metastable levels for neutral tungsten.

5.2.1 PEC and SCD metastable dependence

Both the metastable and temperature dependence of intense spectral lines in the UV region are highlighted in Figure 5.2. Most experimentally observed lines in the W I spectrum[25] decay to and have populations that are driven by one of the six lowest levels. The choice of six metastable states in this section was guided by experimental measurements. However, as will be discussed in Section 5.2.5, many more levels have metastable characteristics. The spectral lines in Figure 5.2 were selected as they are close in wavelength, which allows simultaneous observation with a high-resolution spectrometer. Additionally, the 400.88 nm line is investigated because of its importance for previous experimental measurements as discussed in Section 5.3.2. The 400.88 nm line is mainly dependent on the $^6S_3$ metastable level seen in Figure 5.3 (c). The 498.25 nm W I line is also investigated because the line is dependent on the $^5D_0$ ground similar to the W I 255.14 nm line (though not as strong) which can be seen in Figure 5.3 (d). The importance of observing multiple spectral lines simultaneously to diagnosing metastable fractions will be discussed in Section 5.2.4. The most intense W I lines follow the same trend as the spectral lines shown in Figures 5.2 and 5.3.

The steady-state temperature dependent PEC summed over the individual metastable contributions is indicated by the black dashed line (i.e. the integrand in Equation 3.27 over all metastable states). The PEC dependence on individual metastable levels is represented by the different solid color lines, which are weighted by the steady-state metastable fraction. The total of the individual contributions from the six lowest metastable levels sum to the total steady-state PEC, giving an indication of which metastable levels are important for a spectral line. Spectral lines such as those in Figures 5.2 and 5.3 mainly depend on a single metastable level with a close to linear dependence on one single metastable state. The relative intensities of spectral lines driven from different metastable levels are then sensitive to the relative metastable fraction, which presents a significant challenge to erosion measurements if the relative metastable fraction is not known (as would be the case when the metastable populations are not at their steady-state values). Metastable states may not be in equilibrium when sputtered from a wall or when there is a sudden change in plasma conditions.

The dependence of the S/XB on the metastable fraction has also been investigated indirectly in the data set used by Beigman *et al.*[5] The T_w parameter is an effective proxy for changing the metastable fraction as it changes the population of the low energy levels. The S/XB varies greatly with the T_w parameter; the results presented here are in agreement with this trend. From Equation 3.32, both the numerator (SCD) and denominator (PEC) of the S/XB coefficient depend on the metastable fraction. The PEC values have already been shown in Figure 5.2 to depend on the metastable fraction. The numerator of the S/XB coefficient, the SCD, also has a dependence on the metastable fraction (see Equation 3.32). However, for neutral tungsten, the SCD does not have one dominant metastable contribution. Instead, each metastable component contributes almost equally to the total ionization as indicated in Figure 5.4. The total ionization as a function of electron temperature is plotted as a black dashed line. The solid color lines represent the metastable components weighted by the equilibrium metastable fractions. All metastable components contribute roughly equally to the SCD. Thus, the total value of the SCD coefficient is relatively insensitive to changes in the metastable fraction. As a result, the S/XB largely depends on the same single metastable as the PEC.

Previous erosion measurements used S/XB coefficients that assumed steady-state metastable fractions which could potentially lead to a source of error in the measurements. Section 5.2.6 will explore whether previous experiments were conducted in equilibrium conditions.

5.2.2 Intermediate populating mechanism

Two separate questions are investigated related to the mechanisms for populating levels. First, what transitions are the main populating mechanisms for neutral tungsten excited states? Second, what drives the population of metastable states? From CR theory, it is possible to determine which levels contribute to the population of a given excited state. The

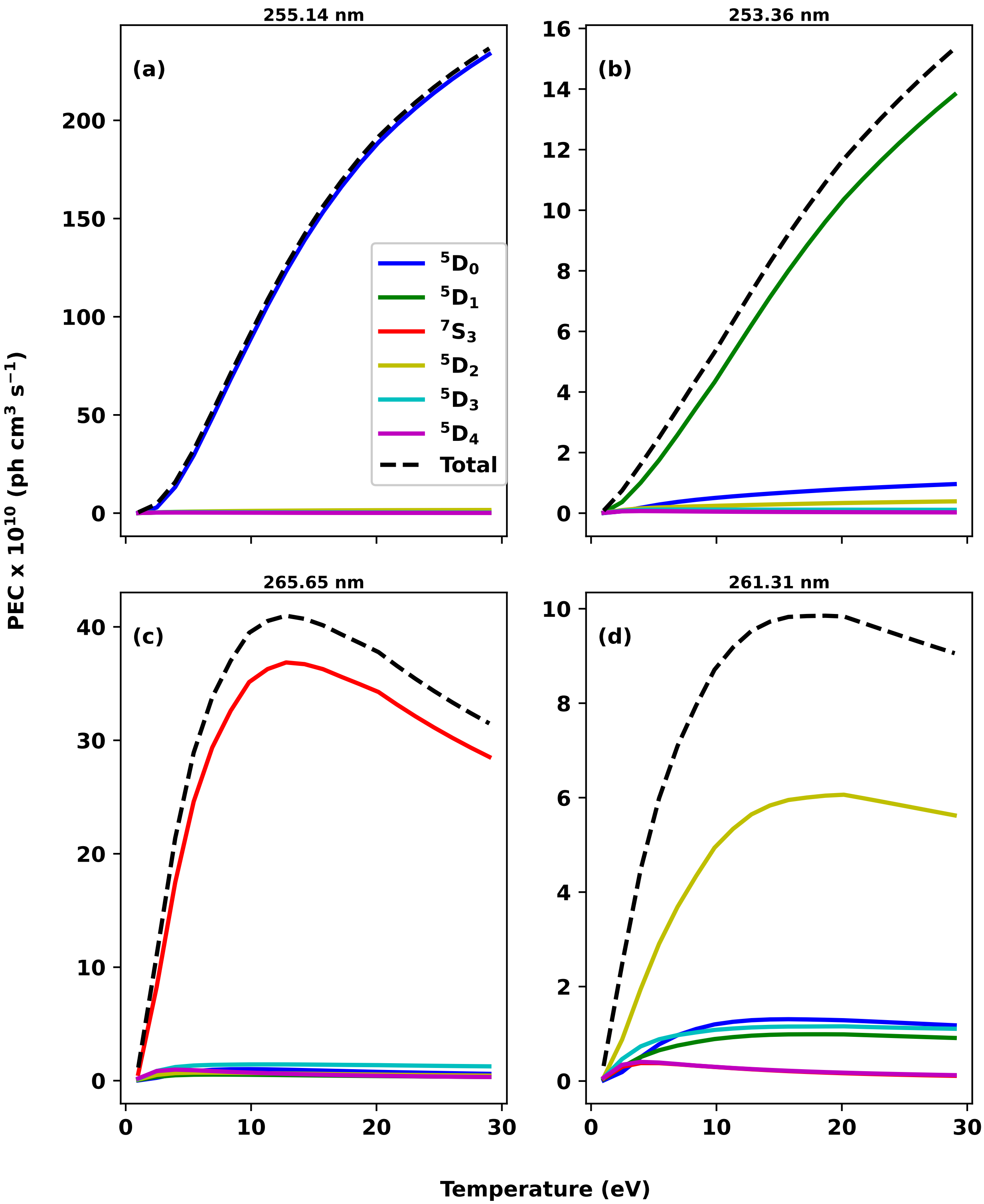

Figure 5.2: PEC values for four intense W I emission lines, for $n_e = 1 \times 10^{13}\mathrm{cm}^{-3}$. The total equilibrium temperature dependence for each PEC is illustrated by the dashed black line. The PECs weighted by their steady-state metastable populations are indicated by the solid colored lines. Results are shown for the (a) 255.14, (b) 253.36, (c) 265.65 and (d) 261.31 nm lines.

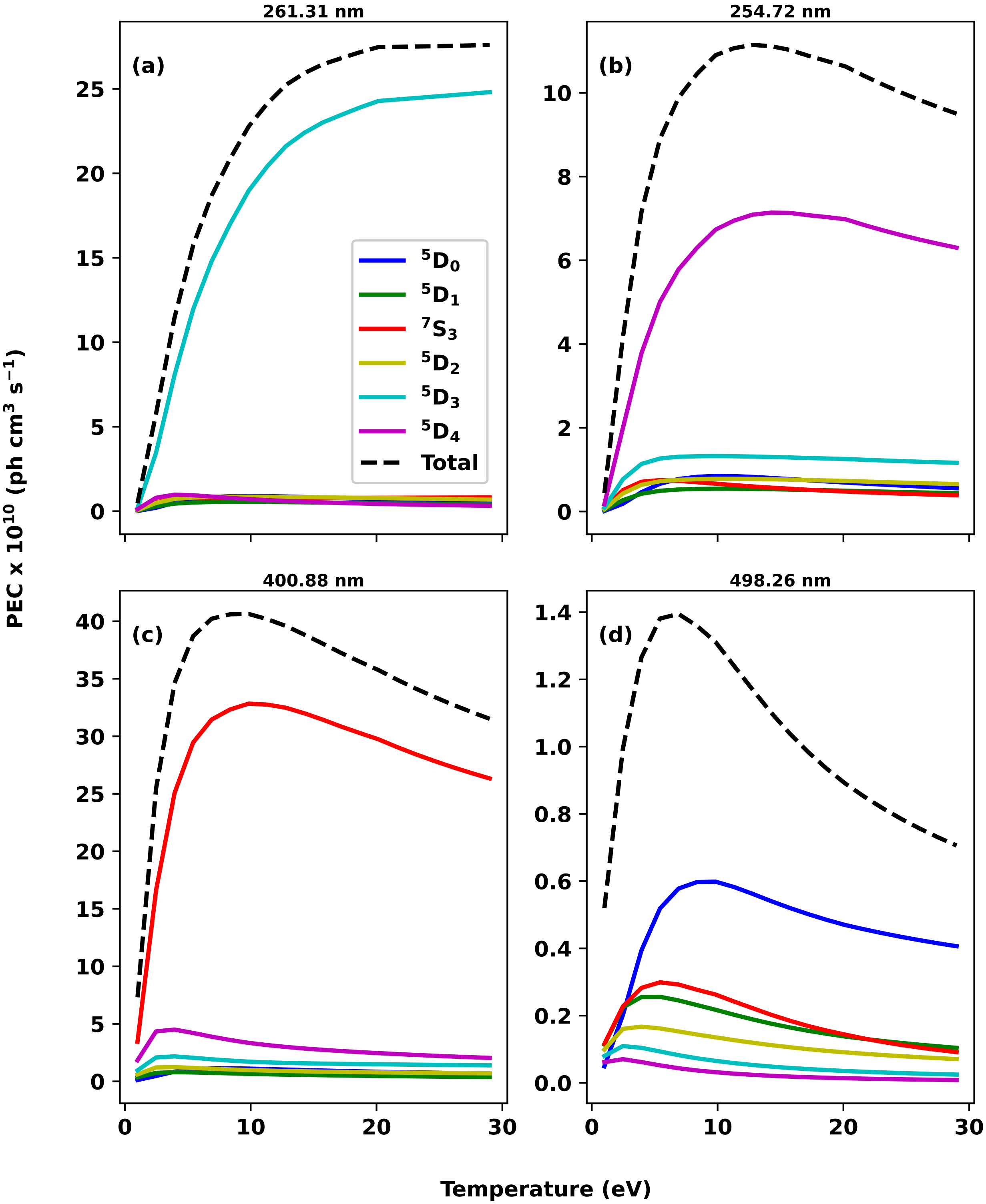

Figure 5.3: PEC values for four intense W I emission lines, for $n_e = 1 \times 10^{13}\text{cm}^{-3}$. The total equilibrium temperature dependence for each PEC is illustrated by the dashed black line. The PECs weighted by their steady-state metastable populations are indicated by the solid colored lines. Results are shown for the (a) 261.31, (b) 254.72, (c) 400.88 and (d) 498.26 nm lines.

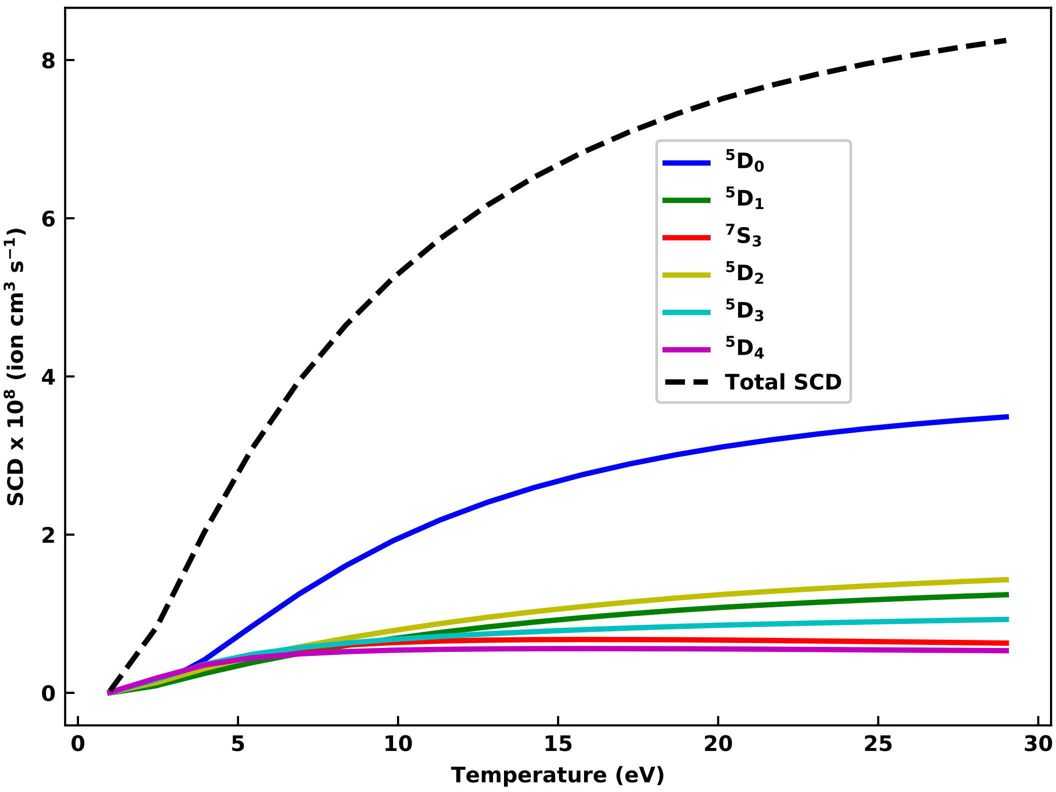

Figure 5.4: SCD values for W I as a function T_e, determined by collisional radiative modeling at $n_\mathrm{e} = 5 \times 10^{13}$ cm^{-3}. The metastable components are plotted with solid colored lines. The dashed line is the summation of the metastable components weighted by their steady-state metastable fractions.

technique, as described in Johnson *et al.*[46] allows for the intermediate levels that populate an excited state of interest to be determined. Figure 5.5 shows the contributing percentages of three different excited states. The energy levels in the plot are ordered in ascending energy along the x-axis. The contribution from the ground state is highlighted by the vertical red line.

Excited states in neutral tungsten can be grouped into two categories: excited states that produce intense spectral lines populated directly from a low energy metastable state and excited states that produce weak spectral lines populated from a variety of different levels. The large W I emission line at 255.14 nm emitted from level $5p^65d6p$ ($^5P_1$) exemplifies the first category. It is clear from Figure 5.5 (a) that almost all of the population comes directly from the ground state (i.e. there is a single peak at the same position as the red line). In contrast, levels that emit weak spectral lines are populated via many different levels. Level $5p^65d6s$ ($^3D_1$) is one such level; it is close in energy to level $5p^65d6p$ ($^5P_1$), has the same spin and yet is populated from many intermediate states (i.e. there are many peaks).

Metastable levels have population on the order of the ground state population. In general, the quasistatic approximation does not hold for these levels; the population changes on a timescale similar to other plasma dynamics such as ELMs and plasma fluctuations. Figure 5.5 (c) shows the population analysis for level $5p^65d6s$ ($^7S_3$), populated mainly via excited states and not directly from the ground. Electrons begin in the ground level and then redistribute through excited states before building up in the metastable level.

5.2.3 Loss rate analysis

Metastable states generally have small loss rates (unless there is significant collisional de-excitation), causing an increase in population relative to other excited states. Metastable levels rarely have an electric dipole radiative transition to a lower level. Low-Z atoms usually have a small number or no metastable levels. In contrast, high-Z atoms with complex electron configurations can have multiple metastable levels.[46] There is generally a clear

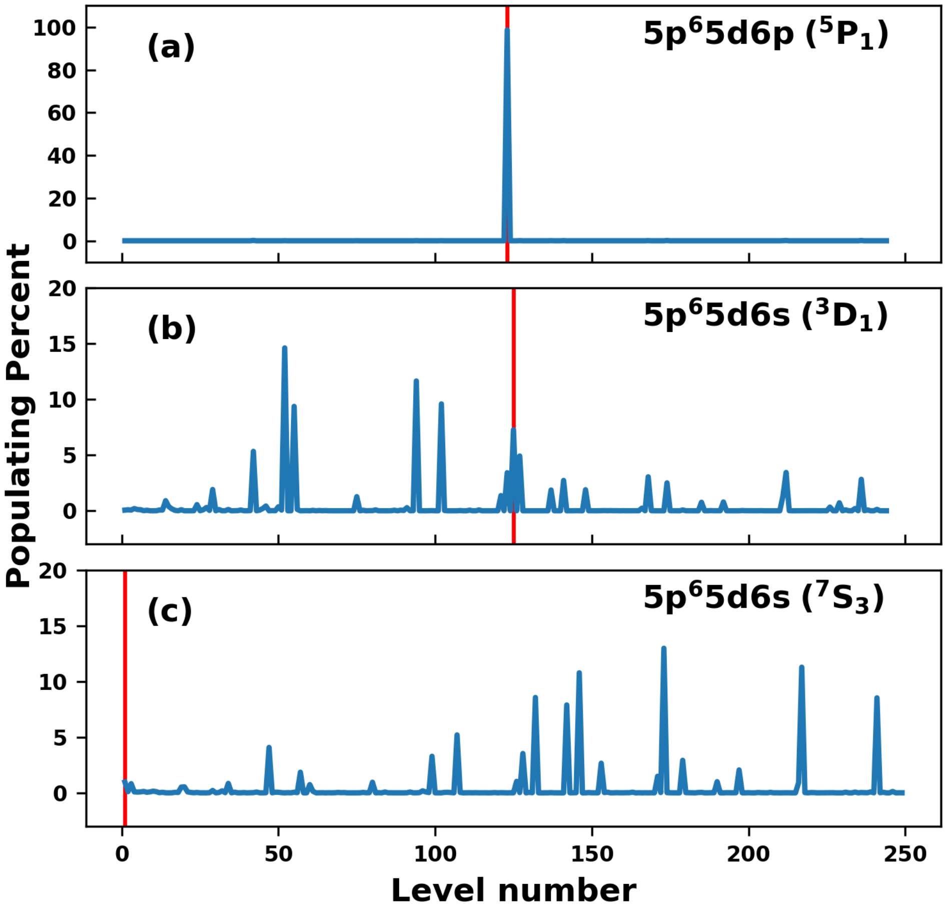

Figure 5.5: Intermediate levels responsible for populating a selection of neutral W energy levels. The red vertical lines in each plot correspond to the ground state contribution. Populating levels for 5p^{6}5d6p(^{5}P$_1$) show most of the population is being excited directly from the ground (a). Populating levels for 5p^{6}5d6s(^{3}D$_1$) display a majority of the population is coming from other excited states and metastable states (b). Populating levels for 5p^{6}5d6s(^{7}S$_3$) indicate a majority of the population is coming from excited states (c).

distinction between metastable and excited levels for low-Z atoms as quantified by loss rates and equilibration times (discussed in Sections 5.2.5 and 5.2.6).

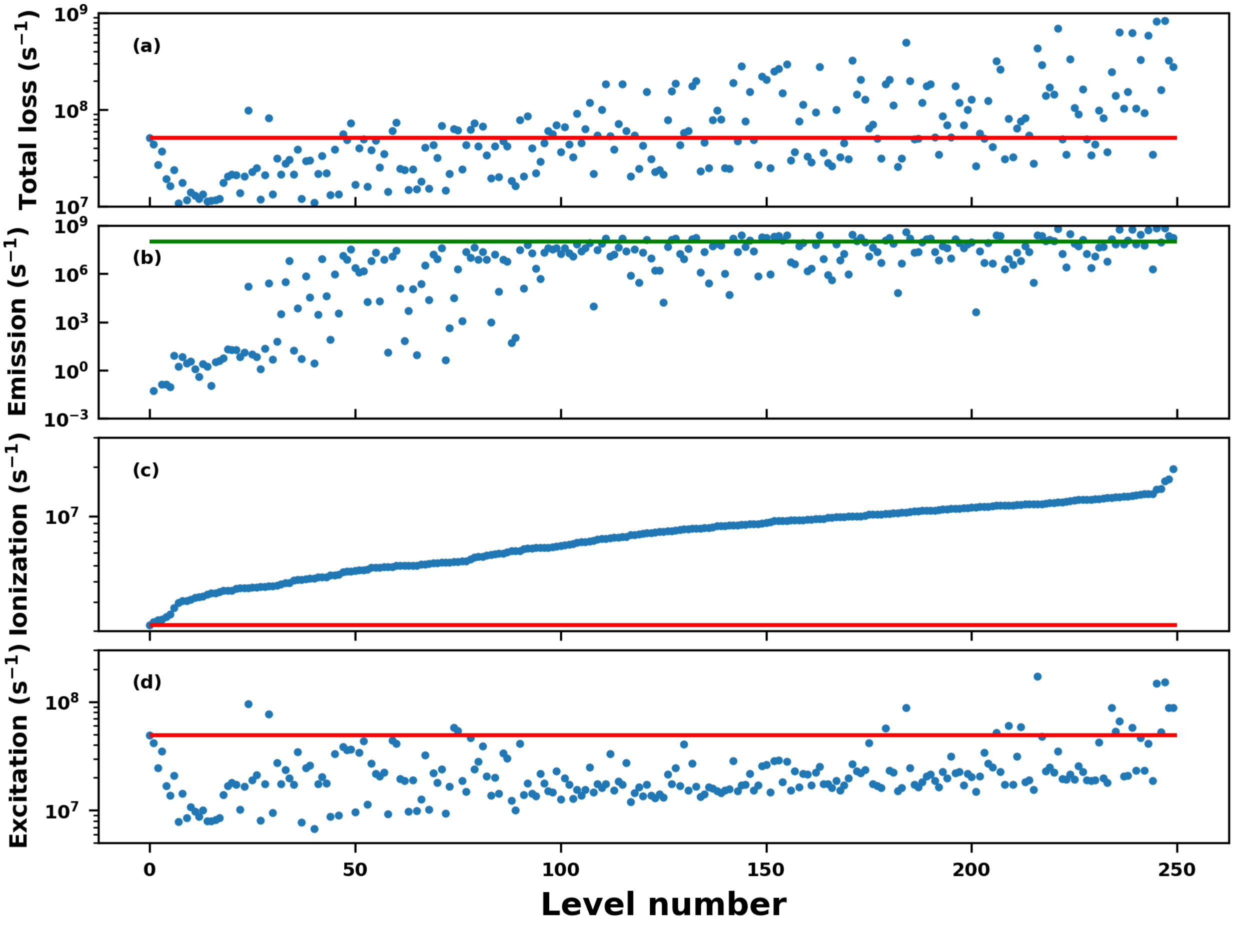

Figure 5.6: Population loss rates from neutral tungsten levels for $T_e = 30$ eV, $n_e = 5 \times 10^{13}$ cm^{-3}. Levels are arranged in ascending energy. Horizontal red lines correspond to ground level loss rates with the horizontal green line representing a typical value for a strong electron dipole transition. The total loss rate out of an energy level (a). The loss rate only from spontaneous emission (b). The loss rate due to ionization (c). The loss rate due to excitation/de-excitation (d).

There are many levels above the ground state of neutral tungsten for which the quasistatic approximation is not valid (this is also true for neutral molybdenum[46,63]). Figure 5.6 highlights the various loss rates (spontaneous emission, ionization and electron-impact excitation/de-excitation) of the 250 levels of neutral tungsten included in an R-matrix calculation at fusion relevant divertor conditions. Of the 250 levels that are considered, 135 have a total loss rate smaller than the ground level, and so might evolve on similar timescales as the ground. The large number of states with small loss rates leads to a buildup of population in these excited states. The smooth trend in Figure 5.6 (c) is an effect of the ionization rate coefficients being proportional to the ionization potential for that level. Spontaneous emission increases with level energy, as seen in Figure 5.6 (b) and is related to the possible number of levels to which spontaneous emission can occur. For light neutral systems, the increase in spontaneous emission is often dramatic because the electric dipole transitions rates are very fast (approximately $1 \times 10^{8}\,\mathrm{s}^{-1}$ for neutral systems). Many levels in neutral tungsten do not have dipole transitions (only 0.7% of possible transitions have a single Einstein A value greater than $1 \times 10^{7}\,\mathrm{s}^{-1}$), which leads in part to the large number of levels that could be considered metastable. The lack of dipole transitions for many of the excited states is reflected in the slow increase in the emission loss rate in Figure 5.6 (b).

Electron-impact excitation/de-excitation dominates the total loss rate for the majority of levels as excitation sets the 'lifetime' of the level. From Figure 5.6 (d), it is clear that many levels have smaller excitation/de-excitation rates than the ground state (shown as data points below the solid red line). The small excitation/de-excitation rates in conjunction with small spontaneous emission values leads to many levels having 'lifetimes' of comparable size to that of the ground state. In fact, 230 out of the 250 levels have excitation/de-excitation rates that are smaller than the ground state. Thus, there are a significant number of levels that could be considered metastable. Transport codes cannot model large numbers of metastable states due to the significant computation resources needed for each metastable state as each state must be tracked independently.[88] The number of metastable levels required to accurately predict spectral line intensities will be investigated in the following sections.

5.2.4 Diagnosing metastable populations

As stated in previous sections, the metastable fraction might be important for erosion measurements as the erosion rate is directly proportional to the S/XB. The dominance of one primary metastable state driving individual spectral lines of neutral tungsten allows for the possibility of measuring the neutral W metastable fraction in a plasma. Once the electron temperature and density are determined, the line intensities for the most intense lines are nearly linearly dependent on a single metastable, allowing for the metastable fraction to be measured from line ratios. For example, the ratio of the ground $5d^4 6s^2$ ($^5D_0$) to metastable $5d^5(^6S)6s$ ($^7S_3$) can be determined from

$$I_{i\rightarrow(^7\mathrm{S}_3)}/I_{j\rightarrow(^5\mathrm{D}_0)} \approx \left(\frac{PEC_{i\rightarrow(^7\mathrm{S}_3)}}{PEC_{j\rightarrow(^5\mathrm{D}_0)}}\right)\left(\frac{N_{(^7\mathrm{S}_3)}}{N_{(^5\mathrm{D}_0)}}\right) \tag{5.1}$$

where I represents the intensities of spectral lines decaying to the $^7S_3$ metastable and $^5D_0$ ground. N is the relative population of the $^7S_3$ metastable and $^5D_0$ ground. By measuring the line ratio, the relative metastable fraction could be determined. The spectral lines in the 252-269 nm region (Figure 5.2) could diagnose the relative metastable fraction as they are each dominantly driven by a single metastable level. The inferred relative metastable population is then a combination of measured spectral intensities and calculated PECs.

5.2.5 Non-quasistatic solutions for neutral tungsten

It has been previously shown that molybdenum atoms are sputtered from a surface as ground state atoms,[63] and it is reasonable to assume that neutral tungsten will behave similarly. In fusion relevant machines, it is possible that neutral tungsten populations are not in steady-state for a significant amount of their lifetime until ionized. It is then necessary to solve the CR system of equations in a time-dependent manner to investigate these effects.

There exist two main methods for solving the time-dependent evolution of the collisional radiative set of equations. First, a quasistatic solution to the CR system is calculated with a specified number of metastable states chosen. A quasistatic solution is used to calculate the metastable cross coupling coefficients (QCD) defined originally by Summers.[40] These QCD values can be thought of as all the possible channels to transfer population from one metastable state to another, both directly and indirectly, through intermediate excited states.

The populations of metastable levels are time-dependently propagated using the QCDs in a set of rate coefficient equations. Excited states always remain in their steady-state population relative to the metastable states at all times. Second, a fully time-dependent solution to the CR system can be achieved; the details of this are described in Johnson *et al.*[46] The fully time-dependent method is the exact solution to the system of equations, as no assumption of time scales are made.

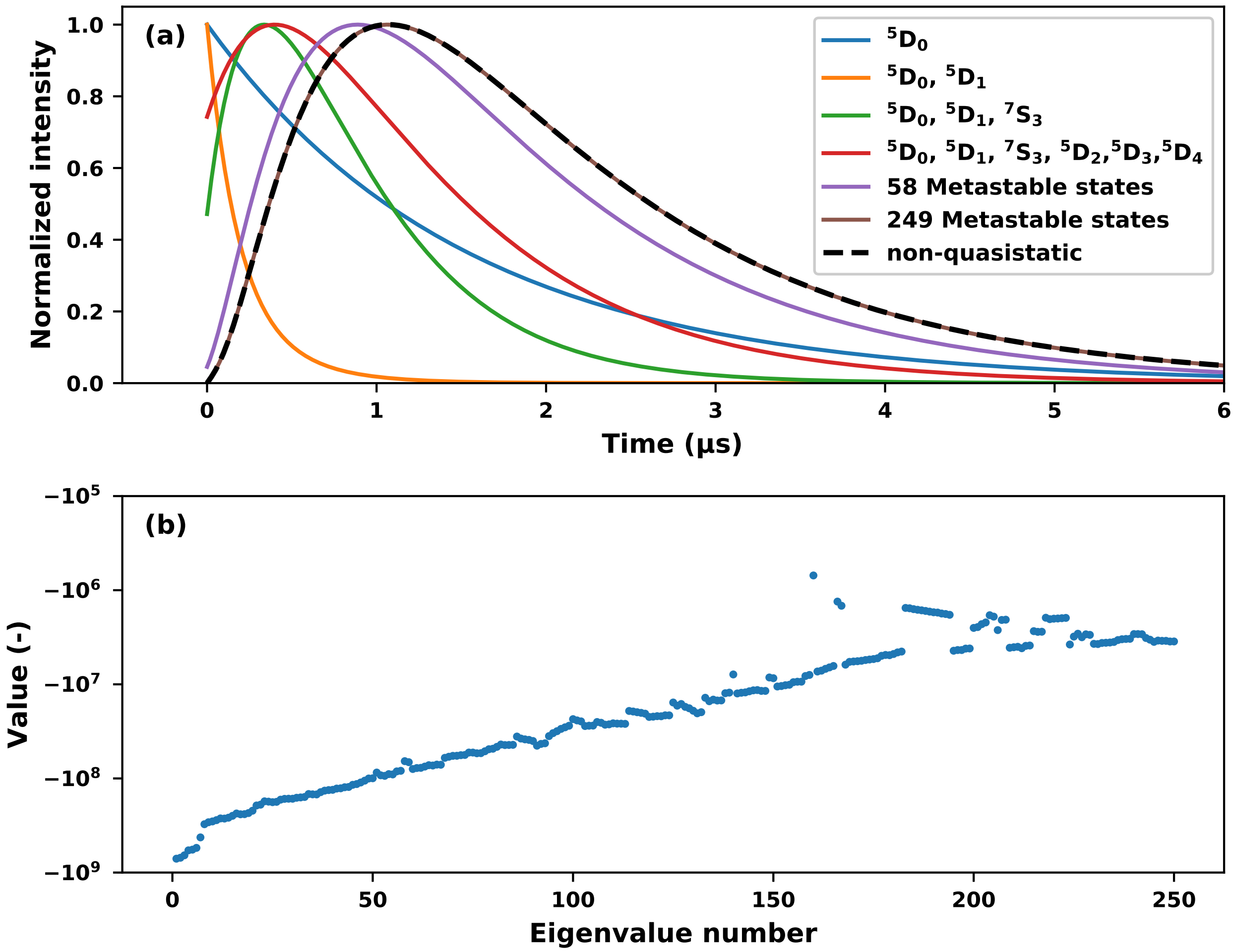

Figure 5.7: A comparison of the non-quasistatic (dashed line) and quasistatic approximations (colored solid lines) with varying numbers of metastable states included (a) for the widely used W I emission line at 400.88 nm. The eigenvalues from the non-quasistatic approximation with less negative numbers corresponding to longer lived states (b). There are a significant number of long-lived states that correspond to the large number of metastable states in neutral tungsten.

Many transport codes use the generalized collisional radiative coefficients as inputs for time-dependent solutions. A system such as neutral tungsten presents a challenge as many levels have significant population, as seen in Figure 5.7, which requires multiple metastable levels to reproduce the time-dependent solution. These large populations lead to the quasistatic solution not being valid for a majority of levels in the calculation. A decision needs to be made regarding which levels to include as metastable for transport calculations. The impact of metastable levels on the time dependence of a spectral line, such as the commonly used W I 400.88 nm line, is shown in Figure 5.7 (a). The fully time-dependent solution is shown as the black dashed line and can be considered the exact solution to the time-dependent system. The quasistatic solutions with varying numbers of metastable states are then shown as the solid-colored lines. As time increases, this calculation converges on the steady-state solution. Interestingly, when no metastable states are included in the calculation (i.e. only the population of the ground state may change time-dependently), the general time evolution of the exact intensity of the 400.88 nm cannot be reproduced.

For the calculation with no metastable levels, the population of the 400.88 nm upper level is driven entirely from the ground state. Thus, the correct time evolution (initial increase, then decrease) of the time-dependent line emission is not produced until the $^7S_3$ level is included as a metastable level. In this model, all population starts in the ground state, and because the 400.88 nm upper level is not populated significantly from the ground state, it takes some time to build up population in the 400.88 nm upper level. Electrons from the ground state must transfer to the $^7S_3$ metastable state, (predominately through the excited states, see Figure 5.5), before the 400.88 nm upper level builds up significant population. The time required for population to transfer from the ground state (proportional to n_e) leads to the delay in peak intensity observed in Figure 5.7 (a). A delay in peak intensity of spectral lines populated from metastable states has been both observed and predicted in neutral molybdenum.[63,46]

The large number of metastable states can be clearly demonstrated when the system of equations is solved time-dependently via the matrix exponentiation method. The eigenvalues of the solution are plotted in Figure 5.7 (b). Large negative eigenvalues represent short-lived states in the system, which are caused by excited states that come into equilibrium relatively quickly. Metastable states are characterized as small negative values, corresponding to the relatively slow time scale in which they come into equilibrium. Not shown in the plot is the eigenvalue of zero that corresponds to the steady-state equilibrium. In light systems, there is a distinction between metastable and excited states; the eigenvalues of excited states are often orders of magnitude larger than metastable states.[46] However, in neutral tungsten, there exists almost a continuum of eigenvalues making it difficult to distinguish between metastable and excited states. The time-dependent intensity of the 400.88 line (Figure 5.7) clearly tracks with the population of the $^7S_3$ level. The impact of the number of metastable states in approximating the non-quasistatic solution is highlighted in Figure 5.7. The accuracy of the approximation is significantly increased going from three to six metastable states; however, there are diminishing returns increasing beyond six metastable states. Once every level is considered metastable, the time-dependent, non-quasistatic solution is recovered. Modeling neutral W excited populations and spectral emission using six metastable states would be a reasonable trade off between accuracy and computational resources. If there was a level of interest which was populated dominantly from a level not included as metastable, this model would be incapable of accurate modeling unless this level was also considered metastable.

5.2.6 Neutral tungsten equilibrium time scales

In equilibrium conditions, metastable fractions are only determined by the electron temperature and density and do not introduce additional free parameters in the modeling. Metastable states become important when the system is driven out of equilibrium by some plasma phenomena (such as ELMs) or the system is slow to reach equilibrium. Many of the previous W I spectral measurements have been preformed at relatively low electron densities

(10^{12} cm^{-3}). Equilibrium times for neutral W metastable states scale almost linearly with electron density, as shown in Figure 5.8. While electron density is the dominant factor in determining equilibrium time-scales, it can also be seen from Figure 7 that the equilibrium time-scale reduces as the electron temperature increases. Note that Figure 5.8 could be used to estimate if a particular experiment has a significant non-steady-state metastable population that needs to be accounted for. Figure 5.8 is for bulk plasma densities; there will be a significant density gradient due to sheath effects. Depending on the experimental setup, it is possible that previous W I spectral measurements included non-steady-state metastable fractions.

Non-steady-state metastable fractions at lower electron densities would artificially increase the S/XB ratio for spectral lines that are populated from the $^7S_3$ metastable, such as the widely used 400.88 nm line, and decrease S/XB ratios for lines populated from the ground. These effects would scale almost linearly with the metastable fraction in Equation 3.27 and lead to over predictions for erosion inferred from spectral lines populated from the $^7S_3$ metastable and would under predict erosion inferred from spectral lines populated from the ground.

In tokamaks, there are multiple different processes and plasma phenomena that could lead to non-equilibrium metastable populations. These include sheath effects (electron density gradient), proton collisions, edge localized modes and non-Maxwellian electron temperature distributions. Sheath effects are of interest because they slow down the time scales required to reach equilibrium; sheaths also exist at all material boundaries. At typical divertor densities ($\sim 1 \times 10^{13}$ cm^{-3}), neutral tungsten comes into equilibrium much faster than plasma phenomena, on the order of a microsecond. Sheath effects in the divertor can produce plasma conditions that significantly increase equilibration times. Transport modeling has demonstrated that tungsten exists almost entirely within the plasma sheath.[1] It is then possible that low electron densities in the sheath cause a significant amount of the spectral line intensity to be produced from non-equilibrium populations.

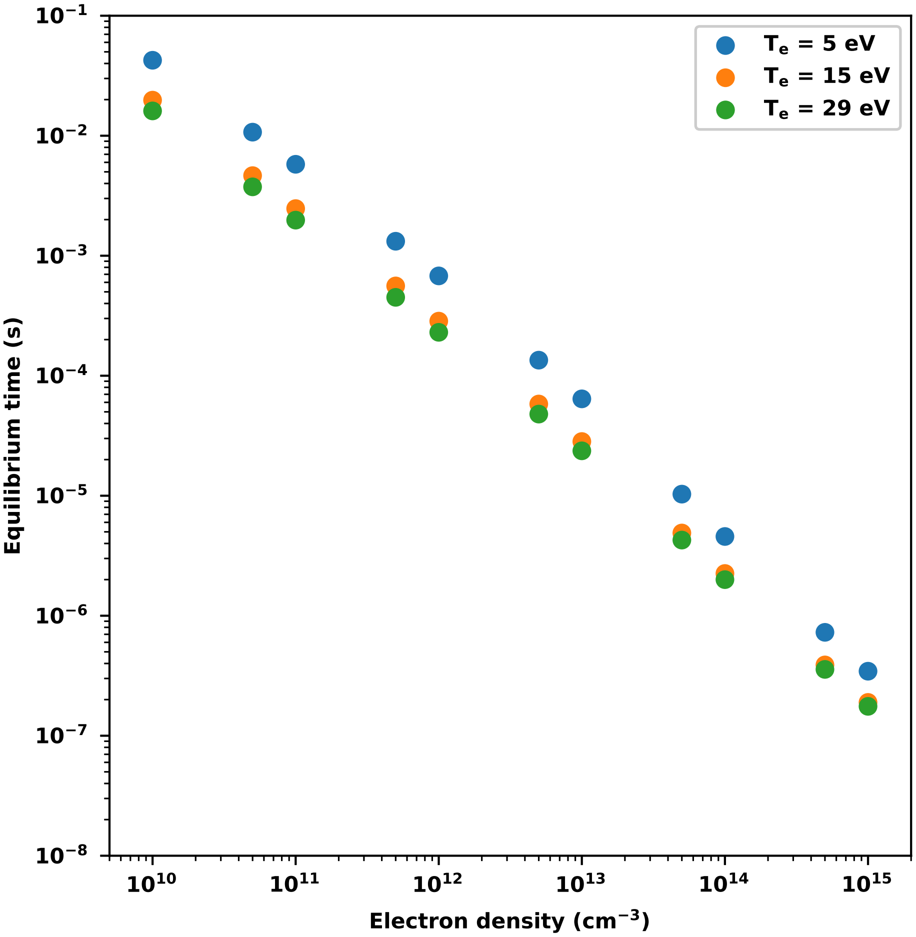

Figure 5.8: The time required for neutral tungsten to come to equilibrium as a function of electron density. The time to reach equilibrium decreases almost linearly with electron density.

5.3 Modeling effective S/XB coefficients in the plasma sheath

Near any surface such as a divertor, a layer of charge separation is spontaneously generated. This layer between the quasineutral bulk plasma and material has a net charge. The layer is referred to as a Debye plasma sheath and is generated by differences in the thermal speed of ions and electrons (a consequence of mass difference between ions and electrons). The Debye sheath is discussed in Section 2.5.2. In most fusion relevant devices, there is a small angle between the magnetic field and surfaces giving rise to an additional sheath called the Chodura sheath or magnetic presheath described in Section 2.5.3.

While the Chodura sheath region is relatively small (1 mm), most of the emission of neutral tungsten comes from within the sheath region (see Guterel *et al.*[1]). Plasma conditions can change drastically (order of magnitude) within the sheath, therefore collisional radiative modeling must account for local plasma conditions in the sheath. The electron density changes quite drastically as seen in Figure 2.19, and because the neutral tungsten CR equilibrium time is determined by electron density (as seen in Figure 5.8), the sheath could significantly increase the time required to reach equilibrium for neutral species.

There has been previous work done to model the impact of the sheath density gradient on the steady-state S/XB for the 400.88 nm W I line by Guterel *et al.*[89] This work used modifications to the electron distribution function in the sheath and the SCD coefficient to calculate ionization scale lengths. An analytical solution was then obtained for the effective S/XB coefficient accounting for the sheath density gradient. However, it will be shown in the upcoming sections that time-dependent effects can also significantly change the S/XB coefficient and represents a major result of this thesis.

5.3.1 Modeling effective S/XB coefficients in the sheath with ColRadPy

The sheath model in this work is a combination of the Debye sheath (when present) and Chodura sheath. The Debye sheath is modeled in the standard form (see Stangeby[90]) outlined in Section 2.5.2. The Chodura sheath used is that of Stangeby.[37] The highlights of this model are discussed in Section 2.5.3. The model takes the form of a Python code using the equation of the Debye sheath and Chodura sheath. The following parameters are used as inputs to the code: T_e is the electron temperature, T_i is the ion temperature , n_bulk is the bulk electron density, m_i is the mass of the main ion species, B_mod is the magnetic field strength and α is the angle the magnetic field makes with a surface. For incident angles α that are greater than the critical angle α^*, the Debye sheath is also present. From these input parameters, the code produces an electron density profile through the sheaths that can be used for CR modeling. The electron temperature is assumed to be constant in the sheath region for this model; however, particle simulations would suggest there is a moderate temperature change but that is not considered here.

The model also requires the velocity of the sputtered tungsten in order to determine the time that the tungsten spends in the sheath. The tungsten impurity atoms are assumed to sputter off the surface with ballistic velocity (neutral particles are not affected by magnetic fields). The velocity is taken to be half the binding energy of tungsten (8.63 eV). While in reality, there is a distribution in sputtering angle; the model here assumes that all tungsten is sputtered normal to the tungsten surface. In this model, tungsten spends the minimum amount of time in the sheath region and thus should be taken as the lower limit of changes to Collisional radiative coefficients due to the sheath. Variation of the neutral tungsten velocity (i.e. sputtered angle) is investigated in Figure 5.18. There is no recombination included in the simulation as recombination rates are small compared to excitation and ionization at divertor plasma conditions.

ColRadPy allows for the CR equations to be solved time-dependently (Section 3.4.2) within the grid points of the sheath. The time-dependent solution is then solved for 10 time points at each density grid. The population of electrons in the neutral tungsten system is evolved at each density grid point, starting with the ending population of the previous grid point. Tungsten that is sputtered from the surface is assumed to start in the ground state; there is experimental evidence of this for neutral molybdenum.[63] The impact of some population not sputtering into the ground state but into the $^7\mathrm{S}_3$ metastable state is investigated in Section 5.3.2. Tracking the time-dependent change in population in the sheath differentiates this model from the previous work of Guterl *et al.*,[89] where the population was assumed to be in steady-state at each grid point. The ending population from the previous grid point is the starting population in the next grid point.

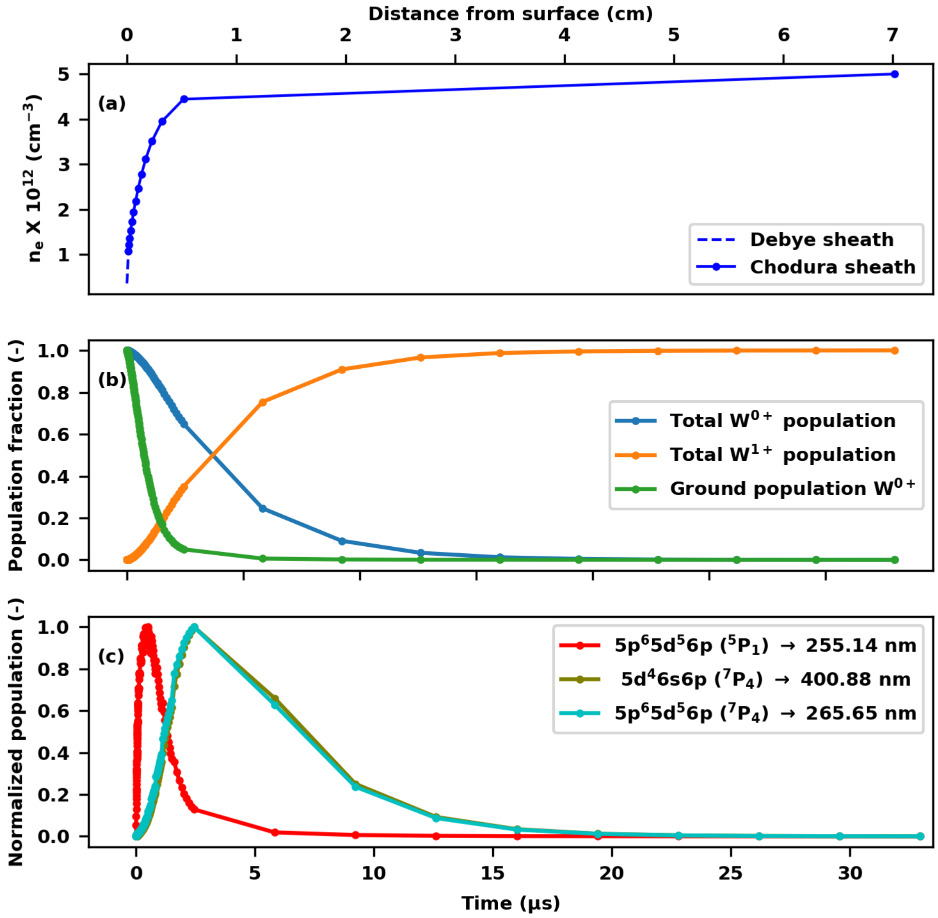

Figure 5.9: The density profile in the Debye and Chodura sheaths (a), time changing population of W^{0+} and W^{1+} (b). The normalized population of levels that produce intense spectral lines (c).

An example of the Chodura sheath model is shown in Figure 5.9 for CTH relevant conditions ($T_\mathrm{e} = 20$ eV, $n_\mathrm{e} = 5 \times 10^{12}$ cm^{-3}, $B_\mathrm{mod} = 0.6$ T, $\alpha = 12°$). The density profile in the sheath region is plotted in Figure 5.9 (a) (note that time can be converted to distance with $v_\mathrm{w} = 2128$ m/s). The Debye sheath (blue dashed line) has five grid points while the Chodura sheath has 15 grid points on a log scale to allow for the steep density gradient to be resolved. The last point in the sheath is the entrance to the Chodura sheath from the bulk plasma. In simulations where not all of the W^{0^+} has ionized within the sheath, the simulation is continued using bulk plasma density until at least 99% of the W^{0^+} has been ionized.

The ionization of W^{0^+} is seen in Figure 5.9 (b). At time $t = 0$, all of the population starts in the ground state of W^{0^+} (blue line). As neutral tungsten atoms are ionized, the W^{1+} (orange line) increases in population. Interestingly, population is drained from the ground state of W^{0^+} through ionization, but there is also significant population that is redistributed to other states within W^{0^+}. This is seen as the difference in the blue and green lines in Figure 5.9 (b). The large number of metastable states in neutral tungsten causes a significant percentage of the population to be stored in states other than the ground. This trend can be seen from the relatively low loss rates in excited levels in Figure 5.6 and the large number of metastables required to reproduce the full time dependent solution in Figure 5.7.

The different time dynamics of excited states that are populated from the $^5\mathrm{D}_0$ ground state and the $^7\mathrm{S}_3$ metastable state can be seen in Figure 5.9 (c). Level $5\mathrm{p}^6 5\mathrm{d}^5 6\mathrm{p}$ ($^5\mathrm{P}_1$) which produces the 255.14 nm spectral line is mainly populated from the ground state (see Figure 5.2 and Figure 5.5). As a result, the population in this level peaks early in the simulation. Because all of the population in this model starts in the ground state, time is needed for population to transfer to the $^7\mathrm{S}_3$ metastable state which populates the excited states indicated by the cyan and olive traces peaking later in time compared to the red trace. Note that excited states populated from the metastables will emit in a higher electron density region compared with lines populated mainly from the ground state.

The model was validated against the work of Guterl *et al.*,[89] which did not consider time-dependent atomic population effects while considering the density gradient. This could be checked against our model by assuming steady-state conditions for the CR model. This simulated model uses an entirely different framework than the analytical formula of Guterl, even ignoring sputtering angle. However, Figure 5.10 (b) shows strong agreement of the effective S/XB produced by the two methods when compared to original bulk S/XB values in (a). This Increases confidence in the simulated method of propagating populations through the sheath region.

5.3.2 Comparison of selected W I S/XB and effective S/XB coefficients

The S/XB method described in detail in Section 3.3.5 is presently the best method for diagnosing tungsten erosion in real time for both current plasma experiments and future fusion devices. The W I 400.88 nm line previously discussed in Chapter 5 is currently the most studied neutral tungsten line for erosion measurements due to large intensity and its emission at visible wavelengths. However, there are very few measurements of erosion spanning the plasma T_e and n_e parameter space of interest to benchmark erosion with the 400.88 nm line. Even more urgent is the need for neutral tungsten CR modeling since there has been a lack until the work presented here. In this work, the time-dependent effective S/XB for many of the most intense W I spectral lines will be compared with both the steady-state bulk S/XB and the steady-state sheath averaged effective S/XB. The UV lines from Figure 5.2 will be investigated because these lines all have a strong dependence on a single metastable level. The sheath model used in this section is the same model as that described in Section 5.3.1 but applied to ITER conditions, ($T_\mathrm{e} = 20$ eV, $n_\mathrm{e} = 5 \times 10^{15}$ cm^{-3}, $B_\mathrm{mod} = 5.3$ T, $\alpha = 3.2°$).

Figure 5.11 shows the effective SCD and PEC coefficients versus time using the sheath model. These two coefficients are integrated over the sheath to get the total number of ionizations and photons emitted in the sheath. The result of this integration is then used to produce the time-dependent effective S/XB coefficients seen in Figures 5.13 and 5.14. Note that these time-dependent effective coefficients are now dependent on the sheath model used, namely the bulk T_e and n_e. The impact on the effective time-dependent S/XB due to variations in the parameters of the Chodura sheath are investigated in Sections 5.3.2.

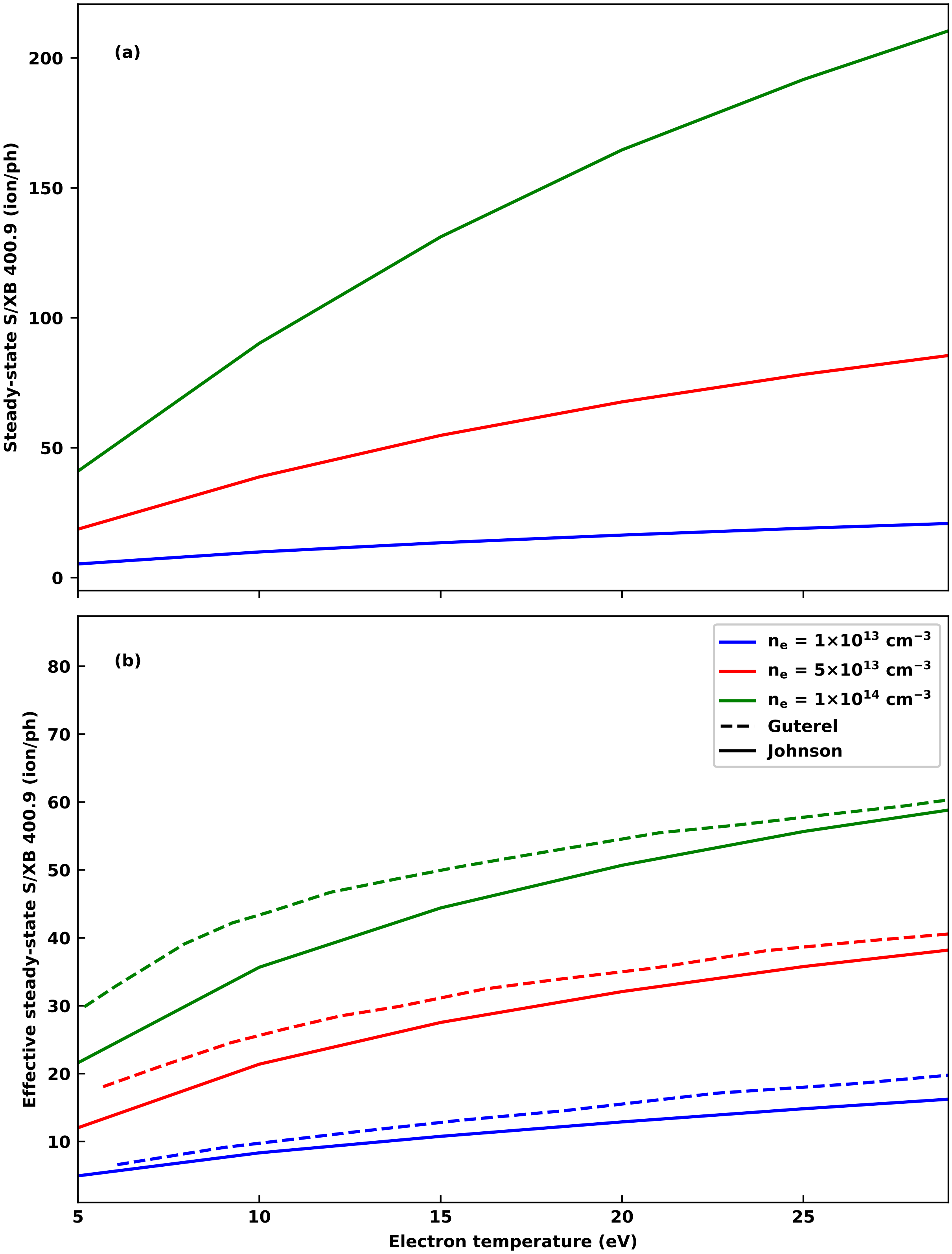

Figure 5.10: Comparison of sheath model from Guterel *et al.*[1] to the sheath model used in this thesis.

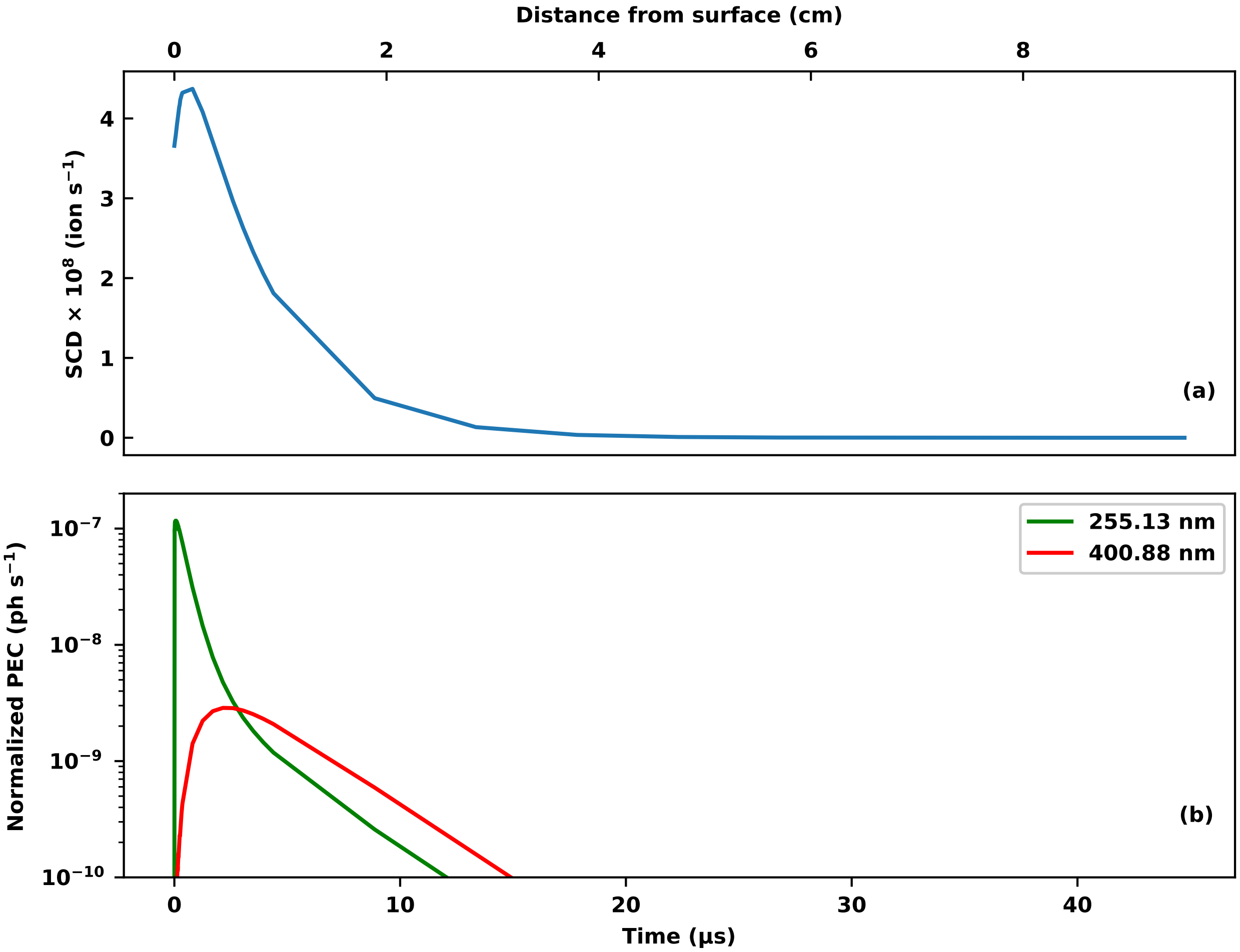

Figure 5.11: Time dependent SCD coefficient (a) and time-dependent PEC coefficients (b) for W I 255.14 in green and W I 400.88 in red. Parameters of the Chodura sheath model are: $T_\mathrm{e} = 20$ eV, $n_\mathrm{e} = 5 \times 10^{12}$ cm^{-3}, $B_\mathrm{mod} = 5.3$ T, $\alpha = 3.2°$.

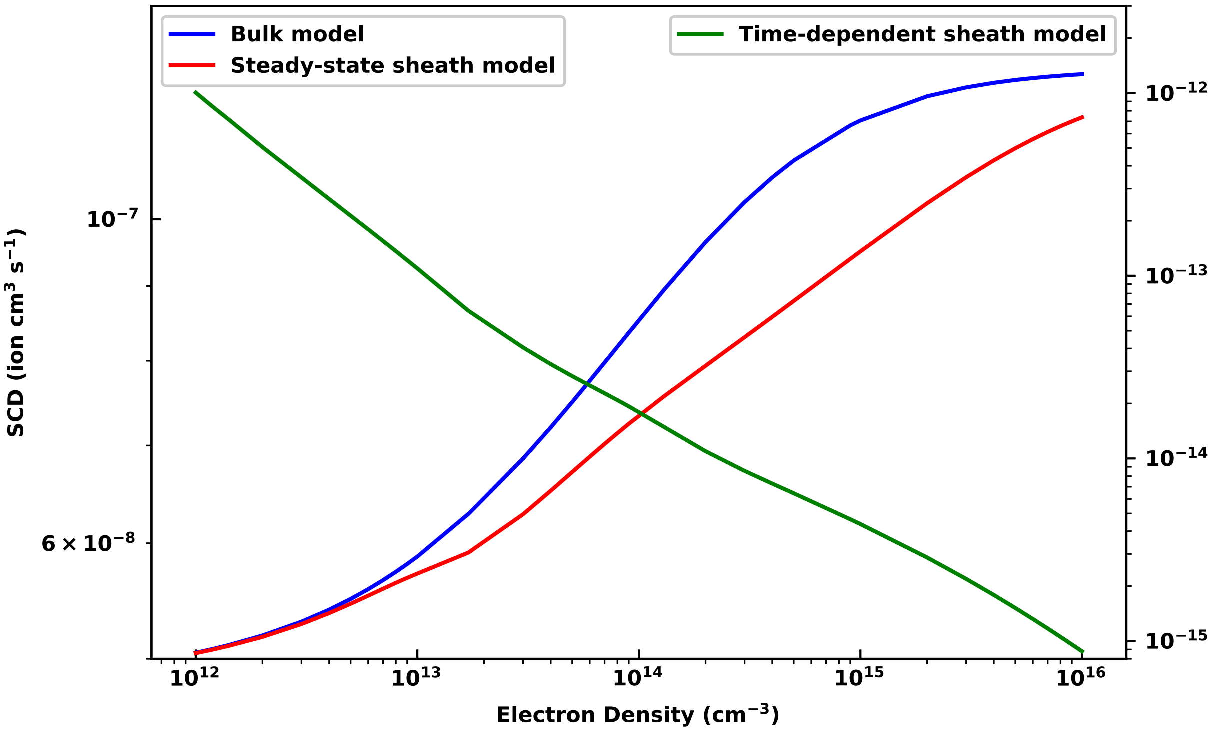

Figure 5.12: W^{0+} SCD coefficient at $T_{\mathrm{e}} = 20$ eV versus electron density. The SCD coefficient using bulk T_{e} and n_{e} values is shown in blue. The steady-state Chodura sheath is depicted in red. The time-dependent solution in the Chodura sheath is the green line.

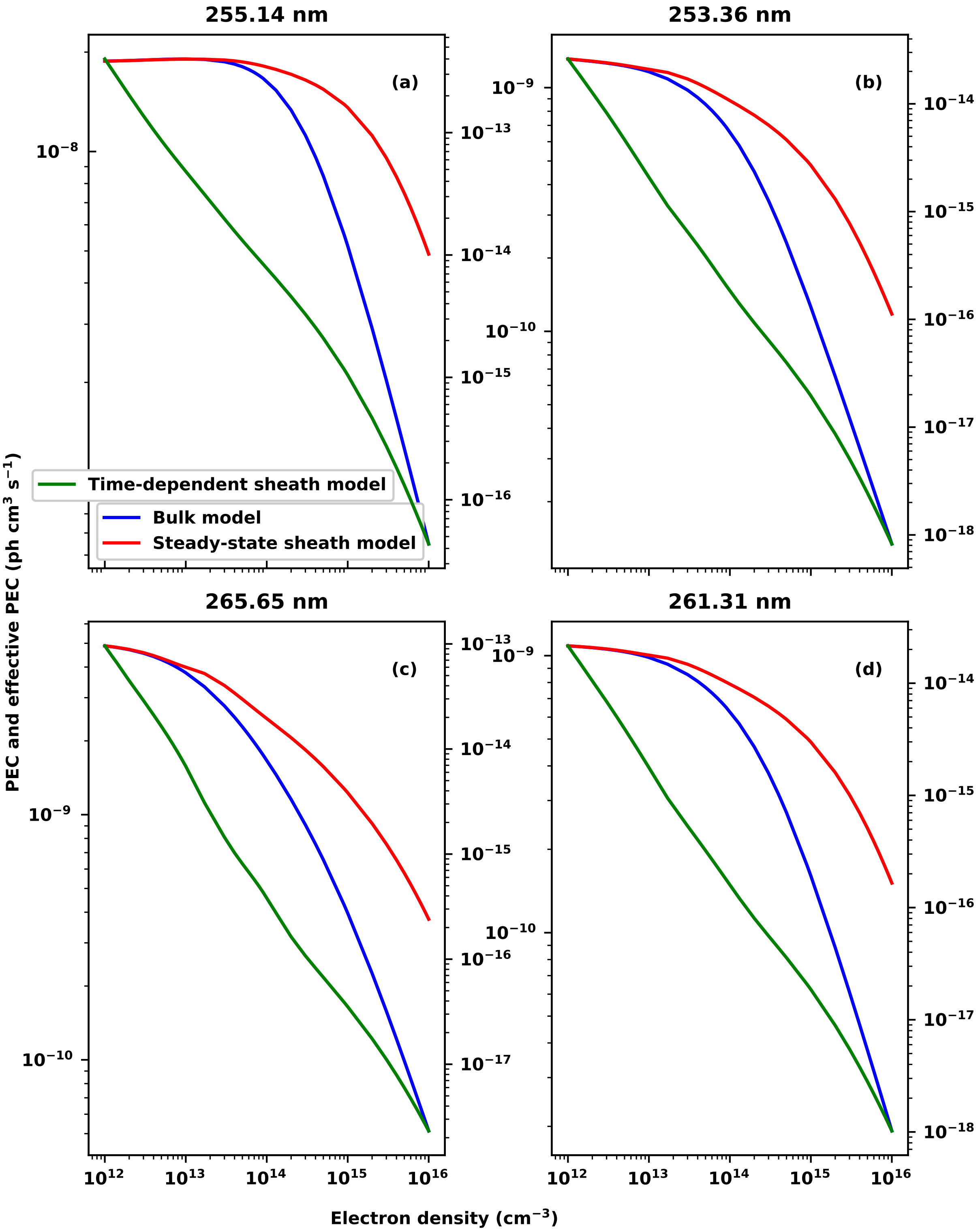

Figure 5.13: Comparison of bulk PEC (blue), steady-state sheath effective PEC (red) and time-dependent sheath effective PEC (green) versus electron density, T_e = 20 eV. Results are shown for the (a) 255.14, (b) 253.36, (c) 265.65 and (d) 261.31 nm lines.

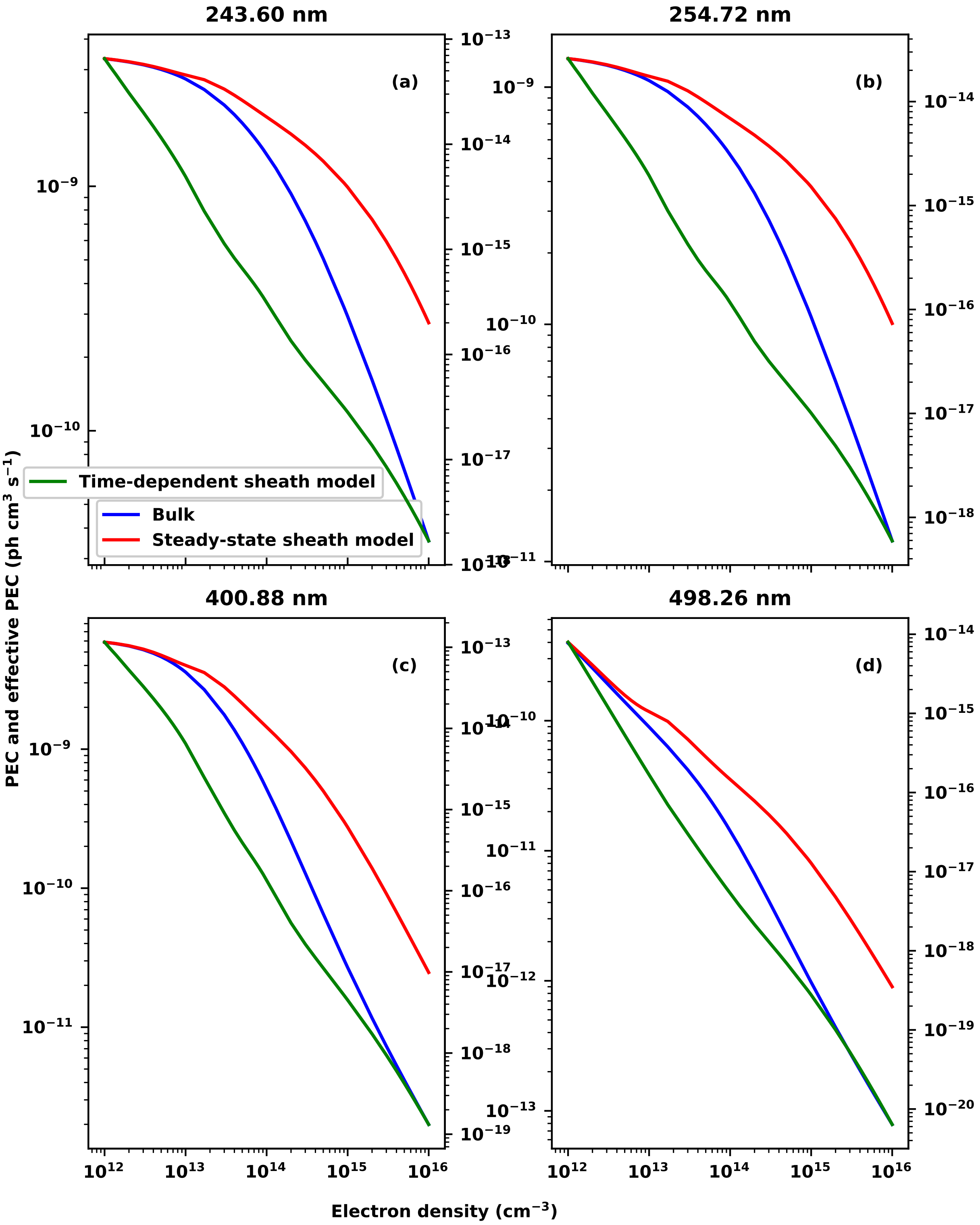

Figure 5.14: Comparison of bulk PEC (blue), steady-state sheath effective PEC (red) and time-dependent sheath effective PEC (green) versus electron density, $T_e = 20$ eV. Results are shown for the (a) 261.31, (b) 243.60, (c) 400.88 and (d) 498.25 nm lines.

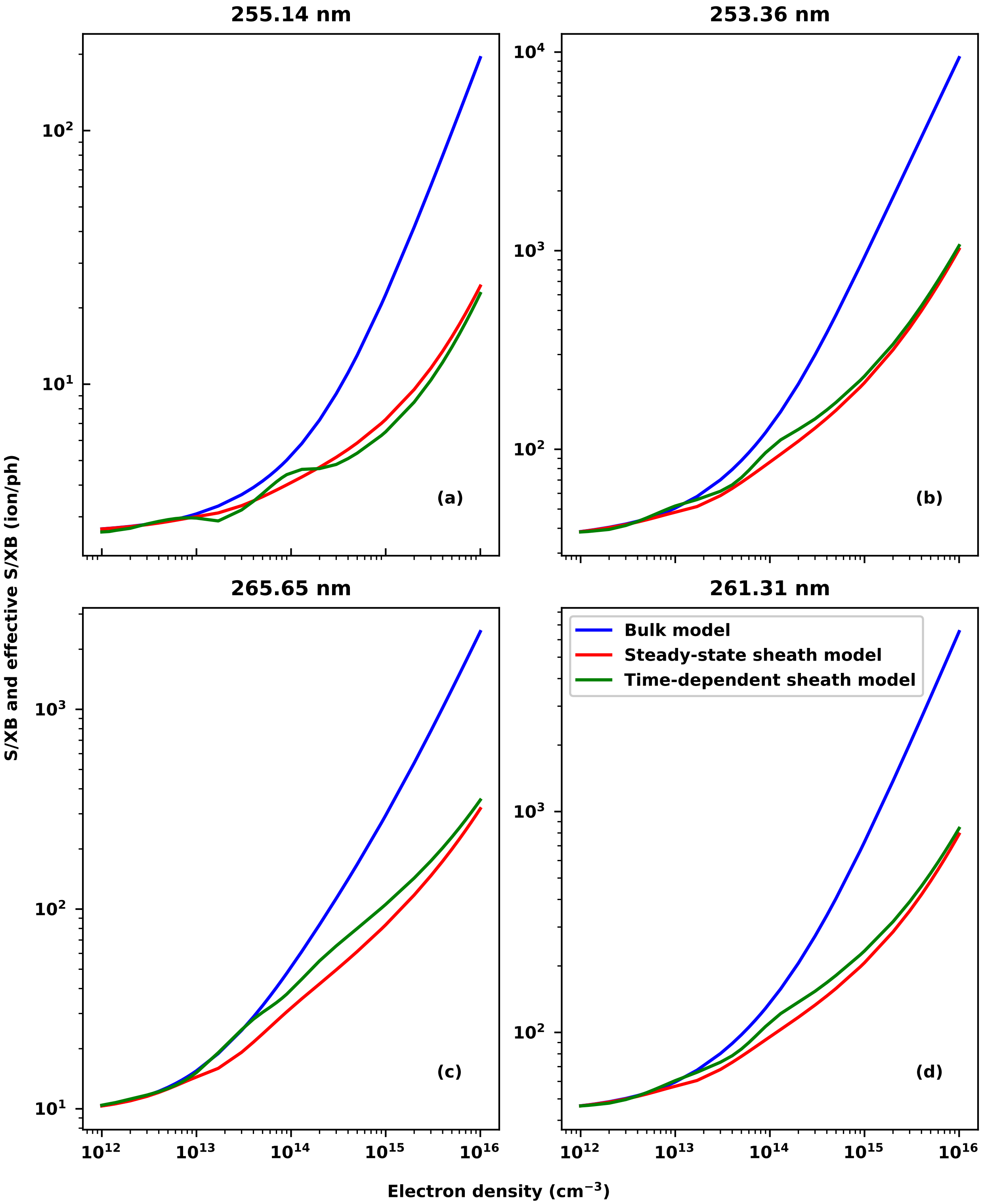

Figure 5.15: Comparison of bulk S/XB (blue), steady-state sheath effective S/XB (red) and time-dependent sheath effective S/XB (green) versus electron density, $T_\mathrm{e} = 20$ eV. Results are shown for the (a) 255.14, (b) 253.36, (c) 265.65 and (d) 261.31 nm lines.

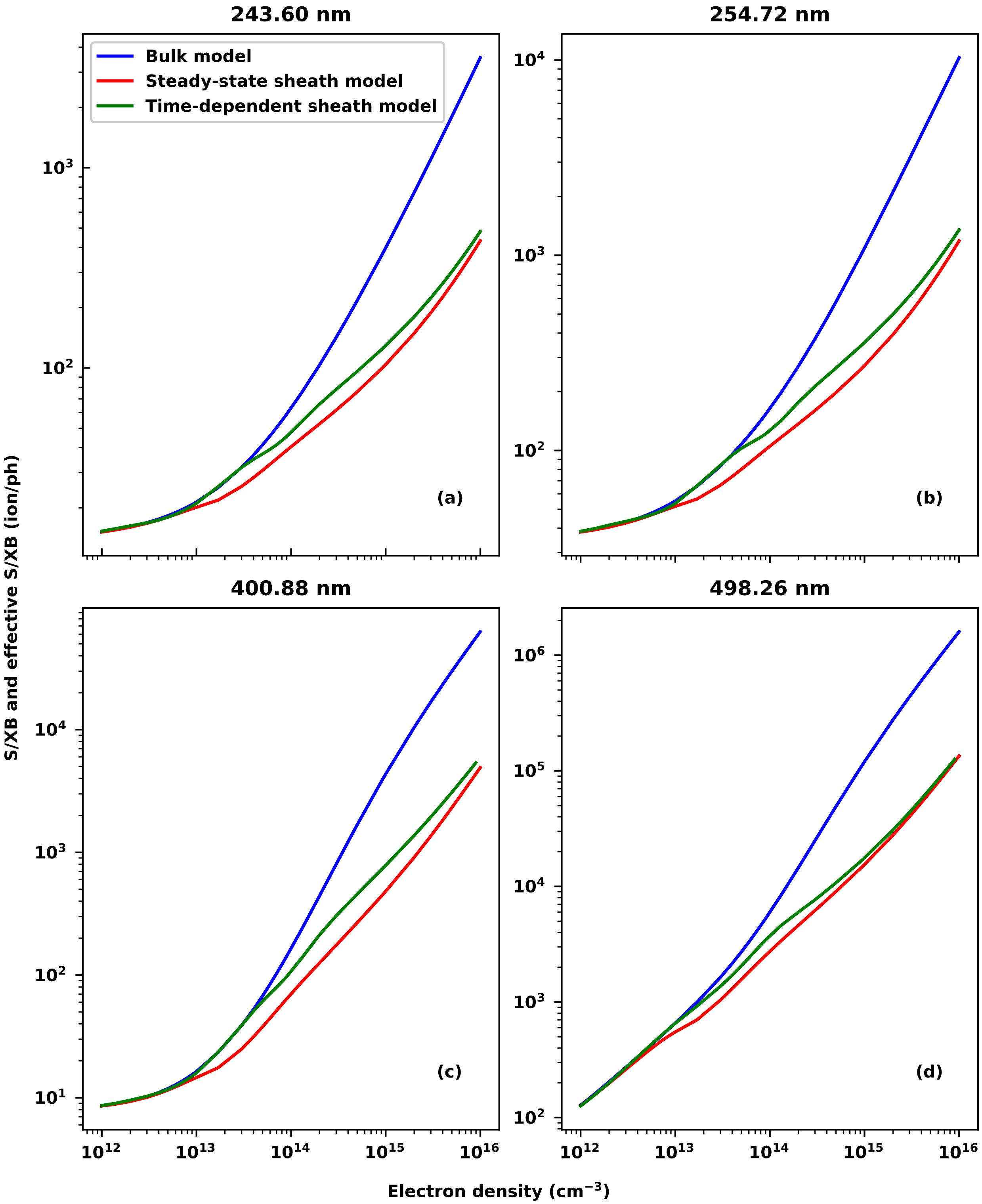

Figure 5.16: Comparison of bulk S/XB (blue), steady-state sheath effective S/XB (red) and time-dependent sheath effective S/XB (green) versus electron density, $T_e = 20$ eV. Results are shown for the (a) 261.31, (b) 243.60, (c) 400.88 and (d) 498.25 nm lines.

The S/XB coefficient is the ratio of the SCD and PEC coefficients. Each of these coefficients is investigated separately first, in order to eliminate any cancellation due to the ratio. It should also be noted that the SCD is of interest on its own as it is used in plasma transport codes such as ERO, so changes in the SCD would have an impact on edge transport code modeling. The SCD coefficient for W I at 20 eV is plotted as a function of density in Figure 5.12. The addition of the sheath model decreases the effective density as seen in Figure 5.9. The SCD coefficient is proportional to electron density so the addition of the sheath causes a decrease in the SCD coefficient. This is consistent with Figure 5.8 showing that low densities take a longer time to come to equilibrium.

Effective PECs are shown in Figures 5.13 and 5.14 for the intense UV lines from Figure 5.2 that are dominated by a single metastable level. Additionally, the widely used 400.88 nm emission line along with the 498.25 nm W I emission line previously observed by Brezinsek *et al.*[86] are also included. These plots show the difference between bulk CR modeling (blue) and Chodura sheath modeling both in steady-state (red) and allowing for the time evolution of W^{0+} states (green). Note that the time-dependent effective PEC coefficient has been integrated through the sheath leaving the coefficient in units of (ph).

The effect of W sputtered velocity on the sheath model

One important input parameter in the Chodura sheath model for sputtering neutral tungsten is the velocity with which the tungsten atoms leave the surface. For a Thompson velocity distribution, the most probable velocity for sputtered particles is half the binding energy (see Behrisch *et al.*[91]). In reality, there could be significant variation to the sputtering velocity dependent on many parameters. As a result, two cases are investigated ($v = v_{\mathrm{w}} \times 10$, $v = v_{\mathrm{w}} \times 0.1$) here in order to establish a bounds on the S/XB coefficient due to sputtering velocity.

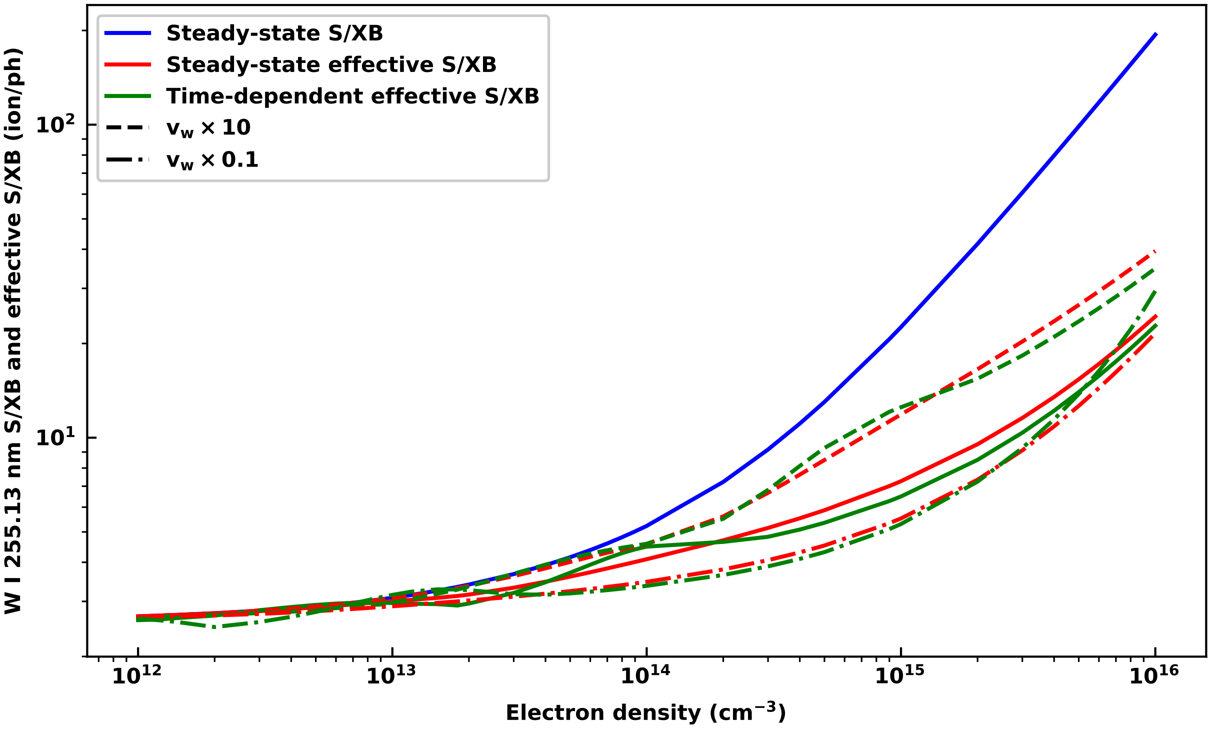

Figure 5.17: Comparison of W I 255.14 nm S/XB versus n_e, at $T_e = 20$ eV for various sputtering velocities (plotted as the dashed lines). The steady-state S/XB is shown in blue, the steady-state Chodura sheath model S/XB is shown in red and the time-dependent Chodura sheath model is shown in green. Variations of the sputtering velocity are indicated as dash-dot and the dashed line.

The variation of the W I 255.14 nm S/XB due to changes in the sputtering velocity is shown in Figure 5.17. The steady-state S/XB (non-sheath model) in blue and the steady-state effective S/XB (Chodura sheath model) in red are plotted alongside the time-dependent effective S/XB (Chodura sheath model) in green for comparison. While there is an interplay of CR effects that impact the exact shape of the line, the dashed line corresponding to a velocity 10 times greater shows a larger S/XB coefficient because at larger velocities the tungsten atoms spend less time in the low density region of the sheath. The simple picture of the 255.14 nm S/XB is that at higher electron density (faster velocity spending less time in the low density sheath) ionization increases giving rise to a larger S/XB. At low electron densities the SCD decreases, so when the tungsten atoms spend more time in the low density region (lower velocity) the S/XB decreases. Though the S/XB is also dependent on the PEC, the PEC will emit in different parts of the sheath depending on sheath parameters, T_e and $\mathrm{n_e}$, this causes the non-monotonic behavior of the S/XB (i.e. the oscillations).

The variation to the W I 400.88 nm S/XB due to changing the sputtering velocity is broadly similar to that of the 255.14 nm and is shown in Figure 5.18; the S/XB is roughly proportional to the velocity. Here the interpretation is a bit clearer than Figure 5.17. At high velocities, more time is spent at higher densities leading to more ionization. The increase in velocity leads to the time-dependent effective S/XB (dashed green line) reproducing the bulk S/XB (blue) for higher electron densities. The behavior of the of 400.88 nm S/XB is consistent with the limiting case of large velocity where the tungsten spends no time within the sheath region and all of the lifetime of the charge state in the bulk plasma. At lower velocities, the tungsten atoms spend more time in the low density region of the sheath, leading to less ionization and a decrease in the S/XB coefficient. Again, the 400.88 nm S/XB is consistent with a slow velocity limiting case where the tungsten spends all its time in the low density region, emitting many photons before being ionized.

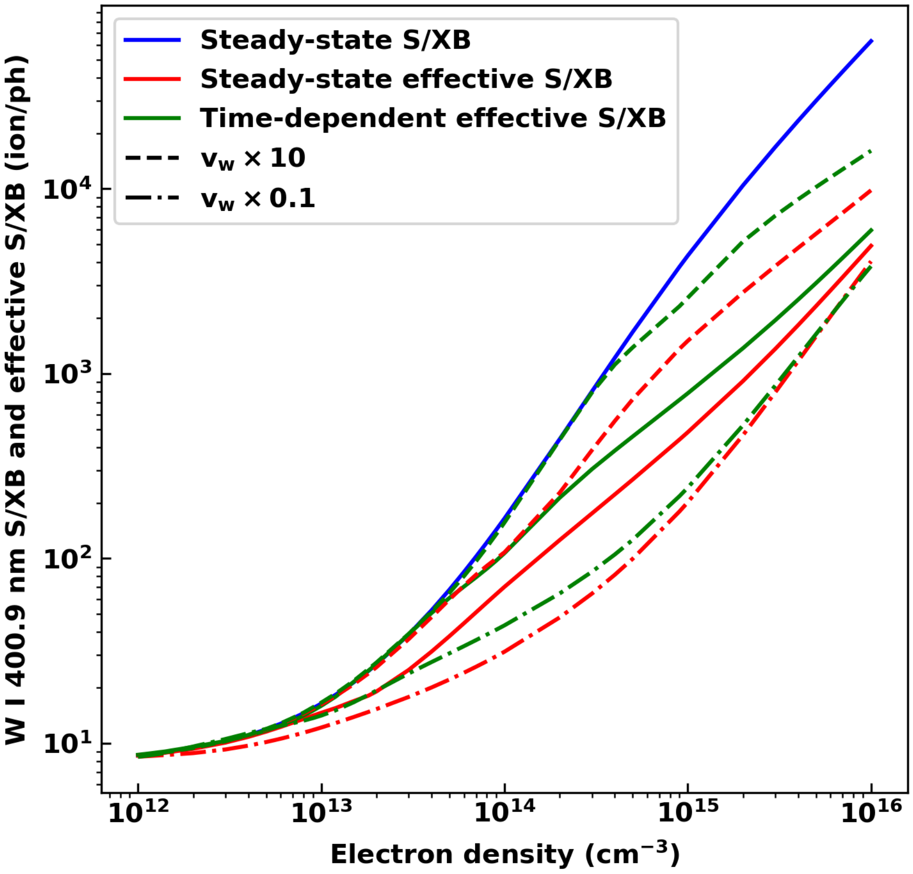

Figure 5.18: Comparison of W I 400.88 nm S/XB versus n_e, at $T_e = 20$ (eV) for various sputtering velocities (plotted as the dashed lines). The steady-state S/XB is shown in blue, the steady-state Chodura sheath model S/XB is shown in red and the time-dependent Chodura sheath model is shown in green. Variations of the sputtering velocity are indicated as the dash-dot and the dashed lines.

Effect of initial metastable fraction on the sheath model

When a CR system has reached steady-state for a set of specified plasma parameters (T_e, n_e), the populations of all levels including metastable levels are in equilibrium. The steady-state population of a given level can change substantially with both temperature and density. Figure 5.19 shows the fractional population in the $^7\mathrm{S}_3$ metastable state versus electron density at multiple temperatures. The decrease in the population of the $^7\mathrm{S}_3$ with electron density can be interpreted in a similar fashion to light systems where population in metastable levels decreases with increasing electron density. The $^7\mathrm{S}_3$ also decreases in population with temperature; this is because transferring population from the $^5\mathrm{D}_0$ ground state requires a spin changing transition. Rate coefficients for spin changing decrease rapidly with increasing electron temperature, making them most effective when the temperature is low and not effective at higher temperatures.

The model described in Section 5.3.1 assumes that neutral tungsten is sputtered from a surface in the ground state. While there is experimental evidence this happens in neutral molybdenum from Marenkov *et al.*,[63] it is quite possible that some fraction of sputtered tungsten starts in a different state. Figures 5.20 and 5.21 investigate the impact of various fractions of sputtered tungsten in the $^7\mathrm{S}_3$ metastable state on the effective S/XB for the W I 400.88 and W I 255.14 nm lines. In this figure, blue is the bulk S/XB, red is the steady-state sheath model S/XB and green is the time-dependent sheath model. Note that the steady-state S/XB sheath model does not depend on initial population as the same steady-state is reached no matter where the electron population starts. The 400.88 nm line is mainly dependent on the $^7\mathrm{S}_3$ metastable, and the 255.14 nm line is mainly dependent on the $^5\mathrm{D}_0$ ground state. As a result, these two S/XB coefficients should be sensitive to the relative population in each driving state. The impact of initial metastable fractional on the S/XB is clear for the 400.88 nm spectral line. The S/XB decreases with increased initial $^7\mathrm{S}_3$ population meaning the 400.88 nm line can be populated much earlier in the sheath because the population does not need to first transfer from $^5\mathrm{D}_0$ to the $^7\mathrm{S}_3$ to then populate

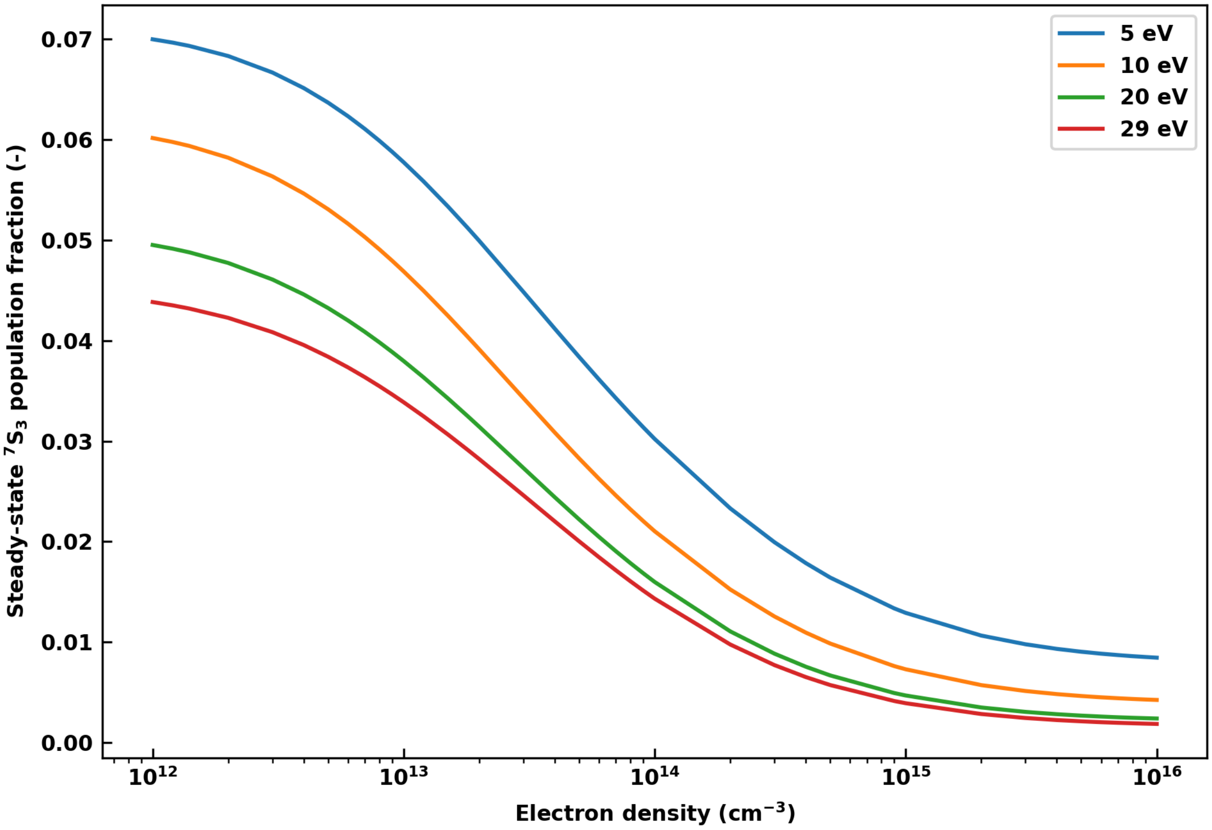

Figure 5.19: Steady-state population fraction of the $^7\mathrm{S}_3$ level versus electron density at multiple T_e values.

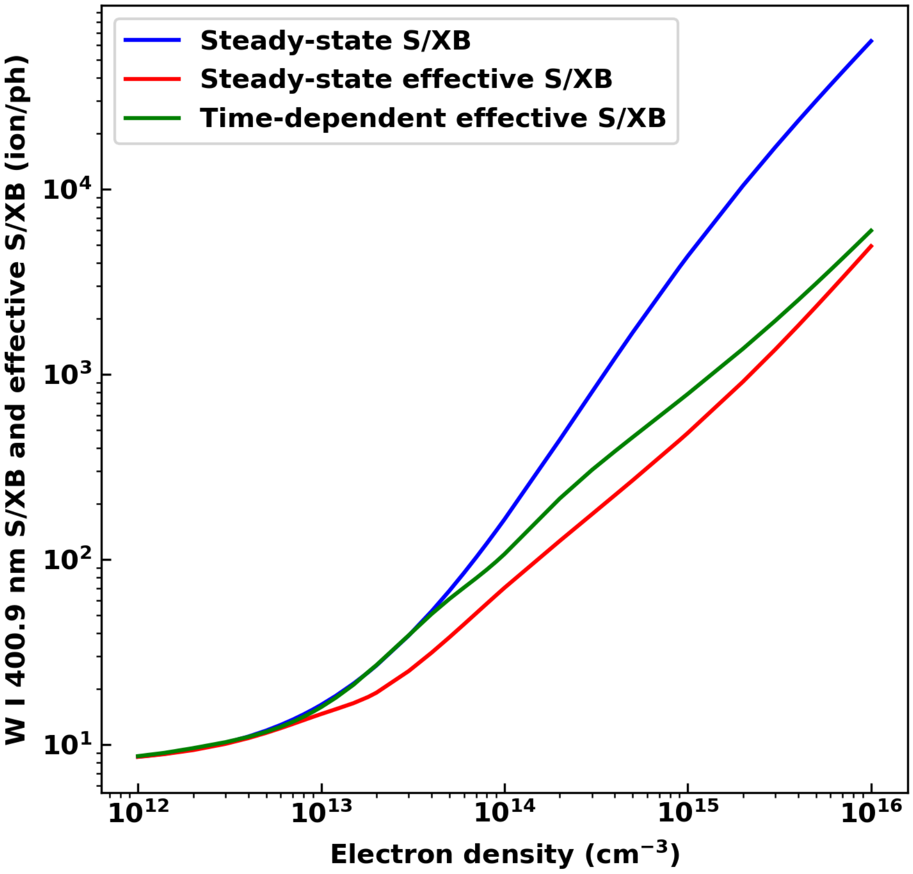

Figure 5.20: Comparison of the W I 400.88 nm S/XB (blue), steady-state effective S/XB (red) and time-dependent S/XB (green) at T_e = 20 (eV) versus n_e while varying the $^7\mathrm{S}_3$ metastable fraction. The solid time-dependent line assumes 100% of the neutral tungsten atoms start in the ground state, the dashed line assumes 0.5% starts in the $^7\mathrm{S}_3$, the dashed-dot line assumes 2% starts in the $^7\mathrm{S}_3$ and the dotted line assumes 10% starts in the $^7\mathrm{S}_3$.

the level that produces the 400.88 nm line. This effect is seen clearly in Figure 5.9 where the population in the level that produces the 255.14 nm emission line (5p^{6}5d^{5}6p (^{5}P$_1$)) peaks earlier than the population in the level that produces the 400.88 nm line.

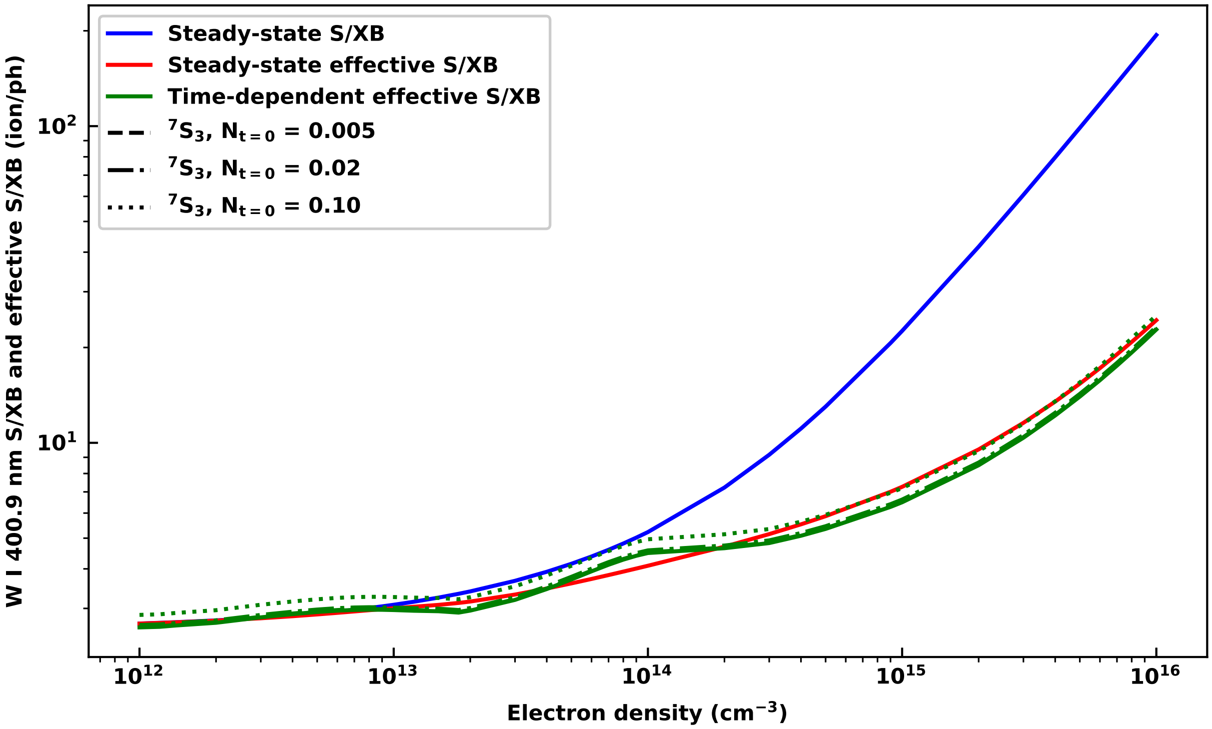

Figure 5.21: Comparison of the W I 255.14 nm S/XB (blue), steady-state effective S/XB (red) and time-dependent S/XB (green) at T_e = 20 (eV) versus n_e while varying the ^{7}S$_3$ metastable fraction. The solid time-dependent line assumes 100% of the neutral tungsten atoms start in the ground state, the dashed line assumes 0.5% starts in the ^{7}S$_3$, the dashed-dot line assumes 2% starts in the ^{7}S$_3$ and the dotted line assumes 10% starts in the ^{7}S$_3$.

The impact of initial population is not as great on the 255.14 S/XB (Figure 5.21). While there is a slight increase in the effective S/XB due to the decrease in initial population of the ^{5}D$_0$, it is not as dramatic as in Figure 5.20 (400.88 nm). The decrease of the initial ^{5}D$_0$ population does not significantly impact the S/XB. This is because even when all of the sputtered tungsten starts in the ^{5}D$_0$ level, population is redistributed quickly from the ground state. When all of the population is in the ^{5}D$_0$ level, the system is far from equilibrium. Figure 5.9 (b) shows that population is quickly removed from the ^{5}D$_0$ and redistributed to other neutral tungsten levels. The fast decrease in the ground state populations means that even when the state starts with 10% less population, the sheath averaged S/XB does not change significantly. This strongly suggests that the most reliable W I spectral lines for use in S/XB diagnostics would be those that are populated from the ground, such as the 255.14 nm line. The line identification work of Chapter 4 would suggest there are no strong lines from this state at visible wavelengths, further motivating the need for UV measurements.

5.4 Comparison of collisional radiative modeling with experimental spectra from CTH

The Langmuir probe describe in Section 2.5 was designed to obtain simultaneous measurements of low charge state tungsten emission along with local T_e and n_e. In the non-sheath collisional radiative model, electron temperature and density are the only two free parameters. When a sheath model is considered, other parameters are introduced; however, T_e and n_e are still the two most sensitive parameters in the model. Constraining T_e and n_e is required to validate the model against CTH plasmas. The spectrometer used for this analysis is described in detail in Section 2.4. For all of the data taken, the spectrometer was run at 500 Hz frame rate, and the power supply for the Langmuir probe was swept at 443 Hz. In order to sample different plasma conditions, the tungsten slug with embedded Langmuir probe was inserted into the plasma between 28-22 cm from the mid-plane for these experiments (note the plasma is limited at 26 cm).

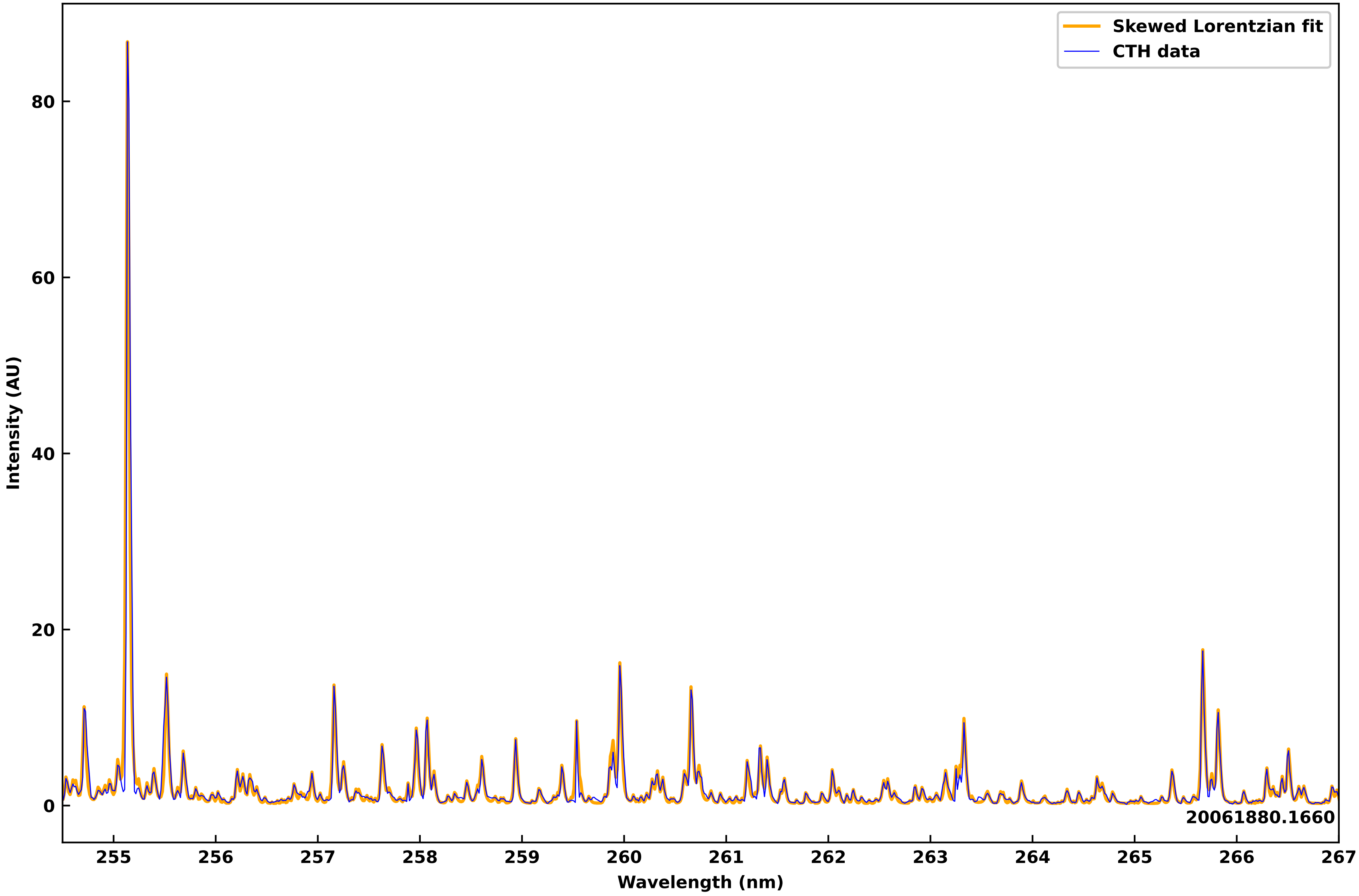

Figure 5.22: Spectroscopy data with the tungsten tipped Langmuir probe inserted to 24 cm into CTH is in blue. The skewed Lorentzian fit to the experimental data is shown in orange.

Data from the spectrometer is fit using least-squares with a function consisting of an arbitrary number of skewed Lorentzian functions with a constant offset. The number of Lorentzians were chosen to be the same as the number of peaks in the spectrum identified by a peak detecting algorithm. Generally, the data from the spectrometer is fit quite well with this function. An example fit to the tungsten spectrum is shown in Figure 5.22. The data in blue corresponds to when the probe is inserted to 24 cm from the CTH mid-plane with the central wavelength chosen to be 261 nm. The fitted function comprised of skewed Lorentzian functions with a constant offset is plotted in orange. Generally, there is good agreement between the data and fitted spectrum. Once the spectrum is fitted, the uncalibrated counts (proxy for emissivity) for a line can be calculated by integrating over the width of the spectral line.

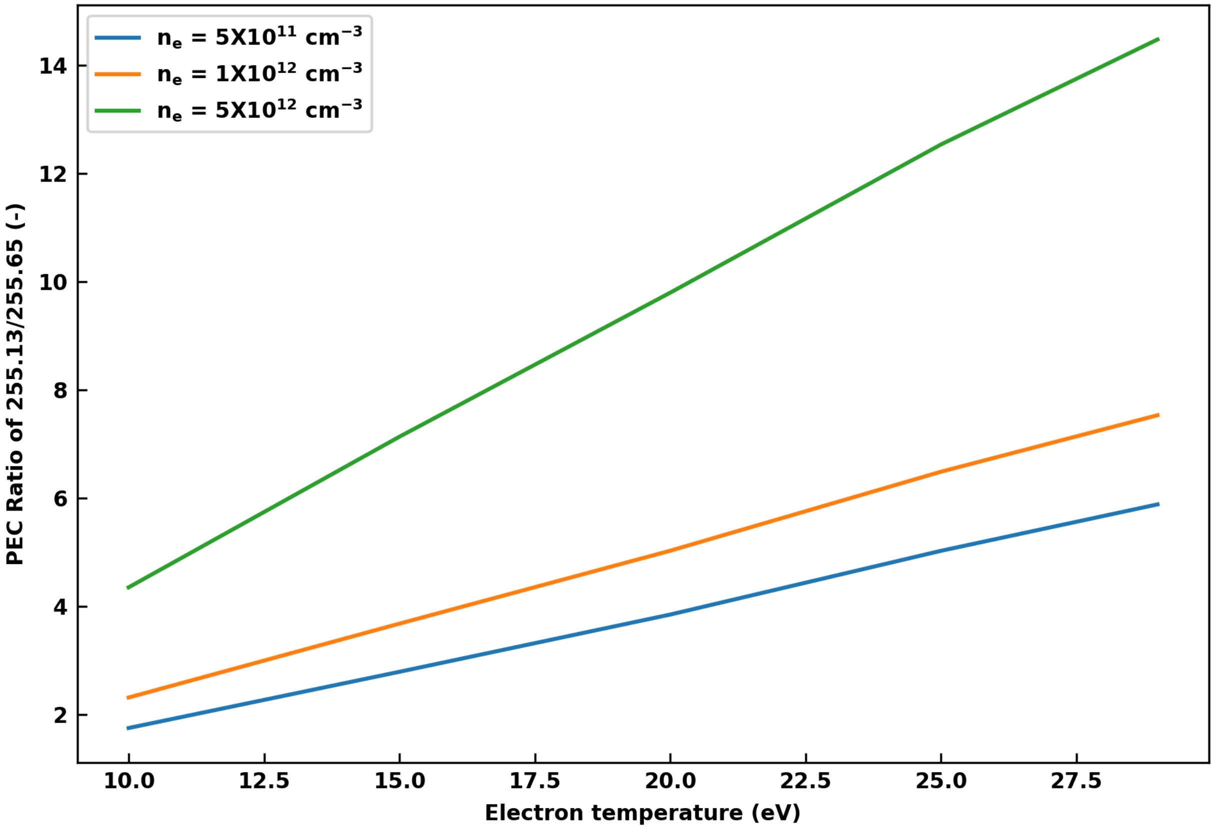

Figure 5.23: PEC ratio of W I 255.14 nm and 265.65 nm emission lines plotted as a function of electron temperature for various electron densities.

5.4.1 Quantification of uncertainties in coronal line ratios

Uncertainties in the line ratio analysis are simplified because the excited states behave in a roughly coronal fashion, as can be seen in Figure 5.5 and is further simplified by the fact that these excited states are dominated by a single metastable level as shown in Figures 5.2 and 5.3. Thus, the uncertainty in the line ratio would have uncertainties in the population modeling and in the A-values. The upper level in each line radiates overwhelmingly to the lower level and doesn't have other strong branches to radiate to. The upper level of the 255.13 nm line radiates 91% to the $^5\mathrm{D}_0$ ground state, and the 265.65 nm line radiates 97% to the $^7\mathrm{S}_3$ metastable level. Because each of these lines radiates dominantly to the ground state or metastable state, the A-value will cancel in coronal line ratio, Equation 3.31. The line ratio then only dependence on the excitation rates from the ground and metastable.

$$I_{j \to i}/I_{l \to k} \approx \frac{q_{\sigma_1 \to j}}{q_{\sigma_2 \to l}} \tag{5.2}$$

The uncertainty in the line ratio then becomes the uncertainty in the two collisional excitation rate coefficients. The fractional uncertainty in the ratio would then be described by the equation below.

$$\frac{\delta_{I_{255}/I_{265}}}{I_{255}/I_{265}} \approx \sqrt{\left(\frac{\delta_{q_{255}}}{q_{255}}\right)^2 + \left(\frac{\delta_{q_{265}}}{q_{265}}\right)^2} \tag{5.3}$$

If the error on a dipole excitation is assumed to be 10%, the excitation rates for the two transitions of $q_{^5D_0 \to 255}$ and $q_{^7S_3 \to 265}$ would lead to an uncertainty on the line ratio of 14%. If an uncertainty of 20% is assumed for each rate, the line ratio ratio would have an uncertainty of 28%. For the error analysis done in Figure 5.26 an error of 10% on the rates were assumed because both transitions are dipole transitions.

5.4.2 Qualification of uncertainty in derived CR coefficients

The unique properties of the neutral tungsten system producing almost coronal PECs allows for the uncertainty to be easily quantified above. However, assigning uncertainties to other CR derived coefficients requires the correlation of the uncertainty of all basic rates. For example, the SCD coefficient depends on the population of each level, and the ionization rate from each level not just a select few pushing this uncertainty quantification beyond the scope of this thesis but the process to assess these uncertainties is described.

To quantify the uncertainty of GCR coefficients, an estimate of the uncertainty of each fundamental atomic rate must be calculated. The uncertainty of fundamental atomic rates can be estimated by making slight changes to the atomic structure of R-matrix or other quantum calculation. Once uncertainties are calculated for each rate, CR modeling can be completed with ColRadPy using Monte Carlo sampling based on the uncertainties of fundamental rates producing uncertainties for the derived coefficients.

5.4.3 Validating the R-matrix neutral tungsten calculation using comparisons to CTH experimental data

Validating the electron impact excitation/de-excitation and spontaneous emission rates from the neutral tungsten R-matrix calculation is challenging. Unlike higher charged systems, no cross-section measurements are available to compare with the quantum calculations. While measurements could be made for ionization from the ground state of neutral tungsten, many of the experimental facilities that could make these measurements are no longer funded. In addition, the NIST database has few measurements of neutral tungsten spontaneous emission coefficients to compare with. Therefore, the best validation comparisons must be done in a plasma environment which includes many additional effects that can impact modeling, the largest likely being the sheath model (including the parameter scans done in previous sections), non-Maxwellian electron distributions and proton collisions. The new tungsten dataset is also not complete since non-perturbative rates are still needed for ionization. Ionization in the model uses ECIP (see Section 3.1.2), which also has the potential to cloud conclusions as these ionization rates are only approximate rates.

The challenges of validating the R-matrix dataset means the best method of benchmarking the predictions is to compare them with multiple spectral lines. The population of different levels (therefore spectral lines) will be impacted differently by the underlying plasma effects (such as sheath conditions). Therefore, by utilizing multiple emission lines (populated from different metastable states), various effects can be distinguished. The first steps to this validation are presented here for two different wavelength regions; future experiments can also expand measurements to the DIII-D tokamak to validate the R-matrix calculation for different plasma conditions.

An extensive survey could be carried out comparing all of the spectral lines from Table 4.1 to fully benchmark the tungsten collisional radiative model. However, this is not done in this thesis as there are a significant amount of free parameters in the model that would need a more detailed treatment than what is provided here. Additionally, a relative calibration was not available for the UV spectrometer which would eliminate a significant amount of experimental uncertainty. There is significant attenuation of UV wavelengths in fibers (see Section 2.2.1). Additionally, the quantum efficiency of the Andor detector is highly peaked in the UV (see Figure 2.6). The spectrometer grating also has a transmission, however, this is even more complicated as it depends on grating angle. These effects could significantly change the relative intensities of lines in the UV wavelength region. As a result of both the experimental uncertainty and need for significant additional modeling needed, a proof of principle here is shown for a few relatively strong UV spectral lines close in wavelength.

The wavelength region of Figure 5.22 has a high density of neutral tungsten lines previously discussed in Section 4.2.1. The ratio of W I 255.14 nm and W I 265.65 nm (see Figure 4.8 for identifications) will be investigated here as it is temperature sensitive. A line ratio that is sensitive to temperature allows the model to be validated more thoroughly than

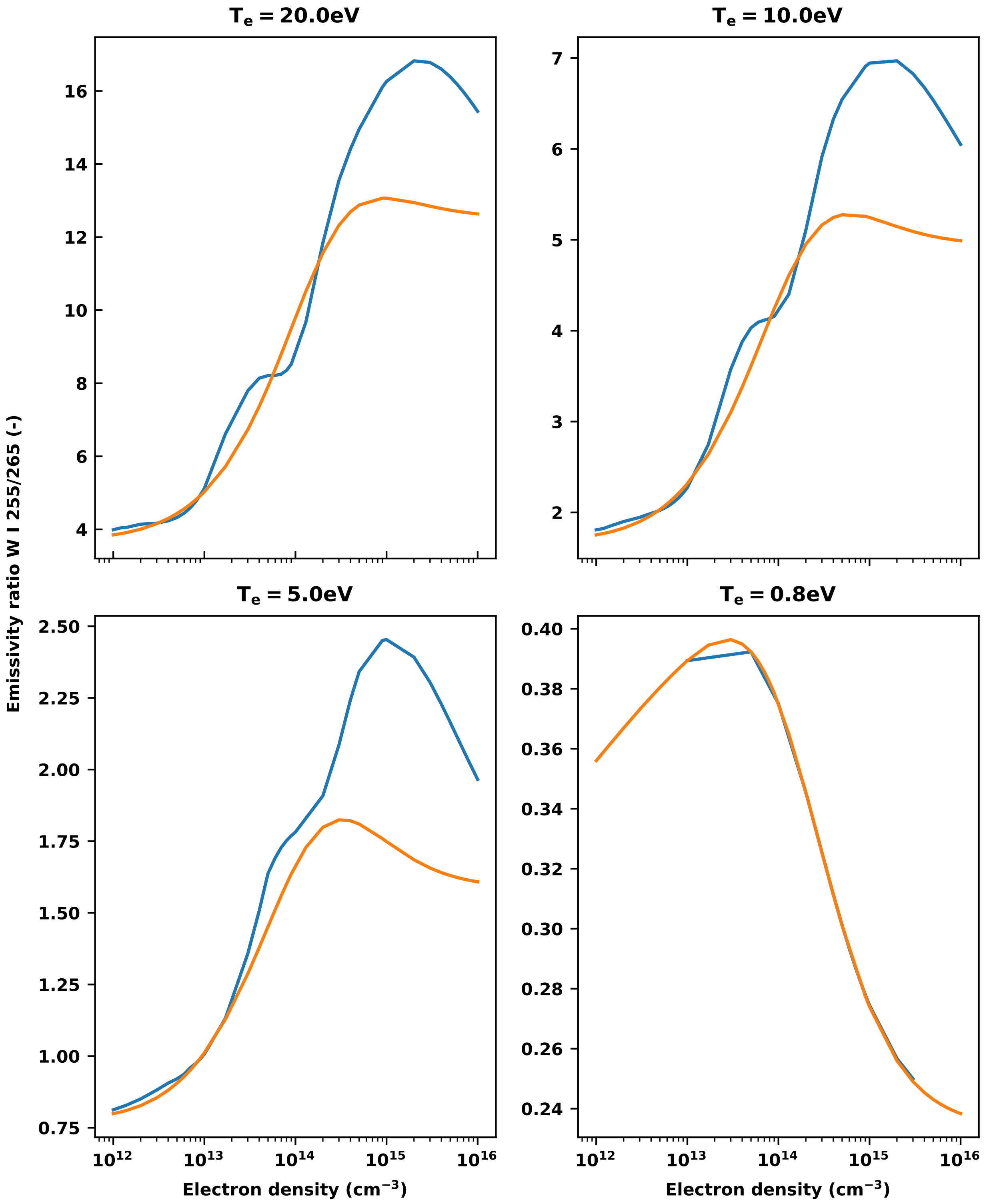

Figure 5.24: Calculated line ratio of emissivities for W I 255.14 nm and 265.65 nm. The line in orange is a bulk model and the line in blue uses a sheath model.

a line ratio that is not sensitive to temperature since line ratios that are not sensitive to temperature would only validate the spontaneous emission coefficients.

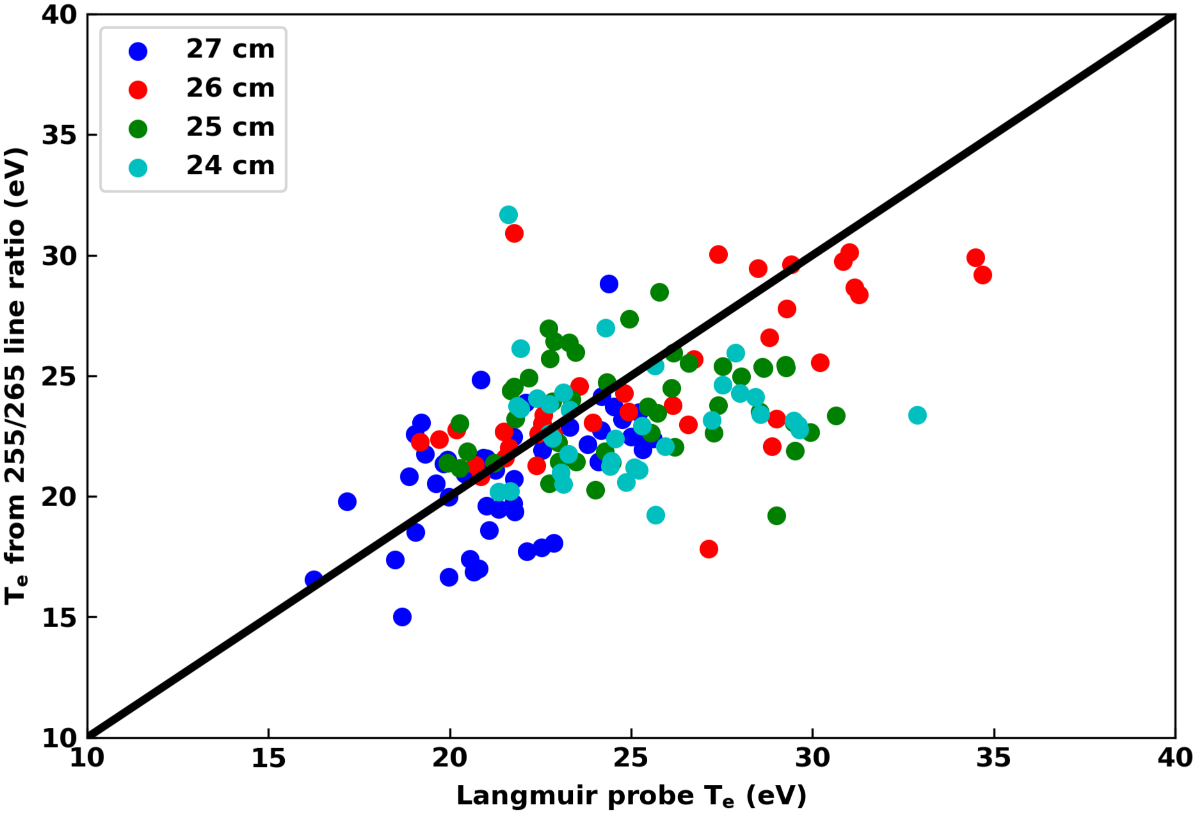

Figure 5.25: Comparison of measured electron temperature from the embedded tungsten Langmuir probe and from line ratio measurements of the W I 255.14 and 265.65 nm lines for four different probe depths.

The comparison of W I spectral lines for CTH plasmas did not incorporate a sheath model. The sheath model can significantly modify calculated CR coefficients at high electron densities as seen in Figures 5.15 and 5.16 for the S/XB. However, the sheath model only slightly modifies these coefficients at low electron density. The ratio of calculated emissivities for the 255/265 nm W I lines behaves similarly as the electron density changes, the ratio is modified only significantly at high electron density. Figure 5.24 shows the emissivity ratio for both a bulk model (orange) and a sheath model (blue) versus density. The sheath model

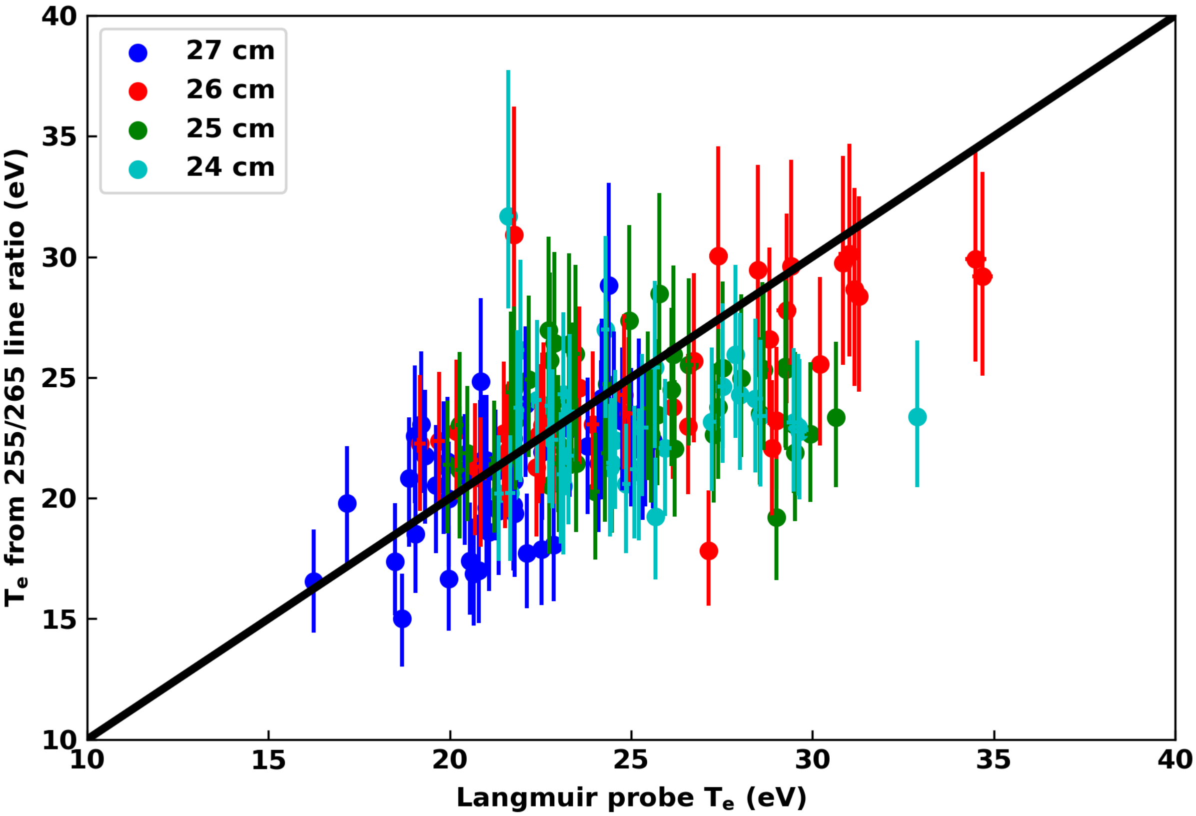

Figure 5.26: Comparison of measured electron temperature from the embedded tungsten Langmuir probe and from line ratio measurements of the W I 255.14 and 265.65 nm lines with error bars from four different probe depths.

does not modify the line ratio significantly at densities relevant for CTH (∼ 30 eV), therefore it has not been included in the modeling of CTH plasmas.

The tungsten atomic data used for comparison to CTH is the same as discussed in Section 5.1.2. The ratio of the 255.14 to 265.65 nm lines has a much stronger dependence on electron temperature with less dependence on electron density. As a result, this ratio provides a good comparison with the temperature measurement of the Langmuir probe. The predicted ratio of the PEC coefficients of the 255.14 to 265.65 nm emission lines is seen in Figure 5.23. This line ratio, while temperature dependent, is also dependent on metastable fraction (see Figure 5.2), and the temperature dependence of the line ratio is most likely due to the metastable fraction also being temperature dependent (see Figure 5.19).

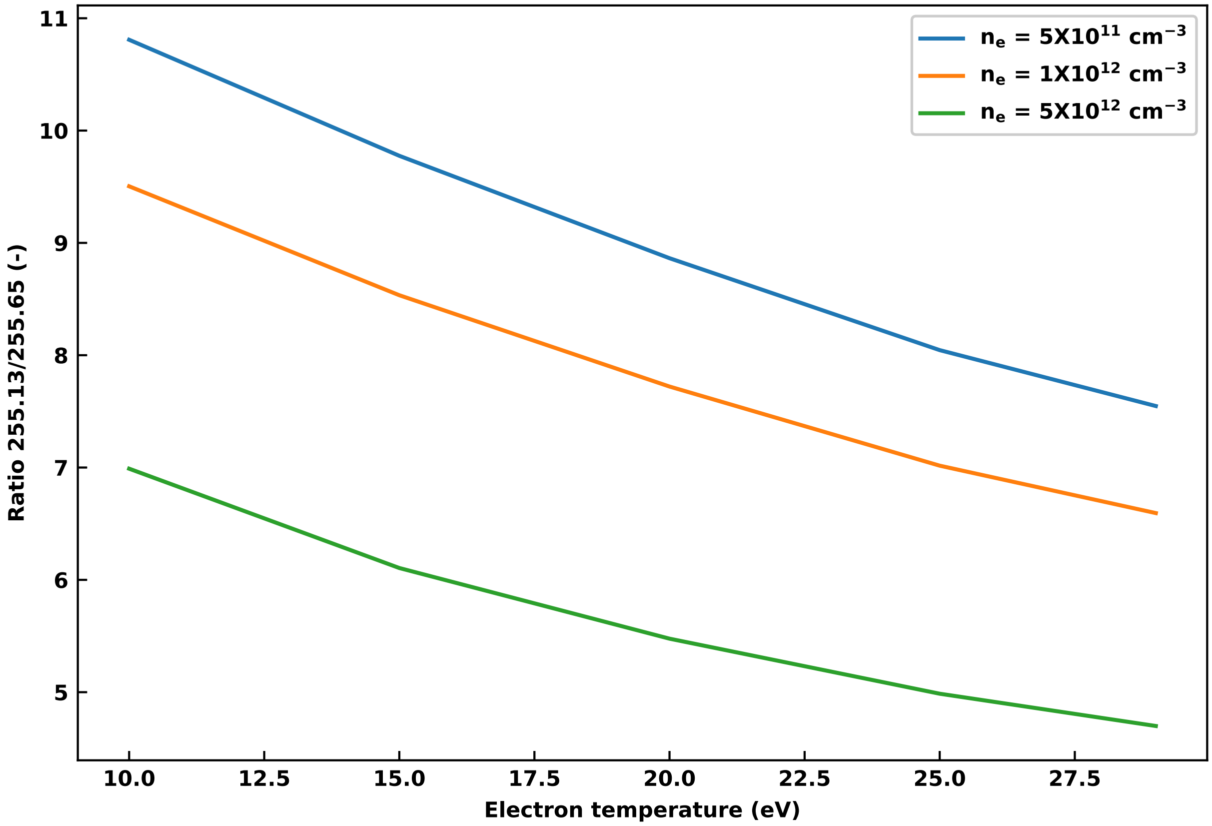

Figure 5.27: PEC ratio of W I 265.65 nm and 269.57 nm plotted as a function of electron temperature for various densities.

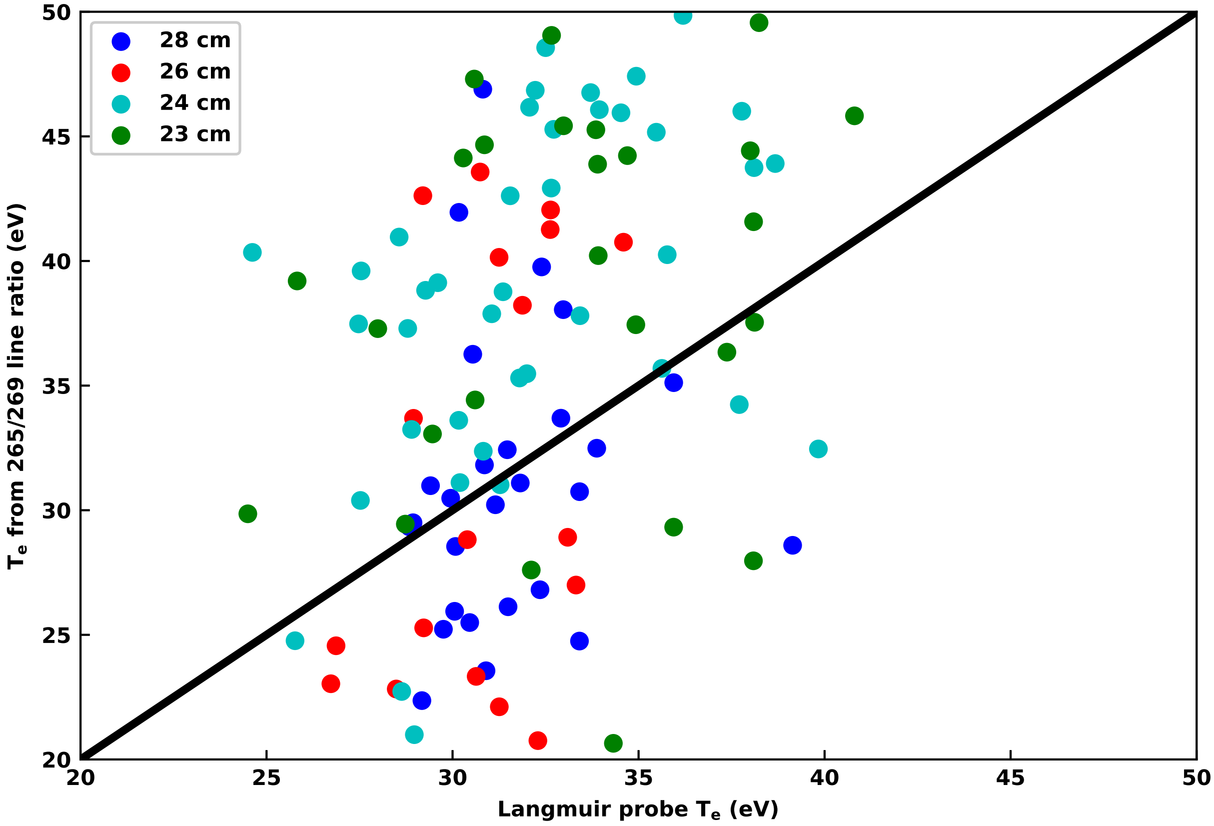

Figure 5.28: Comparison of measured electron temperature from the embedded tungsten Langmuir probe and temperature inferred from line ratio measurements of the W I 265.65 and 269.57 nm lines for four different probe depths.

A sample analysis to obtain temperature and density from the Langmuir probe is shown in Section 2.5. Figure 5.25 shows a comparison of temperature measurements from the Langmuir probe and temperature inferred from the 255.14 to 265.65 nm line ratio as the scattered points. Collisional radiative modeling for the line ratio was completed for the density measured by the Langmuir probe for each spectrometer exposure. A 1:1 line is included in the figure.

Uncertainties from both the Langmuir probe measurement and CR modeling are propagated producing Figure 5.26. The uncertainty of the Langmuir probe was estimated using the standard error method described in Section 2.5.1. As stated before, this method should be treated as a lower bound on the uncertainty from the Langmuir probe. The uncertainty in the Langmuir probe is $\sim$1 eV for most of the sweeps shown here. Uncertainty from the CR modeling was propagated using method describe in Section 5.4.1. The uncertainty of from the CR inferred line ratio varies between 4-8 eV increasing with the measured electron temperature. This is a result of the constant 14.8% uncertainty of the line ratio and the slope of line ratio with electron temperature seen in Figure 5.27.

Most of the temperature pairs agree within a few eV of each other; representing strong agreement between the inferred temperature from the line ratio and measurements from the Langmuir probe, especially considering the limitations of probe measurements as well as uncertainties in the line ratio diagnostics. The data from the plot is an ensemble of four different shots at each of the four different probe locations. The scatter about the 1:1 line has slightly more points below the line suggesting that the inferred temperature from the line ratio method is systematically lower than the temperature from the Langmuir probe.

Figure 5.28 shows a comparison of temperature from the Langmuir probe and temperature inferred from the 265.65 to 269.57 nm line ratio as the scatter points. While there is significantly more scatter in Figure 5.28 than Figure 5.25, there is still relatively good agreement between the temperature measured from the Langmuir probe and temperature inferred from the line ratio of the W I 265.65 nm and 269.57 nm lines. Some of the scatter can likely be attributed to the less intense 266.57 nm line. Collisional radiative modeling for the line ratio was done at the density measured by the Langmuir probe for each spectrometer exposure. A 1:1 line is shown as the black line in the figure. The data from the plot is an ensemble of three different shots for each of the four different probe locations. The density dependence of the W I 265.65 nm to 269.57 line ratio (seen in Figure 5.28) could also be playing a part in the scatter of the experimental data.

In summary, this chapter has shown that careful consideration of the populating mechanisms for excited states in tungsten, along with time-dependent considerations for the metastable states in the plasma sheath, is important for building an accurate model to diagnose tungsten erosion. The atomic data in the model has been benchmarked against spectroscopic measurements on CTH, and there are a number of parameters that should be further constrained for accurate sheath modeling (i.e., the percentage of sputtered tungsten atoms initially in the ground state and the sputtered velocity). High resolution ultraviolet measurements would allow these parameters to be better determined, as well as giving information on metastable populations.

Chapter 6

Conclusion and future work

6.1 Experimental accomplishments

Experimentally, survey spectrometers were installed on both the DIII-D (for the tungsten ring experiment) and CTH devices. Custom LabVIEW software was written to control the spectrometers and store data. The measurements from survey spectrometers were essential in initial neutral tungsten spectral line identification. The survey spectrometers were also instrumental in identifying wavelength regions of interest for a high-resolution spectrometer as well as resolution requirements. The relatively low spectral resolution as well as throughput of the survey spectrometers made it clear that a high-resolution spectrometer capable of more throughput was required. To address these experimental requirements, a new UV optimized high-resolution spectrometer was procured, tested and installed on CTH and will be installed on DIII-D for a campaign with tungsten tiles in a closed divertor. Custom software was written in Python to control both the Andor camera and the Princeton Instruments IsoPlane spectrometer. From collisional radiative modeling, it became clear that electron temperature and density measurements were needed to constrain the models. To make local temperature and density measurements, a single tipped Langmuir probe embedded into a tungsten slug was designed and installed on CTH for electron temperature and density measurements. The new probe provided simultaneous temperature, density and spectroscopy measurements to constrain the CR modeling as expected. Additionally, this was the first direct electron temperature measurement in CTH with current drive.

A spectral survey of W and Mo was carried out in CTH measurements from both the survey and high-resolution spectrometers. The more useful data came from the high-resolution spectrometer$\sim$200-400 nm, where emission lines from W^{0+}, W^{1+} and W^{2+} were identified. No spectral lines from W^{3+} could be identified within this wavelength range; this is consistent with a theoretical model which predicts most strong emission lines at vacuum ultra violet wavelengths (< 180 nm) for that ion. Over 50 W I emission lines were identified in CTH where theoretical predictions are also available (over 30 of these identified for the first time in a fusion relevant plasma). In addition to tungsten, many molybdenum spectral lines were also observed and identified in the UV. As well as providing spectra that can be used to categorize which Mo spectral lines could be used for future diagnostics, the Mo spectra also proved to be useful in analysis of the tungsten probe spectra, as the behavior of background impurity emission lines could be easily observed.

6.2 Theoretical accomplishments

A detailed theoretical investigation of collisional radiative modeling for neutral tungsten has been carried out. To facilitate the theoretical models required to model neutral tungsten emission and Generalized Collisional Radiative (GCR) coefficients, a new collisional radiative code ColRadPy was developed from scratch using Python. ColRadPy was later released to the plasma community as it filled a need in various research applications. ColRadPy is now being used in many different areas of plasma research from basic low temperature to high-temperature fusion relevant plasmas. The ability to solve the collisional radiative system of equations time dependently makes ColRadPy unique among collisional radiative codes (codes like ADAS use the quasistatic approximation to solve this system of equations). The time-dependent feature is potentially required to accurately model the effective S/XB coefficient as the high electron densities likely would be present in experiments such as ITER.

6.3 Results from neutral tungsten measurements and modeling

There have been multiple advances in understanding the neutral tungsten CR system by combining new ColRadPy collisional radiative modeling and the new high quality atomic data that has been generated. The importance of metastable levels in modeling neutral tungsten PECs and GCR coefficients was studied in detail for the first time. Most of the strong tungsten emission lines were shown to be populated by a single metastable level. The intermediate populating mechanisms for CR systems was described for the first time for C, Mo and W. This showed that intense W I emission lines are mostly populated by one excitation from the metastable that dominates the emission rather than being populated from a variety of excited states. CR modeling has established that the large number of metastables in neutral tungsten can be attributed to the large number of levels with smaller loss rates than the ground level. The significant number of metastable levels in conjunction with intense spectral lines being dominated by a single metastable level makes time-dependent modeling of metastable levels potentially necessary for neutral tungsten.

While the time required for neutral tungsten to reach equilibrium is directly proportional to the electron density, fusion plasmas could still have a significant portion of neutral tungsten emission coming from regions that are not in steady-state due to sheath effects. A simple model was developed where density gradients near the wall due to the Chodura/Debye sheath was considered and neutral tungsten sputtered from a surface started in the ground state. Neutral tungsten was assumed to sputter off the surface with a velocity half the binding energy for tungsten and coming off perpendicular to the surface. Modeling shows that for high density plasmas, the sheath averaged effects must be accounted for. Sheath effects can lead to a modification of the S/XB coefficients that are significantly different from bulk plasma parameters. The sheath averaged model can produce differences in the S/XB coefficient of up to an order magnitude. These changes in the S/XB could lead to erosion measurements that are an order of magnitude different from what would be expected from calculations that do not account for the plasma sheath. A basic parameter scan of the sheath model inputs shows that there can be significant modification to the S/XB coefficients with changes in these parameters (initial velocity and starting metastable state). More experimental measurements at different bulk plasma conditions are needed to constrain the uncertainty in these free parameters (i.e. what is initial velocity and starting metastable state).

An experimental measurements of W I emission lines and Langmuir probe data were then compared to theoretical models. For the density region of CTH, a sheath model was shown to not be necessary as the addition of a sheath model only lead to ∼5% difference in calculated values. The line ratio of W I 255.14 nm to 265.65 nm was shown to be in good agreement between the inferred temperature from experimentally measured line ratio and collisional radiative theory when compared with the electron temperature measurements from the Langmuir probe.

6.4 Future work

Future extensions of this work will include the installation of the high-resolution spectrometer on the DIII-D tokamak. The new high-resolution spectrometer will be used for dedicated experiments to test the models developed on CTH; these models will be expanded to different plasma conditions present in DIII-D. The calculated S/XB can also be compared with a measured S/XB in DIII-D. The high-resolution spectrometer will also be useful for erosion and redeposition diagnosis in the SAS-1W campaign which will support other experiments. The next step for the theoretical work is the expansion to W^{1+} modeling. The addition of W^{1+} will allow for net erosion and redeposition to be measured spectroscopically by simultaneously measuring W^{0+} and W^{1+}. Additionally, tungsten could in the future be tracked through the various charge states to better understand divertor leakage and long scale transport of tungsten in the divertor region (tungsten transporting beyond the last closed flux surface). Error propagation from the basic atomic cross-section through the collisional radiative equations through a Monte Carlo method to the derived coefficients should also be investigated. This will give more confidence to the uncertainty propagated through the atomic data. Work on this propagation method is ongoing with He-like systems and could be applied to the more complicated near neutral tungsten systems.

Bibliography

[1] Jerome Guterl, Tyler Abrams, Curtis Johnson, Aaro Einari Jaervinen, H Q Wang, Adam G McLean, Dmitry L Rudakov, William R Wampler, Houyang Guo, and Philip B Snyder. ERO modeling and analysis of tungsten erosion and migration from a toroidally symmetric source in DIII-D divertor. *Nuclear Fusion*, 2019.

[2] A Pospieszczyk, D Borodin, S Brezinsek, A Huber, A Kirschner, Ph Mertens, G Sergienko, B Schweer, I L Beigman, and L Vainshtein. Determination of rate coefficients for fusion-relevant atoms and molecules by modelling and measurement in the boundary layer of TEXTOR. *Journal of Physics B: Atomic, Molecular and Optical Physics*, 43(14):144017, 2010.

[3] Yu. M. Smirnov. Excitation cross sections of low-lying levels of the tungsten atom. *Optics and Spectroscopy*, 104(6):809–817, 2008.

[4] G. Sergienko, B. Bazylev, A. Huber, A. Kreter, A. Litnovsky, M. Rubel, V. Philipps, A. Pospieszczyk, Ph. Mertens, U. Samm, B. Schweer, O. Schmitz, and M. Tokar. Erosion of a tungsten limiter under high heat flux in TEXTOR. *Journal of Nuclear Materials*, 363:96–100, 2007.

[5] I. Beigman, A. Pospieszczyk, G. Sergienko, I. Yu Tolstikhina, and L. Vainshtein. Tungsten spectroscopy for the measurement of W-fluxes from plasma facing components. *Plasma Physics and Controlled Fusion*, 49(11):1833–1847, 2007.

[6] G. J. Van Rooij, J. W. Coenen, L. Aho-Mantila, S. Brezinsek, M. Clever, R. Dux, M. Groth, K. Krieger, S. Marsen, G. F. Matthews, A. Meigs, R. Neu, S. Potzel, T. Pütterich, J. Rapp, and M. F. Stamp. Tungsten divertor erosion in all metal devices: Lessons from the ITER like wall of JET. *Journal of Nuclear Materials*, 438:S42–S47, 2013.

[7] S. Brezinsek, D. Borodin, J.W. Coenen, D. Kondratjew, M. Laengner, A. Pospieszczyk, and U. Samm. Quantification of tungsten sputtering at W/C twin limiters in TEXTOR with the aid of local WF 6 injection. *Physica Scripta T*, T145, 2011.

[8] A. Pospieszczyk, T. Tanabe, V. Philipps, G. Sergienko, T. Ohgo, K. Kondo, M. Wada, M. Rubel, W. Biel, A. Huber, A. Kirschner, J. Rapp, and N. Noda. Operation of TEXTOR-94 with tungsten poloidal main limiters. *Journal of Nuclear Materials*, 290:947–952, 2001.

[9] the way to new energy.

[10] R.A. Pitts, S. Carpentier, F. Escourbiac, T. Hirai, V. Komarov, S. Lisgo, A.S. Kukushkin, A. Loarte, M. Merola, A. Sashala Naik, R. Mitteau, M. Sugihara, B. Bazylev, and P.C. Stangeby. A full tungsten divertor for ITER: Physics issues and design status. *Journal of Nuclear Materials*, 438:S48–S56, July 2013.

[11] A Q Kuang, S Ballinger, D Brunner, J Canik, A J Creely, T Gray, M Greenwald, J W Hughes, J Irby, B LaBombard, B Lipschultz, J D Lore, M L Reinke, J L Terry, M Umansky, D G Whyte, and S Wukitch. Divertor heat ux challenge and mitigation in SPARC. *Astrophysical Journal*, page 28, 2020.

[12] C. H. Skinner, A. A. Haasz, V. Kh. Alimov, N. Bekris, R. A. Causey, R. E. H. Clark, J. P. Coad, J. W. Davis, R. P. Doerner, M. Mayer, A. Pisarev, J. Roth, and T. Tanabe. Recent Advances on Hydrogen Retention in ITERs Plasma-Facing Materials: Beryllium, Carbon, and Tungsten. *Fusion Science and Technology*, 54(4):891–945, November 2008.

[13] A.G. McLean, P.C. Stangeby, B.D. Bray, S. Brezinsek, N.H. Brooks, J.W. Davis, R.C. Isler, A. Kirschner, R. Laengner, C.J. Lasnier, Y. Mu, J. Munoz, D.L. Rudakov, O. Schmitz, E.A. Unterberg, J.G. Watkins, D.G. Whyte, and C.P.C. Wong. Quantification of chemical erosion in the DIII-D divertor and implications for ITER. *Journal of Nuclear Materials*, 415(1):S141–S144, August 2011.

[14] G Sergienko, G Arnoux, S Devaux, G F Matthews, I Nunes, V Riccardo, A Sirinelli, A Huber, S Brezinsek, J W Coenen, Ph Mertens, V Philipps, U Samm, and JET EFDA contributors. Movement of liquid beryllium during melt events in JET with ITER-like wall. *Physica Scripta*, T159:014041, April 2014.

[15] K. Holtrop, D. Buchenauer, C. Chrobak, C. Murphy, R. Nygren, E. Unterberg, and M. Zach. The design and use of tungsten coated tzm molybdenum tile inserts in the diii-d tokamak divertor. *Fusion Science and Technology*, 72(4):634–639, 2017.

[16] P C Stangeby. Assessing material migration through ^{13}C injection experiments. *Journal of Nuclear Materials*, 415(1):S278 – S283, 2011.

[17] T. Pütterich, R. Neu, R. Dux, A. D. Whiteford, M. G. O'Mullane, H. P. Summers, and the ASDEX Upgrade Team. Calculation and experimental test of the cooling factor of tungsten. *Nuclear Fusion*, 50(2):25012, 2010.

[18] S. Brezinsek, A. Pospieszczyk, G. Sergienko, R. Dux, M. Cavedon, M. Faitsch, and K. Krieger. Chemically assisted physical sputtering of Tungsten: Identification via the 6 6 + transition of WD in TEXTOR and ASDEX Upgrade plasmas. *Nuclear Materials and Energy*, 18:50–55, January 2019.

[19] J. Guterl, T. Abrams, C.A. Johnson, A. Jaervinen, H.Q. Wang, A.G. McLean, D. Rudakov, W.R. Wampler, H.Y. Guo, and P. Snyder. ERO modeling and analysis of tungsten erosion and migration from a toroidally symmetric source in the DIII-D divertor. *Nuclear Fusion*, 60(1):016018, January 2020.

[20] S. Brezinsek, A. Kirschner, M. Mayer, A. Baron-Wiechec, I. Borodkina, D. Borodin, I. Coffey, J. Coenen, N. den Harder, A. Eksaeva, C. Guillemaut, K. Heinola, A. Huber, V. Huber, M. Imrisek, S. Jachmich, E. Pawelec, M. Rubel, S. Krat, G. Sergienko, G.F. Matthews, A.G. Meigs, S. Wiesen, A. Widdowson, and JET contributors. Erosion,

screening, and migration of tungsten in the JET divertor. *Nuclear Fusion*, 59(9):096035, September 2019.

[21] E. A. Unterberg. Multiple Tungsten Divertor Source, Migration and Core Impact Characterization for DIII-D ELM-y H-mode Conditions. In *16th International Conference on Plasma-Facing Materials and Components for Fusion Applications*, 2017.

[22] T. Abrams, D. M. Thomas, E. A. Unterberg, and A. R. Briesemeister. Advances in Low-Temperature Tungsten Spectroscopy Capability to Quantify DIII-D Divertor Erosion. *IEEE Transactions on Plasma Science*, PP(99):1–8, 2018.

[23] G. J. Hartwell, S. F. Knowlton, J. D. Hanson, D. A. Ennis, and D. A. Maurer. Design, Construction, and Operation of the Compact Toroidal Hybrid. *Fusion Science and Technology*, 72(1):76–90, 2017.

[24] M. C. Miller, J. D. Hanson, G. J. Hartwell, S. F. Knowlton, D. A. Maurer, and B. A. Stevenson. Design and implementation of a multichannel millimeter wave interferometer for the compact toroidal hybrid experiment. *Review of Scientific Instruments*, 83(10), 2012.

[25] Curtis Alan Johnson, David Ennis, Stuart D Loch, Greg Hartwell, David A Maurer, Steve L Allen, Brian S Victor, Cameron Samuell, Tyler Abrams, Ezekial Unterberg, and Ryan Thomas Smyth. Advances in neutral tungsten ultraviolet spectroscopy for the potential benefit to gross erosion diagnosis. *Plasma Physics and Controlled Fusion*, 2019.

[26] https://www.stellarnet.us.

[27] Princeton Instruments. IsoPlane Manual Version 1.B, 2013.

[28] Kevin Henricus Annemarie Verhaegh. *Spectroscopic investigations of detachment on TCV*. PhD thesis.

[29] Kevin Henricus and Annemarie Verhaegh. Spectroscopic investigations of detachment on TCV. (September), 2018.

[30] Andrew Guthrie. *The characteristics of electrical discharges in magnetic fields*. McGraw-Hill, 1949.

[31] Evgeny V. Shunko. *Langmuir probe in theory and practice*. Universal Publishers, 2009.

[32] H. M. Mott-Smith and Irving Langmuir. The theory of collectors in gaseous discharges. *Phys. Rev.*, 28:727–763, Oct 1926.

[33] P C Stangeby. A problem in the interpretation of tokamak langmuir probes when a fast electron component is present. *Plasma Physics and Controlled Fusion*, 37(9):1031–1037, sep 1995.

[34] Pauli Virtanen, Ralf Gommers, Travis E. Oliphant, Matt Haberland, Tyler Reddy, David Cournapeau, Evgeni Burovski, Pearu Peterson, Warren Weckesser, Jonathan Bright, Stefan J. van der Walt, Matthew Brett, Joshua Wilson, K. Jarrod Millman, Nikolay Mayorov, Andrew R. J. Nelson, Eric Jones, Robert Kern, Eric Larson, CJ Carey, lhan Polat, Yu Feng, Eric W. Moore, Jake Vand erPlas, Denis Laxalde, Josef Perktold, Robert Cimrman, Ian Henriksen, E. A. Quintero, Charles R Harris, Anne M. Archibald, Antonio H. Ribeiro, Fabian Pedregosa, Paul van Mulbregt, and SciPy 1. 0 Contributors. Scipy 1.0: Fundamental algorithms for scientific computing in python. *Nature Methods*, 2020.

[35] Andrew Guthrie, 1915 Guthrie, Andrew, and 1914 Wakerling, R. K. (Raymond Kornelious). *The Characteristics of electrical discharges in magnetic fields*. New York : McGraw-Hill, 1st ed edition, 1949. Includes bibliographical references and index.

[36] R. Chodura. Plasma-wall transition in an oblique magnetic field. *Physics of Fluids*, 25(9):1628–1633, 1982.

[37] P. C. Stangeby. The Chodura sheath for angles of a few degrees between the magnetic field and the surface of divertor targets and limiters. *Nuclear Fusion*, 52(8), 2012.

[38] J A Wesson. Effect of temperature gradient on plasma sheath. *Plasma Physics and Controlled Fusion*, 37(12):1459–1466, dec 1995.

[39] D. R. Bates, A. E. Kingston, and R. W. P. McWhirter. Recombination between electrons and atomic ions. i. optically thin plasmas. *Proceedings of the Royal Society of London A: Mathematical, Physical and Engineering Sciences*, 267(1):297–312, 1962.

[40] H P Summers, W. J. Dickson, M. G. O'Mullane, N R Badnell, A D Whiteford, D. H. Brooks, J. Lang, S. D. Loch, and D. C. Griffin. Ionisation state, excited populations and emission of impurities in dynamic finite density plasmas. I: The generalised collisional-radiative model for light elements. 2005.

[41] J. G. Doyle, H. P. Summers, and P. Bryans. The effect of metastable level populations on the ionization fraction of Li-like ions. *AAP*, 430:L29–L32, Jan 2005.

[42] K. Behringer, HP Summers, B Denne, M Forrest, and M Stamp. Spectroscopic determination of impurity influx from localized surfaces. *Plasma Physics and Controlled Fusion and*, 31:2059, 1989.

[43] H. P. Summers. The ADAS User Manual, version 2.2,. *http://adas.phys.strath.ac.uk/adas/*, 2001.

[44] G. Del Zanna, K. P. Dere, P. R. Young, E. Landi, and H. E. Mason. CHIANTI - An atomic database for emission lines. Version 8. *AAP*, 582:A56, October 2015.

[45] L. Ji, R. K. Smith, and N. S. Brickhouse. Updated atomic data and calculations for X-ray spectroscopy. *Astrophysical Journal*, 756(2), 2012.

[46] C.A. Johnson, S.D. Loch, and D.A. Ennis. ColRadPy: A Python collisional radiative solver. *Nuclear Materials and Energy*, 20:100579, August 2019.

[47] C. P. Ballance. Parallel R-matrix codes. *Parallel R-matrix homepage page.*

[48] R. A. Phaneuf. Experiments on electron-impact excitation and ionization of ions. In *Atomic Processes in Electron-Ion and Ion-Ion Collisions*, pages 117–156. Springer US, 1986.

[49] Philip George. Burke. *R-Matrix Theory of Atomic Collisions Application to Atomic, Molecular and Optical Processes.* Springer Berlin Heidelberg, 2011.

[50] M S Pindzola, F Robicheaux, S D Loch, J C Berengut, T Topcu, J Colgan, M Foster, D C Griffin, C P Ballance, D R Schultz, T Minami, N R Badnell, M C Witthoeft, D R Plante, D M Mitnik, J A Ludlow, and U Kleiman. The time-dependent close-coupling method for atomic and molecular collision processes. *Journal of Physics B: Atomic, Molecular and Optical Physics*, 40(7):R39–R60, mar 2007.

[51] A. Burgess and J. A. Tully. On the analysis of collision strengths and rate coefficients. *Astronomy and Astrophysics*, 254:436–453, 1991.

[52] R T Smyth, C P Ballance, C A Ramsbottom, C A Johnson, D A Ennis, and S D Loch. Dirac R -matrix calculations for the electron-impact excitation of neutral tungsten providing noninvasive diagnostics for magnetic confinement fusion. 052705:1–9, 2018.

[53] Alan Burgess and Hugh P Summers. The recombination and level populations of ions. I - Hydrogen and hydrogenic ions. *Monthly Notices of the Royal Astronomical Society*, 174:345–391, 1976.

[54] R. J. Bates, D. R. and Moffett. Three-Body Recombination of Positive and Negative Ions. I. Ions Recombining in Their Parent Gas. *Proceedings of the Royal Society of London. Series A, Mathematical and Physical Sciences*, 291(1424):1–8, 1966.

[55] Travis E Oliphant. Guide to NumPy. *Methods*, 1:378, 2010.

[56] Ralph Dux. STRAHL User Manual. *IPP Report*, 2006.

[57] D. Naujoks, R. Behrisch, J. P. Coad, and L. C.J.M. De Kock. Material transport by erosion and redeposition on surface probes in the scrape-off layer of JET. *Nuclear Fusion*, 33(4):581–590, 1993.

[58] H. P. Summers, N. R. Badnell, A. R. Foster, A. Giunta, F. Guzmán, L. Menchero, C. H. Nicholas, M. G. O'Mullane, A. D. Whiteford, and A. Meigs. Modelling spectral emission from fusion plasmas. *AIP Conference Proceedings*, 1438:181–188, 2012.

[59] X. Bonnin and D. Coster. Full-tungsten plasma edge simulations with solps. *Journal of Nuclear Materials*, 415(1, Supplement):S488 – S491, 2011. Proceedings of the 19th International Conference on Plasma-Surface Interactions in Controlled Fusion.

[60] Randall LeVeque. *Finite Difference Methods for Ordinary and Partial Differential Equations: Steady-State and Time-Dependent Problems (Classics in Applied Mathematics Classics in Applied Mathemat)*. Society for Industrial and Applied Mathematics, Philadelphia, PA, USA, 2007.

[61] Edward Uhler Condon and George Hiram Shortley. *The Theory of Atomic Spsectra*. University PR., 1933.

[62] Alexander Kramida and Yuri Ralchenko. NIST Atomic Spectra Database, NIST Standard Reference Database 78, 1999.

[63] E. Marenkov, K. Gutorov, and I. Sorokin. Radiation of high-Z atoms sputtered by plasma. *Nuclear Instruments and Methods in Physics Research Section B: Beam Interactions with Materials and Atoms*, 436(October):257–262, 2018.

[64] J. W. Davis and A. A. Haasz. Impurity release from low-Z materials under light particle bombardment. *Journal of Nuclear Materials*, 241-243:37–51, 1997.

[65] A. R. Field, C. Garcia-Rosales, G. Lieder, C. S. Pitcher, and R. Radtke. Spectroscopic measurement of target plate erosion in the asdex upgrade divertor. *Nuclear Fusion*, 36(2):119–132, 1996.

[66] A. Kramida, Yu. Ralchenko, J. Reader, and NIST ASD Team. NIST Atomic Spectra Database (ver. 5.5.3), [Online]. Available: `https://physics.nist.gov/asd` [2018]. National Institute of Standards and Technology, Gaithersburg, MD., 2018.

[67] A E Kramida and T Shirai. Compilation of wavelengths, energy levels, and transition probabilities for W I and W II. *Journal of Physical and Chemical Reference Data*, 35(1):423–683, 2006.

[68] T Abrams, R Ding, H.Y. Guo, D.M. Thomas, C.P. Chrobak, D.L. Rudakov, A.G. McLean, E.A. Unterberg, A.R. Briesemeister, P.C. Stangeby, J.D. Elder, W.R. Wampler, and J.G. Watkins. The inter-ELM tungsten erosion profile in DIII-D H-mode discharges and benchmarking with ERO+OEDGE modeling. *Nuclear Fusion*, 57(5):056034, 2017.

[69] J. G. Watkins, D. Taussig, R. L. Boivin, M. A. Mahdavi, and R. E. Nygren. High heat flux langmuir probe array for the diii-d divertor plates. *Review of Scientific Instruments*, 79(10):10F125, 2008.

[70] R. J. Colchin, D. L. Hillis, R. Maingi, C. C. Klepper, and N. H. Brooks. The filterscope. *Review of Scientific Instruments*, 74(3 II):2068–2070, 2003.

[71] N. H. Brooks, A. Howald, K. Klepper, and P. West. Multichord spectroscopy of the DIII-D divertor region. *Review of Scientific Instruments*, 63(10):5167–5169, 1992.

[72] N. Den Harder, S. Brezinsek, T. Pütterich, N. Fedorczak, G. F. Matthews, A. Meigs, M. F. Stamp, M. C. M. van de Sanden, and G. J. Van Rooij. ELM-resolved divertor erosion in the JET ITER-Like Wall. *Nuclear Fusion*, 56(2):026014, 2016.

[73] D.A. Pappas, B. Lipschultz, B. LaBombard, M.J. May, and C.S. Pitcher. Molybdenum sources and transport in the Alcator C-Mod tokamak. *Journal of Nuclear Materials*, 266-269:635–641, March 1999.

[74] M. J. May, M. Finkenthal, S. P. Regan, H. W. Moos, J. L. Terry, J. A. Goetz, M. A. Graf, J. E. Rice, E. S. Marmar, K. B. Fournier, and W. H. Goldstein. The measurement of the intrinsic impurities of molybdenum and carbon in the alcator C-Mod tokamak plasma using low resolution spectroscopy. *Nuclear Fusion*, 37(6):881–896, 1997.

[75] NSTX-U Five Year Plan for FY2014-2018 .

[76] N. R. Badnell, T. W. Gorczyca, M. S. Pindzola, and H. P. Summers. Excitation and ionization of neutral Cr and Mo, and the application to impurity influx. *Journal of Physics B: Atomic, Molecular and Optical Physics*, 29(16):3683–3715, 1996.

[77] R T Smyth, C A Johnson, D A Ennis, S D Loch, C A Ramsbottom, and C P Ballance. Relativistic R -matrix calculations for the electron-impact excitation of neutral molybdenum. 042713:1–7, 2017.

[78] R. C. Isler, R. J. Colchin, N. H. Brooks, T. E. Evans, W. P. West, and D. G. Whyte. Spectroscopic determinations of carbon fluxes, sources, and shielding in the DIII-D divertors. *Physics of Plasmas*, 8(10):4470–4482, 2001.

[79] G. D. Porter, R. Isler, J. Boedo, and T. D. Rognlien. Detailed comparison of simulated and measured plasma profiles in the scrape-off layer and edge plasma of DIII-D. *Physics of Plasmas*, 7(9):3663–3680, 2000.

[80] D. Borodin, D. Nishijima, R. P. Doerner, S. Brezinsek, A. Kreter, A. Kirschner, J. Romazanov, I. Borodkina, A. Eksaeva, E. Marenkov, and Ch Linsmeier. ERO modeling of beryllium erosion by helium plasma in experiments at PISCES-B. *Nuclear Materials and Energy*, 12:1157–1162, 2017.

[81] K. Behringer, H. P. Summers, B. Denne, M. Forrest, and M. Stamp. Spectroscopic determination of impurity influx from localized surfaces. *Plasma Physics and Controlled Fusion*, 31(14):2059–2099, 2000.

[82] P Quinet, P Palmeri, and É Biémont. Spectroscopic data for atomic tungsten transitions of interest in fusion plasma research. *Journal of Physics B: Atomic, Molecular and Optical Physics*, 44(14):145005, 2011.

[83] D. Nishijima, R. P. Doerner, M. J. Baldwin, A. Pospieszczyk, and A. Kreter. Experimental determination of S/XB values of W I visible lines. *Physics of Plasmas*, 16(12), 2009.

[84] S. Brezinsek, A. Kirschner, M. Mayer, A. Baron-Wiechec, I. Borodkina, D. Borodin, I. Coffey, J. Coenen, N. den Harder, A. Eksaeva, C. Guillemaut, K. Heinola, A. Huber, V. Huber, M. Imrisek, S. Jachmich, E. Pawelec, M. Rubel, S. Krat, G. Sergienko, G.F. Matthews, A.G. Meigs, S. Wiesen, and A. Widdowson. Erosion, screening, and migration of tungsten in the JET divertor. *Nuclear Fusion*, 59(9):096035, 2019.

[85] V. P. Shevelko and L. A. Vainshtein. *Atomic Physics for Hot Plasmas*. Institue of Physics Publishing, 1993.

[86] S Brezinsek, M Laengner, J W Coenen, M G O'Mullane, A Pospieszczyk, G Sergienko, and U Samm. Spectroscopic determination of inverse photon efficiencies of W atoms in the scrape-off layer of TEXTOR. *Physica Scripta*, 2017.

[87] S. P. Preval, N. R. Badnell, and M. G. O'Mullane. Dielectronic recombination of lanthanide and low ionization state tungsten ions: W^{13+} -W^{1+}. *Journal of Physics B: Atomic, Molecular and Optical Physics*, 52(2), 2019.

[88] A. Kirschner, D. Borodin, Stefan Droste, V. Philipps, U. Samm, Gianfranco Federici, A. Kukushkin, and Alberto Loarte. Modelling of tritium retention and target lifetime

of the ITER divertor using the ERO code. *Journal of Nuclear Materials*, 363:91–95, 06 2007.

[89] J. Guterl, C. Johnson, D. Ennis, S. Loche, and P. Snyder. Effects of the Chodura sheath on tungsten ionization and emission in tokamak divertors. *Contributions to Plasma Physics*, (October):1–7, 2019.

[90] P. C. Stangeby. *The plasma boundary of magnetic fusion devices.* Plasma physics series. Institute of Physics Pub, Bristol ; Philadelphia, 2000.

[91] Rainer Behrisch and Wolfgang Eckstein. *Sputtering by particle bombardment: experiments and computer calculations from threshold to MeV energies.* Springer, 2007.

[92] Andor Technology Ltd. Andor user's guide to SDK. 2.102.

Appendices

Appendix A

ColRadPy Documentation

ColRadPy solves the collisional radiative and ionization balance equations for application to fusion, laboratory, and astrophysical plasmas. It produces generalized coefficients that can be easily imported into existing plasma modeling codes and spectral diagnostics. The ColRadPy tutorial is presented here from the documentation. The The ColRadPy repositiory is available at https://github.com/johnson-c/ColRadPy including more detailed documentation of the code.

Tutorial

This tutorial will take the user through the basics of atomic data needed for Collisional Radiative (CR) modeling. The python scripts for these examples can be found in the 'examples' folder.

For a detailed introduction to CR theory see the ColRadPy paper included in the 'user_doc' folder. Summers 2006 also provides a more detailed overview of CR theory.

Neither the local thermodynamic equilibrium (LTE) or conornal approximations are valid for fusion plasmas. These plasmas must be modeled with a collisional radiative (CR) model which includes effects of electron density. Collisional Radiative theory has been updated to included general collisional radiative (GCR) theory, this is outlined in (Summers 2006).

The tutrial will go over the following major topics

Installing ColRadPy Installing ColRadPy

The atomic data input for colradpy is overviewed in Atomic Data and the ADF04 File

Running ColRadPy will be outlined in Running ColRadPy

Built in post processes in ColRadPy is described in Post processing analysis built in functions

Posted processing for advanced users will be outlined in Post processing analysis advanced

The generalized collisional radiative coefficients will be discussed in Generalized radiative coefficients (GCRs)

Functionality for advanced users is outlined in Advanced functionality

Ionization balance is outlined in Ionization Balance

Installing ColRadPy

ColRadPy should work with any python 3.6 distribution. However, ColRadPy is only tested with the anaconda distribution of python 3.6. ColRadPy requires numpy, matplotlib, re, scipy, sys, collections packages. For local installation of ColRadPy In the 'colradpy' directory.

```
python setup.py build
python setup.py install
```

Colradpy can now be called like anyother package.

```
from colradpy import colradpy #import the colradpy class
from colradpy import ionization_balance #import the ionization_balance class
```

Atomic Data and the ADF04 File

Atomic data is generally made by calculating cross-sections (probablity) of transitions. From these cross-sections rates are then made by convolving with a maxwellian temperature distriubtion (or some of distribution) of electron energies with the cross section. The rates produced by this method are what is used in the CR model.

The ADF04 file format from ADAS that is used to hold atomic rate data for input into the CR model.

Electron Impact De/Excitation

Electron impact excitation and deexcitation is what causes transitions be the ground and excited states and within excited states. There rates are stored as "effective collisional strengths" in the adf04 file. These can then be converted to the excitiation and deexcitation rates that are needed for CR modeling.

Electron Impact Ionization

Electrons can also ionize atoms to the next charge state. Ionization can be stored in the adf04 file as reduced ionization rates. ColRadPy is also capable of making ECIP ionization rates. ECIP ionization is a very approximate way of making ionization and should be avoid if possible. Ground and metastable states generally have calculated ionization rates while excited states generally have rates that are supplimented with ECIP.

Radative Recombination

Dielectronic Recombination

Dielectronic recombination is the dominant recombination process in many plasmas. Dielectronic recombination is a two step process. First, there is a resonance capture of a free electron. In this processes a bound electron gains some energy and the free electron loses some energy. Second, the atom radiates a phonton.

Three-Body Recombination

Three-body recombination is calculated from using detailed balance from the ionization. In this process, free electrons and a ion recombine to produce a new ion and one free electron.

Solutions

Once rates from the basic atomic data have been input. ColRadPy can then solve the set of rate equations known as the collisional radiative equations. There are two ways that ColRadPy can solve the CR set of equations. The general user will probably be interested in the first way of solving the CR equations, this is same way ADAS solves the equations. The Quasistatic approximation solves the equations assuming that excited states do not have time changing populations. It assumes that these populations and in their equilbrium values with the ground and any metastable levels. This is the way that ADAS solves the CR set of equations.

ColRadPy is also capable of solving the system of equations time dependently using the matrix exponentialation method. This solution makes no assumptions of equilbrium time scales for excited states. This is an excact solution. In equilbrium, the non-quasistatic and quastistic solutions will be the same.

Running ColRadPy

:ref:`ColRadPy <colradpy>` requires multiple inputs from the user to run. The basic quasistatic run will be discussed first. This should be sufficient for most users. Once the code runs data is store in a dictionary accessed through the '.data' method. The entries of this dictionary and descriptions are documented :ref:`here.<colradpy_dict>`

- Atomic data input file - currently this is limitted to an ADF04 file but there is nothing special about it.
- array of metastable levels - This is an array of levels that includes the ground and any levels that could be considered metastable.
- temperature grid - This is an array of electron temperatures for the calculation in eV.
- Density grid - This is an array of electron densities for the calculation in cm-3.

In this example Be II (Be+) is used because it is a simple system that has a parent ion (the next charge state) that has a metastable. This allows all of the different functionality to be shown and tested.

1. The module must be executed
2. Input file, temperature, density and metastable inputs defined.
3. Ionization, recombination options chosen default values are true

There are are highlevel class definitions that a general user can use. These high level definitions will be shown as well as the more basic definitions that these high level definitions call. A basic user needs to only care about the high level definitions

Below is an example of running ColRadPy. The user chooses an input adf04 file, temperature and density grids as well as the number of metastables. If you don't know how many metastables exist only choose level '0' (the ground) as being metastable. Choices were also made to include ionization and recombination. Note that metastable levels are only important if the plasma is not in equilbrium. In equilbrium metastable fraction is set and will not vary for a given temperature and density.

The 'use_recombination' flag when true will use any recombination rates that are included in the adf04 file.

The 'use_recombination_three_body' flag when true will have ColRadPy make and include three body recombination rates.

Note inorder to have three body recombination there must be some ionization included in the calculation.

The 'use_ionization' flag when true will use any ionization rates that are included in the adf04 file.

The 'suppliment_with_ecip' when true will have ColRadPy make ECIP ionization rates and include these rates anywhere that there are no ionization rates included in the adf04 file.

Note that ionization should always be included in the calculation even if it is just ECIP. Ionization can significantly change both absolute values of PECs as well as relative values of PECs.

```python
import sys
sys.path.append('../') #starting in 'examples' so need to go up one
from colradpy_class import colradpy
import numpy as np

fil = 'cpb03_ls#be0.dat' #adf04 file
temperature_arr = np.linspace(1,100,100) #eV
metastable_levels = np.array([0])   #metastable level, just ground chosen here
density_arr =     np.array([1.e13,4.e14]) # cm-3

#calling the colradpy class with the various inputs
be = colradpy(fil,metastable_levels,temperature_arr,density_arr,use_recombination=Tr
              use_recombination_three_body = True,use_ionization=True,suppliment_wit

be.solve_cr() #solve the CR equations with the quasistatic method
```

'be' is now a colradpy class that has been solved. There are various methods for getting the data out. Data that required ColRadPy to solve the CR set of equations is now stored in the 'processed' sub dictionary. There are many different calls that could be made from the class :ref:`documented here <colradpy>`.

Data from the calculation is now avaible in the '.data' dictionary. Various postpocessing can be done to now analysis the calcuation.

Post processing analysis built in functions

There are some built in functions avaible for post processing analysis these will of use for the general user. The basic functions require minimal knowelge of the underlying datastructure. These basic functions will be overviewed first then a more complex analysis will be presented after.

The theorical spectrum can be plotted describe in Plotting Theorical Spectrum (PEC sticks)

The line ratios versus temperature and density is describe in Plotting PEC ratios

Plotting Theorical Spectrum (PEC sticks)

The theorical spectral spectrum from the adf04 file can be plotted with the below command. The parameters are the lists or arrays of the index of the metastable, temperature and density grids. *WARNING* Note that wavelengths will not match NIST wavelengths unless the adf04 energy levels have been shifted to the NIST values. This generally hasn't been done in the past so there are many adf04 files that don't use NIST energy values.

```
be.plot_pec_sticks([0],[0],[0])
```

Plotting PEC ratios

Spectral line intenties are functions of both electron temperature and density as well as ion density. Different spectral lines will have different functional forms on temperature and density. It is therefore possible to find ratios of spectral lines that are depenended on either temperature or density as the ion density cancels out. It is then possible to dianose electron temperature and density from line ratios where the charge state exists in the plasma.

Temperature ratios can be plotted with the below function. The temperature ratio of the two pecs will be plotted with new figures made for each density and metastable requested. The inputs are the indexes of pec1, pec2, array of densities and array of metastables

```
be.plot_pec_ratio_temp(0,1,[0],[0])
```

```
be.plot_pec_ratio_dens([0],[0],[0])
```

Post processing analysis advanced

Photon emissivity coefficients (PECs)

A theortical spectrum can be made from the PEC coefficients. PEC coefficient are stored in array that has shape (#pecs,metastable,temperature,density). The code below produces a PEC spectrum for on temperature and density. The wavelength and pec arrays share the same length.

```
import matplotlib.pyplot as plt
plt.ion()
met = 0 #metastable 0, this corresponds to the ground state
te = 0 #first temperature in the grid
ne = 0 #frist density in the grid

fig, ax1 = plt.subplots(1,1,figsize=(16/3.,9/3.),dpi=300)
fig.subplots_adjust(bottom=0.15,top=0.92,left=0.105,right=0.965)
ax1.vlines(be.data['processed']['wave_air'],
           np.zeros_like(be.data['processed']['wave_air']),
           be.data['processed']['pecs'][:,met,te,ne])
ax1.set_xlim(0,1000)
ax1.set_title('PEC spectrum  T$_e$=' +str(be.data['user']['temp_grid'][te])+\
              ' eV  ne=' + "%0.*e"%(2,be.data['user']['dens_grid'][ne]) + ' cm$^{-3}$
ax1.set_xlabel('Wavelength (nm)')
ax1.set_ylabel('PEC (ph cm$^{-3}$ s$^{-1}$)')
```

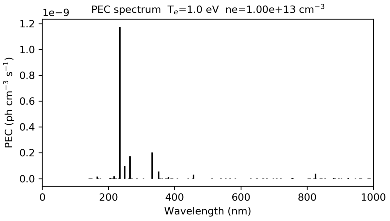

Often the index of a specific pec is wanted to find its temperature or density dependence. This can be accomplished in two basic ways.

1. Upper and lower levels of the transitions are known
2. The wavelength of the transition is known

There is a map from transition numbers to pec index levels. .data['processed']['pec_levels'] has the same order as .data['processed']['wave_air'] and .data['processed']['pecs'].

```
print(np.shape(be.data['processed']['wave_air']),
      np.shape(be.data['processed']['pecs']),
      np.shape(be.data['processed']['pec_levels']))
#(320,) (320, 3, 1, 1) (320, 2)

upper_ind = 7 #ninth excited state
lower_ind = 0  #ground state

pec_ind = np.where( (be.data['processed']['pec_levels'][:,0] == upper_ind) &\
                    (be.data['processed']['pec_levels'][:,1] == lower_ind))[0]

#plot the temeprature dependence of the chosen pec at first density in the grid
fig, ax1 = plt.subplots(1,1,figsize=(16/3.,9/3.),dpi=300)
fig.subplots_adjust(bottom=0.15,top=0.93,left=0.105,right=0.965)
ax1.set_title('Temperature dependence of line ' +\
              str(be.data['processed']['wave_air'][pec_ind]) +' nm',size=10)
ax1.plot(be.data['user']['temp_grid'],be.data['processed']['pecs'][pec_ind[0],met,:,
ax1.set_xlabel('Temperature (eV)')
ax1.set_ylabel('PEC (ph cm$^{-3}$ s$^{-1}$)')

#plot the density dependence of the chosen pec at first density in the grid
fig, ax1 = plt.subplots(1,1,figsize=(16/3.,9/3.),dpi=300)
fig.subplots_adjust(bottom=0.15,top=0.93,left=0.125,right=0.965)
ax1.set_title('Density dependence of line ' +\
              str(be.data['processed']['wave_air'][pec_ind]) +' nm',size=10)
ax1.plot(be.data['user']['dens_grid'],be.data['processed']['pecs'][pec_ind[0],met,te,
ax1.set_xlabel('Density (cm$^{-3}$)')
ax1.set_ylabel('PEC (ph cm$^{-3}$ s$^{-1}$)')
```

If the wavelength of a line of interest is known, the index can be found by looking at the wavelength array. The indices of all pecs that fall within the upper and lower bound of the 'where' statement are returned. PECs can generally be distinguished by the actual value, large lines that are of interest have much large PEC values, this can allow

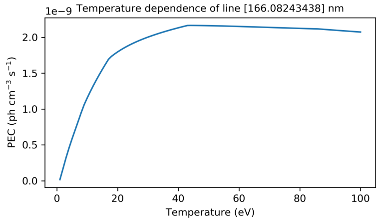

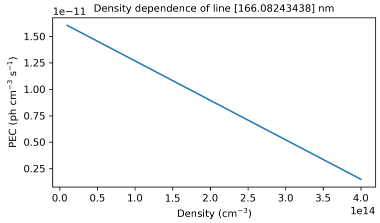

```
#want to find the index of Be I line at 351.55
pec_ind = np.where( (be.data['processed']['wave_air'] <352) &\
                    (be.data['processed']['wave_air'] >351))
print('Wavelength from file ' + str(be.data['processed']['wave_air'][pec_ind[0]]))
#Wavelength from file [351.55028742]
print('PEC upper and lower levels '+ str(be.data['processed']['pec_levels'][pec_ind[0]
#PEC upper and lower levels [[25  2]]
```

Generalized radiative coefficients (GCRs)

The generalized collsional radiative coefficients are calculated by ColRadPy as well. A description of these can be found in (Summers 2006), (Johnson 2019). GCR coefficients are often used as inputs to plasma transport codes. GCR coefficients are also used as inputs to ionization balance calculations which will be discussed later. This allows for different ionization stages to be linked.

For example, the total ionization from one charge state to the other is defined as the SCD. The total recombination from a charge state to the charge state of interest is defined as the ACD. This gives the rate of population transfer from one ionization state to a lower ionization state. The situation for systems with metastable states requires that the effective ionization and recombination rates be metastable resolved. In addition, it requires metastable cross coupling coefficients known as QCD and XCD coefficients.

Generally it is of interest to look at how the GCR coefficients change with some parameter such as temperature. Plots are shown below of the different GCRs.

A physical description of the GCRs can be helpful in interpreting the meaning behind them.

Metastable Cross Coupling Coefficient (QCD)

The QCD coefficient represents the transfer of population from one metastable state to another within the ionization state of interest and includes both direct population transfer between metastable states as well as the transfer via an intermediate excited state.

GCR Ionization Coefficient (SCD)

The total ionization from one charge state to the other is defined as the SCD.

GCR Recombination Coefficient (ACD)

The total recombination from a charge state to the charge state of interest is defined as the ACD.

Metastable Parent Cross Coupling Coefficient (XCD)

The XCD coefficient represents the transfer of population between metastable states from the ionization stage just above the stage of interest. Populations in the upper ionization stage can recombine into the ionization state of interest from one metastable, redistribute through all the states and then ionize back into a different metastable state of the upper ionization state.

GCR Examples

For this example we will look at Be II this is soley because Be III has two metastable states. This means that the XCD will have non-zero values. Remeber the call from before for Be I.

```
import sys
sys.path.append('../')
from colradpy_class import colradpy
import numpy as np

fil = 'cpb03_ls#be1.dat' #adf04 file
temperature_arr = np.linspace(1,100,20) #eV
metastable_levels = np.array([0,1])   #ground and level 1 chosen to be metastable
density_arr =     np.array([1.e13,8.e13,4.e14]) # cm-3
beii = colradpy(fil,metastable_levels,temperature_arr,density_arr,use_recombination=T
              use_recombination_three_body = True,use_ionization=True,suppliment_with
beii.solve_cr()
```

```
#plotting the QCD
import matplotlib.pyplot as plt
plt.ion
fig, ax1 = plt.subplots(1,1,figsize=(16/3.,9/3.),dpi=300)
fig.subplots_adjust(bottom=0.15,top=0.92,left=0.125,right=0.965)
ax1.plot(beii.data['user']['temp_grid'],
         beii.data['processed']['qcd'][0,1,:,0]*1e5,
         label = 'metastable cross coupling coefficient 1->2')

ax1.plot(beii.data['user']['temp_grid'],
         beii.data['processed']['qcd'][1,0,:,0]*1e5,
         label = 'metastable cross coupling coefficient 2->1')
ax1.legend()
ax1.set_title('QCD plot')
ax1.set_xlabel('Temperature (eV)')
ax1.set_ylabel('QCD * 10$^5$ (cm$^{-3}$ s$^{-1}$)')
```

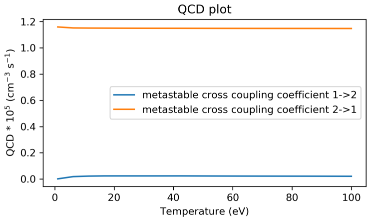

```python
#plotting the SCD
fig, ax1 = plt.subplots(1,1,figsize=(16/3.,9/3.),dpi=300)
fig.subplots_adjust(bottom=0.15,top=0.92,left=0.125,right=0.965)
ax1.plot(beii.data['user']['temp_grid'],
         beii.data['processed']['scd'][0,0,:,0],
         label = 'metastable cross coupling coefficient 1->1+')

ax1.plot(beii.data['user']['temp_grid'],
         beii.data['processed']['scd'][0,1,:,0],
         label = 'metastable cross coupling coefficient 1->2+')

ax1.plot(beii.data['user']['temp_grid'],
         beii.data['processed']['scd'][1,0,:,0],
         label = 'metastable cross coupling coefficient 2->1+')

ax1.plot(beii.data['user']['temp_grid'],
         beii.data['processed']['scd'][1,1,:,0],
         label = 'metastable cross coupling coefficient 2->2+')

ax1.legend(fontsize='x-small',loc='best')
ax1.set_title('SCD plot')
ax1.set_xlabel('Temperature (eV)')
ax1.set_ylabel('SCD (ion cm$^{-3}$ s$^{-1}$)')
```

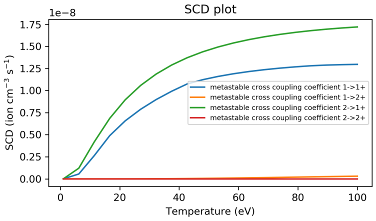

```python
#plotting the ACD
fig, ax1 = plt.subplots(1,1,figsize=(16/3.,9/3.),dpi=300)
fig.subplots_adjust(bottom=0.15,top=0.92,left=0.075,right=0.965)
ax1.plot(beii.data['user']['temp_grid'],
         beii.data['processed']['acd'][0,0,:,0],
         label = 'metastable cross coupling coefficient 1+->1')

ax1.plot(beii.data['user']['temp_grid'],
         beii.data['processed']['acd'][0,1,:,0],
         label = 'metastable cross coupling coefficient 2+->1')

ax1.plot(beii.data['user']['temp_grid'],
         beii.data['processed']['acd'][1,0,:,0],
         label = 'metastable cross coupling coefficient 1+->2')

ax1.plot(beii.data['user']['temp_grid'],
         beii.data['processed']['acd'][1,1,:,0],
         label = 'metastable cross coupling coefficient 2+->2')

ax1.legend(fontsize='x-small',loc='best')
```

```
ax1.set_title('ACD plot')
ax1.set_xlabel('Temperature (eV)')
ax1.set_ylabel('ACD (rec cm$^{-3}$ s$^{-1}$)')
```

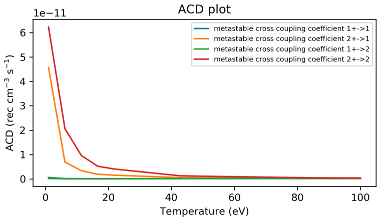

```
#plotting the XCD
fig, ax1 = plt.subplots(1,1,figsize=(16/3.,9/3.),dpi=300)
fig.subplots_adjust(bottom=0.15,top=0.92,left=0.12,right=0.965)
ax1.plot(beii.data['user']['temp_grid'],
         beii.data['processed']['xcd'][0,1,:,0],
         label = 'metastable cross coupling coefficient 1+->2+')

ax1.plot(beii.data['user']['temp_grid'],
         beii.data['processed']['scd'][1,0,:,0],
         label = 'metastable cross coupling coefficient 2+->1+')
ax1.legend(fontsize='x-small',loc='best')
ax1.set_title('XCD plot')
ax1.set_xlabel('Temperature (eV)')
ax1.set_ylabel('XCD (cm$^{-3}$ s$^{-1}$)')
```

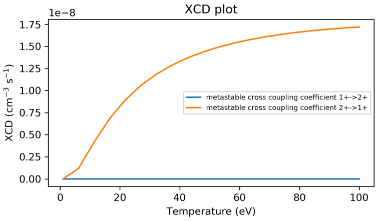

Determining Populating Mechanisms

One feature unique to ColRadPy is the ability to determine the populating mechanism of levels. This allows one to see which levels in a calculation are important to modeling the spectral lines of interest. This allows those that generate the atomic data to know which transitions are required to accurately model spectral lines. With this new analysis technique, it is possible to identify transitions that are the most important and allow for complex systems such as high-Z near neutral systems to be simplified.

ColRadPy also allows the user to determine which intermediate levels populate a level of interest withThis is don if the summation is not carried out from the calculation of the QCD. This allows one to see which levels in a calculation are important to modeling the spectral lines of interest.

```
#plotting the populating levels
plt.figure()
```

```
plt.figure();plt.plot(be.data['processed']['pop_lvl'][0,:,0,0,0]/\
                      np.sum(be.data['processed']['pop_lvl'][0,:,0,0,0]))

plt.figure();plt.plot(be.data['processed']['pop_lvl'][0,:,0,10,0]/\
                      np.sum(be.data['processed']['pop_lvl'][0,:,0,10,0]))

plt.figure();plt.plot(be.data['processed']['pop_lvl'][0,:,0,-1,0]/\
                      np.sum(be.data['processed']['pop_lvl'][0,:,0,-1,0]))

plt.legend()
plt.xlabel('Level number (#)')
plt.ylabel('Populating fraction (-)')

#plotting the populating fraction from the ground versus temperature
plt.figure()
plt.plot(be.data['user']['temp_grid'],
          be.data['processed']['pop_lvl'][10,0,0,:,0]/\
          np.sum(be.data['processed']['pop_lvl'][10,:,0,:,0],axis=0))

plt.xlabel('Temperature (eV)')
plt.ylabel('Populating fraction from ground (-)')
```

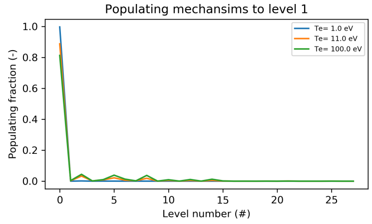

This shows that as temperature increase other excited levels contributed more and more to the first excited state

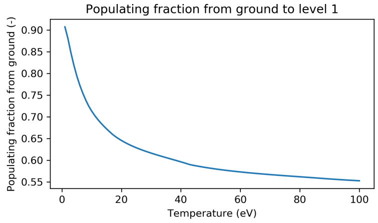

This shows that as the temperature increases the ground tributes less to the total population of level 1.

Advanced functionality

Time dependent CR modeling

ColRadPy is also capable of solving the full collisional radiative matrix time-dependently. This can be important for systems where there is significant population in many excited states or where ultra fast timescales need to be considered. Instead of the quasi-static approximation used in Equation 4 where excited states are assumed to have no population change, the matrix is solved as a system of ordinary differential equations n (t) = An(t). This method used to solve the system of equations was adapted from R. LeVeque.

Case in which with and without a source term can be considered in ColRadPy. The case without a source term can used in a system like a linear machine with views that are transverse to the direction of motion of the particles.

A source term can be used when the line of sight includes a source of particles. The source term could also be used to model the pumping of specific levels with LIF.

```python
import sys
sys.path.append('../')
from colradpy_class import colradpy
import numpy as np
import matplotlib.pyplot as plt

#Time dependent CR modeling
td_t = np.geomspace(1.e-5,.1,1000)
td_n0 = np.zeros(30)
td_n0[0] = 1.

fil = 'cpb03_ls#be0.dat' #adf04 file
temperature_arr = np.array([10]) #eV
metastable_levels = np.array([0])   #metastable level, just ground chosen here
density_arr =     np.array([1.e9]) # cm-3
be = colradpy(fil,metastable_levels,temperature_arr,density_arr,use_recombination=Tru
              use_recombination_three_body = True,use_ionization=True,suppliment_with
              td_t=td_t,td_n0=td_n0,td_source=td_s)
be.solve_cr()
be.solve_time_dependent()

fig, ax1 = plt.subplots(1,1,figsize=(16/3.,9/3.),dpi=300)
fig.subplots_adjust(bottom=0.15,top=0.92,left=0.1,right=0.965)
plt.plot(be.data['user']['td_t'],
         be.data['processed']['td']['td_pop'][0,:,0,0],
         label='Ground')
plt.plot(be.data['user']['td_t'],
         be.data['processed']['td']['td_pop'][1,:,0,0],
         label='level 1')
plt.plot(be.data['user']['td_t'],
         be.data['processed']['td']['td_pop'][-1,:,0,0],
         label='ion')
ax1.legend(fontsize='x-small',loc='best')
ax1.set_title('Time dependent solution of CR Be I no source term')
ax1.set_xlabel('Time (s)')
ax1.set_ylabel('Population (-)')
```

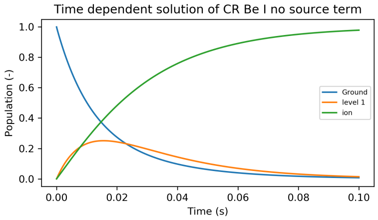

This time dependent collisional radiative model shows the time history for all Be I levels and the ground sate of Be II. This is the non-quasistatic solution, for a light system like Be the which only has one metastable the quasistatic approximation and non-quastatic solutions will give similiar results it is only for heavy species such as Mo and W where the quasistatic approximation starts to break down that this non-quasistatic solution is required.

```python
td_t = np.geomspace(1.e-5,1,1000)
td_n0 = np.zeros(30)
td_n0[0] = 1.
td_s = np.zeros(30)
td_s[0] = 1.
fil = 'cpb03_ls#be0.dat' #adf04 file
temperature_arr = np.array([10]) #eV
metastable_levels = np.array([0])   #metastable level, just ground chosen here
density_arr =     np.array([1.e8]) # cm-3
be = colradpy(fil,metastable_levels,temperature_arr,density_arr,use_recombination=Tru
              use_recombination_three_body = True,use_ionization=True,suppliment_with
              td_t=td_t,td_n0=td_n0,td_source=td_s)

be.solve_cr()
be.solve_time_dependent()

fig, ax1 = plt.subplots(1,1,figsize=(16/3.,9/3.),dpi=300)
fig.subplots_adjust(bottom=0.15,top=0.92,left=0.115,right=0.965)
plt.plot(be.data['user']['td_t'],
         be.data['processed']['td']['td_pop'][0,:,0,0],
         label='Ground')
plt.plot(be.data['user']['td_t'],
         be.data['processed']['td']['td_pop'][1,:,0,0],
         label='level 1')
plt.plot(be.data['user']['td_t'],
         be.data['processed']['td']['td_pop'][-1,:,0,0],
         label='ion')
ax1.legend(fontsize='x-small',loc='best')
ax1.set_title('Time dependent solution of CR Be I with source term')
ax1.set_xlabel('Time (s)')
ax1.set_ylabel('Population (-)')
```

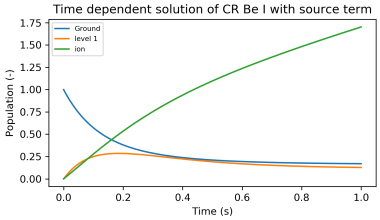

Time dependent solution with a constant source term of particles in the ground state. This could be used to model spectra where there is a constant erosion term from the wall. This could also be use to model level pumping in LIF systems.

Split LS resolved data to LSJ

ColRadPy is able to split PECs from term resolved (LS) into level resolved (LSJ) values. This currently does put PECs at the NIST wavelengths, a user must do this manually for now. In the future this will be done automatically using the NIST database.

```
import sys
sys.path.append('../')
from colradpy_class import *
import numpy as np

he = colradpy('./mom97_ls#he1.dat',[0],np.array([20]),np.array([1.e13]),use_recombina
               use_recombination_three_body = False,use_ionization=True)

he.solve_cr()
he.split_pec_multiplet()

wave_8_3 = np.array([468.5376849,468.5757974,468.5704380])
ind_8_3 = np.where( (he.data['processed']['pec_levels'][:,0] == 8) & \
                    (he.data['processed']['pec_levels'][:,1] == 3))[0]

wave_6_5 = np.array([468.5407225,468.5568006])
ind_6_5 = np.where( (he.data['processed']['pec_levels'][:,0] == 6) & \
                   (he.data['processed']['pec_levels'][:,1] == 5))[0]

wave_7_3 = np.array([468.5524404,468.5905553])
ind_7_3 = np.where( (he.data['processed']['pec_levels'][:,0] == 7) & \
                    (he.data['processed']['pec_levels'][:,1] == 3))[0]

wave_9_4 = np.array([468.5703849, 468.5830890, 468.5804092])
ind_9_4 = np.where( (he.data['processed']['pec_levels'][:,0] == 9) & \
                    (he.data['processed']['pec_levels'][:,1] == 4))[0]

wave_6_4 = np.array([ 468.5917884, 468.5757080, 468.5884123])
ind_6_4 = np.where( (he.data['processed']['pec_levels'][:,0] == 6) & \
                    (he.data['processed']['pec_levels'][:,1] == 4))[0]


wave_468 = np.hstack((wave_8_3,wave_6_5,wave_7_3,wave_9_4,wave_6_4))
pecs_468 = np.vstack((he.data['processed']['split']['pecs'][ind_8_3[0]],
                      he.data['processed']['split']['pecs'][ind_6_5[0]],
                      he.data['processed']['split']['pecs'][ind_7_3[0]],
```

```
                      he.data['processed']['split']['pecs'][ind_9_4[0]],
                      he.data['processed']['split']['pecs'][ind_6_4[0]]))[np.argsort(
wave_468 = wave_468[np.argsort(wave_468)]



plt.figure()
plt.vlines(wave_468,np.zeros_like(wave_468),pecs_468[:,0,0,0])
```

Ionization Balance

An ionization balance can be used to get the relative abundances of charge states in a given species. The relative populations of charge states are solved using the GCR coefficient that are calculated from the CR set of equations. A matrix similiar to the CR matrix is assembled using the GCR rate coefficients. The QCD rates transfer population between metastable states in one ionization stage. SCD is the ionization from one charge stage to the next. ACD is the recombination from one charge stage to the previous stage and the XCD is population transfer between metastable states through the next charge state.

ColRadPy is capable of preforming time dependent as well as time independent ionization balance calculations. The values for time independent ionization balance are solved by looking at the sencond longested lived eigenvalue of the system. The equations are then solved at eight times this value ensure that equilbrium of the system has been reached.

An example of the ionization balance code is run for Be from the example 'example/ion_bal.py'. First for a time dependent case and then for a time independent case. In the plot of the time dependent abundances are shown as the solid lines and the time independent limits are shown as the dashed lines.

```
import sys
sys.path.append('../')
from colradpy_class import colradpy
import numpy as np
import matplotlib.pyplot as plt
from ionization_balance_class import ionization_balance

#the adf04 files
fils = np.array(['cpb03_ls#be0.dat','cpb03_ls#be1.dat','be2_adf04','be3_adf04'])
temp = np.linspace(5,100,5) #temp grid
dens = np.array([1.e11,1.e14]) #density grid
metas = [np.array([0,1]),np.array([0]),np.array([0,1]),np.array([0])]#number of metas
                           #this should match the metastables at the top of the adf04
                           #this information is used to calculate the QCD values
                           #without it only the SCD, ACD and XCD for a species will b

time = np.linspace(0,.01,1.e4)

ion = ionization_balance(fils, metas, temp, dens, keep_species_data = True)
ion.populate_ion_matrix()

ion.solve_no_source(np.array([1,0,0,0,0,0,0]),time)

ion.solve_time_independent()

plt.ion
fig, ax1 = plt.subplots(1,1,figsize=(16/3.,9/3.),dpi=300)
fig.subplots_adjust(bottom=0.15,top=0.99,left=0.11,right=0.99)
ax1.plot(time*1e3,ion.data['pops'][0,:,1,1],label='be0, met0',color='b')
```

```
ax1.hlines(ion.data['pops_ss'][0,0,1,1],0,10,color='b',linestyle=':')

ax1.plot(time*1e3,ion.data['pops'][1,:,1,1],label='be0, met1',color='g')
ax1.hlines(ion.data['pops_ss'][1,0,1,1],0,10,color='g',linestyle=':')

ax1.plot(time*1e3,ion.data['pops'][2,:,1,1],label='be1, met0',color='r')
ax1.hlines(ion.data['pops_ss'][2,0,1,1],0,10,color='r',linestyle=':')

ax1.plot(time*1e3,ion.data['pops'][3,:,1,1],label='be2, met0',color='c')
ax1.hlines(ion.data['pops_ss'][3,0,1,1],0,10,color='c',linestyle=':')

ax1.plot(time*1e3,ion.data['pops'][4,:,1,1],label='be2, met1',color='m')
ax1.hlines(ion.data['pops_ss'][4,0,1,1],0,10,color='m',linestyle=':')

ax1.plot(time*1e3,ion.data['pops'][5,:,1,1],label='be3, met0',color='y')
ax1.hlines(ion.data['pops_ss'][5,0,1,1],0,10,color='y',linestyle=':')

ax1.plot(time*1e3,ion.data['pops'][6,:,1,1],label='be4',color='k')
ax1.hlines(ion.data['pops_ss'][6,0,1,1],0,10,color='k',linestyle=':')

ax1.legend(fontsize='x-small')

ax1.set_xlabel('Time (ms)')
ax1.set_ylabel('Fractional Abundance (-)')
```

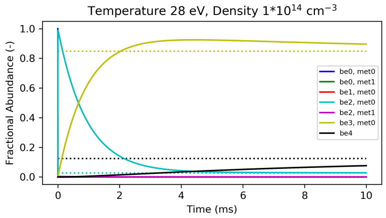

The time independent solution as a function of electron temperature is shown below.

```
temp = np.linspace(2,100,200) #temp grid
ion = ionization_balance(fils, metas, temp, dens, keep_species_data = False)
ion.populate_ion_matrix()
ion.solve_time_independent()


fig, ax1 = plt.subplots(1,1,figsize=(16/3.,9/3.),dpi=300)
fig.subplots_adjust(bottom=0.15,top=0.99,left=0.11,right=0.99)

ax1.plot(temp,ion.data['pops_ss'][0,0,:,1],label='be0, met0',color='b')

ax1.plot(temp,ion.data['pops_ss'][1,0,:,1],label='be0, met1',color='g')

ax1.plot(temp,ion.data['pops_ss'][2,0,:,1],label='be1, met0',color='r')

ax1.plot(temp,ion.data['pops_ss'][3,0,:,1],label='be2, met0',color='c')

ax1.plot(temp,ion.data['pops_ss'][4,0,:,1],label='be2, met1',color='m')
```

```

ax1.plot(temp,ion.data['pops_ss'][5,0,:,1],label='be3, met0',color='y')

ax1.plot(temp,ion.data['pops_ss'][6,0,:,1],label='be4',color='k')

ax1.legend(fontsize='x-small')

ax1.set_xlabel('Temperature (eV)')
ax1.set_ylabel('Fractional Abundance (-)')
```

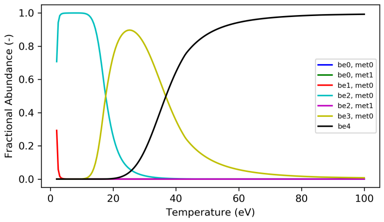

Thermal charge exchange

Thermal charge exchange here reffers to the process of charge exchange exchange with neutrals (generally H) that in a maxwellian distribution. Note that this is for charge exchange at the edge of the plasma and not beam which would have a almost a delta function for the temperature. The rate of thermal change exchange then depends on the temperature and the density of the neutral specie.

In order to reduce array sizes for code speed, the neutral temperature and density arrays are required to be the same size as the electron temperature and density. This allow the CX portion to just be added on as another column (almost like another recombination) instead of needing to make the populations f(met,Te,ne,Th,nh). When electron temperature and density are run as pairs the neutral tmperature and density will be urn as a pair.

Error bar analysis from atomic data

Appendix B

Impurity spectral line identification in CTH

This appendix is broad strokes attempt to identify most of the large impurity lines observed in CTH. A theoretical spectrum calculated with ColRadPy is over-plot with CTH data from many known low-Z species in CTH such as B, C, N and O. The level splitting of low-Z species allows for relatively easy identification as the features often including multiple lines close in wavelength. The tables were generated from the output of ColRadPy which used the ADAS recommended data for B, C, N, and O in their respective "ADASX" directories. These files were split from term resolution (LS) to level resolution (LSJ) after which the energies were shifted to NIST. Note that this approach will only identify electron dipole transitions and only those whose levels are identified in NIST.

A number of W I, W II and W III are listed at the end this appendix. These are possible tungsten lines that either require more work to positively identify (ruling out other possibilities) or for the case of W I lines that had no corresponding transition in the *R*-matrix calculation due to missing configurations.

Table B.1: C II spectral lines identified in CTH

NIST Wavelength (nm)	Upper Level	Lower Level
250.913	$2p^3(^2D_{3/2})$	$2s2p^2(^2P_{1/2})$
251.174	$2p^3(^2D_{3/2})$	$2s2p^2(^2P_{3/2})$
251.206	$2p^3(^2D_{5/2})$	$2s2p^2(^2P_{3/2})$
513.295	$2s2p(3P)3p\ (^4P_{3/2})$	$2s2p(3P)3s\ (^4P_{1/2})$
513.328	$2s2p(3P)3p\ (^4P_{5/2})$	$2s2p(3P)3s\ (^4P_{3/2})$
513.726	$2s2p(3P)3p\ (^4P_{1/2})$	$2s2p(3P)3s\ (^4P_{1/2})$
513.917	$2s2p(3P)3p\ (^4P_{3/2})$	$2s2p(3P)3s\ (^4P_{3/2})$
514.35	$2s2p(3P)3p\ (^4P_{1/2})$	$2s2p(3P)3s\ (^4P_{3/2})$
514.516	$2s2p(3P)3p\ (^4P_{5/2})$	$2s2p(3P)3s\ (^4P_{5/2})$
515.109	$2s2p(3P)3p\ (^4P_{3/2})$	$2s2p(3P)3s\ (^4P_{5/2})$
657.805	$2s^2 3p(^2P_{3/2})$	$2s^2 3s(^2S_{1/2})$
658.288	$2s^2 3p(^2P_{1/2})$	$2s^2 3s(^2S_{1/2})$

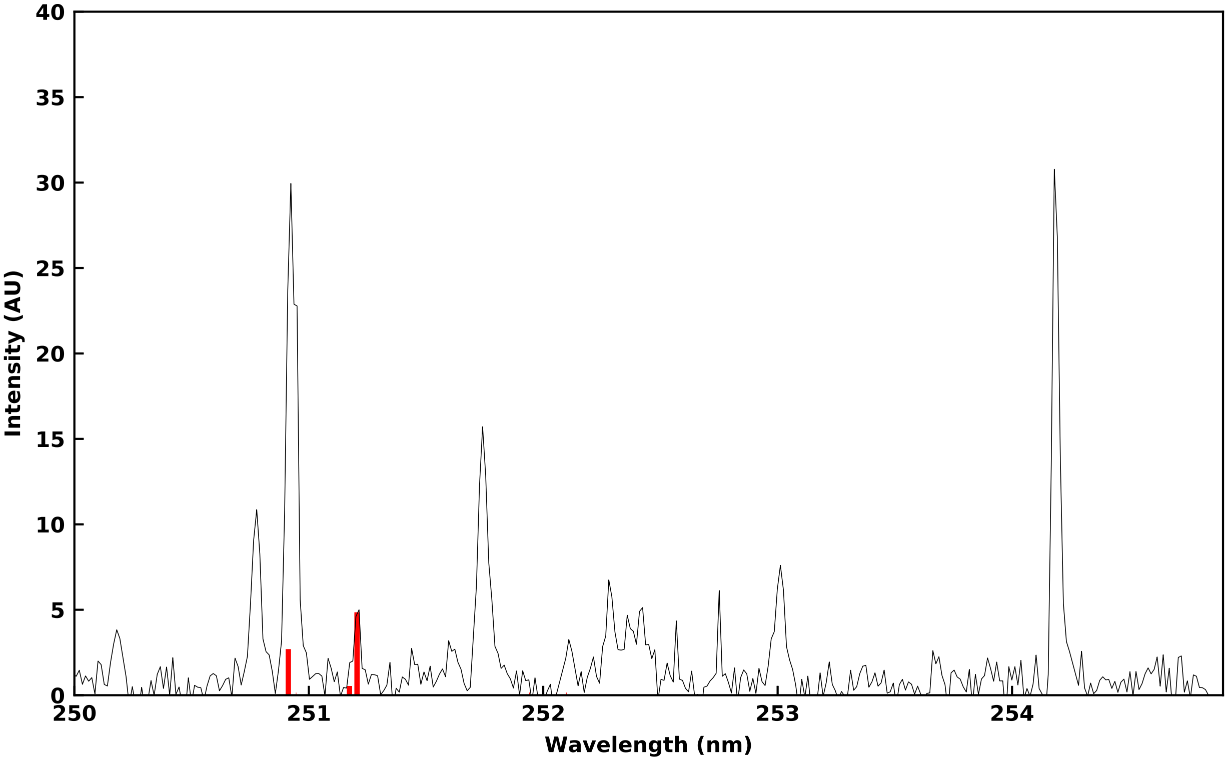

Figure B.1: CTH comparison to CR C II modeling

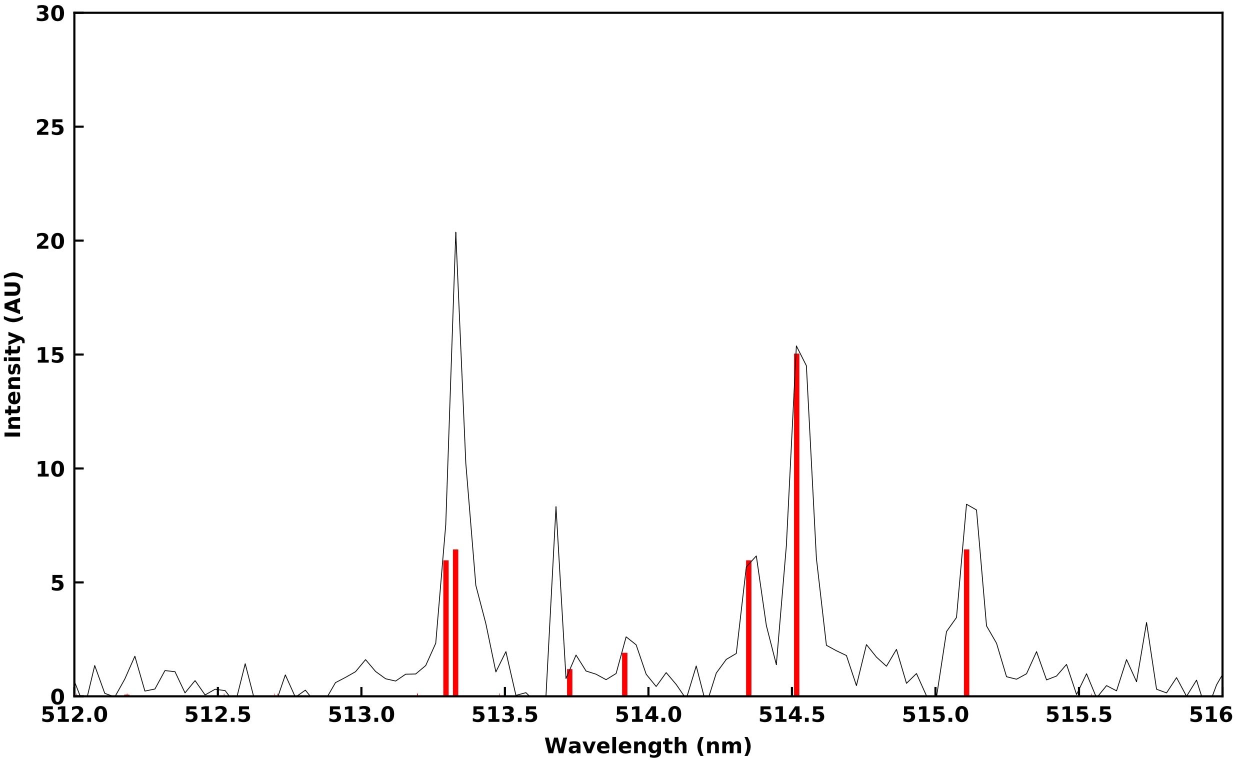

Figure B.2: CTH comparison to CR C II modeling

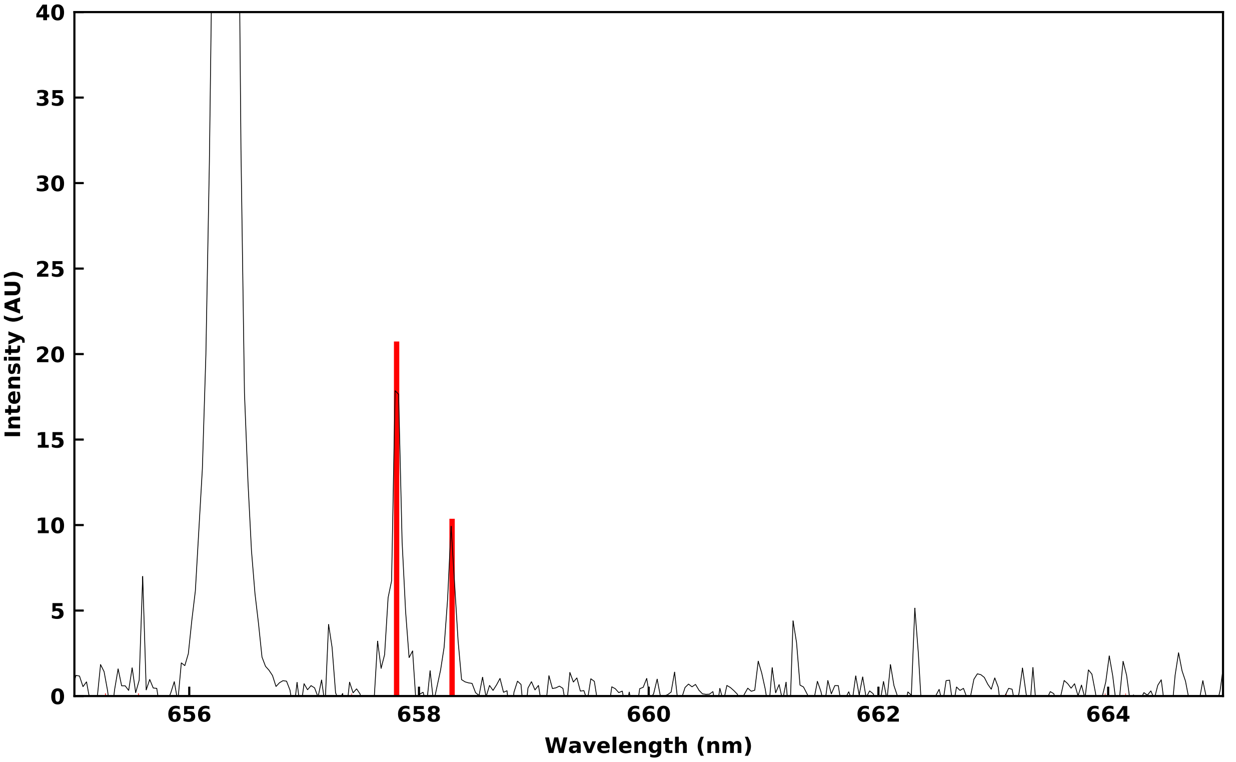

Figure B.3: CTH comparison to CR C II modeling

Table B.2: C III spectral lines identified in CTH

NIST Wavelength (nm)	Upper Level	Lower Level
229.687	$1s^2 2p^2(^1D_2)$	$1s^2 2s2p(^1P_1)$
464.742	$1s^2 2s3p(^3P_2)$	$1s^2 2s3s(^3S_1)$
465.025	$1s^2 2s3p(^3P_1)$	$1s^2 2s3s(^3S_1)$
465.147	$1s^2 2s3p(^3P_0)$	$1s^2 2s3s(^3S_1)$

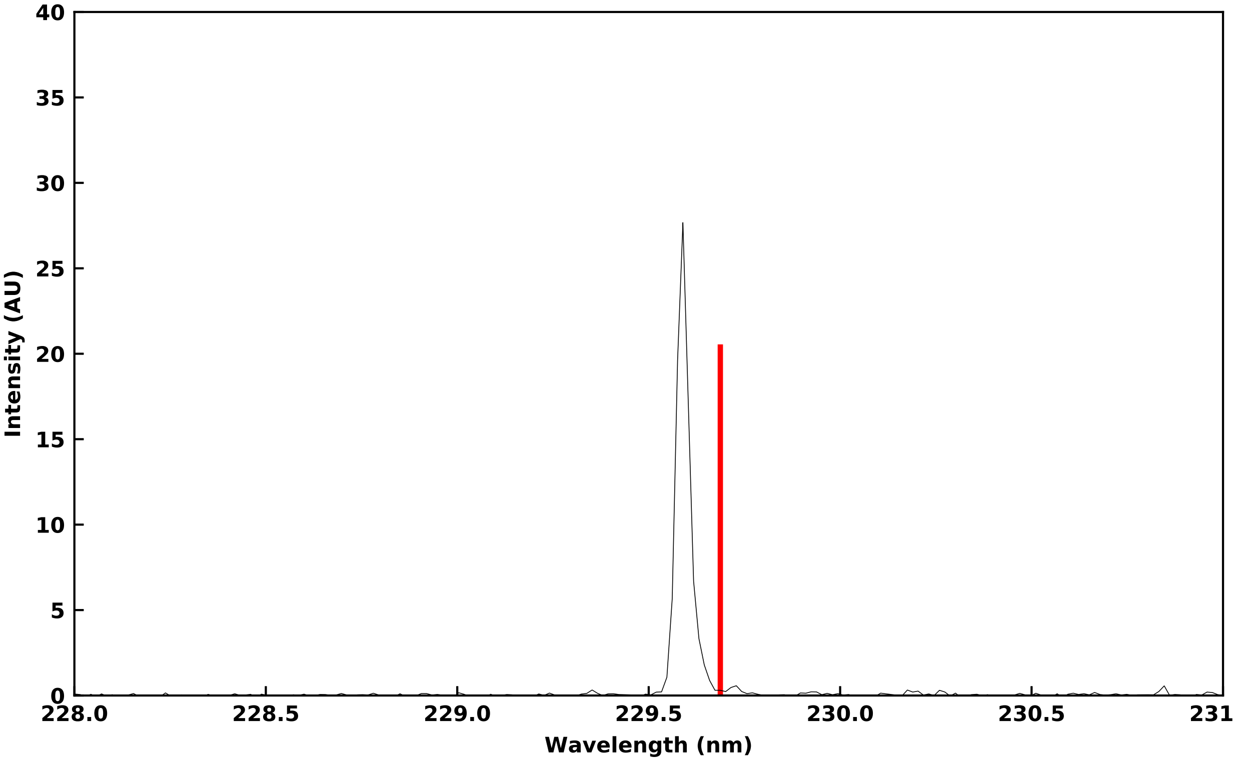

Figure B.4: CTH comparison to CR C III modeling

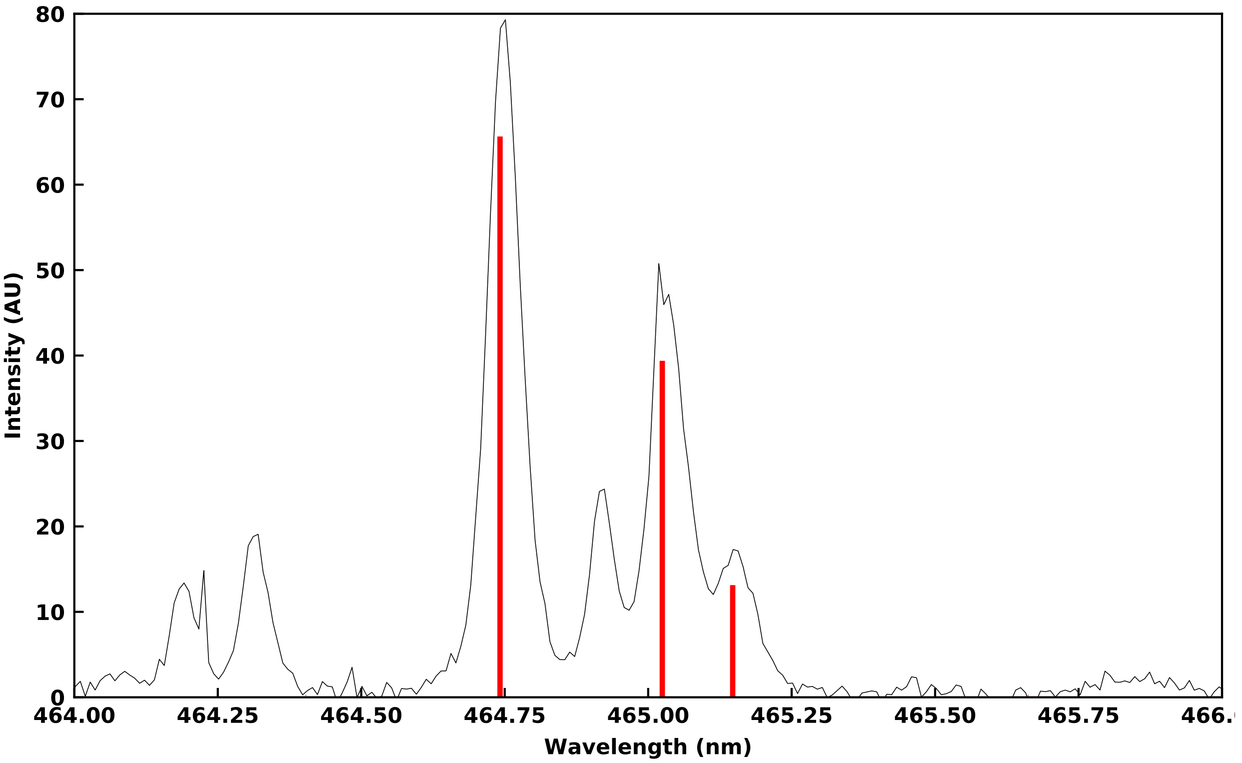

Figure B.5: CTH comparison to CR C III modeling

Table B.3: N II spectral lines identified in CTH

NIST Wavelength (nm)	Upper Level	Lower Level
343.714	$2\mathrm{s}^2 2p3p(^1\mathrm{S}_0)$	$2\mathrm{s}^2 2p3s(^1\mathrm{P}_1)$
399.5	$2\mathrm{s}^2 2p3p(^1\mathrm{D}_2)$	$2\mathrm{s}^2 2p3s(^1\mathrm{P}_1)$
460.148	$2\mathrm{s}^2 2p3p(^3\mathrm{P}_2)$	$2\mathrm{s}^2 2p3s(^3\mathrm{P}_1)$
460.715	$2\mathrm{s}^2 2p3p(^3\mathrm{P}_1)$	$2\mathrm{s}^2 2p3s(^3\mathrm{P}_0)$
461.387	$2\mathrm{s}^2 2p3p(^3\mathrm{P}_1)$	$2\mathrm{s}^2 2p3s(^3\mathrm{P}_1)$
462.139	$2\mathrm{s}^2 2p3p(^3\mathrm{P}_0)$	$2\mathrm{s}^2 2p3s(^3\mathrm{P}_1)$
463.054	$2\mathrm{s}^2 2p3p(^3\mathrm{P}_2)$	$2\mathrm{s}^2 2p3s(^3\mathrm{P}_2)$
464.309	$2\mathrm{s}^2 2p3p(^3\mathrm{P}_1)$	$2\mathrm{s}^2 2p3s(^3\mathrm{P}_2)$
489.512	$2\mathrm{s}^2 2p3p(^1\mathrm{P}_1)$	$2\mathrm{s}2\mathrm{p}^3(^1\mathrm{D}_2)$
566.663	$2\mathrm{s}^2 2p3p(^3\mathrm{D}_2)$	$2\mathrm{s}^2 2p3s(^3\mathrm{P}_1)$
567.602	$2\mathrm{s}^2 2p3p(^3\mathrm{D}_1)$	$2\mathrm{s}^2 2p3s(^3\mathrm{P}_0)$
567.956	$2\mathrm{s}^2 2p3p(^3\mathrm{D}_3)$	$2\mathrm{s}^2 2p3s(^3\mathrm{P}_2)$
568.621	$2\mathrm{s}^2 2p3p(^3\mathrm{D}_1)$	$2\mathrm{s}^2 2p3s(^3\mathrm{P}_1)$
571.077	$2\mathrm{s}^2 2p3p(^3\mathrm{D}_2)$	$2\mathrm{s}^2 2p3s(^3\mathrm{P}_2)$
648.205	$2\mathrm{s}^2 2p3p(^1\mathrm{P}_1)$	$2\mathrm{s}^2 2p3s(^1\mathrm{P}_1)$

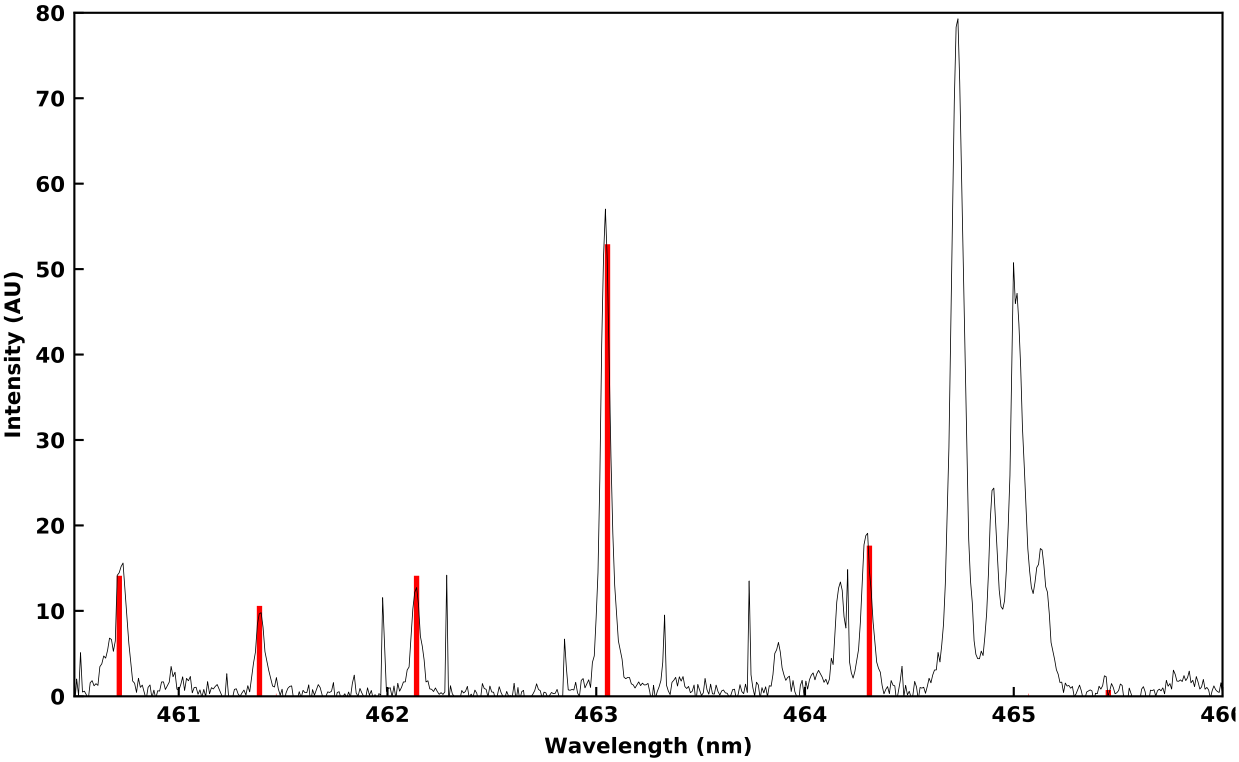

Figure B.6: CTH comparison to CR N II modeling

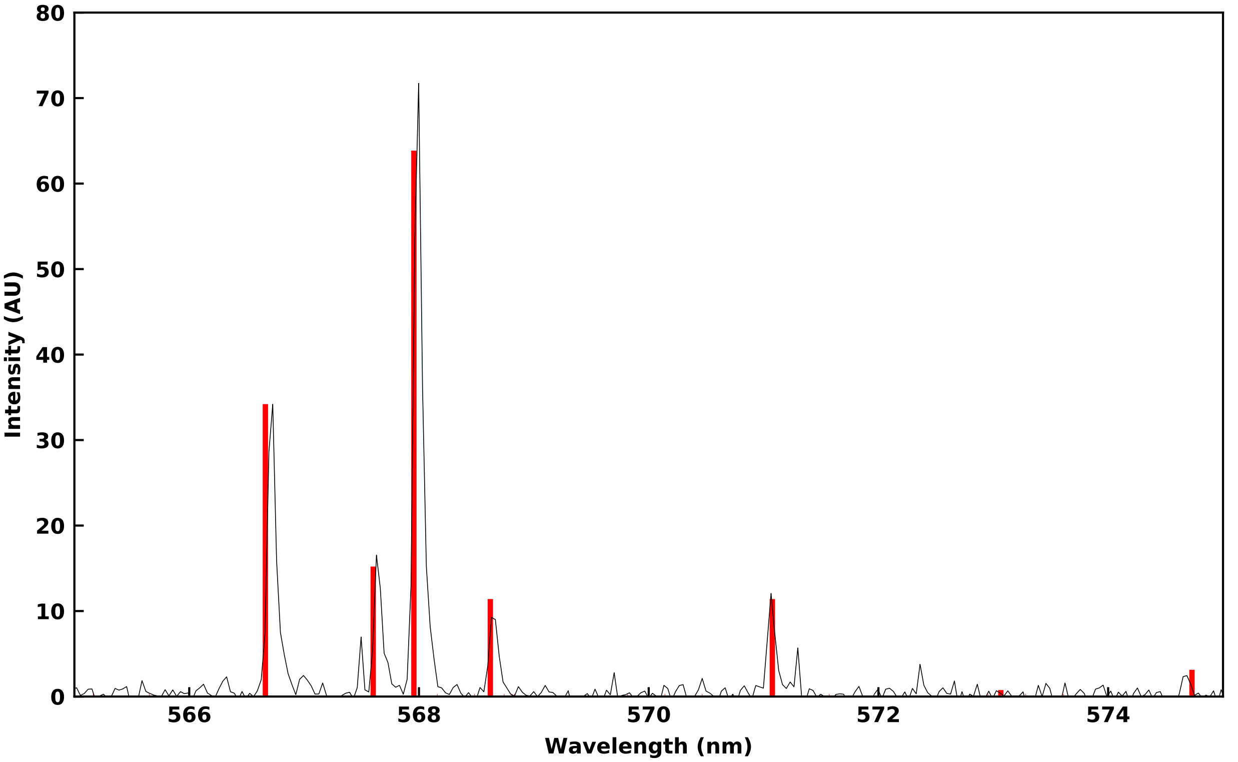

Figure B.7: CTH comparison to CR N II modeling

Table B.4: N III spectral lines identified in CTH

NIST Wavelength (nm)	Upper Level	Lower Level
335.398	2s2p(3P)3p ($^4\mathrm{P}_{3/2}$)	2s2p(3P)3s ($^4\mathrm{P}_{1/2}$)
335.432	2s2p(3P)3p ($^4\mathrm{P}_{5/2}$)	2s2p(3P)3s ($^4\mathrm{P}_{3/2}$)
336.58	2s2p(3P)3p ($^4\mathrm{P}_{1/2}$)	2s2p(3P)3s ($^4\mathrm{P}_{3/2}$)
336.736	2s2p(3P)3p ($^4\mathrm{P}_{5/2}$)	2s2p(3P)3s ($^4\mathrm{P}_{5/2}$)
337.407	2s2p(3P)3p ($^4\mathrm{P}_{3/2}$)	2s2p(3P)3s ($^4\mathrm{P}_{5/2}$)
374.595	2s2p(3P)3p ($^4\mathrm{S}_{3/2}$)	2s2p(3P)3s ($^4\mathrm{P}_{1/2}$)
375.469	2s2p(3P)3p ($^4\mathrm{S}_{3/2}$)	2s2p(3P)3s ($^4\mathrm{P}_{3/2}$)
377.103	2s2p(3P)3p ($^4\mathrm{S}_{3/2}$)	2s2p(3P)3s ($^4\mathrm{P}_{5/2}$)
409.736	$2\mathrm{s}^2 3p(^2\mathrm{P}_{3/2})$	$2\mathrm{s}^2 3s(^2\mathrm{S}_{1/2})$
410.339	$2\mathrm{s}^2 3p(^2\mathrm{P}_{1/2})$	$2\mathrm{s}^2 3s(^2\mathrm{S}_{1/2})$
451.088	2s2p(3P)3p ($^4\mathrm{D}_{3/2}$)	2s2p(3P)3s ($^4\mathrm{P}_{1/2}$)
451.485	2s2p(3P)3p ($^4\mathrm{D}_{7/2}$)	2s2p(3P)3s ($^4\mathrm{P}_{5/2}$)
451.814	2s2p(3P)3p ($^4\mathrm{D}_{1/2}$)	2s2p(3P)3s ($^4\mathrm{P}_{1/2}$)
452.356	2s2p(3P)3p ($^4\mathrm{D}_{3/2}$)	2s2p(3P)3s ($^4\mathrm{P}_{3/2}$)
485.87	2s2p(3P)3d ($^4\mathrm{F}_{3/2}$)	2s2p(3P)3p ($^4\mathrm{D}_{1/2}$)
485.898	2s2p(3P)3d ($^4\mathrm{F}_{5/2}$)	2s2p(3P)3p ($^4\mathrm{D}_{3/2}$)
486.717	2s2p(3P)3d ($^4\mathrm{F}_{9/2}$)	2s2p(3P)3p ($^4\mathrm{D}_{7/2}$)
486.717	2s2p(3P)3d ($^4\mathrm{F}_{9/2}$)	2s2p(3P)3p ($^4\mathrm{D}_{7/2}$)
487.36	2s2p(3P)3d ($^4\mathrm{F}_{5/2}$)	2s2p(3P)3p ($^4\mathrm{D}_{5/2}$)
488.414	2s2p(3P)3d ($^4\mathrm{F}_{7/2}$)	2s2p(3P)3p ($^4\mathrm{D}_{7/2}$)

Table B.5: N IV spectral lines identified in CTH

NIST Wavelength (nm)	Upper Level	Lower Level
347.872	$1\mathrm{s}^2 2s3p(^3\mathrm{P}_2)$	$1\mathrm{s}^2 2s3s(^3\mathrm{S}_1)$
348.3	$1\mathrm{s}^2 2s3p(^3\mathrm{P}_1)$	$1\mathrm{s}^2 2s3s(^3\mathrm{S}_1)$
348.493	$1\mathrm{s}^2 2s3p(^3\mathrm{P}_0)$	$1\mathrm{s}^2 2s3s(^3\mathrm{S}_1)$

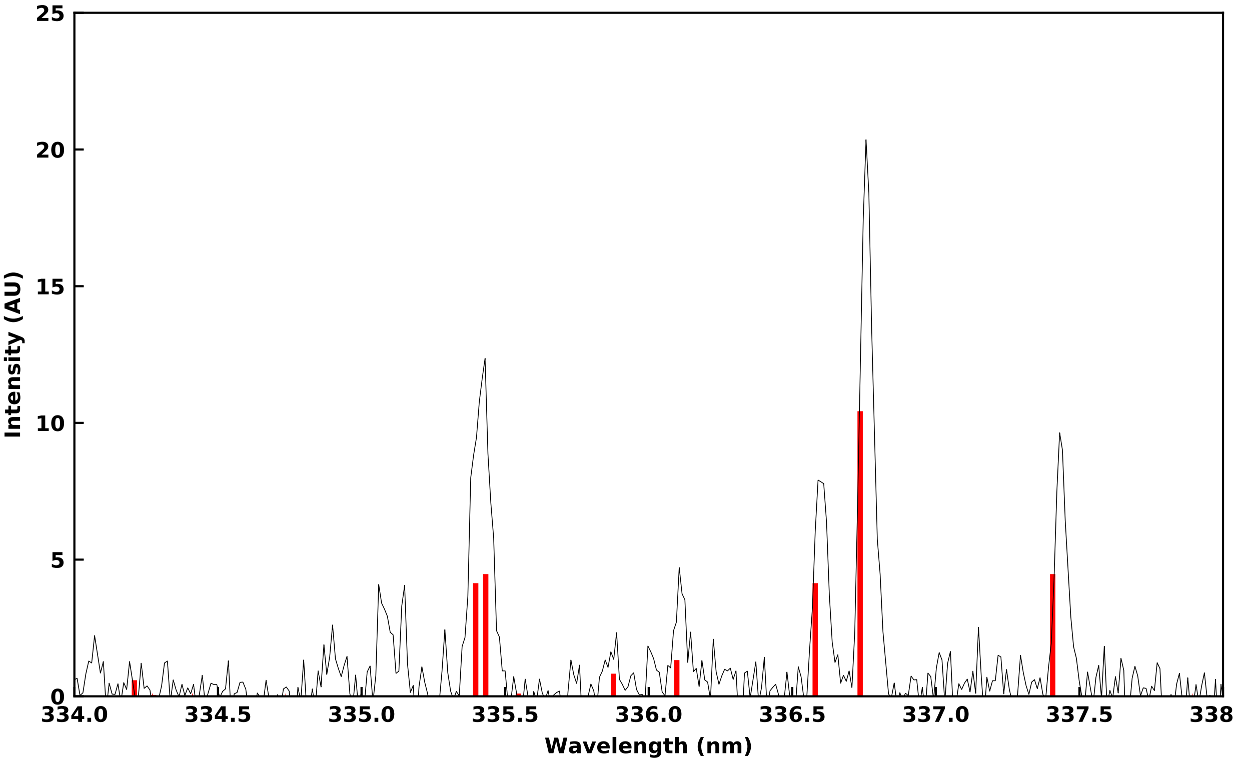

Figure B.8: CTH comparison to CR N III modeling

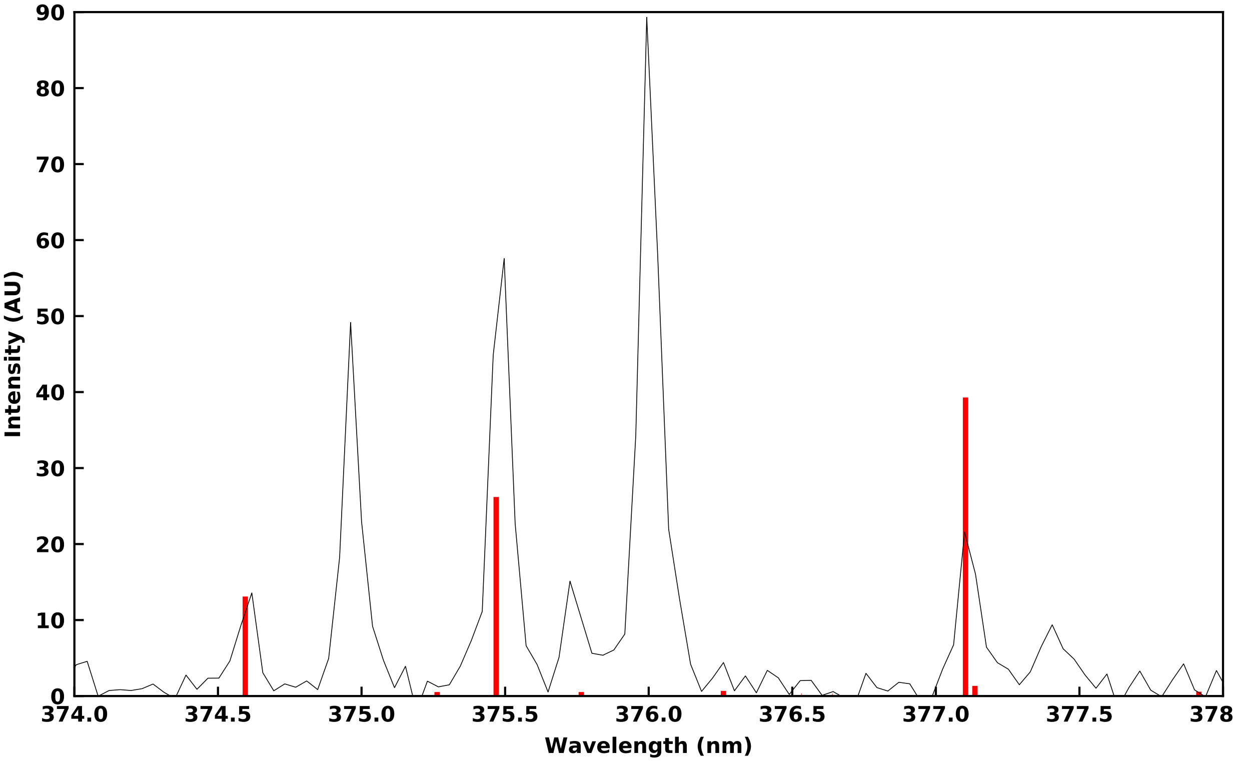

Figure B.9: CTH comparison to CR N III modeling

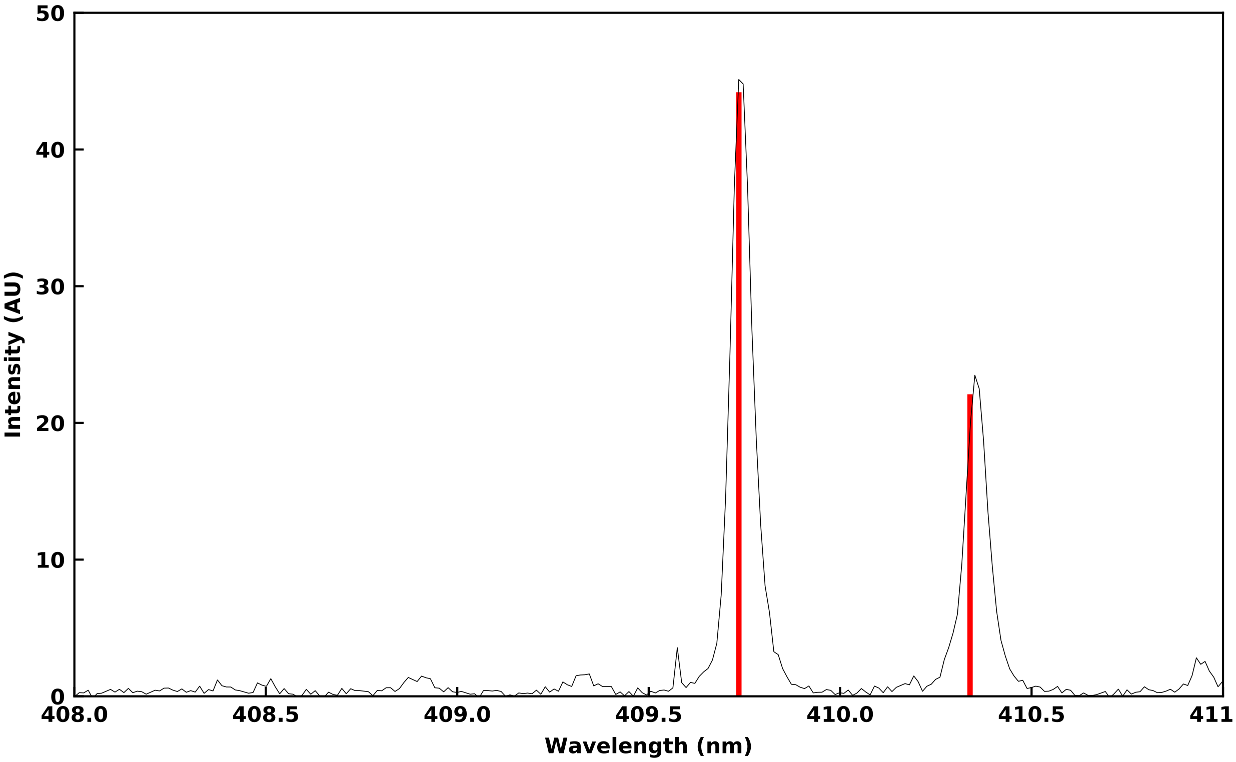

Figure B.10: CTH comparison to CR N III modeling

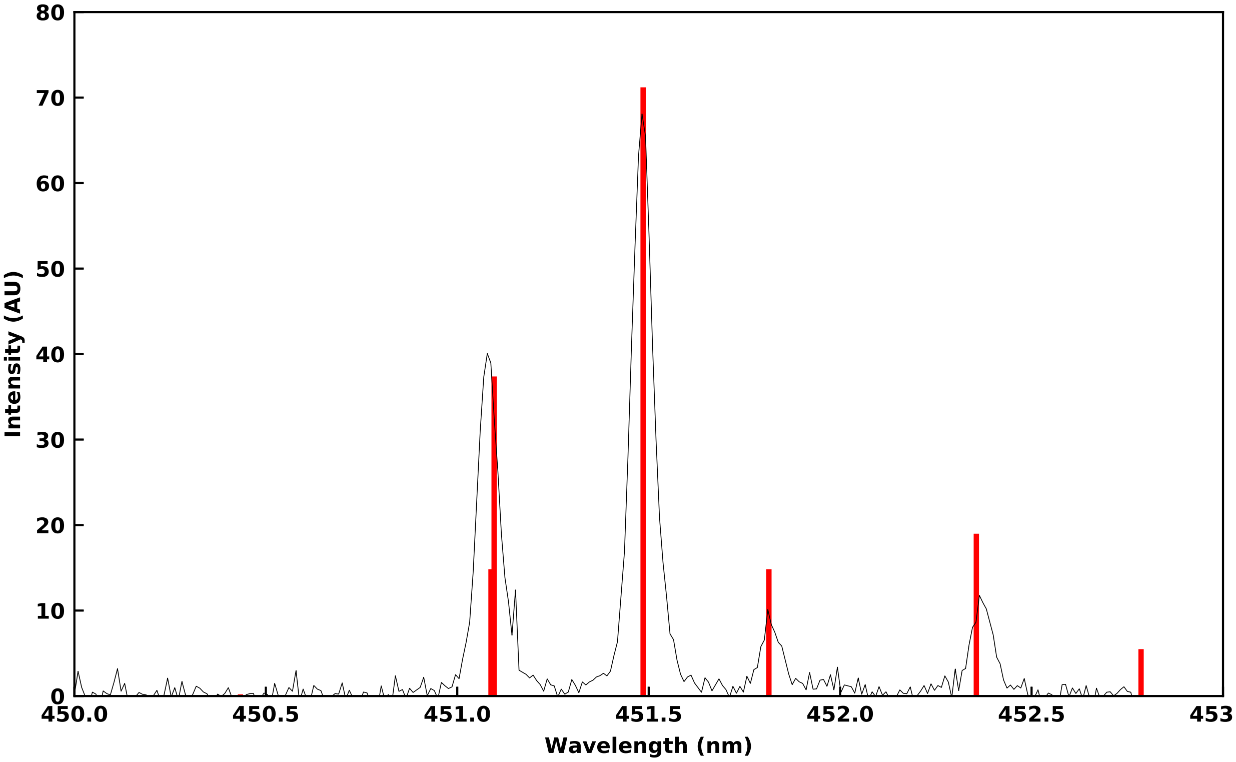

Figure B.11: CTH comparison to CR N III modeling

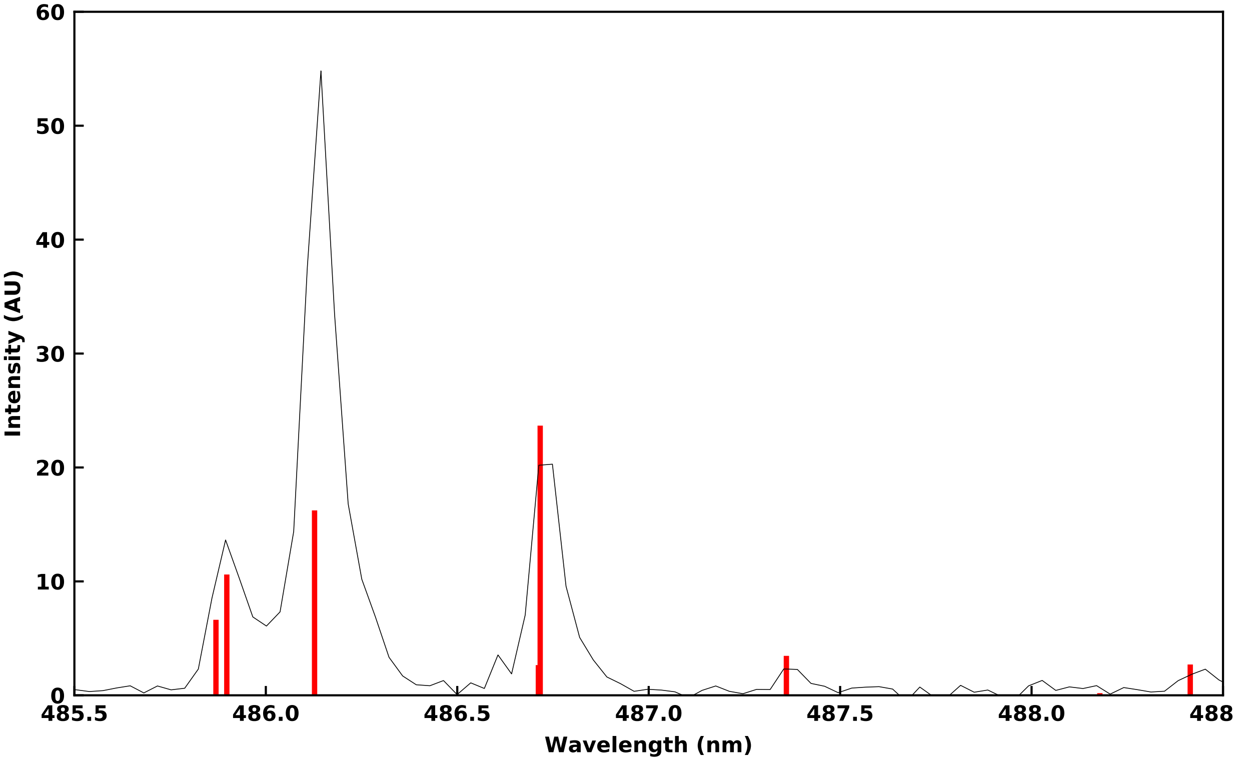

Figure B.12: CTH comparison to CR N III modeling

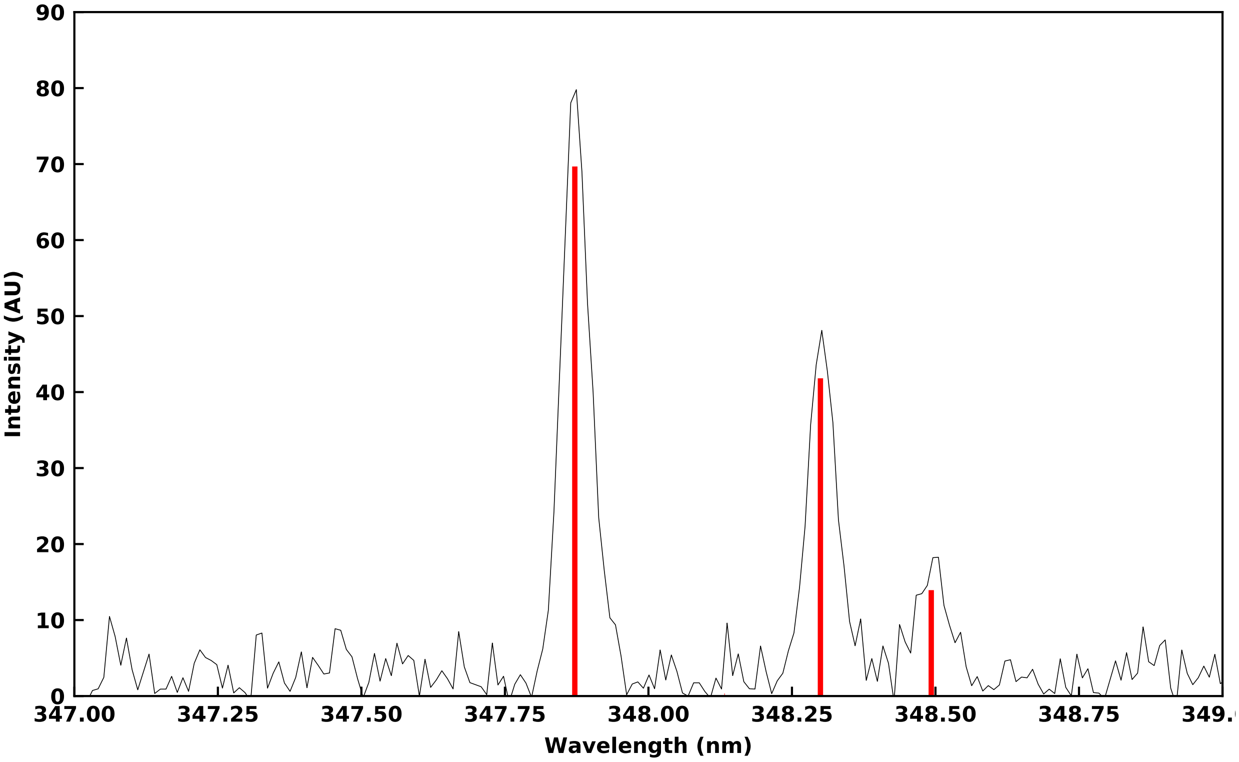

Figure B.13: CTH comparison to CR N IV modeling

Table B.6: O II spectral lines identified in CTH

NIST Wavelength (nm)	Upper Level	Lower Level
371.274	$2\mathrm{s}^2 2p^2(3P)3p(^4\mathrm{S}_{3/2})$	$2\mathrm{s}^2 2p^2(3P)3s(^4\mathrm{P}_{1/2})$
372.732	$2\mathrm{s}^2 2p^2(3P)3p(^4\mathrm{S}_{3/2})$	$2\mathrm{s}^2 2p^2(3P)3s(^4\mathrm{P}_{3/2})$
374.948	$2\mathrm{s}^2 2p^2(3P)3p(^4\mathrm{S}_{3/2})$	$2\mathrm{s}^2 2p^2(3P)3s(^4\mathrm{P}_{5/2})$
394.504	$2\mathrm{s}^2 2p^2(3P)3p(^2\mathrm{P}_{3/2})$	$2\mathrm{s}^2 2p^2(3P)3s(^2\mathrm{P}_{1/2})$
397.326	$2\mathrm{s}^2 2p^2(3P)3p(^2\mathrm{P}_{3/2})$	$2\mathrm{s}^2 2p^2(3P)3s(^2\mathrm{P}_{3/2})$
398.271	$2\mathrm{s}^2 2p^2(3P)3p(^2\mathrm{P}_{1/2})$	$2\mathrm{s}^2 2p^2(3P)3s(^2\mathrm{P}_{3/2})$
406.962	$2\mathrm{s}^2 2p^2(3P)3d(^4\mathrm{F}_{3/2})$	$2\mathrm{s}^2 2p^2(3P)3p(^4\mathrm{D}_{1/2})$
406.988	$2\mathrm{s}^2 2p^2(3P)3d(^4\mathrm{F}_{5/2})$	$2\mathrm{s}^2 2p^2(3P)3p(^4\mathrm{D}_{3/2})$
407.215	$2\mathrm{s}^2 2p^2(3P)3d(^4\mathrm{F}_{7/2})$	$2\mathrm{s}^2 2p^2(3P)3p(^4\mathrm{D}_{5/2})$
407.586	$2\mathrm{s}^2 2p^2(3P)3d(^4\mathrm{F}_{9/2})$	$2\mathrm{s}^2 2p^2(3P)3p(^4\mathrm{D}_{7/2})$
441.49	$2\mathrm{s}^2 2p^2(3P)3p(^2\mathrm{D}_{5/2})$	$2\mathrm{s}^2 2p^2(3P)3s(^2\mathrm{P}_{3/2})$
441.698	$2\mathrm{s}^2 2p^2(3P)3p(^2\mathrm{D}_{3/2})$	$2\mathrm{s}^2 2p^2(3P)3s(^2\mathrm{P}_{1/2})$
463.886	$2\mathrm{s}^2 2p^2(3P)3p(^4\mathrm{D}_{3/2})$	$2\mathrm{s}^2 2p^2(3P)3s(^4\mathrm{P}_{1/2})$
464.181	$2\mathrm{s}^2 2p^2(3P)3p(^4\mathrm{D}_{5/2})$	$2\mathrm{s}^2 2p^2(3P)3s(^4\mathrm{P}_{3/2})$
464.913	$2\mathrm{s}^2 2p^2(3P)3p(^4\mathrm{D}_{7/2})$	$2\mathrm{s}^2 2p^2(3P)3s(^4\mathrm{P}_{5/2})$
465.084	$2\mathrm{s}^2 2p^2(3P)3p(^4\mathrm{D}_{1/2})$	$2\mathrm{s}^2 2p^2(3P)3s(^4\mathrm{P}_{1/2})$
466.163	$2\mathrm{s}^2 2p^2(3P)3p(^4\mathrm{D}_{3/2})$	$2\mathrm{s}^2 2p^2(3P)3s(^4\mathrm{P}_{3/2})$
467.623	$2\mathrm{s}^2 2p^2(3P)3p(^4\mathrm{D}_{5/2})$	$2\mathrm{s}^2 2p^2(3P)3s(^4\mathrm{P}_{5/2})$
672.139	$2\mathrm{s}^2 2p^2(3P)3p(^2\mathrm{S}_{1/2})$	$2\mathrm{s}^2 2p^2(3P)3s(^2\mathrm{P}_{3/2})$

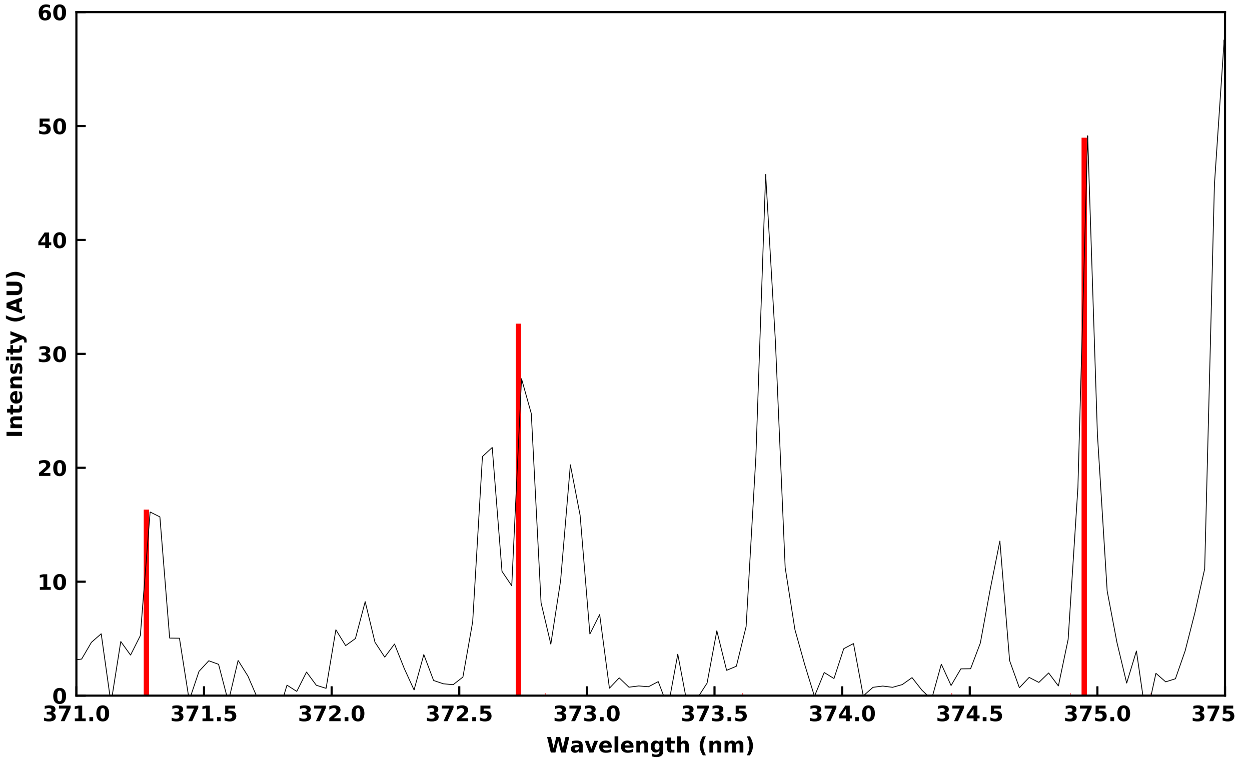

Figure B.14: CTH comparison to CR O II modeling

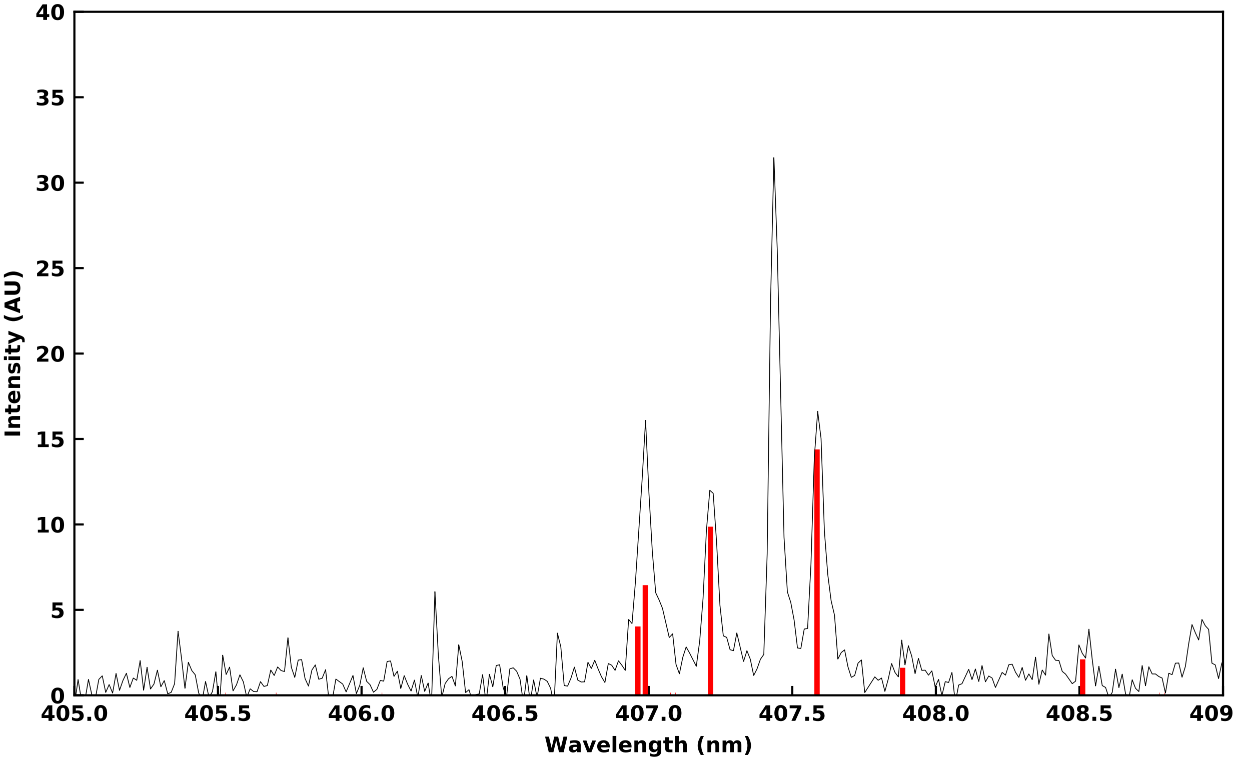

Figure B.15: CTH comparison to CR O II modeling

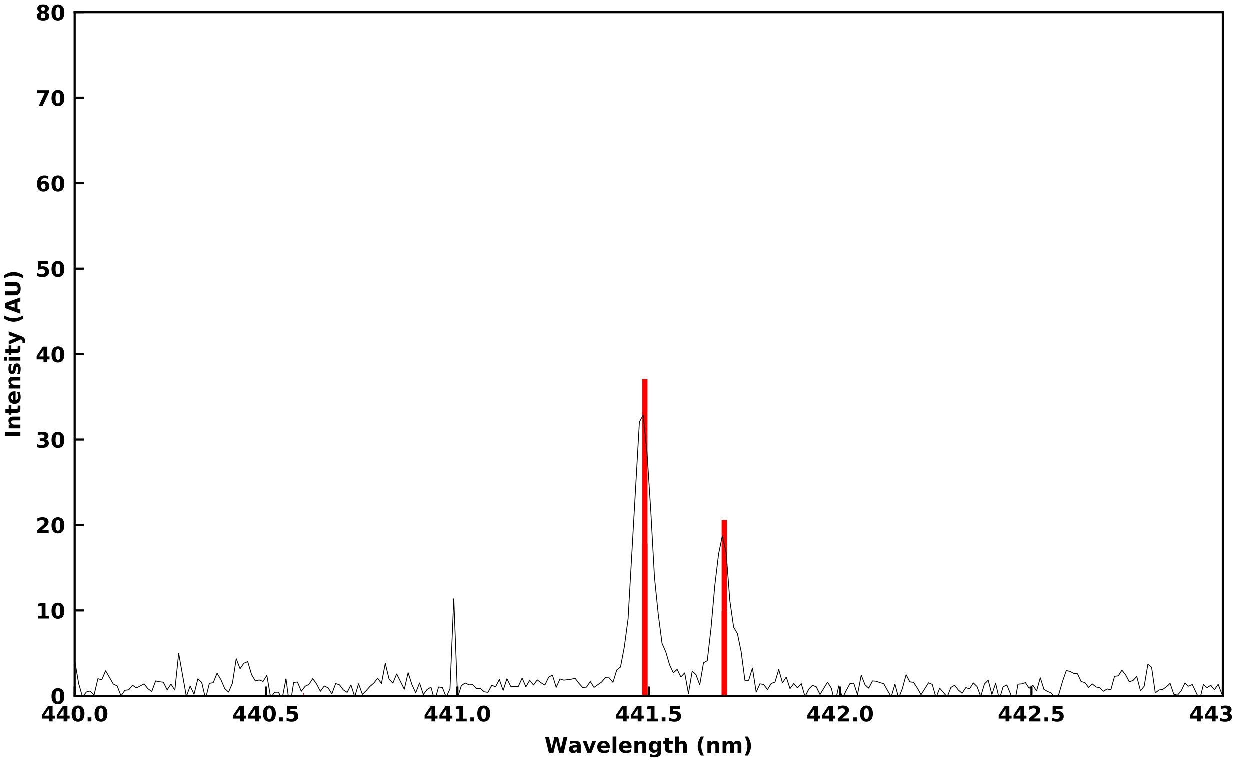

Figure B.16: CTH comparison to CR O II modeling

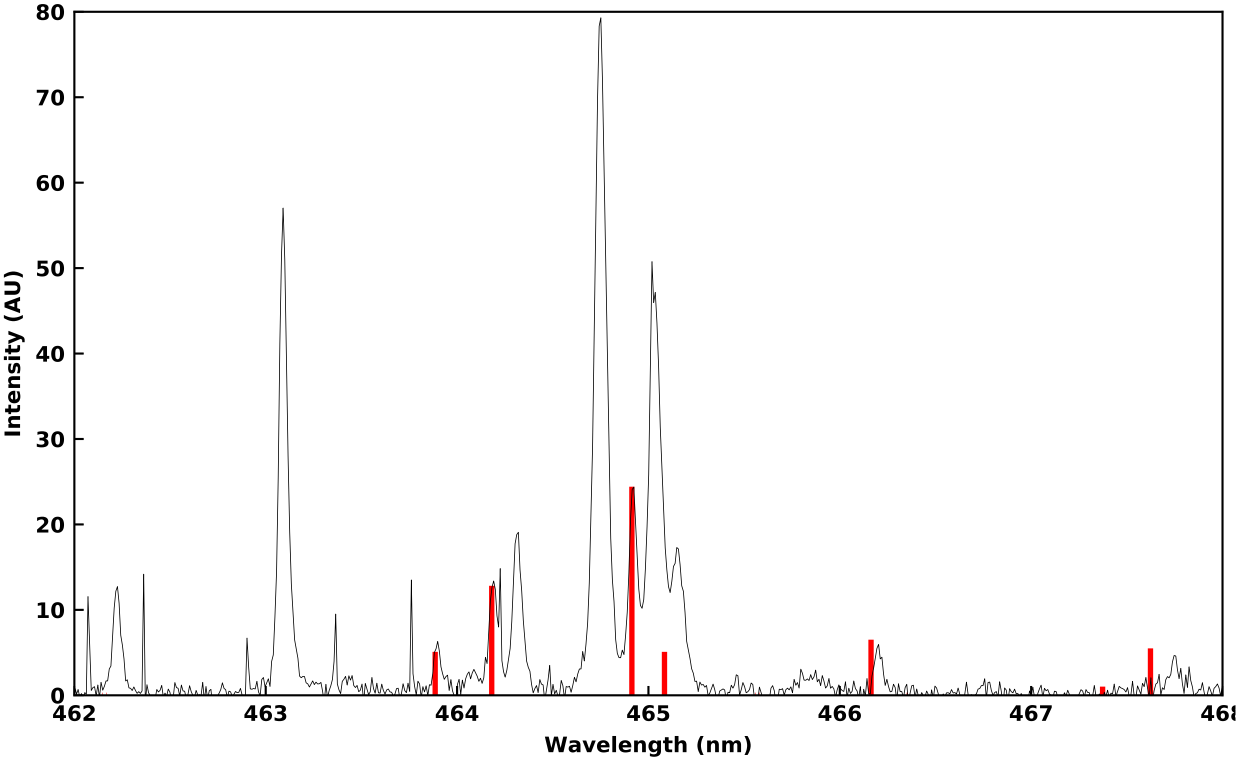

Figure B.17: CTH comparison to CR O II modeling

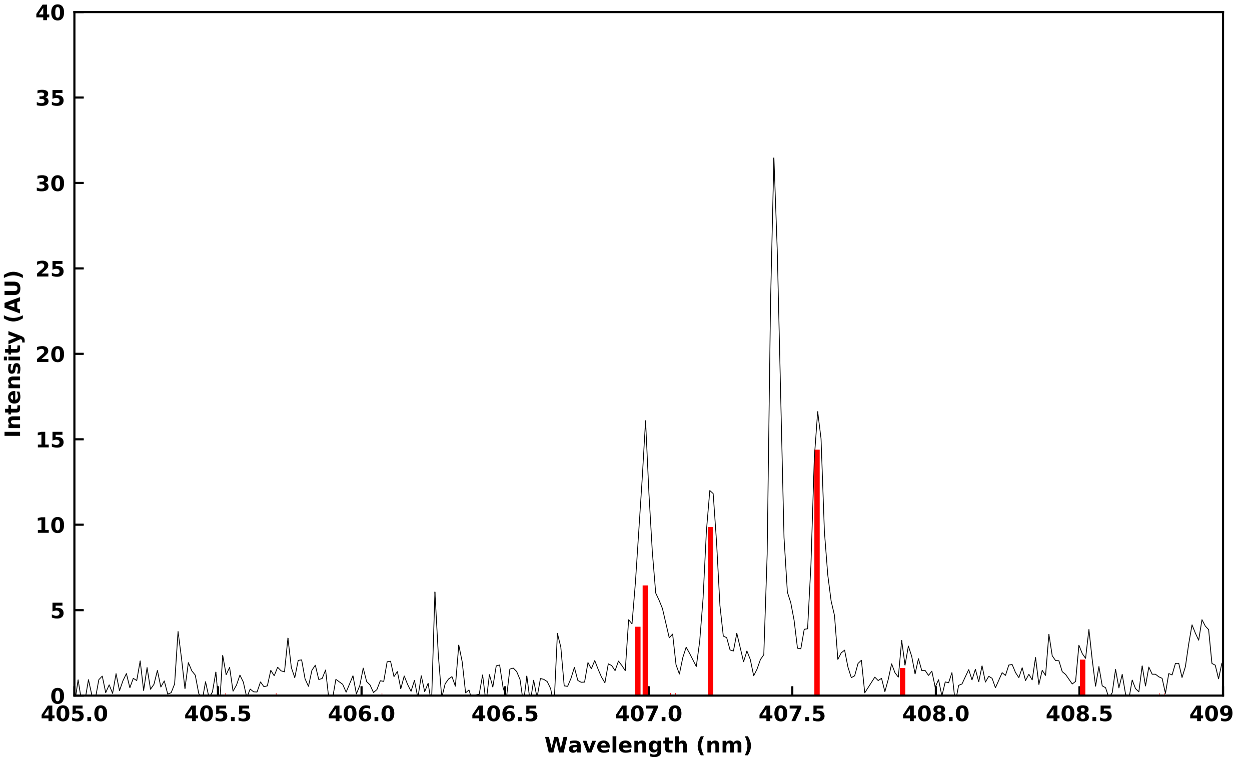

Figure B.18: CTH comparison to CR O II modeling

Table B.7: O III spectral lines identified in CTH

NIST Wavelength (nm)	Upper Level	Lower Level
245.497	$2s^22p(2P)3p(^1S_0)$	$2s^22p(2P)3s(^1P_1)$
298.378	$2s^22p(2P)3p(^1D_2)$	$2s^22p(2P)3s(^1P_1)$
304.299	$2s^22p(2P)3p(^3P_0)$	$2s^22p(2P)3s(^3P_1)$
304.71	$2s^22p(2P)3p(^3P_2)$	$2s^22p(2P)3s(^3P_2)$
305.928	$2s^22p(2P)3p(^3P_1)$	$2s^22p(2P)3s(^3P_2)$
375.47	$2s^22p(2P)3p(^3D_2)$	$2s^22p(2P)3s(^3P_1)$
375.723	$2s^22p(2P)3p(^3D_1)$	$2s^22p(2P)3s(^3P_0)$
375.988	$2s^22p(2P)3p(^3D_3)$	$2s^22p(2P)3s(^3P_2)$
377.403	$2s^22p(2P)3p(^3D_1)$	$2s^22p(2P)3s(^3P_1)$
379.127	$2s^22p(2P)3p(^3D_2)$	$2s^22p(2P)3s(^3P_2)$
559.225	$2s^22p(2P)3p(^1P_1)$	$2s^22p(2P)3s(^1P_1)$

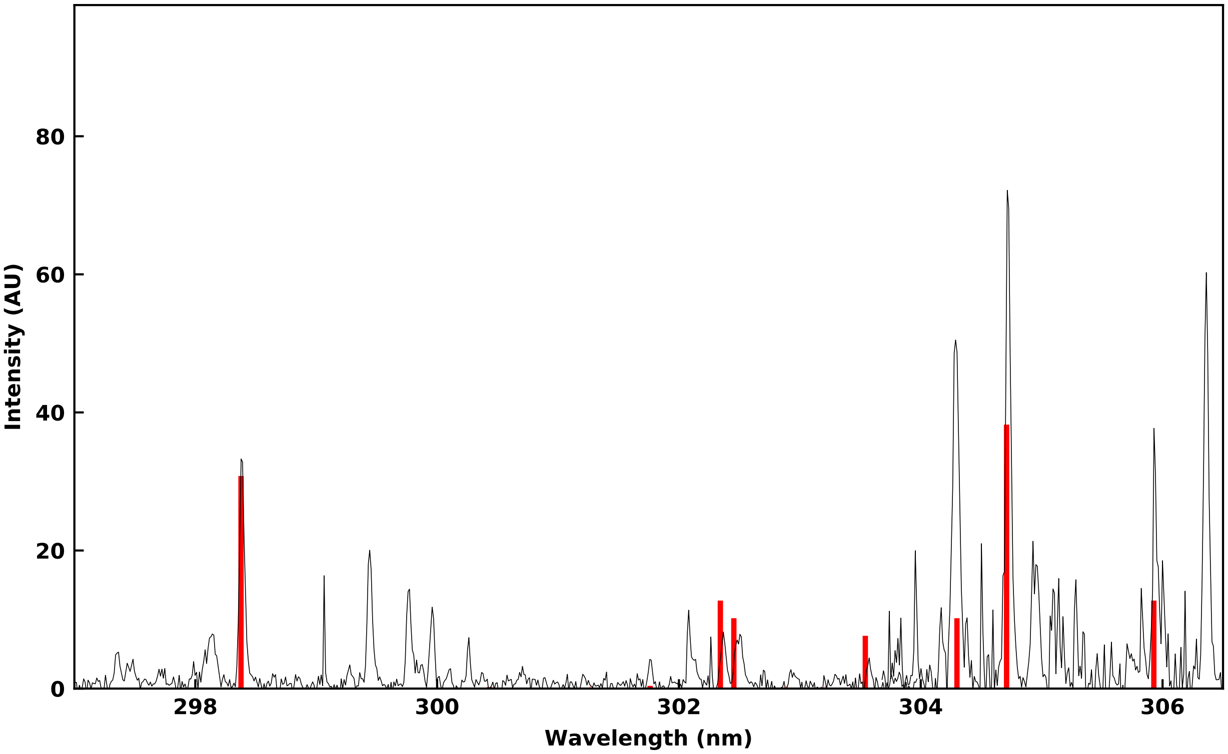

Figure B.19: CTH comparison to CR O III modeling

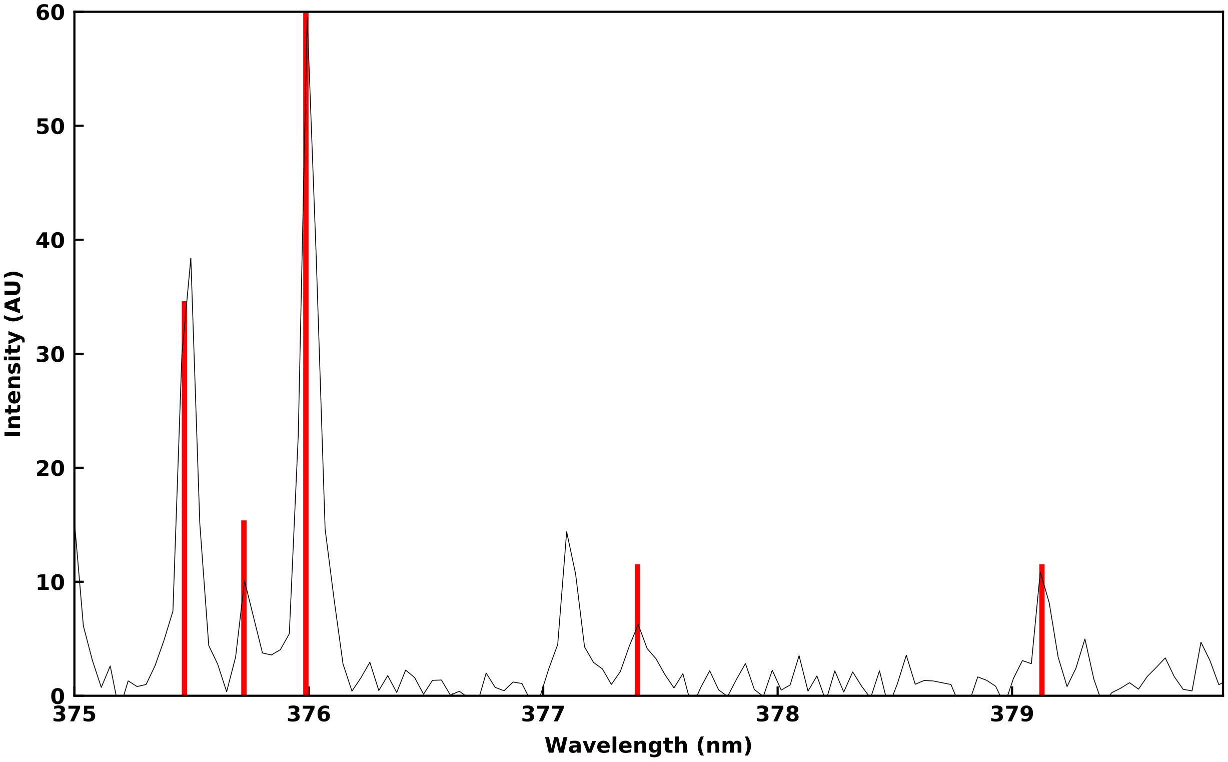

Figure B.20: CTH comparison to CR O III modeling

Figure B.21: CTH comparison to CR O IV modeling

Table B.8: O IV spectral lines identified in CTH

NIST Wavelength (nm)	Upper Level	Lower Level
228.558	$2p^2(3P)3d(^4\mathrm{P}_{3/2})$	2s2p(3P)4d ($^4\mathrm{P}_{1/2}$)
249.347	2s2p(1P)3p ($^2\mathrm{S}_{1/2}$)	2s2p(3P)3d ($^2\mathrm{P}_{1/2}$)
249.375	2s2p(3P)3p ($^4\mathrm{P}_{5/2}$)	2s2p(3P)3s ($^4\mathrm{P}_{3/2}$)
249.927	2s2p(3P)3p ($^4\mathrm{P}_{1/2}$)	2s2p(3P)3s ($^4\mathrm{P}_{1/2}$)
250.181	2s2p(3P)3p ($^4\mathrm{P}_{3/2}$)	2s2p(3P)3s ($^4\mathrm{P}_{3/2}$)
250.773	2s2p(3P)3p ($^4\mathrm{P}_{1/2}$)	2s2p(3P)3s ($^4\mathrm{P}_{3/2}$)
250.922	2s2p(3P)3p ($^4\mathrm{P}_{5/2}$)	2s2p(3P)3s ($^4\mathrm{P}_{5/2}$)
251.737	2s2p(3P)3p ($^4\mathrm{P}_{3/2}$)	2s2p(3P)3s ($^4\mathrm{P}_{5/2}$)
306.343	$2s^2 3p(^2\mathrm{P}_{3/2})$	$2s^2 3s(^2\mathrm{S}_{1/2})$
307.16	$2s^2 3p(^2\mathrm{P}_{1/2})$	$2s^2 3s(^2\mathrm{S}_{1/2})$
338.121	2s2p(3P)3p ($^4\mathrm{D}_{5/2}$)	2s2p(3P)3s ($^4\mathrm{P}_{3/2}$)
338.121	2s2p(3P)3p ($^4\mathrm{D}_{5/2}$)	2s2p(3P)3s ($^4\mathrm{P}_{3/2}$)
339.019	2s2p(3P)3p ($^4\mathrm{D}_{1/2}$)	2s2p(3P)3s ($^4\mathrm{P}_{1/2}$)
339.68	2s2p(3P)3p ($^4\mathrm{D}_{3/2}$)	2s2p(3P)3s ($^4\mathrm{P}_{3/2}$)
340.97	2s2p(3P)3p ($^4\mathrm{D}_{5/2}$)	2s2p(3P)3s ($^4\mathrm{P}_{5/2}$)
372.594	2s2p(3P)3d ($^4\mathrm{F}_{5/2}$)	2s2p(3P)3p ($^4\mathrm{D}_{3/2}$)
372.594	2s2p(3P)3d ($^4\mathrm{F}_{5/2}$)	2s2p(3P)3p ($^4\mathrm{D}_{3/2}$)
372.903	2s2p(3P)3d ($^4\mathrm{F}_{7/2}$)	2s2p(3P)3p ($^4\mathrm{D}_{5/2}$)
373.668	2s2p(3P)3d ($^4\mathrm{F}_{3/2}$)	2s2p(3P)3p ($^4\mathrm{D}_{3/2}$)
373.685	2s2p(3P)3d ($^4\mathrm{F}_{9/2}$)	2s2p(3P)3p ($^4\mathrm{D}_{7/2}$)

Table B.9: O V spectral lines identified in CTH

NIST Wavelength (nm)	Upper Level	Lower Level
278.101	$1s^2 2s3p(^3\mathrm{P}_2)$	$1s^2 2s3s(^3\mathrm{S}_1)$
278.699	$1s^2 2s3p(^3\mathrm{P}_1)$	$1s^2 2s3s(^3\mathrm{S}_1)$
278.985	$1s^2 2s3p(^3\mathrm{P}_0)$	$1s^2 2s3s(^3\mathrm{S}_1)$

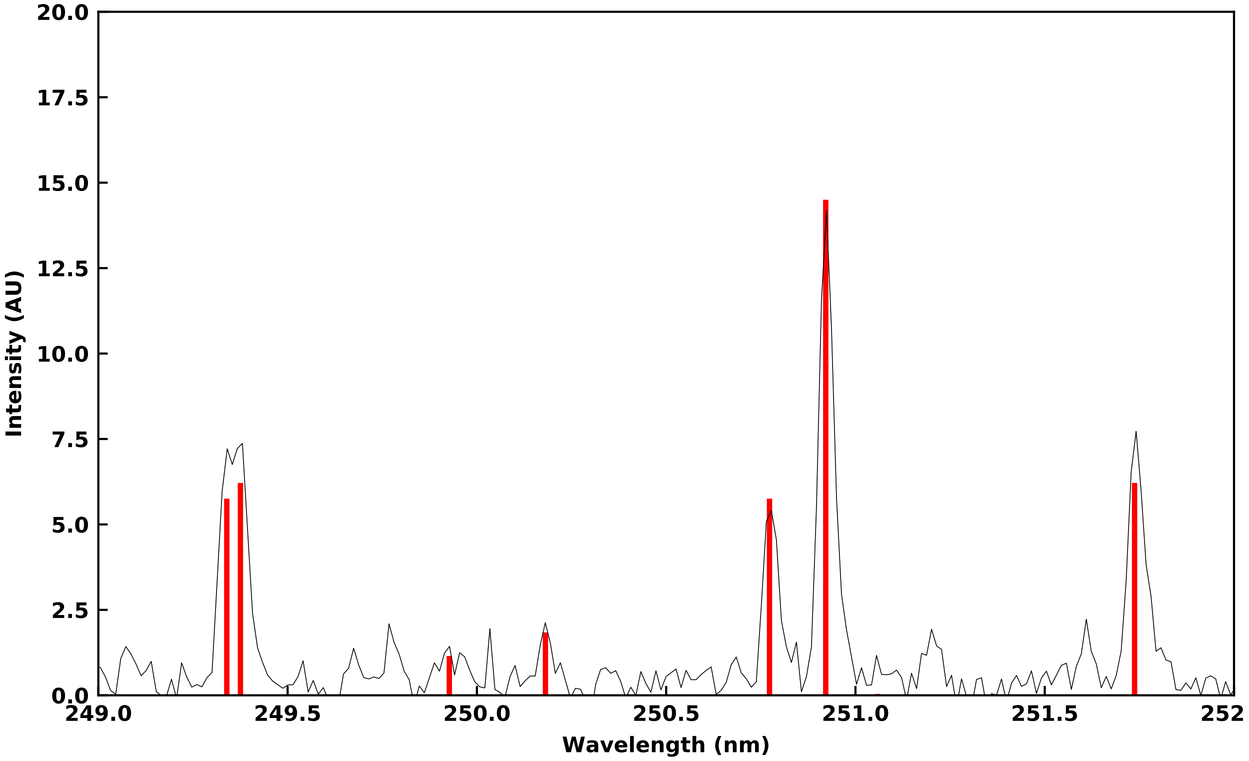

Figure B.22: CTH comparison to CR O IV modeling

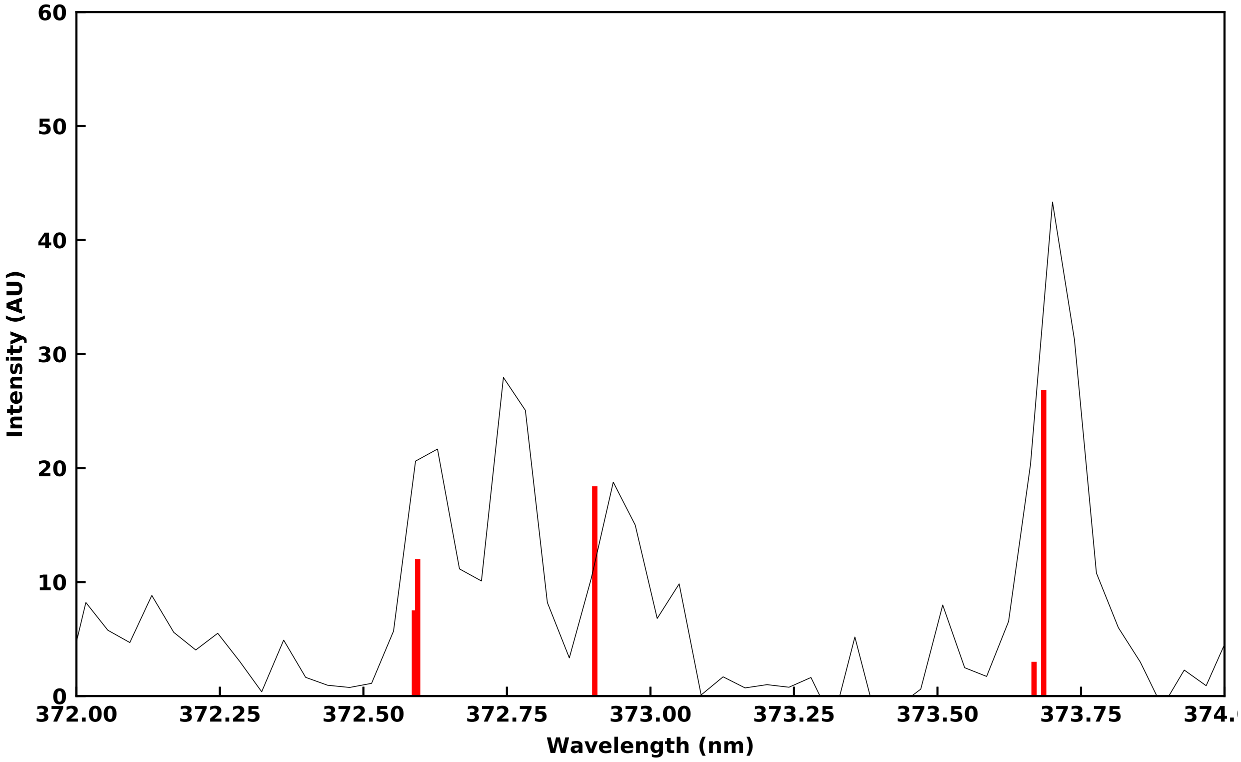

Figure B.23: CTH comparison to CR O IV modeling

Table B.10: Table of W I emission lines observed in CTH along with level identifications where possible. Spectral lines that were either not in the *R*-matrix calculation or spectral lines that came from levels that could not be confidently shifted to NIST energies have "No ID" for the level identification. The comment column states why the spectral line is included in the appendix instead of Chapter 4.

NIST Wavelength (nm)	Upper Level	Lower Level	Comment
246.279	$5p^6 5d^5 6s$ ($^1D_2$)	$5p^6 5d^4 6s^2$ ($^5D_1$)	Blend
248.013	$5d^4 6s6p$ ($^5F_2$)	$5p^6 5d^4 6s^2$ ($^5D_1$)	Blend
294.739	No ID	No ID	Not in WDX
304.969	$5d^4 6s6p$ ($^3F_2$)	$5p^6 5d^5 6s$ ($^7S_3$)	Blend (N V)
306.493	$5d^3 6s^2 6p$ ($^3G_3$)	$5p^6 5d^4 6s^2$ ($^5D_2$)	Blend
308.483	No ID	No ID	Not in WDX
308.491	$5d^4 6s6p$ ($^5F_2$)	$5p^6 5d^4 6s^2$ ($^5D_1$)	Blend
314.140	No ID	No ID	Not in WDX
321.556	$5d^3 6s^2 6p$ ($^5F_5$)	$5p^6 5d^4 6s^2$ ($^5D_4$)	Blend
325.966	$5d^4 6s6p$ ($^5H_3$)	$5p^6 5d^4 6s^2$ ($^5D_3$)	Blend
328.220	$5d^4 6s6p$ ($^1H_5$)	$5p^6 5d^4 6s^2$ ($^5D_4$)	Blend (O III)
331.139	No ID	No ID	Not in WDX
332.620	No ID	No ID	Not in WDX
333.169	$5d^4 6s6p$ ($^3F_4$)	$5p^6 5d^4 6s^2$ ($^3D_3$)	Blend
404.559	$5d^4 6s6p$ ($^5F_2$)	$5p^6 5d^5 6s$ ($^7S_3$)	Blend (Ar II)
407.061	$5d^4 6s6p$ ($^7P_2$)	$5p^6 5d^4 6s^2$ ($^5D_1$)	Blend (O II)
407.436	$5d^4 6s6p$ ($^7D_3$)	$5p^6 5d^5 6s$ ($^7S_3$)	Blend (C II)
410.270	$5d^4 6s6p$ ($^5D_3$)	$5p^6 5d^4 6s^2$ ($^5D_4$)	Blend (N III)

Table B.11: Table of W II emission lines observed in CTH experiments along with level identifications where possible. Note that the final WD1 calculation has not yet been completed, this might more confidence in these W II emission lines.

NIST Wavelength (nm)	Upper Level	Lower Level	Comment
257.144	$5d^4(^5D)6p$ ($^6F_{5/2}$)	$5d^4(^5D)6s$ ($^6D_{5/2}$)	WD1 not strong
265.803	$5d^4(^5D)6p$ ($^6F_{3/2}$)	$5d^4(^5D)6s$ ($^6D_{3/2}$)	WD1 not strong
266.433		$5d^4(^5D)6s$ ($^6H_{1/2}$)	WD1 not strong
269.771	$5d^4(^5D)6s$ ($^6D_{3/2}$)		WD1 not strong
276.426	$5d^4(^5D)6s$ ($^6D_{1/2}$)		WD1 not strong
277.650			WD1 not strong
364.141			WD1 not strong

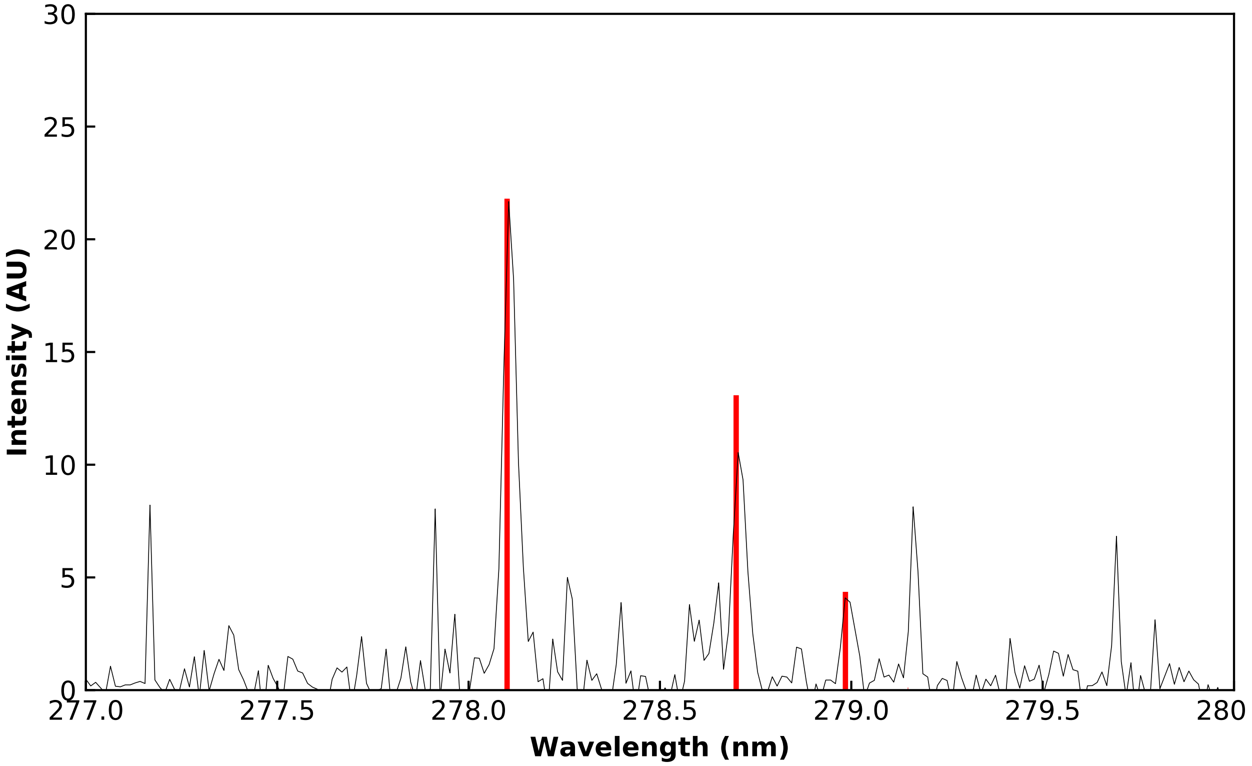

Figure B.24: CTH comparison to CR O V modeling

Table B.12: Table of W III emission lines observed in CTH experiments along with level identifications where possible and confidence.

NIST Wavelength (nm)	Upper Level	Lower Level	Comment
203.761			No Calculation
207.835			No Calculation
209.465			No Calculation
215.216			No Calculation
216.090			No Calculation
216.379			No Calculation
219.305			No Calculation
223.125			No Calculation
225.601			No Calculation
227.045	$5d^3(4F)6p\ (^5F_2)$	$5d^3(4P)6s\ (^5P_1)$	No Calculation
257.957	$5d^3(4F)6p\ (^5F_5)$	$5d^3(2H)6s\ (^3H_4)$	No Calculation

Appendix C

Hardware drawing and descriptions

C.1 Spectrometer control software and calibration

The spectrometer is controlled with the Python code spec_save.py.

This in addition to making calls the individual classes to control the Isoplane 320 spectrometer (spec_mono.py) and the Andor Newton 920 camera (spec_cam.py), the class stores all relevant data for the spectrometer, camera and spectral data. The script can be run in two different operational modes. First, the spectrometer can be controlled from a interactive Python prompt. This operational mode would generally be used for alignment or operation where user input needed but a trigger is not needed. The second mode runs the spectrometer in a producer-consumer manner where one thread controls the spectrometer and the other allows the user to access data as well as change spectrometer parameters. The user is still able to interact with a Python prompt and all of the data produced from the spectrometer in the first process. A second process is run in a while loop that loads spectrometer settings from the specdata dictionary that were modified in the first process and then waits for a trigger.

C.1.1 Isoplane 320 spectrometer control software

The Acton IsoPlane spectrometer detailed in Section 2.4 can be controlled using Princeton Instruments' LightField, WinSpec or SpectraSense software. While these programs provide a prebuilt interface for controlling the spectrometer, they can not be easily integrated into a custom control program to control both the spectrometer and the Andor camera. The spectrometer can also be controlled from a computer using serial commands over a USB interface. A custom python interface has been written to send serial commands over the

USB interface, this allows the user choose the which of the three gratings to be used, the central grating position and width of the motorized slit.

The spectrometer wavelength window is changed with the GOTO command.[27] This command specifies the central wavelength at the output of the spectrometer. The command allows the user to choose the wavelength for a wavelength window. The GOTO command accepts destination wavelength in nm as a floating number with precision up to three digits after the decimal.

C.1.2 Andor Newton 920 control software

The Andor Newton 920 camera detailed in Section 2.4.2 is controlled via a USB interface through the Andor Software Development Kit (SDK). The SDK gives access to camera control through the dynamic link library which can be accessed through a variety of programming languages including C++. The SDK does not support Python, however, the C++ libraries can be accessed through Python with the use of Cython. Cython allows Python like coding practices but is compiled to C++ then automatically wraps the interface code producing modules that can be called directly from python. Cython facilitates wrapping the independent C++ interface to the SDK with python modules.

All of the user definable camera settings can be modified though the python interface. An extensive list of the camera settings is given in the Andor SDK User's guide[92] as well as detailed functionality of each SDK module. In most operational cases the user will change the sensor size of the camera, integration time, number of exposures to take within a shot and trigger operation.

C.1.3 Spectrometer dispersion calibration

The dispersion across the CCD at the exit plan of the spectrometer given a central wavelength setting (discussed in Section C.1.1) can be calculated with the dimensional parameters of the spectrometer, dimensional parameters of the CCD, grating grooves/mm, slit size and order of diffraction through the spectrometer (for this thesis always first order). This is calculated with the python script.py. While the calculated dispersion across the CCD is surprisingly accurate, an experimentally measured correction to the dispersion must be applied to the spectrometer to obtain wavelength accuracies that are acceptable for spectral line identification. The a new correction was obtained experimentally for the calculated dispersion every time the focus of the spectrometer was changed or the spectrometer was moved.

The experimental correction works by changing the central wavelength of a spectrometer so that a known spectral line is moved from being centered on pixel 0 to being centered on pixel 1023. This allow for the difference between the calculated position of the spectral line in pixels and experimental measured position of the spectral in pixels to be measured. The process for a few steps is shown in Figure C.1.

After this process has been run, a quadratic function is fit to the difference between the calculated and measured wavelength positions versus pixel number of the CCD. A quadratic function was chosen because it is the simplest function that looks like experimental data. A fit to the difference is shown in Figure C.2. This process can be done with any spectral known spectral line. The correction at all wavelengths has the same general concave up shape however, there is a slight wavelength dependence. Depending on the accuracy required for an experiment, it would best to choose calibration lines that are close to the wavelength range to be calibrated.

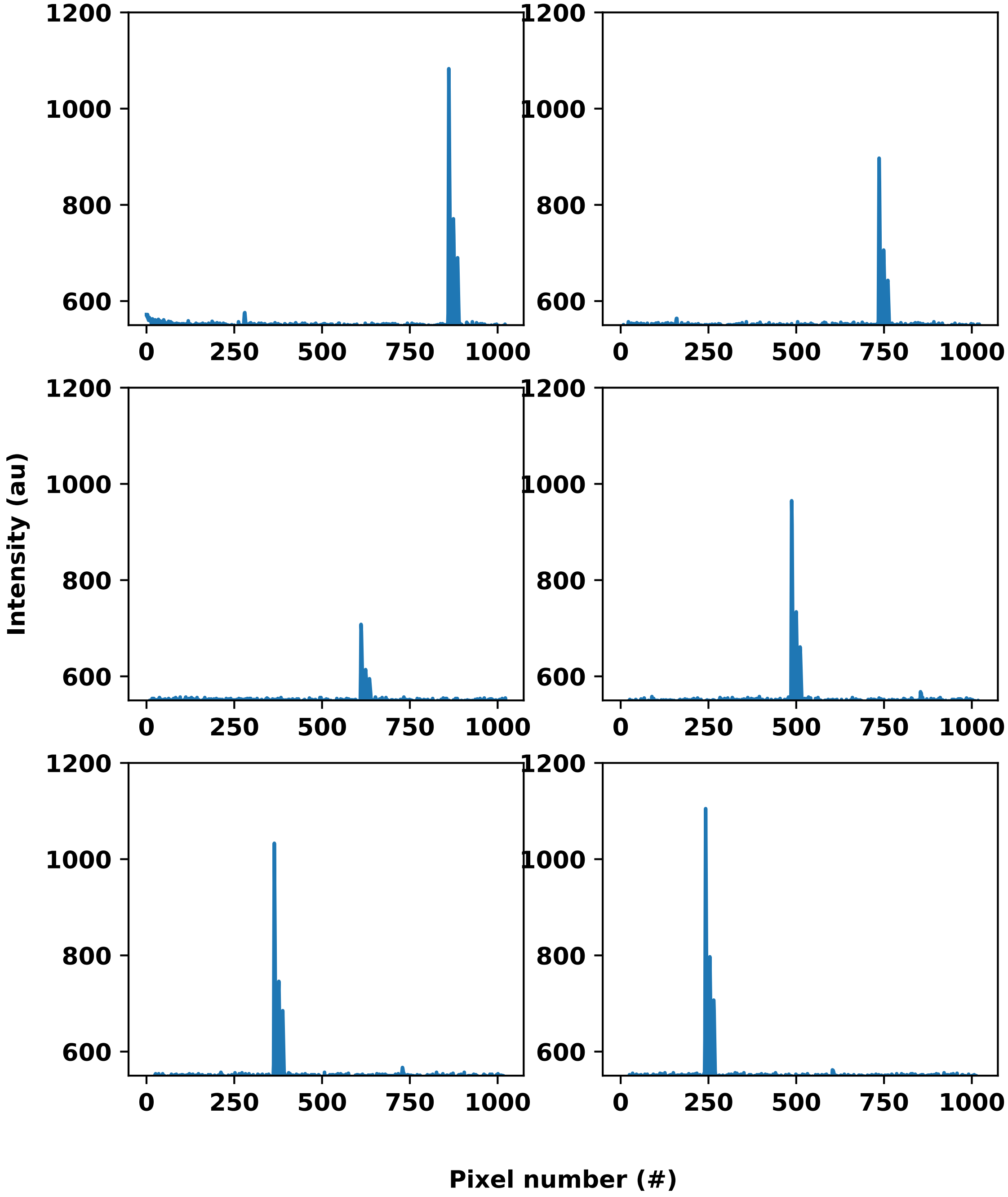

Figure C.1: Hg spectral feature at 265 nm moved across the CCD by moving the central wavelength of the spectrometer.

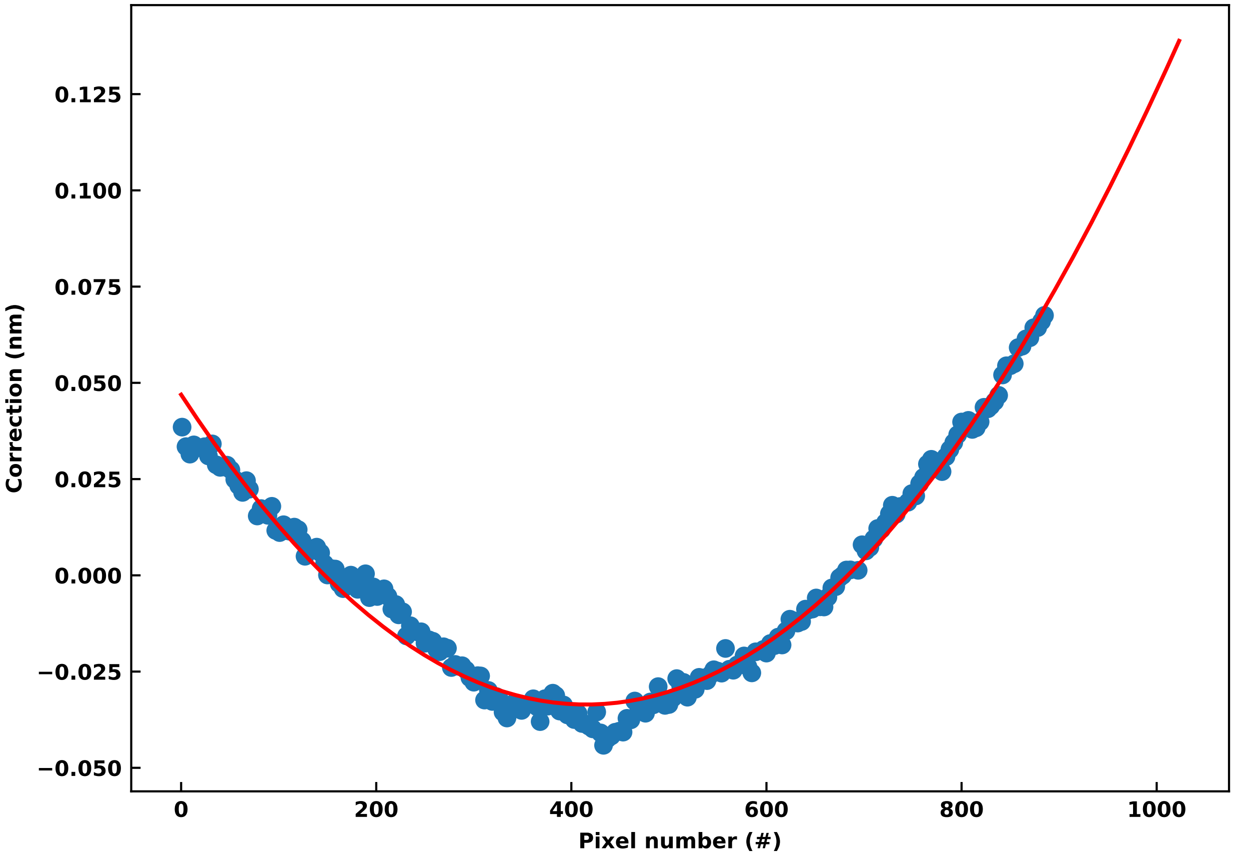

Figure C.2: Difference between the fitted centroid of the line versus the NIST observed wavelength value in nm for each central wavelength setting is shown as the blue scatter points. The quadratic fit to the scatter points is the red line. The correction to the calculated dispersion is then a function of CCD pixel number